

Non-contact acoustic excitation and associated nonlinear dynamics of small levitated objects

by Mehdi Akbarzadeh

Thesis submitted in fulfilment of the requirements for
the degree of

Doctor of Philosophy

under the supervision of Associated Prof. Sebastian Oberst, and
co- supervision of Associated Prof. Benjamin Halkon

University of Technology Sydney
Faculty of Engineering and IT
July 2024

CERTIFICATE OF ORIGINAL AUTHORSHIP

I, Mehdi Akbarzadeh, declare that this thesis is submitted in fulfilment of the requirements for the award of Doctor of Philosophy, in the School of Mechanical and Mechatronic Engineering / Faculty of Engineering and IT, at the University of Technology Sydney.

This thesis is wholly my own work unless otherwise referenced or acknowledged. In addition, I certify that all information sources and literature used are indicated in the thesis.

This document has not been submitted for qualifications at any other academic institution.

This research is supported by the Australian Government Research Training Program.

Signature: Production Note:
 Signature removed prior to publication.

Date: *30 June 2024*

ACKNOWLEDGMENT

First, I would like to express my heartfelt gratitude to my supervisor, Associate Professor Sebastian Oberst, for his invaluable guidance and support throughout this research. His profound knowledge of nonlinear dynamics and nonlinear time series analysis and serious attitude toward academic research will benefit me throughout my life. I also sincerely thank Associate Professor Ben Halkon, my co-supervisor, and Dr. Shahrokh Sepehrirahnama for their sincere help, support, and advice in my research.

I especially want to thank my lovely wife, Arezou, for her endless support during these years. Her emotional support, especially during the COVID-19 lockdown, has been a pillar of strength. She always inspired me with her hard work and persistence, encouraging me never to give up. This thesis will always remind me of her kindness, love, and encouragement. I would also like to thank my son, Ayrik. His presence was a source of joy and motivation throughout this journey. Finally, I want to express my deepest gratitude and love to my parents for their selfless support and continuous understanding.

During my candidature, I encountered significant and unforeseen challenges, primarily due to the global COVID-19 pandemic and subsequent border closures. The pandemic caused many interruptions and delays, significantly affecting my study plan. Due to the COVID-19 pandemic and the closure of Australia's borders, I was stuck in my home country, Iran, for 18 months. I had no access to my scholarship, university labs, or the academic environment during this time. The total duration of my PhD was 45 months, of which I spent 18 months (40%) in my home country. Despite these obstacles, I persevered and completed my research. This journey has been a testament to resilience and determination, and I am deeply grateful to everyone who supported me.

LIST OF CONTRIBUTION

Conference paper:

- 1- M. Akbarzadeh, S. Oberst, S. Sepehrirahnama, Y. K. Chiang, B. J. Halkon, A. Melnikov, D. A. Powell, A Numerical Study of Acoustic Radiation Forces for the Contactless Excitation of a Microcantilever, in NODYCON Conference Proceedings Series, Springer International Publishing, 2021, pp. 335 – 345.
- 2- M. Akbarzadeh, S. Oberst, S. Sepehrirahnama and B. Halkon, B., Application of SINDy for the discovery of governing equations of a trapped particle in an acoustic radiation force field, Conf. Proceedings of NODYCON 2023, Italy, Rome, 18-22 June 2023.
- 3- M. Akbarzadeh, S. Oberst, S. Sepehrirahnama and B. Halkon, Sensitivity and bifurcation analysis of an analytical model of a trapped object in an externally excited acoustic radiation force field, Conf. Proceedings of NOVEM23. Auckland, 1-10.
- 4- M. Akbarzadeh, S. Oberst, S. Sepehrirahnama and B. Halkon, Modulated acoustic radiation force in a carrier standing wave, Virtual Conf. of Acoustofluidics 2021.

Poster:

- 1- M. Akbarzadeh, S. Oberst, S. Sepehrirahnama and B. Halkon, Recurrence plots for the analysis of nonlinear dynamical behaviour of a particle trapped in an external induced radiation force field, 10TH INTERNATIONAL SYMPOSIUM ON RECURRENCE PLOTS 2023, Tsukuba, Japan.

Journal paper:

- 1- M. Akbarzadeh, S. Oberst, and B. Halkon, Manipulation of an acoustically levitated object using externally excited standing waves, major revision submitted to JASA.

- 2- M. Akbarzadeh, B. Halkon, and S. Oberst, Sparse identification of nonlinear dynamics applied to the levitation of acoustically large objects, in preparation for submission.
- 3- M. Akbarzadeh, S. Oberst, and B. Halkon, Nonlinear dynamical analysis of a particle trapped in an acoustic radiation force in a carrier standing wave, in preparation for submission.

TABLE OF CONTENT

CERTIFICATE OF ORIGINAL AUTHORSHIP.....	ii
ACKNOWLEDGEMENTS.....	iii
LIST OF CONTRIBUTION	iv
TABLE OF CONTENT.....	vi
LIST OF FIGURES	x
LIST OF TABLES.....	xvii
NOMENCLATURE	xviii
ABSTRACT	xxiv
CHAPTER 1: LITERATURE REVIEW AND THESIS OUTLINE.....	1
1.1. Introduction.....	1
1.2. Mathematical description of acoustic radiation force.....	2
1.2.1. Homotopy perturbation method.....	2
1.2.2. Eulerian mean excess pressure.....	3
1.2.3. Reynolds stress.....	6
1.3. Literature review.....	8
1.3.1. Static (time averaging) component.....	9
1.3.2. Dynamic (time varying) component.....	16
1.4. Application of acoustic radiation forces in non-contact excitation and particle manipulation.....	18
1.4.1. Dual-frequency ultrasound beams.....	18
1.4.2. Non-contact excitation.....	20
1.4.3. Numerical study: contactless excitation of microcantilever.....	22
1.4.4. Particle manipulation and acoustic levitation.....	27
1.5. Research motivation and gaps.....	31

1.5.1. Aim and objectives.....	32
1.5.2. Research questions.....	34
1.5.3. Thesis outline.....	34
CHAPTER 2: VIBRATION CONTROL OF A LEVITATED OBJECTS THROUGH EXTERNAL EXCITATION.....	37
2.1. Introduction.....	37
2.2. Gorkov formulation.....	37
2.3. Theoretical modelling.....	38
2.4. Numerical simulation.....	43
2.4.1. Numerical simulation based on finite element method (FEM).....	44
2.4.2. Numerical simulation based on time averaged method.....	48
2.5. Numerical and theoretical model validation.....	49
2.6. Effects of external excitation on acoustic radiation force sign.....	55
2.7. Nonlinear dynamical model of the acoustic radiation forces.....	56
2.8. Asymptotic methods.....	57
2.8.1. Nonlinear free undamped vibration analysis.....	58
2.8.1.1. Global residue harmonic balance method (GRHBM).....	58
2.8.1.2. Homotopy perturbation method with multiple expanding parameters (HPMEP).....	62
2.8.2. The effect of the viscosity on the nonlinear response.....	65
2.8.3. Parametric study of analytical solutions.....	68
2.9. Conclusion.....	72
CHAPTER 3: EXPERIMENTS AND STATISTICAL ANALYSIS.....	74
3.1. Introduction.....	74
3.2. Statistical model and Sobol sensitivity analysis.....	75

3.2.1. Optimizing time step selection in numerical solutions: A statistical approach.....	75
3.2.2. Sobol’s method of sensitivity analysis.....	77
3.3. Numerical frequency response and bifurcation diagram.....	79
3.4. Experimental analysis.....	82
3.4.1. Tiny-Lev and levitated object properties.....	83
3.4.2. Experimental set up.....	85
3.4.3. Filtering method in experimental time series data.....	87
3.4.4. Experimental verification.....	89
3.4.5. Experimental bifurcation diagram.....	94
3.5. Conclusion.....	98
CHAPTER 4: DATA-DRIVEN MODELLING FOR LARGE OBJECT MOTION.....	101
4.1. Introduction.....	101
4.2. SINDy algorithm.....	102
4.3. Nonlinear time series analysis techniques – system identification.....	105
4.3.1. Phase space reconstruction	105
4.3.2. Recurrence plot.....	106
4.3.3. Recurrence networks and motifs.....	107
4.4. Results from the application of the SINDy algorithm.....	107
4.4.1. Application of the SINDy algorithm to time series data based on the noise free theoretical model.....	107
4.4.2. Application of the SINDy algorithm to a time series model based on the noisy theoretical model.....	109
4.4.3. SINDy for acoustically small object: Experimental time series data.....	111

4.4.4. SINDy for acoustically large object: Experimental time series data.....	113
4.5. Results for nonlinear time series analysis - System identification.....	124
4.6. Conclusion.....	128
CHAPTER 5: CONCLUSION.....	130
5.1. Summery.....	131
5.2. Recommendations for future work.....	135
5.2.1. Multi-object dynamics.....	135
5.2.2. More analysis for SINDy coefficients and its library functions.....	136
5.2.3. Nonlinear dynamics and synchronization.....	136
REFERENCES.....	138
APPENDIX.....	156

LIST OF FIGURES

Fig. 1.1.	The interaction between incoming acoustic waves (with a specific frequency and wavelength, λ) and an object, resulting in scattered waves. This interaction creates an interference pattern, which generates an acoustic radiation force acting on the object.....	1
Fig. 1.2.	Boundary of acoustic radiation force for a) rigid object: the time-averaged radiation force on the object can be found by integrating the mean excess pressure over the object surface, S_0 , b) compressible object: the integration in Eq. (1.1) must be applied over the moving object surface, S	7
Fig. 1.3.	Scattered pressure distribution around the object according to numerical simulation, with magnification showing the finite element model in COMSOL Multiphysics to find radiation forces on a compressible sphere; adopted from [61].....	15
Fig. 1.4.	The dual-frequency ultrasound beam method, using two different frequencies (ω_a and ω_b), focused on a point to generate a dynamic radiation force.....	19
Fig. 1.5.	A comparison between a) first, b) second, and c) third resonance frequency for ultrasound radiation force and base excitation obtained in the Huber's experiment adopted from [36].....	23
Fig. 1.6.	a) A 3D Finite element model of microcantilever, b) Three first mode shapes c) A 3D finite element model of microcantilever surrounded in a fluid domain, adopted from [32].....	23
Fig. 1.7.	The frequency response of the lowest three resonances of the microcantilever obtained by two excitation methods: a, b) boundary load excitation (a: displacement, b: phase) and c, d) acoustic wave excitation (c: displacement, d: phase), adopted from [32].....	25
Fig. 1.8.	A comparison between numerical simulation and some points of the experimental results presented in [37] near a) the first resonance frequency and b) the second resonance frequency when the amplitude of the boundary load excitation in numerical simulation is F_0	26

Fig. 1.9.	The sign of the acoustic contrast factor, ϕ , determines whether a particle is attracted to or repelled from a pressure node in a plane standing wave field with wavelength of λ	29
Fig. 2.1.	A spherical object within an acoustic radiation force field with external sinusoidal excitation. (a) Schematic of an oscillatory object with mass M_o oscillating around its equilibrium position, 0; (b) mechanical model with nonlinear stiffness (k_s). $Z_o = A_o \sin(\omega_o t)$ denotes the object oscillation caused by external disturbance, $Z_{ex} = A_{ex} \sin(\omega_{ex} t)$, with its (c) experimental set up; c) photo of experimental setup with levitated object.....	39
Fig. 2.2.	A 2D axi-symmetrical finite element.....	45
Fig. 2.3.	The 3D model of a spherical object immersed in a water domain.....	47
Fig. 2.4.	a) Velocity field, and b) scattered pressure around the object in the fluid domain ($r = 20 \mu\text{m}$).....	48
Fig. 2.5.	Simulation steps in COMSOL Multiphysics to calculate \bar{F}_{rad} for a spherical object with a radius of $10 \mu\text{m}$, a) Modelling, b) meshing, c) velocity field (m/s), and d) sound pressure level (dB).....	48
Fig. 2.6.	A comparison of obtained acoustic radiation force (ARF) between a) King formulation [62], FEM (our 3D COMSOL simulation presented in section 2.4.1), and Gorkov formulation [64] versus the sphere radius, b) the same comparison plotted against the dimensionless parameter kr	50
Fig. 2.7.	Acoustic radiation force (ARF) vs the distance between object centre and the velocity node (VN) for a) an object with $r = 10 \mu\text{m}$, and b) $r = 40 \mu\text{m}$	50
Fig. 2.8.	The acoustic contrast factor for an oscillatory object trapped in an acoustic radiation force field using data provided in [118]. The non-zero mean value is for the time-averaged component of the radiation force which matches the results of Eqs. (2.22) and (2.23). The object's location corresponds to different spatial positions within the acoustic field during its oscillation, as the force is time-averaged and evaluated under steady-state conditions.....	51

Fig. 2.9.	The acoustic contrast factor and $\langle C_m(t)^2 \rangle$ with respect to the oscillation amplitude oscillation, showing the variation of \bar{F}_{rad} from positive to negative value. The vertical “dot-dash line” represents the theoretical limit for the maximum value of the external excitation amplitude.....	52
Fig. 2.10.	The symmetry in the field variables a) acoustic pressure, and b) velocity field, in case of acoustic radiation force cancellation when $r = 20 \mu\text{m}$ and $kA_0 = 1.202$	53
Fig. 2.11.	A comparison of \bar{F}_{rad} for some non-spherical objects using the current FEM study which shows similar behaviour to the spherical object in Fig. 2.9.....	54
Fig. 2.12.	A comparison of the acoustic radiation force function obtained from the current study, Eq. (2.22), FEM (Eq. (2.25)), and the time-averaged radiation force, Eq. (2.27), with respect to kr for an oscillating object, showing both (a) negative and (b) positive contrast factors as function of the oscillation amplitude kA_0 , and deviation occurs at $kr \sim 0.3$	55
Fig. 2.13.	a) The acoustic radiation force function, Y_{st} , plotted against non-dimensional value of object oscillation, A_0/r and b) The acoustic radiation force function, Y_{st} , plotted against non-dimensional value of object position, z/r [37].....	55
Fig. 2.14.	The nonlinear frequency deviation obtained by Eq. (2.87) for first order and second order of GRHBM and HPMPE.....	69
Fig. 2.15.	The effect of the higher order terms in Taylor series in expanding $\sin(\theta)$ in calculating natural frequency using Eq. (2.61).....	69
Fig. 2.16.	The effect of the density on the linear natural frequency according to the King model.....	70
Fig. 2.17.	The effect of the compressibility on the linear natural frequency.....	70
Fig. 2.18.	A comparison study between analytical solution obtained by AGM and numerical simulation for two different initial condition: a) $z(t = 0) = \lambda/8$, and b) $z(t = 0) = \lambda/16$	71
Fig. 2.19.	The effect of the viscosity on the a) phase and the b) nonlinear frequency deviation of oscillation for various initial condition	71

Fig. 3.1.	Time step convergence study using a box plot. The whiskers show the minimal and maximal values, the edges of the box indicate the 25 – and 75 – percentile the red line represents the median and the notches show the 95% confidence interval of the median. Non-overlapping notches show non-significant difference in median estimates of the relative error.....	77
Fig. 3.2.	Results of the variance-based sensitivity analysis when S_1 and S_T are the first-order and total sensitivity coefficient, respectively. Importance ranking of the coefficients in Eq. (2.35) by sensitivity analysis using uniformly distribution. The external excitation has the strongest influence on the C_3 coefficient in the equation of motion (Eq. (2.35)), C_2 is having a rather small influence on the dynamics.....	79
Fig. 3.3.	A comparison between the predicted frequency responses from Eq. (2.35) with the experimental results [118] for an object trapped in a standing wave levitator. The observed jump between different states indicates a softening behaviour. The theoretical predicted curve was generated by increasing the frequency, corresponding to the “sweep up” scenario in the experimental work.....	80
Fig. 3.4.	The bifurcation diagram for a spherical object trapped in an oscillating radiation force field using Eq. (2.35), $\omega_o = 10$ Hz. The chaotic (C) or quasi-periodic (QP) area from $A_{in} \sim 0$ to $A_{in} \sim 0.05$ indicates the intricate high-order periodic behaviour in low amplitude, the jump (J) phenomenon occurs at $A_{in} \sim 0.06$, period-doubling bifurcation (PDB) can be observed at $A_{in} \sim 0.5$ and increasing in periodic solutions or period adding bifurcations (PAB) occurs at $A_{in} > 0.7$	81
Fig. 3.5.	a) A single ultrasonic transducer, b) Simulation illustrating acoustic traps [125]. c) Visualization of traps exhibiting maximum strength in the middle. d) Image showcasing the Tiny-Lev apparatus with a spherical object levitated in mid-air.....	83
Fig. 3.6.	a) Ultrasonic transducers arranged on one plate of the Tiny-Lev, b) the tool used for inserting particles into the standing wave’s node, c) visual inspection process employing a ruler.....	84

Fig. 3.7.	a) The analytical balance device used for particle mass measurement, b) statistical box plot illustrating particle density.....	85
Fig. 3.8.	a) Entire Experimental setup located within the hemi-anechoic chamber. b) Schematic representation of the complete experimental setup.....	86
Fig. 3.9.	a) A segment of the measured time series data in the experimental work, b) the same time series data in Fig. 3.9a after applying the GHKSS filter, and c) zoomed-in area of a peak in the measured time series data, and d) the same peak after applying the GHKSS filter.....	89
Fig. 3.10.	Fig. 3.10. Linear relationship in period-1 of oscillation and more frequencies, which could relate to bifurcation phenomena in some frequencies. b-d) PSD of the object's response at points marked by arrows in, with the red line indicating the threshold for identifying dominant frequencies.....	90
Fig. 3.11.	Statistical analysis of a) frequency and b) phase difference, between external excitation and object response at various external excitation frequencies ($n = 20$ measurements). The notches indicate that phase and frequency differences are not significantly different anymore for frequencies greater than 20 Hz, and c) linear relationship between shaker input voltage and measured LDV signal on Tiny-Lev vibrations, and d) on spherical object response employing excitation frequencies ranging from 10 Hz to 100 Hz.....	91
Fig. 3.12.	Linear relationship between shaker input and LDV voltage for Tiny- Lev vibrations (10–100 Hz) with irregular x-axis intervals from manual adjustments.....	93
Fig. 3.13.	Fig. 3.13. Linear relationship between shaker input and LDV voltage for object vibrations (10–100 Hz) with irregular x-axis intervals due to manual adjustments.....	93
Fig. 3.14.	a) Levitated object in the Tiny-Lev on a vibrating shaker, with a red hue from LDV laser illumination; b) drilled hole in the Tiny-Lev's top plate showing the object; c) laser beam path through the hole.....	95

Fig. 3.15.	The bifurcation diagram for an acoustically small object ($kr < 1$) derived analytically from Eq. (2.35) (solid line), and experimental data (dots).....	96
Fig. 3.16.	The bifurcation diagram for an acoustically large object ($kr > 1$) derived analytically from Eq. 2.35 (solid line), and experimental data (dots).....	98
Fig. 4.1.	Schematic of SINDy algorithm to identify governing equation from nonlinear time series data including a time history of the states X and derivatives \dot{X} . $[\Xi]$ and $[\eta]$ are unknown coefficients.....	104
Fig. 4.2.	Error estimation values according to Eq. (4.7) evaluating the resilience of the SINDy algorithm to theoretical noisy time series data. Here, σ represents the standard deviation of the Gaussian noise deliberately added to the system.....	110
Fig. 4.3.	Nonlinear time series data a) the theoretical dynamical equation of motion and the b) measured by the LDV and collected by oscilloscope. This data set and a library of nonlinear functions of the state variables are used to determine the matrix coefficients of $[\Xi]$ and $[\eta]$ and c) sparse identified model.....	112
Fig. 4.4.	A comparison between a) the theoretical dynamical equation of motion and the b) experimental data which shows the s well-captured by sparse identified system and c) sparse identified model.....	113
Fig. 4.5.	Comparison of experimentally measured data and SINDy predictions using averaged coefficients from Table 4.2 with filtered data for example 1. The plot highlights the accuracy of the SINDy algorithm in predicting the system dynamics.....	115
Fig. 4.6.	PSD of original signal measured by LDV before applying filter, after applying filter and according to Eq. (4.13) for example 1.....	117
Fig. 4.7.	Comparison of experimentally measured data and SINDy predictions using averaged coefficients from Table 4.5 with filtered data for example 2.....	118

Fig. 4.8.	PSD of original signal measured by LDV before applying filter, after applying filter and according to Eq. (4.15) for example 2.....	118
Fig. 4.9.	Comparison of experimentally measured data and SINDy predictions using averaged coefficients from Table 4.6 with filtered data for example 3.....	120
Fig. 4.10.	PSD of original signal measured by LDV before applying filter, after applying filter and according to Eq. (4.16) for example 3.....	120
Fig. 4.11.	a) Bifurcation diagram for an acoustically large object: analytical (solid line) vs. experimental data (dots), showing discrepancies due to Gorkov's small-object assumption. b) Comparison of the SINDy results (red), and experimental data (blue), highlighting deviations at higher excitation amplitudes due to the polynomial-based library limitations. Some distinct regions with different dynamics are selected for further analysis.....	123
Fig. 4.12.	a) MI test for selecting time delay of τ and b) FNN functions for selecting embedding dimension of m , according to case studies presented in Table 4.5.....	125
Fig. 4.13.	Fig. 4.13. Motifs for a) regular harmonic motion related to network in Table 4.2: case 1, and b) irregular quasi-periodic motion related to network in Table 4.2: case 2.....	128

LIST OF TABLES

Table 1.1.	A comparison between King, Yosioka and Gorkov's formulation, $(kr \ll 1)$	9
Table 1.2.	Steps, aim and objectives of the thesis.....	33
Table 2.1.	Baseline parameters [61].....	46
Table 2.2.	Comparison of FEM perturbation result based on the 3D model with 2D-axisymmetric model and analytical results.....	49
Table 2.3.	Dimensions for calculating the acoustic radiation force using the 3D FEM for some simple nonspherical objects.....	54
Table 4.1.	Application of the SINDy algorithm to a time series model based on theoretical model taken from Chapter 2: Case studies, their coefficients extracted and phase portraits.....	109
Table 4.2.	Coefficient predicted by SINDy for case 1 according to four measurements.....	114
Table 4.3.	Coefficient predicted by SINDy for case 2 according to four measurements.....	117
Table 4.4.	Coefficient predicted by SINDy for case 3 according to four measurements.....	119
Table 4.5.	Three different filtered time series data and their PSD, obtained by measuring voltage by using LDV in the experimental setup, when A_{in} varies from 0.25 mm to 2.5 mm for an object with a radius of 1.87 mm , with the external excitation frequency of $\omega_{in} = 32$ Hz.....	125
Table 4.6.	Reconstructed phase space, RP, and RN for three case studies presented in Table 4.5.....	126

NOMENCLATURE

F_{rad}	Acoustic radiation force
S_{ij}	Acoustic radiation stress tensor
n_j	Normal vector on the surface
A	Object surface
$A(u)$	A general differential operator
$f(r)$	A known analytical function
Ω	Domain in Eq. (1.2)
$B\left(u, \frac{\partial u}{\partial n}\right)$	Boundary operator in Eq. (1.2)
Γ	Boundary of the domain Ω in Eq. (1.2)
P	Pressure
v	Velocity
ρ	Density
∇_i	Gradient operator
δ_{ij}	Kronecker delta
p	Embedding parameter in HPM
L	Linear part of the Eq. (1.2)
N	Nonlinear part of the Eq. (1.2)
$\nabla\phi$	Gradient of potential function of velocity

A/B	Fox-Wallace parameter in Eq. (1.13)
∇^2	Laplace operator
(r, θ, t)	Cylindrical coordinates in a plane
k	Wave number
V_p	Spherical object volume
E_{ac}	Acoustic energy density
P_a	Amplitude of the incident pressure field
z	Distance between the pressure node and the object centre
κ	Compressibility
c	Speed of sound
U	Force potential
$\langle P_{in} \rangle$	Time-averaged of incident pressure
$\langle V_{in} \rangle$	Time-averaged of incident velocity
f_1 and f_2	Monopole and dipole coefficients in Gorkov formula
(λ, μ)	Lame elastic constants
$\nabla = \frac{\partial}{\partial x_i} \vec{e}_i, i = 1, 2, 3$	Del operator
$\nabla \times (\cdot)$	Curl operator of (\cdot)
∇u	displacement gradient
(Ψ, Ω)	Field displacements

J_n	Bessel function of the first kind
a_n, b_n, c_n	Expansion coefficients
ε_n	Neumann factor
Y_n	Bessel function of the second kind
H_n	Hankel function of the second kind
σ_{ik}	Stress tensor
T	Absolute temperature in Eq. (1.36)
κ	Thermal conductivity in Eq. (1.36)
ω, f	Frequency
t	Time
a and r	Object radius
Y_{mn}	Dynamic radiation force function
φ	Phase-shift
η	The loss factor
ϕ	Acoustic contrast factor,
kx	Linearized acoustic radiation force
m and M_0	Mass
g	Gravity acceleration
$x, \dot{x}, \ddot{x}, \dots$	Displacement and its time derivatives

b_1 and b_2	Constants in Eq. (1.55)
ξ	Object's distance from a pressure node
λ	Acoustic wavelength
k_s	Nonlinear softening spring constant
$Z_o(t)$	Object's response
$Z_{ex}(t)$	External excitation
A_o	Object's amplitude
$C_1(t)$ and $C_2(t)$	Time components of the acoustic pressure
$\varphi(t)$	Phase modulation in the incident pressure field
γ_1 and γ_2	Constant coefficients in Eq. (2.17)
a_n and b_n	Amplitudes of the harmonic forces in Eq. (2.20)
\bar{F}_{rad}	Time averaged of acoustic radiation force
C_d	Drag coefficient
C_1, C_2, C_3	Constant coefficients in Eq. (2.35)
$\theta, \dot{\theta}, \ddot{\theta}$	Dimensionless displacement of object and its time derivatives
ΘF	Nonlinear amplitude function
Z	Acoustic resistance
$\Gamma(n)$	Gamma function

E_R	Relative error
$V(Y)$	Variance of the(Y)
V_i	Variance because of the first order effects
S_i	First-order sensitivity coefficient for the i^{th} parameter
S_{ij}	Second and higher order sensitivity coefficient for each parameter
S_{Ti}	Total sensitivity coefficient for the i^{th} parameter
A_{in}	Amplitude of external excitation
v_o	Voltage measured by the LDV
A_o	Amplitude of object oscillation
V_o	Amplitude of object velocity
$MI(X, Y)$	Mutual information between two random variables X and Y
$P(X, Y)$	Joint probability distribution
$P(X), P(Y)$	Marginal probability distribution functions of X and Y
τ	Time delay
m	Embedded dimension
ε	Threshold value in Eq. (4.2)
H	Heaviside function

$\Theta(X)$	A library matrix of potential candidate nonlinear functions in SINDy
$X(t)$	State space variable in SINDy
Ξ, η	Unknown matrices of coefficients in SINDy
$f_n(\vec{x}_n, t_m, u)$	Unknown function in SINDy

ABSTRACT

Acoustic radiation force occurs when an object scatters part of the incident momentum from an acoustic wave. Most studies focus on the acoustic field, while the dynamic response of objects in the acoustic radiation force field is less explored. This research addresses this gap by applying external excitation to manipulate the force's magnitude and direction. A theoretical model is developed, demonstrating that the acoustic contrast factor depends on the properties of the spherical object, fluid characteristics, and the external excitation properties. This model is extended to non-spherical objects using a finite element analysis. Then, by using the Gorkov formulation, a mathematical model is developed for the governing equation of motion, like the Duffing equation. The system's dynamic sensitivity is analysed using the Sobol indices, revealing that external vibrations can significantly alter the system's response. Using experimental time series data and the Sparse Identification of Nonlinear Dynamics (SINDy) algorithm, the nonlinear differential equations of motion for the object oscillating in an acoustic radiation force field are extracted. Bifurcation diagrams reveal the system's transition from regular to irregular motion. Recurrence plots and motifs classify these dynamics, offering insights into controlling the system and studying the nonlinear dynamics of levitated objects.

CHAPTER 1: LITERATURE REVIEW AND THESIS OUTLINE

1.1. Introduction

One of the most interesting phenomena in the nonlinear acoustic field is the acoustic radiation force (F_{rad}), which occurs when incident acoustic waves interact with scattered waves from an object positioned in the path of the incoming acoustic wave with wavelength λ [1-3] (Fig. 1.1). Many applications have been developed to exploit this force; for example, some of these applications are lab-on-a-chip technology [4-10], medical diagnostics [11-13], levitation [14-19], biomedical research [20-26], sorting, separation, and particle manipulation [27-33], and (operational) modal analysis by non-contact excitation [34-37].

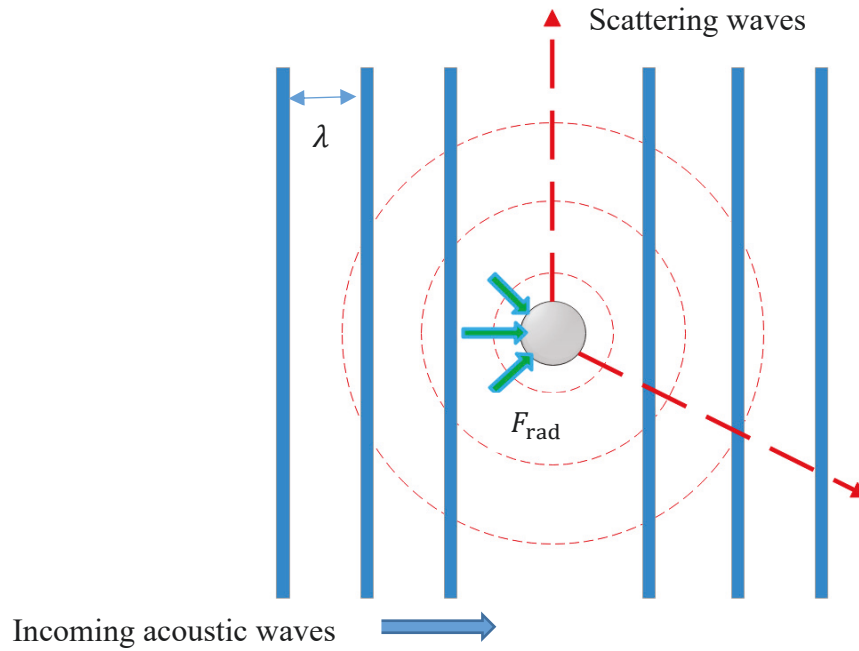


Fig. 1.1. The interaction between incoming acoustic waves (with a specific frequency and wavelength, λ) and an object, resulting in scattered waves. This interaction creates an interference pattern, which generates an acoustic radiation force acting on the object.

The acoustic radiation force is known to be static when the incident field is continuous with constant amplitude, but it can become dynamic for a continuous wave-field for which intensity varies with time [38,39].

1.2. Mathematical description of acoustic radiation force

Mathematically, the acoustic radiation force can be calculated by integrating the acoustic radiation stress tensor, S_{ij} , on the object's surface, A , as [40-42]

$$F_{\text{rad}} = \iint_A S_{ij} n_j dA, \quad (1.1)$$

where n_j represents the normal vector on the surface. Acoustic radiation force can be calculated by solving the scattering problem and determining the stress tensor. The fundamental equations for calculating the acoustic radiation stress tensor result from applying the perturbation theory and time averaging method to continuity and Navier-Stokes equations [42-50].

1.2.1. Homotopy perturbation method

The basic idea behind a perturbation technique is the transforming of a nonlinear differential equation into an infinite number of linear ones. The small parameter determines not only the accuracy of the perturbation approximations but also the validity of the perturbation method [51]. The Homotopy Perturbation method (HPM) is a type of perturbation method that does not require the presence of a small parameter (perturbation parameter) in the equation which makes it versatile for a wide range of applications [51-53]. While the literature presents the perturbation method for deriving fundamental equations of acoustic radiation force [5], this section demonstrates that the same equations can be readily derived using the HPM. The main objective of this section is to obtain the acoustic radiation force formulation from the Navier- stokes and continuity equations, by means of the HPM [52,53]. To show the basic ideas of the HPM, the following equation is considered [51-53]

$$A(u) - f(r) = 0, r \in \Omega, \quad (1.2)$$

with the boundary condition of:

$$B\left(u, \frac{\partial u}{\partial n}\right) = 0, r \in \Gamma, \quad (1.3)$$

where A is a general differential operator, B a boundary operator, $f(r)$ a known analytical function and Γ is the boundary of the domain Ω , A can be divided into two parts which are L and N , where L is linear and N is nonlinear part of the Eq. (1.2). Therefore Eq. (1.2) can be rewritten as follows

$$L(u) + N(u) - f(r) = 0, r \in \Omega, \quad (1.4)$$

Homotopy perturbation structure is shown as:

$$H(v, p) = (1 - p) [L(v) - L(u_0)] + p[A(v) - f(r)] = 0, \quad (1.5)$$

where:

$$v(r, p): \Omega \times [0, 1] \rightarrow R, \quad (1.6)$$

in Eq. (1.5), $p \in [0, 1]$ is an embedding parameter and u_0 is the first approximation that satisfies the boundary condition. The solution of Eq. (1.5) can be assumed and written as a power series in p , as following

$$u = \lim_{p \rightarrow 1} (v_0 + pv_1 + p^2v_2 + \dots). \quad (1.7)$$

1.2.2. Eulerian mean excess pressure

In calculating the acoustic radiation forces using the perturbation theory, the first-order quantities are used to obtain the second-order quantities and, accordingly, the acoustic radiation stress tensor, S_{ij} . In this procedure, the acoustic radiation force can be calculated by considering terms up to the second-order quantities, while higher-order terms are ignored. While the time average of the first-order terms is zero, the time average of the second-order terms over one period is non-zero. To obtain fundamental equations, the HPM is applied to the Navier-Stokes equations and the continuity equation, for an ideal fluid flow in an arbitrary direction of x [44]. The tensor form of Navier-Stokes equations, and continuity equation for an ideal fluid can be presented as Eq. (1.8a) and (1.8b) [44]. By expanding the parameters until the third order, the pressure (P), velocity (v), and density (ρ) can be written as Eq. (1.8c)

$$-\nabla_{,i} P \delta_{ij} = \rho \left(v_j \nabla_{,i} v_i + \frac{\partial v_j}{\partial t} \right), \quad (1.8a)$$

$$\dot{\rho} + (\rho v_i)_{,i} = 0, \quad (1.8b)$$

$$\begin{aligned} P(x, t) &\sim P_0 + pP_1(x, t) + p^2P_2(x, t) + p^3P_3(x, t), \\ v(x, t) &\sim 0 + pv_1(x, t) + p^2v_2(x, t) + p^3v_3(x, t), \\ \rho(x, t) &\sim \rho_0 + p\rho_1(x, t) + p^2\rho_2(x, t) + p^3\rho_3(x, t), \end{aligned} \quad (1.8c)$$

When, ∇_i is the gradient operator, and δ_{ij} is the kronecker delta. According to the HPM and substituting Eq. (1.8c) into Navier-Stokes equations Eq. (1.8a) and rearranging based on powers of p , these equations are obtained

$$p^0 \times \left[\rho_0 \left(\frac{\partial}{\partial t} v_1(x, t) \right) + \frac{\partial}{\partial x} P_1(x, t) \right] = 0, \quad (1.9)$$

and

$$p^1 \times \left[\rho_0 v_1(x, t) \left(\frac{\partial}{\partial x} v_1(x, t) \right) + \rho_1(x, t) \left(\frac{\partial}{\partial t} v_1(x, t) \right) + \rho_0 \left(\frac{\partial}{\partial t} v_2(x, t) \right) + \frac{\partial}{\partial x} P_2(x, t) \right] = 0, \quad (1.10)$$

by solving the Eq. (1.9), the solution can be obtained as

$$\left(\frac{\partial}{\partial t} v_1(x, t) \right) = -\frac{1}{\rho_0} \frac{\partial}{\partial x} P_1(x, t), \quad (1.11)$$

by substituting the Eq. (1.11) into Eq. (1.10) and solving for the second order of the pressure, one can obtain

$$-\frac{\partial}{\partial x} P_2(x, t) = \rho_0 v_1(x, t) \left(\frac{\partial}{\partial x} v_1(x, t) \right) - \rho_1(x, t) \left(\frac{1}{\rho_0} \frac{\partial}{\partial x} P_1(x, t) \right) + \rho_0 \left(\frac{\partial}{\partial t} v_2(x, t) \right). \quad (1.12)$$

The barotropic equation of state, $P_1/P_0 = (\rho_1/\rho_0)^n$ is used, when $n = 1 + A/B$ and A/B is the Fox-Wallace parameter which characterizes the nonlinearity of the fluid. Also, we know that in an ideal fluid $-\nabla\phi(x, t) = v(x, t)$, which means that an ideal fluid is irrotational and the velocity, $v(x, t)$, can be described by a potential function, ϕ . By replacing the second order of the velocity with the second order of the potential function of velocity, $-\frac{\partial}{\partial x} \phi_2(x, t) = v_2(x, t)$, and by defining the sound velocity as $c_0^2 = (P_0/\rho_0)$, the second order of the pressure can be obtained as [9]

$$P_2(x, t) = \left(\frac{\partial}{\partial t} \phi_2(x, t) \right) + \frac{n}{n+1} (\rho_0 c_0^2)^{-\frac{1}{n}} P_1(x, t)^{\frac{n+1}{n}} - \frac{1}{2} \rho_0 v_1(x, t)^2. \quad (1.13)$$

For a linear fluid ($n = 1$), and the second order of the pressure can be re-written as

$$P_2(x, t) = \left(\frac{\partial}{\partial t} \phi_2(x, t) \right) + \frac{1}{2\rho_0 c_0^2} P_1(x, t)^2 - \frac{1}{2} \rho_0 v_1(x, t)^2, \quad (1.14)$$

the third order of the pressure also, can be obtained similarly by the coefficient of p^2

$$p^2 \times \left[\rho_1(x, t) v_1(x, t) \left(\frac{\partial}{\partial x} v_1(x, t) \right) + \rho_0 v_1(x, t) \left(\frac{\partial}{\partial x} v_2(x, t) \right) + \right. \quad (1.15)$$

$$\left. \rho_0 v_2(x, t) \left(\frac{\partial}{\partial x} v_1(x, t) \right) + \rho_1(x, t) \left(\frac{\partial}{\partial t} v_2(x, t) \right) + \rho_2(x, t) \left(\frac{\partial}{\partial t} v_1(x, t) \right) + \right.$$

$$\left. \rho_0 \left(\frac{\partial}{\partial t} v_3(x, t) \right) + \frac{\partial}{\partial x} P_3(x, t) \right] = 0,$$

by solving Eq. (1.15) the third order of the pressure can be obtained as

$$P_3(x, t) = \rho_0 \frac{\partial \phi_3(x, t)}{\partial t} + \frac{1}{\rho_0 c_0^2} P_1(x, t) P_2(x, t) - \frac{1}{3 \rho_0^2 c_0^4} P_1(x, t)^3 - \quad (1.16)$$

$$\rho_0 (v_1(x, t) \cdot v_2(x, t)) = 0,$$

In HPM we can continue the procedure to achieve a desired accuracy. The third order of the pressure, Eq. (1.16), has not been reported in any publications, but considering its much smaller value compared to the second-order pressure, it is a reasonable decision to ignore the third-order and higher solutions [41]. By applying the time averaged operator, $\langle \cdot \rangle$, on the Eq. (1.14), the time averaged of second order pressure, called the Eulerian mean excess pressure [5], can be obtained which is a nonzero value as

$$\langle P_2 \rangle = \frac{1}{2 \rho_0 c_0^2} \langle P_1 \rangle^2 - \frac{\rho_0}{2} \langle |\vec{v}_1|^2 \rangle. \quad (1.17)$$

The obtained results for the second order of the pressure are like which were reported by [38,41]. It is termed ‘‘Eulerian’’ because it is evaluated at any position of a given point, as opposed to a ‘‘Lagrangian’’ one. The velocity field can also be obtained using the HPM. Using the same approach for continuity equation [44]

$$p^0: \rho_0 \left(\frac{\partial}{\partial x} v_1(x, t) \right) + \frac{\partial}{\partial t} \rho_1(x, t) = 0, \quad (1.18)$$

and

$$p^1: \left(\frac{\partial}{\partial x} v_1(x, t) \right) \rho_1(x, t) + \left(\frac{\partial}{\partial x} v_2(x, t) \right) \rho_0 + \frac{\partial}{\partial t} \rho_2(x, t) = 0, \quad (1.19)$$

from the Eq. (1.18), and by using the barotropic equation of state [38], and for a linear fluid, and by replacing the first order of the potential function of the velocity in the equation, one can obtain

$$\nabla^2 \phi_1 = \left(\frac{\partial^2}{\partial x^2} \phi_1(x, t) \right) = \frac{1}{c_0^2} \left(\frac{\partial^2}{\partial t^2} \phi_1(x, t) \right), \quad (1.20)$$

Eq. (1.20) is the well-known acoustic wave equation that is the starting point of investigating acoustic radiation force. To obtain the first order of velocity field, these boundary conditions are related to the object geometry and object and medium compressibility. This equation has been solved in the literature for simple geometrical objects such as spheres and cylinders. Because the boundary conditions can be stated in a polar coordinate system for spheres or cylinders, the wave equation should be transferred to the polar coordinate system. Therefore, the Laplace operator, ∇^2 , should be transferred to the polar system [55,56]. Hence, the Laplace operator for the two radial and angular directions can be re-written as

$$\nabla^2 = \left(\frac{\partial^2}{\partial r^2} + \frac{1}{r} \frac{\partial}{\partial r} + \frac{1}{r} \frac{\partial^2}{\partial \theta^2} \right), \quad (1.21)$$

by using the Laplace operator in polar system, the Eq. (1.20) converts to

$$\nabla^2 \phi_1 = \left(\frac{\partial^2}{\partial r^2} + \frac{1}{r} \frac{\partial}{\partial r} + \frac{1}{r} \frac{\partial^2}{\partial \theta^2} \right) \phi_1(r, \theta, t) = \frac{1}{c_0^2} \left(\frac{\partial^2}{\partial t^2} \phi_1(r, \theta, t) \right), \quad (1.22)$$

by using the separation variables method and assuming that $\phi_1(r, \theta, t) = \phi_1(r)\theta_1(\theta)T_1(t)$ the boundary value problems for the Eq. (1.22), can be presented by

$$\left(\frac{r^2}{\phi_1(r)} \frac{d^2 \phi_1}{dr^2} + \frac{r}{\phi_1} \frac{d\phi_1}{dr} + (kr)^2 \right) = -\frac{1}{\theta} \frac{d^2 \theta}{d\theta^2} = m, \quad (1.23)$$

in Eq. (1.23) the first equation for $\phi_1(r)$ is the well-known Bessel equation [21], where k is the wave number and m is a positive integer number. Bessel functions and spherical harmonics often appear when solving scattering problems in spherical and cylindrical coordinate. Multipole expansion techniques can then be used to decompose the scattered field into simpler components, providing a more manageable way to analyse and understand the scattering process [54-57].

1.2.3. Reynolds stress

In an ideal fluid, the acoustic radiation stress tensor may consist of the mean excess pressure and the Reynolds stresses [58,59]. If the object boundary is fixed, with a slip condition at the boundary, the time-averaged radiation force on the object is found by

integrating the mean excess pressure over the object surface, S_0 [60-62]. However, we know that the object surface is free to move in response to the movements of the fluid, hence applying this integration over the moving object surface, S is paramount (Fig. 1.2).

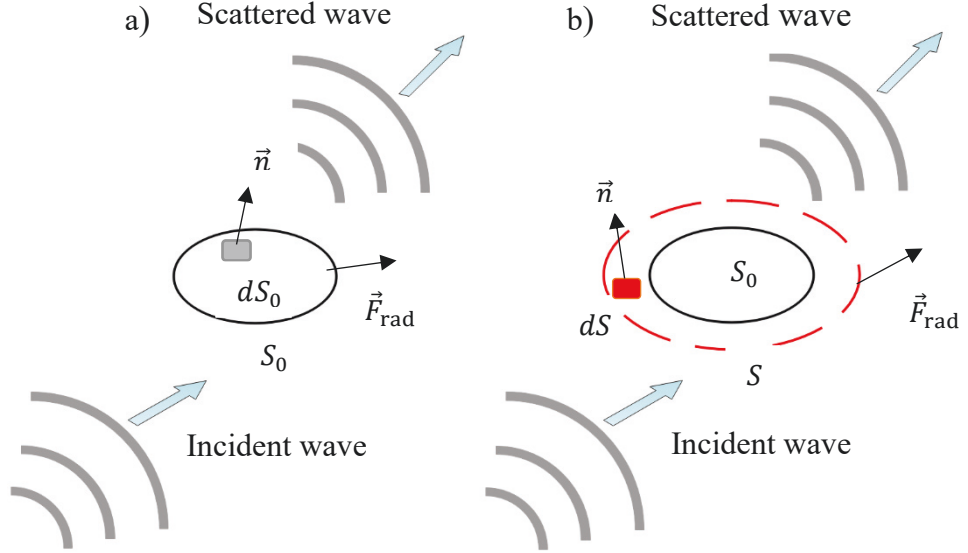


Fig. 1.2. Boundary of acoustic radiation force for a) rigid object: the time-averaged radiation force on the object can be found by integrating the mean excess pressure over the object surface, S_0 , b) compressible object: the integration in Eq. (1.1) must be applied over the moving object surface, S .

Yosioka and Kawasima showed that a correction term called Reynolds stress should be added to the mean excess pressure. The mathematical description of Reynolds stress is discussed in the following. In the Eulerian coordinate system, the continuity equation (Eq. 1.8b) can be written as [63]

$$\frac{\partial \rho}{\partial t} + v_k \frac{\partial \rho}{\partial x_k} + \rho \frac{\partial v_i}{\partial x_i} = 0, \quad (1.24)$$

multiplying Eq. (1.24) by v_j and add the result to the Navier-Stokes equations [44], and by using the product rule of differentiation

$$\frac{\partial(\rho v_k)}{\partial t} + \frac{\partial(\rho v_i v_j)}{\partial x_i} = -\frac{\partial P}{\partial x_i}, \quad (1.25)$$

The term of $(\rho v_i v_j)$ is called Reynolds stress and demonstrates the time-averaged transport of the momentum density ρv_i with velocity v_j across an area normal to the direction x_i . $v_i v_j$ is the dyadic product of velocity and is a 3×3 -unit matrix. Then, the

acoustic radiation stress tensor, S_{ij} , is defined as summation of Eulerian mean excess pressure and Reynolds stresses as [61]

$$S_{ij} = \langle P_2 \rangle \delta_{ij} + \rho v_i v_j. \quad (1.26)$$

Eq. (1.26) describes the acoustic radiation stress tensor, which represents the stresses exerted on an obstacle surface when subjected to an acoustic field. This tensor provides valuable information about how the acoustic waves interact with the object, including the magnitude, direction, and distribution of the stresses experienced by the surface. Understanding the acoustic radiation tensor enables us to study the dynamics of objects within acoustic environments which help us for developing theories and methodologies to compute acoustic radiation forces for various geometries.

1.3. Literature review

In the context of acoustic radiation force, the terms “static” and “dynamic” are inherently tied to the timescales over which the force is observed and analysed. The “static” acoustic radiation force refers to the time-averaged force resulting from the interaction of acoustic waves with an object. This force is considered constant when observed over timescales much longer than the acoustic wave period, effectively averaging out the rapid oscillations and dynamic interactions originating from continuous wave-object interactions. The acoustic radiation force’s “dynamic” component pertains to variations occurring over shorter timescales, where temporal fluctuations in the acoustic field or the object’s response are significant. These fluctuations can arise from modulations in the acoustic wave’s amplitude, frequency, or phase, leading to time-dependent forces that induce oscillatory motions or deformations in the object. Understanding the interplay between static and dynamic acoustic radiation force and their associated timescales is crucial for accurately characterising and utilising these forces in various applications, such as non-contact modal excitation and elasticity imaging [31-39].

Closed-form formulae are widely available in the literature for computing static (time-averaged) and dynamic (time-varying) acoustic radiation forces acting on objects with simple geometries, such as acoustically small spheres, cylinders, and ellipsoids [59-74]. However, no closed-form analytical solutions exist for acoustically large objects to calculate the acoustic radiation force. While spherical harmonics and perturbation techniques provide promising approaches [75], they often necessitate complex numerical or semi-analytical methods rather than straightforward analytical solutions.

Consequently, although analytical formulas are well-established for acoustically small objects, numerical simulations remain indispensable for studying small and large objects. Here, “acoustically small” and “acoustically large” are terms used to describe the size of an object relative to the acoustic wavelength.

1.3.1. Static (time averaging) component

In the literature, “acoustic radiation force” typically refers to the static component of the time-averaged force. In contrast, “dynamic acoustic radiation force” describes the time-varying component. King was the first person to present an analytical model for the acting acoustic radiation force on solid small spheres, which is small relative to the wavelength of the sound, placed in a standing acoustic wave field immersed in an ideal fluid [62]. Yosioka and Kawasima extended King’s theory to encompass compressible small spheres [63]. Gorkov developed a formulation for the acoustic force based on time-averaged kinetic and potential energies within stationary acoustic fields [64].

Gorkov’s theory, when applied to acoustically small and compressible objects, predicts that the acoustic radiation force acts as the gradient of a potential function. The King, Yosioka, and Gorkov’s formulation are succinctly presented in Table 1.1.

Table 1.1. A comparison between King, Yosioka and Gorkov’s formulation, ($kr \ll 1$).

Theory	Acoustic radiation force formula	Variables
King	$V_p E_{ac} k \sin(2kz) \hat{\rho}$	$V_p = 4\pi r^3/3$
		$E_{ac} = P_a^2/(4\rho_0 c_0^2)$
		$\hat{\rho} = (5\tilde{\rho} - 2)/(2\tilde{\rho} + 1),$ $\tilde{\rho} = \rho_1/\rho_0$
Yosioka, Kawasima	$V_p E_{ac} k \sin(2kz) (\hat{\rho} - \tilde{\kappa})$	$\tilde{\kappa} = \kappa_1/\kappa_0, \kappa_0 = 1/(\rho_0 c_0^2),$ $\kappa_1 = 1/\rho_1 c_1^2$
Gorkov	$-\nabla U,$ $U = V_p \left(\frac{f_1}{2} \kappa_0 \langle P_{in} \rangle^2 - \frac{3f_2}{4} \rho_0 \langle V_{in} \rangle^2 \right)$	$f_1 = 1 - \tilde{\kappa},$ $f_2 = \frac{2(\tilde{\rho} - 1)}{2\tilde{\rho} + 1}$

In the Table 1.1, k is the wave number, r is the radius of the particle, V_p is the spherical object volume, E_{ac} being the acoustic energy density, P_a is the amplitude of the incident pressure field, z is the distance between the pressure node and the centre of the small object or particle in the wave direction, ρ , κ , and c are the density, compressibility, and speed of sound with indices 0 and 1 denoting the fluid and the particle respectively, U is the force potential when the force can be written as $F_{rad} = -\nabla U$ and ∇ represent the gradient operator. $\langle P_{in} \rangle$ and $\langle V_{in} \rangle$ are the time-averaged incident pressure and velocity field, and f_1 and f_2 are the monopole and the dipole coefficients in Gorkov formula. To calculate the acoustic radiation force on particles the Gorkov's formulation has been coded in the COMSOL Multiphysics "*Particle Tracing for Fluid Flow*" interface. But this formulation neglects thermo-viscous effects and only applies to acoustically small particles [61]. According to the formulation presented in Table.1.1 The Yosioka's formula adds a correction term of $\tilde{\kappa}$, into the King's formula to take the compressibility into account and the Gorkov and Yosioka formula are equivalent, and both give the same results. Farran was the first researcher who extended the theory of the scattering of the plane waves of sound by isotropic solid cylindrical and spherical objects, by considering the shear waves. His work reveals that how sound waves interact with solid cylinders and spheres. According to this theory, the equation of motion of a solid elastic medium can be written as [65]

$$(\lambda + 2\mu)\nabla\Lambda - \mu\nabla \times (2\omega) = \rho_1 \frac{\partial^2 u}{\partial t^2}, \quad (1.27)$$

in Eq. (1.27) (λ, μ) are lame elastic constants, $\nabla = \frac{\partial}{\partial x_i} \vec{e}_i$, $i = 1, 2, 3$ is the del operator, $\Lambda = div(u) = \nabla \cdot u$ is the dilatation and is the divergence of displacement vector u , $\nabla \times (\cdot)$ is the curl operator of (\cdot) , 2ω is the dual rotation vector of displacement gradient ∇u , and ρ_1 is density of the object. By assuming that the displacement u including scaler, Ψ , and vector potential, Ω , functions

$$u = -\nabla\Psi + \nabla \times \Omega, \quad (1.28)$$

according to Eq. (1.28) displacement has two parts, first is associated with compressional waves and the second is associated with shear waves. Substituting Eq. (1.28) into Eq. (1.27):

$$(\lambda + 2\mu)\nabla\nabla^2\Psi - \mu\nabla \times \nabla^2\Omega = \rho_1 \frac{\partial^2 u}{\partial t^2}, \quad (1.29)$$

the field displacements Ψ, Ω must satisfy Eq. (1.28), and should be harmonic

$$\nabla^2\Psi = \frac{1}{c_1^2} \frac{\partial^2 \Psi}{\partial t^2}, \text{ and } \nabla^2\Omega = \frac{1}{c_2^2} \frac{\partial^2 \Omega}{\partial t^2}, \quad (1.30)$$

where

$$c_1^2 = \frac{\lambda+2\mu}{\rho_1}, c_2^2 = \frac{\mu}{\rho_1}, \quad (1.31)$$

in the cylindrical coordinate, Ψ, Ω can be obtained as

$$\Psi = \sum_{n=0}^{\infty} a_n J_n(k_1 r) \cos(n\theta), \Omega = \sum_{n=0}^{\infty} b_n J_n(k_2 r) \sin(n\theta), \quad (1.32)$$

where J_n is the Bessel function of the first kind, a_n, b_n are expansion coefficients, k is the wave number. From Eq. (1.28) and Eq. (1.32), the displacement field can be obtained in cylindrical coordinates. Also, the stress field can be obtained from the continuum mechanics and by using the displacement field. By solving the wave equation in spherical coordinate, the incident and scattered acoustic wave pressure for a nonviscous fluid medium can be obtained as [65]:

$$\begin{aligned} P_i &= P_0 \sum_{n=0}^{\infty} \varepsilon_n (-j)^n J_n(kr) \cos(n\theta), \\ P_s &= P_0 \sum_{n=0}^{\infty} c_n [J_n(kr) - jY_n(kr)] \cos(n\theta) = \\ &P_0 \sum_{n=0}^{\infty} \varepsilon_n d_n (-j)^n H_n(kr) \cos(n\theta), \end{aligned} \quad (1.33)$$

where ε_n is Neumann factor $\varepsilon_0 = 1, \varepsilon_n = 2 (n = 1, 2, \dots)$, $j = \sqrt{-1}$, Y_n is the Bessel function of the second kind, H_n is the Hankel function of the second kind, and c_n is the expansion coefficient. To calculate $a_n, b_n, c_n (d_n)$ there are three boundary conditions:

- 1- At the interface surface, the normal component of stress in the solid must be equal to the pressure in the fluid.
- 2- At the interface surface, the normal component of displacement in the solid must be equal to the normal component of displacement in the fluid.
- 3- At the surface of the solid, the tangential components of shearing stress must vanish.

By transferring the boundary conditions to the spherical coordinate, Farran calculated the scattering by a solid spherical object. The analysis for the cylindrical coordinates is like the spherical case coordinate case [37]. Farran's groundbreaking study marked a significant achievement by introducing a novel perspective to sound scattering. Specifically, his approach revolutionized considering non-spherical objects in studying acoustic interactions.

Using the Farran's results, Hasegawa et al. calculated the acoustic radiation force acting on a solid cylindrical object in a plane progressive sound field by an analytical formulation [66]. Hasegawa et al.'s formulation had the strength that it was the first attempt to calculate acoustic radiation force on non-spherical objects, but some shortages remain; for example, this theory is very limited and only valid for cylindrical objects, and other geometrical shapes fall outside of this theory realm.

Wu et al. studied analytically and experimentally the acoustic radiation force exerted on long, rigid cylindrical objects whose axes are perpendicular to the direction of the propagation of sound waves [67]. In this theory, they used boundary conditions similar to those applied in King's theory, but by using the coordinate transformation, they transferred the boundary conditions to a cylindrical coordinate system. The great advantage of this study was reporting experimental data that agreed with results obtained theoretically. This work was a good example of a comparison between theory and experiment, and the deviation between obtained results shows other factors that are not included in the theory and their effect on the radiation force magnitude. Although Wu et al. did not discuss these unknown factors, this deviation may be because of temperature changes, media losses, and other nonlinear properties.

Mitri is a researcher who has worked extensively on static and dynamic acoustic radiation force on non-spherical objects [68-74]. He presented an analytical approach for calculating the acoustic radiation forces on elastic and viscoelastic cylinders in a quasi-standing wave field. [68]. Also, he presented an analytical formulation to obtain the acoustic radiation forces exerted on the spherical shells and layered cylinders [69]. In this study and to obtain the acoustic field inside, the boundary conditions were considered at the inner and outer surfaces of the shell, and the shell material was assumed to be elastic and viscoelastic. Also, he found that the acoustic radiation forces in the near and far fields were equivalent. Moreover, he studied the acoustic radiation moment analytically and

found that it results in the rotation of the spherical objects irradiated by a Bessel beam [73].

Doinikov was the first researcher to study the effect of fluid viscosity on acoustic radiation force [76], and by considering the effects of viscosity, he expanded our understanding of how the surrounding medium influences the interaction between sound waves and particles. He presents a general formula to calculate the acoustic radiation force exerted on a spherical particle in an axisymmetric sound field immersed in a viscous heat-conducting fluid. The important feature of Doinikov's theory is that it does not depend on particle size compared to the fluid viscous, thermal, and sound wavelengths. Doinikov obtained a general formulation for the acoustic radiation force, which can be applied to different spherical particles such as liquid drops, gas bubbles, spherical shells, rigid or elastic spheres, etc. As a result of scattered waves from the spheres, Doinikov derived a solution to consider acoustic streaming, which forms a foundation for comprehending the complexities of acoustic radiation force in realistic fluid environments. Doinikov considered the equations of motion of a viscous fluid as [76]:

$$\frac{\partial}{\partial t}(\rho v_i) = \frac{\partial}{\partial x_k}(\sigma_{ik} - \rho v_i v_k), \quad (1.34)$$

$$\frac{\partial \rho}{\partial t} + \frac{\partial}{\partial x_k}(\rho v) = 0, \quad (1.35)$$

$$\rho T \left(\frac{\partial s}{\partial t} + v_i \frac{\partial s}{\partial x_i} \right) = (\sigma_{ik} + p \delta_{ik}) \frac{\partial v_i}{\partial x_k} + \frac{1}{2} \frac{\partial}{\partial x_i} \left(\kappa \frac{\partial T}{\partial x_i} \right). \quad (1.36)$$

The Eq. (1.34) describes the momentum equation in fluid dynamics, the Eq. (1.35) describes the continuity equation in continues media, and the Eq. (1.36) describes the Maxwell's relation which is the combination of first and second law of the thermodynamics. In these equations, σ_{ik} is the stress tensor, T is the absolute temperature, and κ is the thermal conductivity. In his model, he considered the rotation in fluid caused by viscosity, and assumed that the velocity can be defined by a scalar term as the velocity potential function and vorticity velocity potentials of first order as [76]:

$$\vec{v} = \vec{\nabla} \phi + \vec{\nabla} \times \vec{\Psi}, \quad (1.37)$$

In an ideal fluid, the force on a sphere aligns with the direction of wave propagation. However, Doinikov's study reveals significant variations in forces between viscous and

non-viscous fluids. Specifically, spheres move toward wave propagation when a plane progressive wave applies viscous radiation pressure. In contrast, for gas bubbles in liquid, with wave frequencies exceeding a certain coefficient of the resonant frequency of the gas bubble, the pressure acts opposite to the wave propagation. Doinikov highlights that viscosity introduces an additional force on objects in the sound field. He concludes that viscosity can be neglected when the particle radius far exceeds the boundary layer thickness, and radiation force becomes a substantial component of the total force. Conversely, viscosity becomes non-negligible when the boundary layer thickness equals or surpasses the particle radius, significantly influencing the force exerted on the object. Analytical research, despite the ability to provide acceptable results for calculating the radiation force and how it changes, only allows a partial study of this issue due to the complexity of the geometry of the problem. For this reason, in recent years, numerical modelling of the acoustic radiation force has been considered by some researchers. Glynne-Jones et al. presented a finite element-based method to calculate radiation force acting on elastic particles of arbitrary size and geometry [61]. The proposed model was based on the propagation of the acoustic waves in non-viscous mediums and the linear scattering model. In their work and for a compressible sphere, as shown in Fig. 1.3, numerical simulation was done by constructing a 2D model implemented in COMSOL v.4.0a, and they showed that for an axisymmetric structure, the simulation time was a few seconds. They compared and verified the results they obtained with existing analytical solutions. Their work uses the perturbation analysis to obtain the second-order terms of the acoustic pressure and the velocity field.

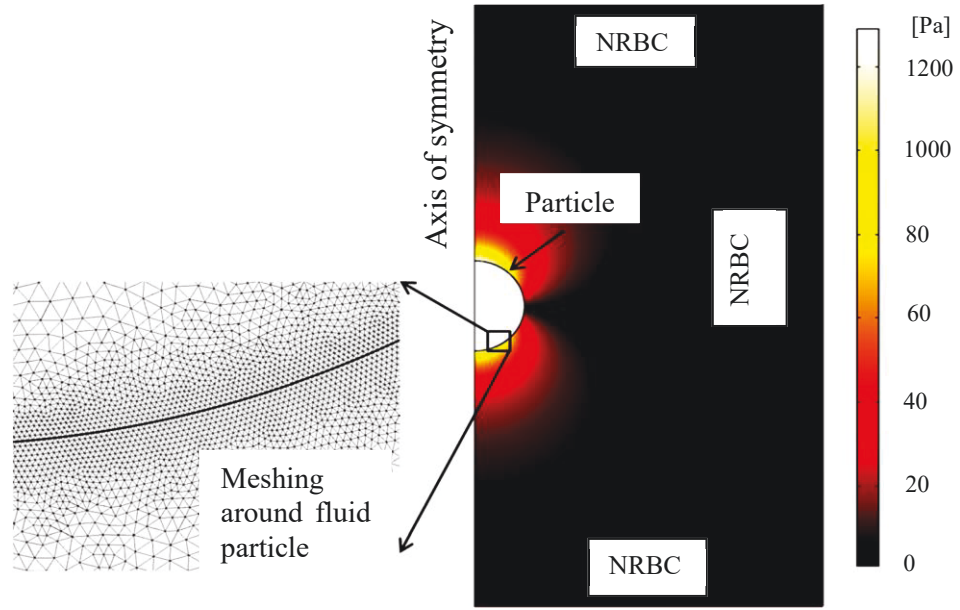


Fig. 1.3. Scattered pressure distribution around the object according to numerical simulation, with magnification showing the finite element model in COMSOL Multiphysics to find radiation forces on a compressible sphere; adopted from [61].

Their model was axisymmetric, and the particle was presented in a semicircular domain, and the fluid was shown as a rectangular domain surrounding it. NRBCs mean non-reflecting boundary conditions (NRBCs) that delimit the computational domain and allow an acoustic field to be introduced by specifying pressure conditions over the boundary. Lim and Sepehrirahnama used the multipole expansion method to compute acoustic radiation force and moment on rigid spheres and spheroids. They conducted finite element simulations for validating their results and found a good agreement between numerical and analytical results for small-sized spheres and ellipsoids [21]. Additionally, Sepehrirahnama et al. extended their numerical calculations to spheres in a viscous fluid. Their method incorporated multipole series and Stokeslet to compute radiation force in a viscous medium. The solution involved obtaining first-order velocity and pressure from the multipole series and calculating volumetric force in acoustic streaming [42]. Compared to the static acoustic radiation force, few papers have investigated the dynamic acoustic radiation force. In recent years, dynamic acoustic radiation force has become of practical importance in medicine tissue imaging or elastography, and non-contact excitation [34-37].

1.3.2. Dynamic (time varying) component

As discussed in the previous section, the acoustic radiation force becomes dynamic for a continuous wavefield in which the intensity varies with time. There are four most employed methods in the literature for producing dynamic (time-varying) acoustic radiation forces [77-79]:

- Frequency Modulation: Modulating the frequency of the acoustic wave can introduce variations in the acoustic radiation force. By changing the frequency dynamically, one can influence the force acting on objects.
- Amplitude Modulation: Varying the amplitude of the acoustic wave over time can also result in dynamic changes in the radiation force.
- Parametric Excitation: Changing the properties of the medium or the object itself, can dynamically change the acoustic radiation force.
- Dual-Frequency Beams: Using ultrasound beams with two different frequencies can lead to generation of dynamic acoustic radiation forces.

Silva et al. presented a theory to calculate dynamic acoustic radiation force produced by dual-frequency ultrasound beams in ideal fluids [38]. Using a low-amplitude dual frequency plane wave, they calculated the dynamic acoustic radiation force exerted on solid elastic spheres made of Brass and Steele. They obtained two analytical formulations for dynamic and static acoustic radiation pressure and calculated the static and dynamic acoustic radiation forces accordingly. Finally, they concluded that the three different sources affect the dynamic radiation force magnitude during the interactions between the acoustic waves and the object. The first interaction is the momentum rate exchange due to object vibration, which causes fluid mass variation. The second interaction results from the second-order velocity potential, and the third interaction is due to the dynamic radiation stresses

Also, Silva et al. investigated the parametric amplification of dynamic radiation force induced by acoustic waves in fluids [77]. Their method accounted for fluid nonlinearity and resolved the scattering problem to compute the radiation force accurately. To validate their findings, they conducted experiments measuring dynamic radiation force on an acrylic sphere submerged in degassed water and ethyl alcohol. This study addressed a previous limitation where fluid nonlinearity was disregarded, enhancing accuracy across various difference frequencies.

Moreover, they explored multifrequency radiation force, which can be used in vibro-acoustography, which is a promising imaging technique with implications in biological science [78]. The method offers enhanced image fidelity by simultaneously capturing multiple tissue images, each corresponding to a spectral line of multifrequency radiation force. Multifrequency radiation force can be produced by a polychromatic propagated acoustic beam in a fluid. In their work, they presented an analytical approach for the dynamic radiation force exerted on a rigid sphere by a plane wave containing N frequency components. They found that the generated radiation force is consist of up to $N(N - 1)/2$ distinct frequency components. Moreover, because of the nonlinear nature of the wave propagation, the exerted radiation force is mainly caused by parametric amplification [78]. According to their paper, if an object is acoustically excited by a polychromatic acoustic beam with different frequencies $\omega_m, m = 1, 2, \dots, N$, then the multifrequency radiation force, $f_t(t)$, can be found as follows

$$f_t(t) = \sum_{\substack{m,n=1 \\ m>n}}^N f_{mn}(t) \quad (1.38)$$

where $f_{mn}(t)$ is the component of the multifrequency radiation force, $f_t(t)$, at difference frequencies $\omega_{mn} = \omega_m - \omega_n > 0, m > n$. After solving the scattering problem, they presented an analytical formula to calculate $f_t(t)$, as

$$f_{\Delta\omega} = \pi a^2 E_0 \sum_{\substack{m,n=1 \\ m>n}}^N Y_{mn} e^{-i(\omega_{mn}t - k_{mn}z_0)}, \quad (1.39)$$

when E_0 is the acoustic energy density, a is the object radius, and Y_{mn} is the dynamic radiation force function, and can be found in Ref. [38]. Mitri and Fatemi presented an analytical approach to calculate acting dynamic acoustic radiation force on cylindrical shells in ideal fluid [79]. In their work, the radiation force generated by interference of a pair of low power, ultrasonic frequencies (dual beam mode). Then, by solving the scattering problem, they presented a formula to calculate exerted radiation force on cylindrical shells. According to their findings the radiation force consists of three parts, as

$$F_{\text{rad}} = F_{S1} + F_{S2} + F_D \quad (1.40)$$

where F_{S1} and F_{S2} are static radiation force because of each individual wave, separately, and F_D is the dynamic radiation force in difference, $\Delta\omega$. Finally, they calculated the dynamic radiation force as follows

$$F_D = E_D Y_D \cos(\Delta\omega t - \varphi) \quad (1.41)$$

where E_D , Y_D and φ are the energy density, and the dynamic radiation force function, and phase-shift, respectively [79].

1.4. Application of acoustic radiation forces in non-contact excitation and particle manipulation

Dynamic and static acoustic radiation forces find diverse applications, notably in non-contact excitation utilizing dual beam frequencies, particle manipulation, and levitation [32-41]. In this section, some of these applications are mentioned and briefly described.

1.4.1. Dual-frequency ultrasound beams

In the literature, the dual-frequency ultrasound beam method presented as a way for generating dynamic acoustic radiation force and found various applications, such as tissue imaging and non-contact excitation [34-37]. If an object acoustically excited through a pair of ultrasound frequencies, ω_a and ω_b , the exerted acoustic radiation force has five components, a component at $\omega = 0$ called static acoustic radiation force, three component at high frequency $\omega_a + \omega_b$, $2\omega_a$, and $2\omega_b$ and a component at the difference frequency (Fig. 1.4), $\Delta\omega = \omega_b - \omega_a$.

In dual-frequency ultrasound beams, the first order of the potential functions of velocity for each ultrasound acoustic wave can be written by [35]

$$\begin{aligned} \phi_a(x, t) &= \phi_{ai}(x, t) + \phi_{as}(x, t), \\ \phi_b(x, t) &= \phi_{bi}(x, t) + \phi_{bs}(x, t), \end{aligned} \quad (1.42)$$

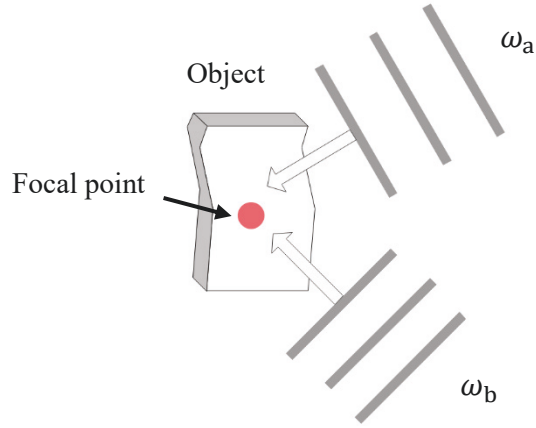


Fig. 1.4. The dual-frequency ultrasound beam method, using two different frequencies (ω_a and ω_b), focused on a point to generate a dynamic radiation force.

(i, s) indices show the incident and scattered waves, respectively. Using Eq. (1.1) the dynamic radiation force can be obtained as [38]

$$F_{\text{rad}} = \iint_A \left\{ \rho_0 \frac{\partial(\phi_a + \phi_b)}{\partial t} + \frac{\rho_0}{2c_0^2} \left(\frac{\partial(\phi_a + \phi_b)}{\partial t} \right)^2 - \frac{\rho_0}{2} |\nabla(\phi_a + \phi_b)|^2 + (\nabla(\phi_a + \phi_b) \otimes \nabla(\phi_a + \phi_b)) \right\} dA, \quad (1.43)$$

the \otimes sign donates the dyadic product, by assuming that the potential function of the velocity is a harmonic function as [25]

$$\begin{aligned} \phi_a(x, t) &= |\phi_a| \cos(\omega_a t), \\ \phi_b(x, t) &= |\phi_b| \cos(\omega_b t), \end{aligned} \quad (1.44)$$

and by using these two Trigonometric relations

$$\begin{aligned} \cos(\omega_a t) \cdot \cos(\omega_b t) &= \frac{1}{2} \cos((\omega_b + \omega_a)t) + \frac{1}{2} \cos((\omega_b - \omega_a)t), \\ \sin(\omega_a t) \cdot \sin(\omega_b t) &= \frac{1}{2} \cos((\omega_b - \omega_a)t) - \frac{1}{2} \cos((\omega_b + \omega_a)t), \end{aligned} \quad (1.45)$$

Eq. (1.43) can be re-written as

$$\begin{aligned}
F_{\text{rad}} = & \iint_A \left\{ \rho_0 \omega_a |\phi_a| (\sin \omega_a t) + \frac{\rho_0}{2c_0^2} \omega_a^2 |\phi_a|^2 (\cos \omega_a t)^2 - \frac{\rho_0}{2} |\nabla(|\phi_a|)|^2 (\cos \omega_a t)^2 \right. \\
& \left. + (\nabla \phi_a \otimes \nabla \phi_a) (\cos \omega_a t)^2 \right\} dA + \\
& \iint_A \left\{ \rho_0 |\phi_b| (\sin \omega_b t) + \frac{\rho_0}{2c_0^2} \omega_b^2 |\phi_b|^2 (\cos \omega_b t)^2 - \frac{\rho_0}{2} |\nabla(|\phi_b|)|^2 (\cos \omega_b t)^2 \right. \\
& \left. + (\nabla \phi_b \otimes \nabla \phi_b) (\cos \omega_b t)^2 \right\} dA + \\
& \iint_A \left\{ \frac{\rho_0}{2c_0 c_0^2} \omega_a \omega_b |\phi_b| |\phi_b| (\cos(\omega_b - \omega_a) t) - \rho_0 \nabla |\phi_a| \cdot \nabla |\phi_b| (\cos(\omega_b - \omega_a) t) \right. \\
& \left. + (\nabla \phi_b \otimes \nabla \phi_b) (\cos(\omega_b - \omega_a) t) \right\} dA \\
& \iint_A \left\{ -\frac{\rho_0}{2c_0^2} \omega_a \omega_b |\phi_b| |\phi_b| (\cos(\omega_b + \omega_a) t) - \rho_0 \nabla |\phi_a| \cdot \nabla |\phi_b| (\cos(\omega_b + \omega_a) t) \right. \\
& \left. + (\nabla \phi_b \otimes \nabla \phi_b) (\cos(\omega_b + \omega_a) t) \right\} dA.
\end{aligned} \tag{1.46}$$

By taking time average of Eq. (1.46), and by considering that

$$\begin{aligned}
\frac{1}{T} \int_T (\cos \omega t)^2 dt &= \frac{1}{2}, \\
\frac{1}{T} \int_T (\sin \omega t) dt &= 0,
\end{aligned} \tag{1.47}$$

they presented radiation force has two static components, one related to the first wave and another related to second wave and has dynamic components at $2\omega_a$, $2\omega_b$, $\Delta\omega = (\omega_b - \omega_a)$ and $(\omega_b + \omega_a)$. In the literature, the component at the difference frequency, $\Delta\omega$, called dynamic acoustic radiation force [38].

1.4.2. Non-contact excitation

Huber et al. were the first to suggest dual beam mode for non-contact excitation of different range sizes of objects, from microcantilever to guitar body, to obtain their resonant frequencies. In dual beam mode they assumed that the velocity potential function can be expressed as [34-37]

$$\phi = A \cos \left(2\pi f_a - \frac{\Delta\varphi}{2} \right) t + A \cos \left(2\pi f_b + \frac{\Delta\varphi}{2} \right) t. \tag{1.48}$$

Two ultrasound waves have same amplitude A , their frequencies are f_a and f_b , respectively, and $\Delta\varphi$ is the phase difference between two waves. In this case, the dynamic acoustic radiation force acting on the object, is proportional to the square of the velocity potential function. As discussed previously, the exerted dynamic acoustic radiation force has four components. First, a component at frequency difference $\Delta f = f_b - f_a$, second and third components at $2f_a$ and $2f_b$, and forth component at $f_b + f_a$. To perform non-

contact excitation in audible frequency range f_a and f_b , are chosen close to each other, and symmetric about a central frequency f_c as

$$\begin{aligned} f_a &= f_c - \frac{\Delta f}{2}, \\ f_b &= f_c + \frac{\Delta f}{2}. \end{aligned} \quad (1.49)$$

In many experiments, except Δf component other components will be more than audible frequency range and can be neglected, therefore, the only time-varying component of interest for the modal analysis in audible frequency range is the radiation force component at the difference frequency of Δf , in this case, the dynamic acoustic radiation force can be written as [37]

$$F_{\text{rad}} = F_0 \cos[(2\pi\Delta f)t + \Delta\phi]. \quad (1.50)$$

In 2006, Huber et al. suggested dynamic acoustic radiation force for non-contact excitation of a pipe organ reed. He compared and discussed the results obtained using single, dual, and confocal ultrasound transducers in (AM) and two-beam modes, along with results obtained using a mechanical shaker and audio excitation using a speaker [34]. In another paper, Huber et al. performed non-contact excitation of hard-drive suspensions using ultrasound radiation force. This paper was like the previous work for operation deflection shape of a pipe organ reed but with a different case study. The head gimbal assembly suspension used in this study was a roughly 10 – 14.5 mm length cantilever structure with an average width of about 4 – 6 mm [35]. Using the acoustic radiation force, Huber et al. used focused acoustic waves to conduct a non-contact excitation of microcantilevers and coupled microcantilever arrays [36]. The diameter of the focal spot produced by this transducer is 3 mm, it is much bigger than microcantilever dimension, and it can be assumed that the entire microcantilever (Mikromasch CSC12-E silicon AFM, $(350 \times 35 \times 1 \mu\text{m}^3)$) is uniformly excited [36]. An operation deflection shape was conducted using acoustic radiation force to obtain the first three resonance frequencies of the microcantilever. Then, results were compared with those obtained by base excitation, which shows a good agreement. Also, Huber et al. used acoustic radiation force for non-contact excitation of a classical guitar. In previous studies, he demonstrated that it is possible to use the ultrasound radiation force in the air for operation deflection shape of objects ranging in size from microcantilevers that are a few hundred microns in length to hard drive suspensions and other cantilevers a few centimetres long [37]. In this study, he demonstrated that the ultrasound radiation force excitation technique could also be used

for non-contact excitation of larger objects such as acoustic guitars. He measured the frequency response and deflection shapes of a Cordoba 45R (70–800 Hz) and compared results with mechanical shaker excitation. As noted, Huber’s papers focus primarily on identifying resonance frequencies and mode shapes rather than mentioning the applied acoustic force magnitude. To address this gap and estimate the acoustic force, in the next section a numerical simulation was conducted using COMSOL Multiphysics software.

1.4.3. Numerical study: contactless excitation of microcantilever

In this section, the numerical study of contactless excitation of microcantilevers is discussed, directly linking to the broader theme of using dynamic acoustic radiation forces for non-contact excitation. By exploring the behaviour of microcantilevers under acoustic excitation, the study provides deeper insights into the mechanisms and potential applications of acoustic radiation forces in non-contact scenarios. Additionally, it offers an opportunity to build on the work done by Huber in experimental studies. While Huber effectively demonstrated acoustic forces for non-contact excitation, his research did not include simulations to quantify the forces exerted on the objects. To extend this work, numerical simulations were employed using COMSOL Multiphysics to model the system, focusing on acoustic-structure interactions driven by first-order pressure fluctuations. This simulation-based approach complements Huber’s experimental findings and provides a more detailed understanding of the forces involved. Moreover, the work sets the foundation for the modelling techniques presented in Chapter 2, where the analysis is extended to include second-order time-averaged acoustic radiation forces, offering a more comprehensive understanding of non-contact excitation and its applications. Here, a numerical study is conducted to determine the vibration response of a silicon microcantilever based on the Huber et al.’s experimental results. Boundary load and acoustic wave excitation techniques are employed to identify the first three resonance frequencies of the microcantilever and their corresponding mode shapes [36]. Comparing the numerical responses with Huber et al.’s experimental results suggests that the dynamic acoustic radiation force behaves similarly to a uniform boundary load. The numerical analysis reveals resonance peaks at 11.4 kHz, 72.1 kHz, and 198 kHz, which show good agreement with Huber’s findings, as shown in Fig. 1.5. Subsequently, the dynamic acoustic radiation force is estimated using the resonance frequencies obtained from the numerical simulation.

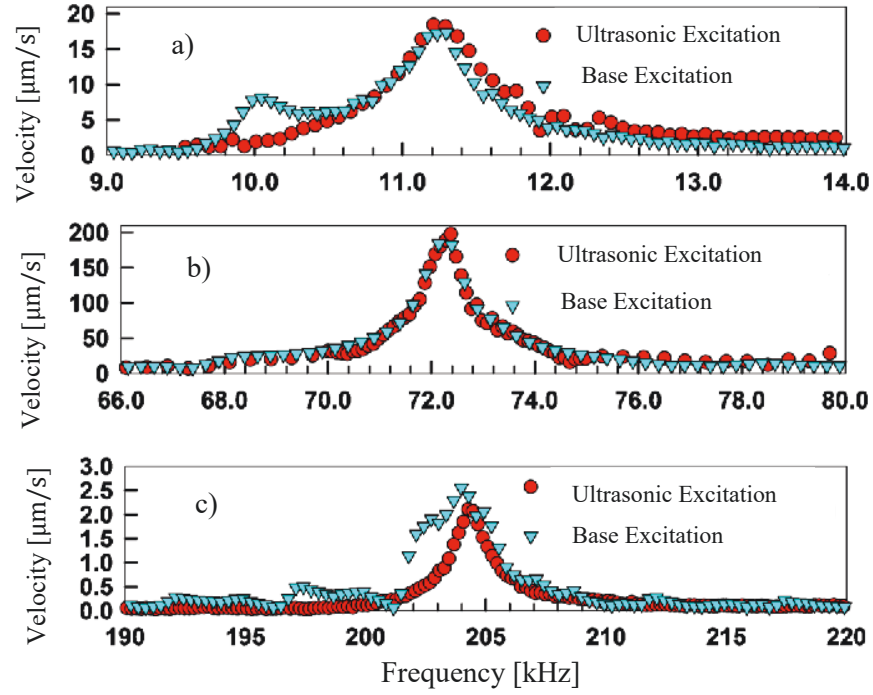


Fig. 1.5. A comparison between a) first, b) second, and c) third resonance frequency for ultrasound radiation force and base excitation obtained in the Huber's experiment adopted from [36].

To obtain the first three resonance frequencies, the mode shapes, and the exerted radiation force, A numerical simulation using COMSOL Multiphysics (Fig. 1.6) was conducted to model a microcantilever, and its results were compared with experimental findings from [36].

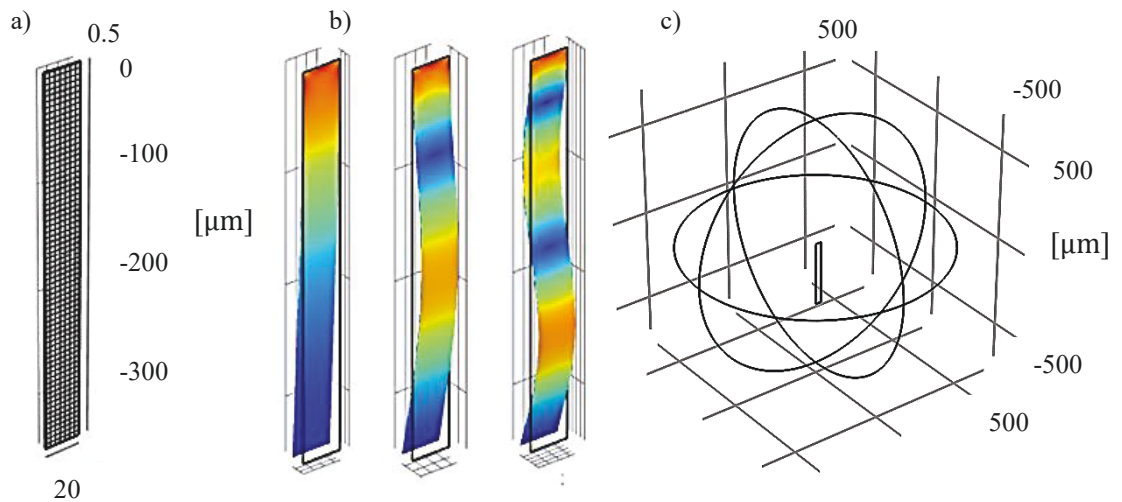


Fig. 1.6. a) A 3D Finite element model of microcantilever, b) three first mode shapes, and c) a 3D finite element model of microcantilever surrounded in a fluid domain, adopted from [32].

Resonant frequencies are obtained using boundary load and acoustic plane pressure wave excitations. According to [36], dynamic acoustic radiation force uniformly excites the microcantilever, allowing it to be modelled as a harmonic boundary load. In Huber's work, the force frequency is known and adjustable via amplitude modulation, but its amplitude remains unknown.

To do analysis by boundary load excitation, the solid mechanics physics in COMSOL was selected, using a linear elastic microcantilever. A mapped mesh of 18,033 cube-shaped elements was generated and fixed boundaries were used to clamp the beam (Fig.1.6a). A boundary pressure load of 1 N/m^2 amplitude and a frequency range of 5 kHz to 210 kHz was applied using 1 kHz frequency steps. Using both the pressure acoustics module, and the solid mechanics module within the acoustic-structure interaction Multiphysics interface in frequency domain, the microcantilever was excited using a plane acoustic wave of 10 Pa amplitude and three first mode shapes obtained (Fig.1.6b). The fluid domain has been modelled as a spherical region surrounding the microcantilever (Fig 1.6c). Due to free tetrahedral meshing of both, the solid and fluid domain, this model includes with 127,003 tetrahedral elements many more elements than the boundary load excitation model in which the solid domain only was meshed. The boundary condition for the fluid at the outer boundary of the spherical domain is that of spherical wave radiation which allows acoustic waves to exit the domain without reflection (i.e. fulfilling the Sommerfeld radiation condition) [80].

Fig.1.7a shows the frequency response of the microcantilever tip with the lowest three resonances obtained with boundary load excitation. The first three resonant peaks are determined at 11.4 kHz, 72.6 kHz, and 198 kHz and are in good agreement with Huber's experimental results showing less than 0.5% difference (11.2 kHz, 72.4 kHz, and 204 kHz) [37]. Using acoustic wave excitation, the first three resonances are obtained at the same frequencies obtained by boundary load excitation as shown in Fig.1.7b.

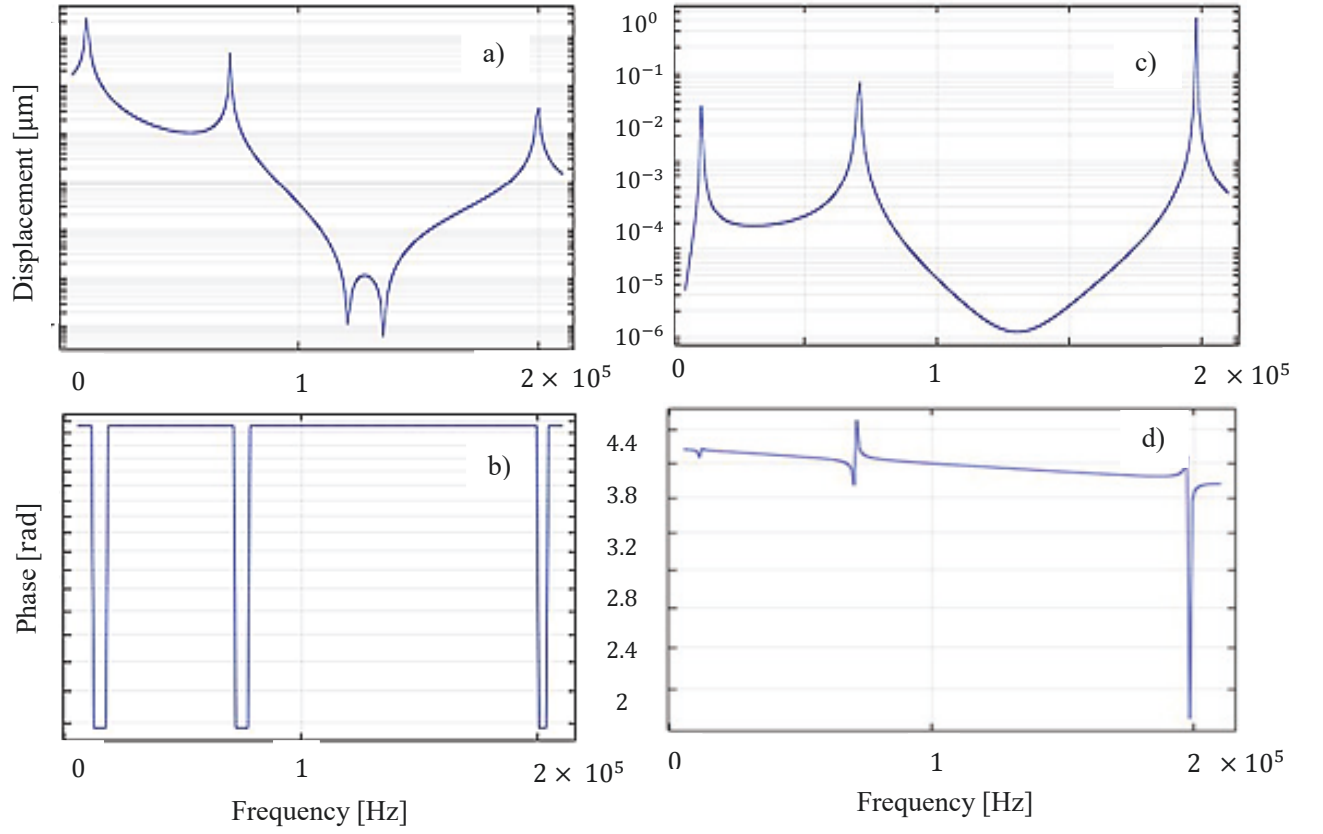


Fig. 1.7. The frequency response of the lowest three resonances of the microcantilever obtained by two excitation methods: a, b) boundary load excitation (a: displacement, b: phase) and c, d) acoustic wave excitation (c: displacement, d: phase), adopted from [32].

Based on the numerical simulation, and the obtained resonant frequencies the dynamic acoustic radiation force can be estimated. By comparing different excitation methods, we can approximate the known response of the system. However, another unknown parameter in this experiment is damping which has been considered in the following as “loss factor” in terms of material damping. The loss factor η depends on other parameters such as temperature or frequency and by increasing frequency the loss factor decreases [81]; for silicon, η is generally expected to lie between 0.001 and 0.1 [81]. the acoustic radiation force can be expressed as [37]

$$F_{\text{rad}} = F_0 \cos[(2\pi\Delta f)t], \quad (1.51)$$

with Δf being its resonance frequency. To estimate the amplitude F_0 of the acoustic radiation force we adjust the input force so that the output of the microcantilever tip speed corresponds to the value measured by Huber et al. [37] as presented in Fig.1.5.

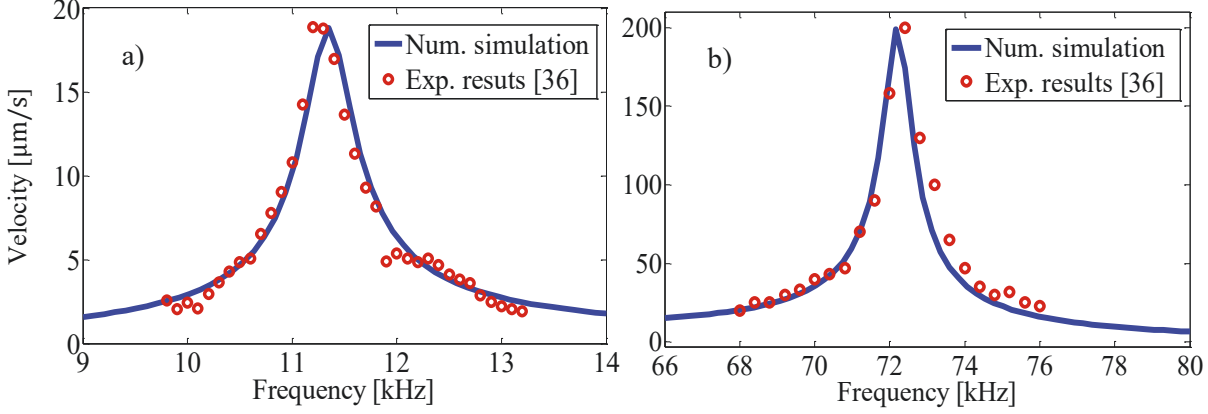


Fig. 1.8. A comparison between numerical simulation and some points of the experimental results presented in [36] near a) the first resonance frequency and b) the second resonance frequency when the amplitude of the boundary load excitation in numerical simulation is F_0 .

As shown in Fig. 1.8a, for the first resonant frequency and if $\eta = 0.04$ and $F_0 = 8.0 \times 10^{-5} \text{ N/m}^2$, the frequency responses of the computational model match well those of the experiments. For the first resonant frequency, f_1 , and the radiation force we can hence write

$$F_{\text{rad}}(f_1) = 8.0 \times 10^{-5} \cos[(2\pi \times (11.4 \times 10^3))t] \text{ N/m}^2. \quad (1.52)$$

Similarly, as shown in Fig. 1.8b, for the 2nd resonant frequency, if $\eta = 0.01$ and $F_0 = 2.45 \times 10^{-3} \text{ N/m}^2$, the response is similar to that found in experiments and the radiation force can be written as

$$F_{\text{rad}}(f_2) = 2.45 \times 10^{-3} \cos[(2\pi \times (72.1 \times 10^3))t] \text{ N/m}^2, \quad (1.53)$$

finally, for the 3rd resonant frequency, f_3 , if $\eta = 0.0055$, the radiation force expression becomes

$$F_{\text{rad}}(f_3) = 6.54 \times 10^{-2} \cos[(2\pi \times (198 \times 10^3))t] \text{ N/m}^2. \quad (1.54)$$

Due to having at least two unknowns, forcing and damping, the latter having different components including anchor and radiation losses, or internal damping, which has yet to be studied experimentally, no clear answer can be obtained here.

If one considered nonlinear vibrations of the microcantilever as related to nonlinear stiffness or nonlinear damping, the estimated acoustic radiation force would have to change. The absolute deviation between the magnitudes of the forces, as calculated using linear and nonlinear assumptions, depends on the kind, the degree, and the strength of the nonlinearity involved [81]. The finite element method could calculate the radiation force exerted on a nonlinear microcantilever by knowing all those nonlinear parameters for stiffness, damping, etc.

Huber et al. [34-37] studied non-contact excitation to determine natural frequencies and deflection shapes, providing key insights into acoustic radiation forces. This thesis builds on their work by investigating the dynamic response of levitated objects in acoustic fields. It introduces an experimental setup to study their behaviour under external vibrations. Unlike Huber's approach, which focused on dynamic reaction for frequency and shape analysis, this research examines object responses within acoustic radiation forces for levitated objects, adding to existing knowledge.

1.4.4. Particle manipulation and acoustic levitation

Manipulation and control of particle movement can be applied in various ways. Traditional methods for particle manipulation include magnetic fields [82], electric fields, and dielectric manipulation [83]. However, these techniques heavily depend on the electrical and magnetic properties of the particles involved. In contrast, acoustic waves offer a versatile approach to manipulating a wide range of particles [84]. Compared to other types of forces, the use of acoustic radiation force has very low limitations and only depends on the existence of differences between structure properties and host fluid properties. Methods based on the acoustic radiation forces show minimal adverse effects compared to conventional techniques relying on electric and magnetic fields, particularly notable in biological applications. Unlike electric fields, which can generate excessive heat and potentially cause overheating concerns, ultrasonic waves generate little to no heat during their application, ensuring the safety of delicate biological samples. For example, acoustic radiation forces do not interfere with iron balance, a critical consideration in many biological and biomedical contexts where magnetic fields can

disrupt cellular processes [85,86]. Therefore, there is a compelling need to investigate the mechanisms behind the generation and application of acoustic radiation forces [82-86]. Additionally, acoustic levitation has emerged as a powerful tool across various fields, including volumetric displays, additive manufacturing, and microfluidics, demonstrating its versatility and broad potential applications [87,88]. Volumetric displays leverage the ability of acoustic levitation to manipulate particles in mid-air, creating three-dimensional visualizations without the need for a physical screen.

In additive manufacturing, acoustic levitation is utilized for precise, non-contact manipulation of materials, enabling innovative fabrication techniques. The ability to levitate and merge droplets or particles has been applied to build structures layer by layer, offering advantages in precision and cleanliness over traditional methods [89]. Research in this area, such as that by Andrade et al. has highlighted the potential for acoustic levitation in creating complex geometries and handling sensitive materials without contamination [90]. In microfluidics, acoustic levitation plays a crucial role in lab-on-a-chip applications, where it is used for tasks such as cell sorting, mixing, and manipulation of droplets. Guo et al. explored using acoustofluidic techniques to achieve high-throughput and precise control over fluidic processes. These applications demonstrate the versatility of acoustic levitation in advancing micro-scale operations, particularly in biomedical research and diagnostics [91].

Phased array levitators have revolutionized acoustic manipulation by enabling precise, non-contact control of objects through dynamically modulated acoustic fields [92,93]. It is an array of ultrasonic transducers that is set to combine and focus sound energy at specific points in the fluid volume (in front of the array). Each transducer helps create an ultrasonic wave at a specific point. Seah et al. [94] conducted a groundbreaking study on dexterous ultrasonic levitation of millimetre-sized objects in the air, showcasing the precise manipulation capabilities of phased array levitator systems. By dynamically modulating acoustic fields, they achieved stable levitation and controlled translation, rotation, and orientation of particles with high accuracy, even in free air. This approach allowed for effective manipulation of various object sizes and materials, emphasizing the potential of ultrasonic levitation for non-contact applications such as material handling and assembly [94]. Building on these advancements, Marzo et al. [95] introduced a novel method utilizing ultrasonic phased arrays to create holographic acoustic fields for three-dimensional levitation and manipulation. Through phase-shifting individual transducers,

they demonstrated precise control over particle positioning and motion, enabling simultaneous levitation of multiple particles and dynamic manipulation along complex trajectories. Their work highlighted the versatility of holographic acoustic methods in generating intricate pressure fields for stable and precise particle trapping. Together, these studies underscore the potential of phased array systems in advancing the field of acoustic manipulation.

In acoustic manipulation, being able to control the magnitude and direction of the exerted acoustic radiation forces and produce alternating pushing and pulling forces is desired. One factor determining the direction of the acoustic radiation force is the acoustic contrast factor, denoted as ϕ . This dimensionless parameter, which is caused by the interaction between the sound waves emitted in the medium and the particle in its path, determines the direction of the acoustic radiation forces, and according to the Gorkov's formulation, it depends on the ratio of density and compressibility of the particle to the surrounding fluid (Fig. 1.9).

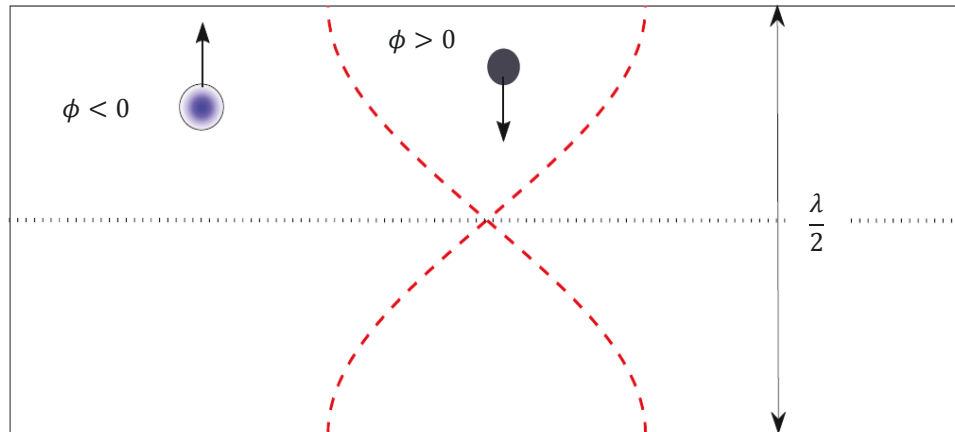


Fig. 1.9. The sign of the acoustic contrast factor, ϕ , determines whether a particle is attracted to or repelled from a pressure node in a plane standing wave field with wavelength of λ .

There are some techniques to produce acoustic radiation forces with pushing and pulling effects beyond the particles and medium density and compressibility, such as Gaussian Beams [96,97], cross-plane beams [98], and Bessel beams [99-101] with some restrictions. For example, in the case of Bessel beams, the negative radiation force emerges in specific frequency-beam angle values depending on the target object properties, and the generated negative radiation forces have small values compared with the positive (pushing) force. In the case of Gaussian beams, the off-axis component of

radiation force is positive, which may lead to instability. Several recent theoretical studies have pioneered methods for generating negative (pulling) radiation forces in the context of acoustic manipulation [102-108]. The interaction between the fluid and the levitated objects in the acoustic radiation force field is nonlinear in nature. Several recent studies have significantly advanced the understanding of the dynamic behaviour of levitated objects.

Dolev et al. investigated the stability of acoustic traps under varying frequencies, offering key insights into the conditions necessary for maintaining equilibrium [109]. Paneva et al. examined the effects of fluid viscosity on levitated object dynamics, emphasizing the role of medium properties in influencing behaviour [110]. Sugita et al. analysed nonlinear responses in high-amplitude acoustic fields, presenting both theoretical and experimental studies on a nonlinear dynamic model for single-axis standing-wave acoustic levitation. They focused on the nonlinear coupling between radial and axial vibrations and explored its effect on levitation stability. The model predicts that levitation stability can be lost due to forced axial vibrations. Using acoustic potential theory, the acoustic radiation force acting on a levitated spherical particle was derived and expanded into a power series to incorporate nonlinear terms. The equation of motion was analysed, and asymptotic solutions were compared with experimental data. The study concluded that axial vibrations reduce the natural radial frequency, destabilizing radial equilibrium. A stability criterion was proposed, showing that the critical axial vibration amplitude for instability depends on sound wavelength and standing wave geometry, matching experimental observations of levitation failure [111].

Research on levitated liquid droplets has focused on droplet shape oscillations [112]. Ilisar and Bucher implemented a feedback controller to improve control over acoustically suspended objects [113]. Studies on the instability of solid particles, such as those by Rudnik and Barmatz, explored resonant chamber-based acoustic levitators. These studies revealed that the presence of levitated particles alters the resonant frequency, creating a velocity-dependent acoustic radiation force. This force can act as negative damping at higher velocities, leading to particle instability [114]. Foresti et al. investigated the stability of spherical and ellipsoidal particles in acoustic fields under varying viscosity conditions, providing valuable insights into the role of medium properties [115]. Similarly, Pérez et al. conducted experimental research on the dynamics of an acoustically levitated sphere within a single-axis classical acoustic levitator, adding to the

understanding of particle motion in controlled acoustic environments [116]. The dynamics of the levitated particle in mid-air were analysed as follows

$$m\ddot{x} = -b_2\dot{x}|x| - b_1\dot{x} - kx - mg \quad (1.55)$$

here, kx represents the linearized acoustic radiation force, calculated using Hooke's Law of linear spring stiffness, mg denotes the gravitational force, b_1 and b_2 are constants utilized for linear or nonlinear damping [116]. While these constants were determined through experimental work, no explicit justifications were provided for the assumption of linear acoustic radiation force. Using experimental analysis, Andrade et al. showed that some nonlinear effects, such as the jump phenomenon, harmonic generation, and hysteresis, can be observed for a small particle levitated between an acoustic transducer and reflector [117].

Fushimi et al. investigated the nonlinear dynamics of an acoustic levitator under external perturbation and derived a Duffing-like equation using the Gorkov formulation [118]. Through the study of bifurcation phenomena, they identified that system parameters, such as the frequency of the applied external excitation, significantly influence the nonlinear behaviour of the levitated object. They further observed that the force-displacement relationship is linear only for small displacements, beyond which nonlinear effects become prominent.

1.5. Research motivation and gaps

Since most studies in the literature have focused on the behaviour of the acoustic field and the generation of acoustic radiation forces, the main motivation of this study is to address the gap in understanding these forces by applying external sinusoidal excitation to the force field. This approach allows us to examine the resulting changes in the force and, subsequently, in the dynamic behaviour of the levitated object. For this purpose, some tools and techniques in the field of nonlinear dynamics are used, such as analytical and numerical methods in nonlinear problems, bifurcating diagram analysis, statistical analysis, and sensitivity analysis. Nonlinear time series analysis techniques, such as recurrence plots (RPs) and recurrence networks (RNs), are also employed in this study. Additionally, the data-driven method (DDM) of sparse identification of nonlinear dynamics (SINDy) is used to reconstruct the equation of motion from the experimentally extracted time series data. These methods enable the identification and analysis of complex dynamics, offering insights into the system's behaviour and providing a more

comprehensive understanding of the underlying nonlinear processes. To ensure coherence and avoid redundancy, the relevant literature review on these tools and techniques has been integrated into the relevant chapters and explained in the sections discussing these methods before their application. After a literature review, three important gaps in the understanding of acoustic radiation forces and the dynamic behaviour of levitated objects are going to be investigated as justified by the literature review.

- a) **We have currently a limited understanding of the levitated object's dynamics:** This research aims to fill this gap by considering the dynamic behaviour of the trapped object under the influence of external sinusoidal excitation. In this case, theoretical and analytical methods, along with numerical simulations, are used to study the effect of external excitation on the forces exerted on the object and, consequently, its dynamic behaviour.
- b) **Bifurcation analysis, recurrence plots and networks to classify system behaviour for acoustically large objects:** The generation of experimental bifurcation diagrams and the use of recurrence plots and networks for analysing system dynamics contribute to a deeper understanding of the complex behaviour of levitated objects in different dynamical regimes for acoustically small and large objects.
- c) **Linear and duffing modelling shortcomings:** Several studies in this field have utilized linear models or the well-known Duffing equation to characterize acoustic traps. However, the limitations of these models have led to a need for a deeper understanding of the dynamic behaviour of levitated objects, especially acoustically large objects. This research addresses this gap by introducing the Sparse Identification of Nonlinear Dynamics (SINDy) algorithm to extract the nonlinear differential equation of motion from experimental time series data.

1.5.1. Aim and objectives

The study is structured into six interconnected steps. The key aims and objectives for each step are outlined in Table 1.2.

Table 1.2. Steps, aim and objectives of the thesis.

	Step	Aim	Objectives
1	Theoretical approach for acoustic radiation force (ARF)	Developing a robust theoretical foundation for understanding the ARF exerted on small objects.	1-Applying Gorkov theory to model ARF on small objects. 2-Utilizing COMSOL simulation to enhance theoretical insights. 3-Applying analytical methods to investigate governing equation of motion analytically.
2	Sensitivity analysis and bifurcation diagram	Investigating the sensitivity of ARF dynamics and exploring bifurcation phenomena through theoretical analysis and experimentation.	1-Conducting sensitivity analysis to identify key parameters influencing ARF. 2-Developing bifurcation diagrams based on theoretical predictions. 3-Experimentally characterizing the setup and extract nonlinear time series data to validate theoretical expectations.
3	Experiment validation	Validating theoretical predictions through experimental analysis, emphasizing the transition from small to large objects	1-Validating theoretical bifurcation diagrams for small objects through experiments. 2-obtaining bifurcation diagrams for large objects. 3-Assessing and comparing experimental results with theoretical expectations.
4	Nonlinear time series analysis	Investigating large object behaviour in different dynamical regimes using advanced nonlinear time series analysis techniques.	1-Reconstructing the phase space using nonlinear time series data. 2-Applying recurrence plots and network analysis to unravel intricate large object dynamics and detect motifs to quantify object behaviour in various dynamical regimes.
5	Applying SINDy algorithm	Extracting nonlinear equations of motion for both small and large objects.	1-Applying Sparse Identification of Nonlinear Dynamics (SINDy) to extract equations of motion. 2-Exploring the implications of the extracted equations for both small and large objects.
6	Conclusion and future directions	Synthesizing findings and propose implications for the broader acoustic radiation force community.	1-Summarizing key results and insights obtained from each step. 2-Highlighting the potential for future research and the development of new techniques for trapping, handling, and levitating objects using acoustical energy.

1.5.2. Research questions

Based on the aim and objectives, the research questions can be summarized as follows

1. How does external excitation impact the magnitude and direction of acoustic radiation forces on levitated objects?
2. What is the dynamic behaviour of acoustically small and large objects trapped in acoustic radiation force fields under external mechanical excitation?
3. Can SINDy algorithm accurately extract nonlinear equations of motion from experimental time series data for large acoustically objects, complementing the predictions of Gorkov's theory for small objects, and how can we effectively characterize the nonlinear behaviour of the system using its experimental time series data?

1.5.3. Thesis outline

Chapter 1 presents a literature review of acoustic radiation forces, theories, and formulations (King, Yosioka, Gorkov, etc.) and then discusses the gaps, aims and objectives, and research questions of the thesis.

In Chapter 2, the theory of the Gorkov potential function and its acoustic contrast factor are re-examined considering the scenario of a harmonic disturbance that causes an acoustically spherical object to undergo rigid-body oscillations in an ideal fluid in a standing plane ultrasonic wave field. In this context, the direction and magnitude of time-averaged acoustic radiation force and the dynamic behaviour of the levitated object are of interest, especially when using an additional external energy source, such as the control of vibrations in vibrating platforms. A nonlinear governing equation of motion is obtained by applying Newton's second law. By changing the amplitude of the external excitation, positive, negative, and zero acoustic radiation forces can be achieved. External excitation amplitude dependence and force inversion are new features that can be used in acoustic manipulation for non-contact dynamic properties of the smallest objects. This is interesting because it raises the question of whether, in principle, the potential field can be used to control the acoustic radiation force on an object through an external perturbation, leaving other field parameters intact. Then, a three-dimensional numerical model of the acoustic radiation force presented in COMSOL was created, which validated the theoretical results. The advantage of the 3D finite element proposed model in comparison with previous studies in the literature is that it can be used to study objects

with non-rotational symmetry, multi-object interaction, and near-wall analysis for future research. Nonlinear dynamic analysis often uses asymptotic methods to study complex systems. In Chapter 2, after introducing some of these effective methods in this field, these methods will be used to theoretically investigate the system's dynamic behaviour for governing equations of motion describing acoustically small objects within an acoustic radiation force field. In Chapter 3, using the theoretical formulation presented in Chapter 2, the bifurcation behaviour is studied, and this is shown together with a sensitivity analysis to represent the system's dynamic behaviour in specific regimes of the bifurcation diagram. In this Chapter, the governing equation of motion is solved using the Runge–Kutta order fourth, and the appropriate time step is selected utilizing a statistical observation and based on the variance of results shown by a box plot diagram. The system's behaviour sensitivity is investigated by calculating the Sobol indices in relation to various system parameters, including coefficients related to levitated object and fluid properties, external vibration frequency, and amplitude. An experimental setup to extract nonlinear time series data will be discussed in this Chapter. Recently, SINDy approach has been proposed to identify nonlinear dynamical systems from time series data. SINDy assumes that the equations of motion have only a few important terms. In Chapter 4, SINDy algorithm is applied to reconstruct the nonlinear differential equation of motion of a levitated acoustically small and large object trapped in an acoustic radiation force field, using experimental time series data. In the first step, the aim is to evaluate the robustness of the SINDy algorithm against noisy data. The study confirms the theoretical robustness of SINDy against noise in low-noise conditions, while experimental data filtering is recommended for high-noise data. Here, and due to the nonlinear nature of the problem, the GHKSS filter is used, which effectively reduces the noise in the experimental data. Also, Chapter 4 discusses nonlinear time series analysis, recurrence plot, recurrence network, and SINDy algorithm. Recurrence is a fundamental property of dynamical systems, and recurrence plots (RPs), a powerful tool for visualizing and analysing a nonlinear system's behaviour, are used to study the system in its phase space. In this case, the system's phase space must be reconstructed using its time series data to obtain RPs. The first minimum of the mutual information (MI) and false nearest neighbours (FNN) method is used to reconstruct the phase space using experimental nonlinear time series data. Using the generated adjacency matrix, recurrence networks are formed, and motifs are searched for to classify the dynamics of the system.

Chapter 5 is the conclusion and future directions. It is hoped that this connection between nonlinear time series analysis, SINDy, and the acoustic radiation force community will spur new techniques for trapping, handling, and levitating small objects using acoustical energy.

CHAPTER 2: VIBRATION CONTROL OF A LEVITATED OBJECTS THROUGH EXTERNAL EXCITATION

2.1. Introduction

As highlighted in the literature review, the non-contact manipulation of samples in the air has emerged as a foundational technology across various disciplines, ranging from engineering to medicine [82-124]. While acoustic levitation stands out as a promising method in this regard, most research efforts have been directed toward characterizing the properties of the acoustic field rather than exploring the dynamic behaviour of levitated objects. This Chapter seeks to bridge this gap by studying the nonlinear dynamics of solid objects levitated acoustically by using theoretical and numerical modelling.

2.2. Gorkov formulation

According to the literature review, analytical expressions of acoustic radiation force, F_{rad} , were reported for simple geometries such as spherical objects much smaller than the wavelength ($kr \ll 1$) and are therefore treated as particles [60-64]. Gorkov used the principle of conservation of momentum and far-field scattering to derive the same analytical expression for the force. Gorkov assumed that F_{rad} can be described by time-averaged of potential and kinetic energy of the acoustic field presented and presented his formulation for an acoustically small particle placed in standing acoustic wave field [64]. According to this formulation, the acoustic radiation force can be is the gradient of a potential function

$$F_{\text{rad}} = \nabla[U], \quad (2.1)$$

when the potential function can be defined by

$$U = V_p \left(\frac{f_1}{2} \kappa_0 \langle P_{\text{in}} \rangle^2 - \frac{3f_2}{4} \rho_0 \langle V_{\text{in}} \rangle^2 \right), \quad (2.2)$$

when $\langle P_{\text{in}} \rangle$ and $\langle V_{\text{in}} \rangle$ are the time-averaged incident pressure and velocity field, respectively, and f_1 and f_2 are the monopole and the dipole coefficients as

$$f_1 = 1 - \tilde{\kappa}, f_2 = \frac{2(\tilde{\rho}-1)}{2\tilde{\rho}+1}, \quad (2.3)$$

for a one-dimensional planar harmonic acoustic standing wave field, the Gorkov formulation can be simplified to [64]

$$F_{\text{rad}} = V_p E_{\text{ac}} k \phi(\tilde{\rho}, \tilde{\kappa}) \sin(2kz), \quad (2.4)$$

in which $\phi(\tilde{\rho}, \tilde{\kappa})$ is referred to as the acoustic contrast factor and can be expressed by

$$\phi(\tilde{\rho}, \tilde{\kappa}) = \left[\frac{1}{3} \frac{(5\tilde{\rho}-1)}{(2\tilde{\rho}+1)} - \tilde{\kappa} \right]. \quad (2.5)$$

The acoustic contrast factor represents the directional sensitivity of acoustic radiation force acting on objects in a fluid medium. It quantifies how the acoustic field affects the movement of objects relative to the surrounding fluid. $E_{\text{ac}} = \frac{P_a^2}{4\rho_0 c_0^2}$ denotes the acoustic energy density when $\tilde{\kappa}$ and $\tilde{\rho}$ are relative compressibility and density, respectively [5].

2.3. Theoretical modelling

In this section, the theory of Gorkov potential function and its acoustic contrast factor are revisited considering a scenario of a harmonic excitation. The incident pressure, P_{in} , due to a plane standing wave, acting on a solid sphere trapped in an acoustic field e.g. by an acoustic levitator within a lossless fluid can be written as [5]

$$P_{\text{in}} = P_a \cos(k\xi) \cos(\omega_1 t), \quad (2.6)$$

when P_a is the pressure amplitude, k is the acoustic wave number, ξ is the object's distance from a pressure node, ω_1 is the standing wave frequency, and t is the time. While it is common to reference the distance from a pressure antinode, it has instead been chosen to reference the distance from a pressure node in this formulation. This is consistent with acoustic radiation force theories, where objects tend to stabilise or be trapped near the pressure nodes due to the balance of forces [59,60]. Since the relationship between nodes and antinodes is straightforward, with the distance between them being half a wavelength, either reference is physically consistent. In the absence of external excitation, the steady-state component of the radiation force acts as a nonlinear restoring force with a nonlinear softening spring constant of k_s [118], attracting the objects towards an acoustic trap. The trap sits either at the pressure node (PN) or the velocity node (VN) [125-127]. After

applying external excitation, the object can oscillate around its equilibrium position, O with a distance denoted by z within the range of $(0 \leq z \leq \lambda/4)$, with λ being acoustic wavelength, relative to its nearest PN (Fig. 2.1).

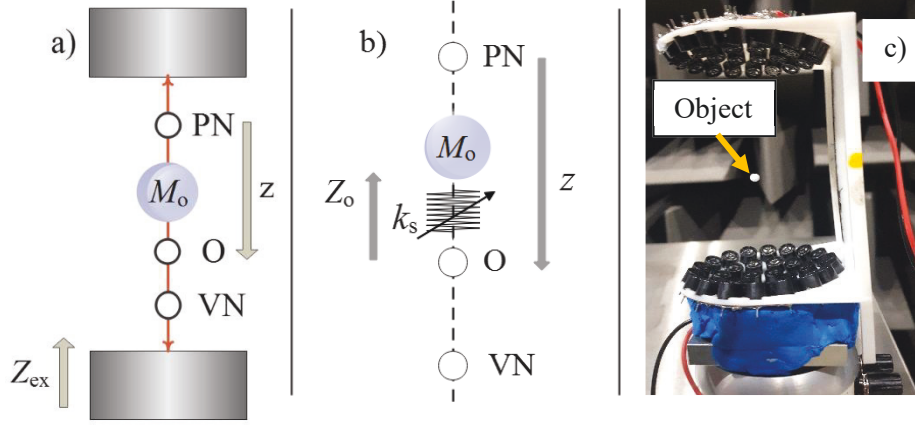


Fig. 2.1. A spherical object within an acoustic radiation force field with external sinusoidal excitation. (a) Schematic of an oscillatory object with mass M_o oscillating around its equilibrium position, O; (b) mechanical model with nonlinear stiffness (k_s). $Z_o = A_o \sin(\omega_o t)$ denotes the object oscillation caused by external disturbance, $Z_{ex} = A_{ex} \sin(\omega_{ex} t)$, with its (c) experimental set up; (c) photo of experimental setup with levitated object.

The external harmonic excitation can be described by,

$$Z_{ex}(t) = A_{ex} \sin(\omega_{ex} t), \quad (2.7)$$

where ω_{ex} is the frequency of the external disturbance to apply the acoustic field, and A_{ex} denotes its amplitude.

To exert control and manipulation over the levitated object within an acoustic radiation force field using an external disturbance, the existence of a relationship between the levitated object's response and the external excitation is presumed. It is assumed that by applying a simple external harmonic excitation, the object exhibits a simple harmonic response around point O, which means (1) the amplitude of the object, denoted by A_o , and (2) the object frequency, ω_o , is a function of the external excitation properties. In this scenario, by this assumption the object's response, $Z_o(t)$ can be written as

$$Z_o(t) = A_o \sin(\omega_o t). \quad (2.8)$$

In this scenario, P_{in} affects the object, which oscillates with Z_o around position 0 at a distance z from its nearest P.N., Since the oscillation is low-amplitude and doesn't perturb the acoustic field much, the time-varying pressure field can be written, as follows,

$$P_{\text{in}}(z, t) = P_a \cos\left(k(z - Z_o(t))\right) \cos(\omega_1 t). \quad (2.9)$$

Expanding Eq. (2.9) using trigonometric relation of $\cos(\alpha - \beta) = \cos(\alpha)\cos(\beta) + \sin(\alpha)\sin(\beta)$, the incident pressure field can be re-written as

$$\begin{aligned} P_{\text{in}}(z, t) &= P_a \cos(kz) \cos(kA_o \sin(\omega_o t)) \cos(\omega_1 t) + \\ &P_a \sin(kz) \sin(kA_o \sin(\omega_o t)) \cos(\omega_1 t) = P_a \cos(kz) C_1(t) + \\ &P_a \sin(kz) C_2(t), \end{aligned} \quad (2.10)$$

which shows the acoustic pressure acting upon the object with amplitude modulation inducing a dynamic F_{rad} component, when $C_1(t)$ and $C_2(t)$ represent the time components of the acoustic pressure. When we use the linear scattering assumption, one may ask this question that does this pressure field presented in Eq. (2.7) satisfy the wave equation [59]. To answer this question, we insert the Eq. (2.7) into the wave equation directly to see what happens, the wave equation can be stated as

$$\nabla^2 P_{\text{in}} = \frac{\partial^2 P_{\text{in}}}{\partial t^2}, \quad (2.11)$$

by expanding Eq. (2.11), we have

$$\begin{aligned} \cos(\omega_1 t) \cos(kA_o \sin(\omega_o t)) &= \cos(\omega_1 t) \cos(kA_o \sin(\omega_o t)) + \dots \\ &- 2 \left(\frac{\omega_o}{\omega_1}\right) kA_o \sin(\omega_1 t) \cos(\omega_o t) \sin(kA_o \sin(\omega_o t)) + \dots \\ &- \left(\frac{\omega_o}{\omega_1}\right)^2 kA_o \cos(\omega_1 t) \sin(\omega_o t) \sin(kA_o \sin(\omega_o t)) + \dots \\ &- \left(\frac{\omega_o}{\omega_1}\right)^2 (kA_o)^2 \cos(\omega_1 t) \cos^2(\omega_o t) \cos(kA_o \sin(\omega_o t)). \end{aligned} \quad (2.12)$$

At the limit of $(\omega_o/\omega_1) \ll 1$, only the first term on the right-hand side of the Eq. (2.12) remains, so that Eq. (2.9) can be considered a valid solution. According to the Eq. (2.10),

the oscillation of the object modulates the incident pressure field, and this modulation can be described by two ways, an amplitude modulation or a phase modulation as below

$$P_{\text{in}}(z, t) = A_1(t) \cos(kz) \cos(\omega_1 t) + A_2(t) \sin(kz) \cos(\omega_1 t), \quad (2.13)$$

where

$$A_1(t) = P_a \cos(kA_o \sin(\omega_o t)), \quad (2.14)$$

$$A_2(t) = P_a \sin(kA_o \sin(\omega_o t)).$$

Eq. (2.13) shows that the incident pressure can be described by two parts. Without an external excitation $\omega_o = 0$ or $A_o = 0$, and in this case P_{in} becomes $P_a \cos(\omega t) \cos(kz)$ and the second part in Eq. (2.13) becomes zero. It can be assumed that the first part shows the pressure because of the acoustic pressure field produced by the standing acoustic wave and the second part shows an additional term because of the external excitation. In Eq. (2.13) $A_1(t)$ and $A_2(t)$ shows the amplitude modulation in the incident pressure field. One way of observing dynamic acoustic radiation force is in amplitude-modulated mode when a single ultrasound beam amplitude is modulated [128-132]. Therefore, in the case of applying an external excitation, we anticipate seeing some dynamic components and dynamic behaviour, too.

The incident pressure can be rewritten as

$$P_{\text{in}}(z, t) = \frac{P_a}{2} \left(\cos(\omega t - \varphi(t)) + \cos(\omega t + \varphi(t)) \right) \cos(kz) + \frac{P_a}{2} \left(\sin(\omega t + \varphi(t)) - \sin(\omega t - \varphi(t)) \right) \sin(kz), \quad (2.15)$$

where

$$\varphi(t) = kA_o \sin(\omega_o t). \quad (2.16)$$

Eq. (2.15) is derived from Eq. (2.13) by applying trigonometric product-to-sum identities to decompose the oscillatory terms. This reformulation explicitly separates the pressure field into components modulated by the phase term $\varphi(t) = kA_o \sin(\omega_o t)$, which accounts for the dynamic influence of external excitation. The first term represents the primary acoustic pressure field, while the second term highlights the modulation introduced by the object's oscillatory motion. The term $\varphi(t)$ shows the phase modulation in the incident pressure field. It can be observed that the modulation depth in both case of amplitude or phase modulation can be controlled using the value of kA_o . By assuming the origin at the

PN (Fig. 2.1.b)), the time-dependent position of the object can be described as $\xi(t) = z - Z_o(t)$ the acoustic radiation force profile can be described by the sinusoidal function [118]

$$F_{\text{rad}} = \gamma_1 \sin(\gamma_2 \xi(t)), \quad (2.17)$$

by using King or Yoshioka's formula γ_1 and γ_2 can be defined, for example, by looking at the King's formula to calculate the F_{rad} for a spherical object in a standing acoustic wave field [62]:

$$F_{\text{rad}} = 2\pi\rho_0|\Phi|^2(kr)^3 \frac{1+\frac{2}{3}(1-\rho_0/\rho_1)}{(2+\rho_0/\rho_1)} \sin(2kz), |\Phi| = P_a/(\rho_0\omega), \quad (2.18)$$

where $|\Phi|$ is the magnitude of the incident wave velocity potential, P_a is the amplitude of the incident pressure field, r is the radius of the rigid sphere, k is the wave number, ω is the wave frequency, z is the distance between the pressure node and the center of the sphere in the wave direction, and ρ is the density and 0 and 1 index denotes to the fluid and the spherical object, respectively, γ_1 and γ_2 can be defined by [62]

$$\gamma_1 = 2\pi\rho_0 \left| \frac{P_a}{\rho_0\omega_1} \right|^2 (kr)^3 \frac{1+\frac{2}{3}(1-\rho_0/\rho_1)}{(2+\rho_0/\rho_1)}, \gamma_2 = 2k, \quad (2.19)$$

assuming that the acoustic radiation force is time-dependent in general, Fourier series expansion can be applied (T being the period time of F_{rad}), as follows [128,129],

$$F_{\text{rad}} = a_0 + \sum_{n=1}^{\infty} \{a_n \cos(2n\pi t/T) + b_n \sin(2n\pi t/T)\}, \quad (2.20)$$

where a_n and b_n denote the amplitudes of the harmonic forces as components of the dynamic acoustic radiation force [32]; while a_0 represents the time-averaged static component, denoted by \bar{F}_{rad} . To calculate \bar{F}_{rad} , Gorkov theory is used [64]. By applying $\frac{\partial}{\partial t} v_1(z, t) = -\frac{1}{\rho_0} \frac{\partial}{\partial t} P_1(z, t)$, [5] and Eq. (2.13), the velocity field in the presence of a harmonic disturbance becomes

$$V_{\text{in}}(z, t) = \frac{P_a\omega_1}{\rho_0 c_0} (\sin(kz) \int C_1(t) dt - \cos(kz) \int C_2(t) dt), \quad (2.21)$$

in calculating $V_{\text{in}}(z, t)$ we perform indefinite integration over time and disregard the resulting constant values [5], substituting the pressure and the velocity field into the

Gorkov potential $f(P_{\text{in}}^2, V_{\text{in}}^2)$ and \bar{F}_{rad} , the steady-state acoustic radiation force becomes

$$\bar{F}_{\text{rad}} = 4k\pi r^3 E_{\text{ac}} \phi(\tilde{\kappa}, \tilde{\rho}) \sin(2kz), \quad (2.22)$$

where $E_{\text{ac}} = \frac{P_{\text{a}}^2}{4\rho_0 c_0^2}$ denotes the acoustic energy density, $(\tilde{\kappa}, \tilde{\rho})$ are relative compressibility and density, respectively [5]. In Eq. (2.22) the contrast factor $\phi(\tilde{\kappa}, \tilde{\rho})$ includes the contribution from the harmonic disturbance, which is instead expressed as follows,

$$\phi(\tilde{\kappa}, \tilde{\rho}) = \frac{1}{3} \left[\frac{(2\alpha+3\beta)\tilde{\rho}-(3\beta-\alpha)}{2\tilde{\rho}+1} - \alpha\tilde{\kappa} \right], \quad (2.23)$$

where $\alpha = 2\langle C_1(t)^2 - C_2(t)^2 \rangle$ and $\beta = (2\omega_1^2)\langle (\int C_1(t)dt)^2 - (\int C_2(t)dt)^2 \rangle$. In the absence of external excitation, $\alpha = \beta = 1$ and Eq. (2.23) simplifies to

$$\phi(\tilde{\kappa}, \tilde{\rho}) = \frac{1}{3} \left[\frac{5\tilde{\rho}-2}{2\tilde{\rho}+1} - \tilde{\kappa} \right]. \quad (2.24)$$

According to previous studies by Bruus [5], the directional movement of a spherical object in an acoustic radiation force field is typically determined by the fixed properties of the surrounding fluid and medium. Here, Eq. (2.22), derived using the time-averaged formulation of the acoustic radiation force, aligns with Bruus's methodology and relies on second-order, time-averaged quantities obtained through perturbation analysis of the Navier-Stokes and continuity equations. However, this study introduces a novel aspect, as demonstrated by Eq. (2.23), the application of external excitation to the acoustic radiation force field. This introduces new parameters of (α, β) —the oscillation properties—which alters the contrast factor, traditionally dependent only on the properties of the spherical object and the fluid. Consequently, this enables control over the directional movement of the spherical object, including the ability to produce alternating pushing, pulling, or even zero forces as desired.

2.4. Numerical simulation

Unlike analytical methods, which are often restricted to simple geometries, numerical methods are used to model and analyse the acoustic radiation force acting on arbitrarily shaped objects, including complex structures like biological cells or irregular objects [61].

Furthermore, numerical simulations can be used to validate theoretical models and experimental observations. By comparing simulation results with analytical solutions or experimental data, the accuracy of the models can be evaluated, and their predictive capabilities can be enhanced.

2.4.1. Numerical simulation based on finite element method (FEM)

In this section, first, a 2D model utilizing the finite element method (FEM) in COMSOL software is introduced. This model, inspired by the work of Glynne-Jones et al. [61], and employing the perturbation method, conducts a numerical simulation to calculate acoustic radiation forces acting on geometrically symmetrical objects. Subsequently, a 3D COMSOL model is developed to extend the simulation and computation of acoustic radiation forces to objects of varying geometric shapes. Finally, the numerical results are validated against theoretical formulas tailored for acoustically small spherical objects. To implement the perturbation solution method in COMSOL Multiphysics, the second-order momentum fluxes as functions of first-order acoustic quantities need to be obtained. These fluxes can be derived from a computationally efficient, numerical, linear, first-order acoustic scattering simulation in a finite element method (FEM) framework. Once these first-order quantities are determined, the radiation force on any object can be calculated using Eq. (1.1) [61]. In the case of an ideal fluid, the radiation stress can be described by the first order of the acoustic radiation force field variables, as outlined in Eq. (1.33). By calculating the first-order pressure and velocity using COMSOL Multiphysics and selecting the external surface of the spherical object as the integration boundary, the radiation force can be accurately calculated.

Unlike theoretical formulations, the force expression provided in Eq. (1.1) applies to objects of all sizes when the radiation stress is defined by Eq. (1.33). Also, in the case of an oscillatory force field consist of an incident pressure of two modulated parts outlined in Eq. (2.13) and by using the superposition principle, the acoustic radiation force can be assumed to be a modulation of two fields as given by

$$\bar{F}_{\text{rad}} = \oint_s \sum_{m=1}^2 \langle C_m(t)^2 \rangle \left(\frac{1}{2\rho_0 c_0^2} P_1^2 - \frac{\rho_0}{2} |\vec{v}_1|^2 + \rho_0 (\vec{v}_1 \otimes \vec{v}_1) \right) \vec{n} ds, \quad (2.25)$$

with \otimes denoting the dyadic product and \vec{n} is the surface normal unit vector. It is noteworthy to mention here that the force computation used in FEM is independent of the surface of integration due to the conservation of flux if it is located outside the spherical

object. For small spherical objects, selecting an integration surface at a larger distance can improve numerical accuracy because the integral is evaluated over a greater number of elements, which enhances numerical stability. This approach does not necessarily allow for larger element sizes in the FEM mesh but ensures that the surface is sufficiently discretised for accurate numerical evaluation.

In the 2D numerical simulation, the acoustic radiation force acting on a spherical object submerged in a fluid domain under the influence of a standing wave is examined. The model, depicted in Fig. 2.2, is constructed using the Acoustic-Structure Interaction interface in a 2D axisymmetric geometry. The model demonstrates axial symmetry, with the axis positioned on the left-hand boundary of Fig 2.2. The spherical object is represented by a semi-circular domain with its base along z axis, while a rectangular domain depicts the surrounding fluid. Cylindrical wave radiation boundaries define the computational domain, enabling the introduction of an acoustic field by specifying pressure conditions over the boundary. Additionally, these boundaries absorb most of the acoustic energy incident upon them from the scatterer, and a background pressure field defines the standing wave.

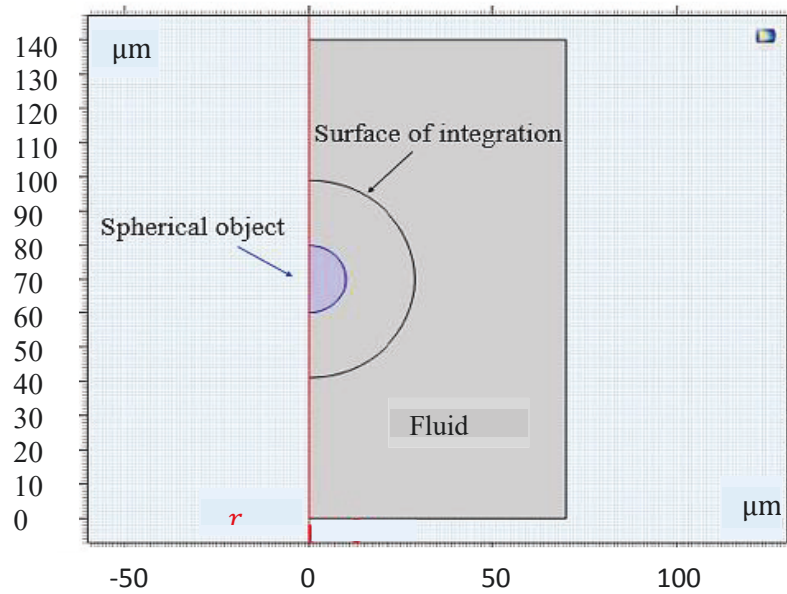


Fig. 2.2. A 2D axisymmetric finite element.

The baseline parameters of both the object and the fluid were selected to conduct a parameter study and facilitate comparison with a previous study [61] (see Table 2.1).

Table 2.1. Baseline parameters [61].

Parameter	Value
Speed of sound in the spherical object	6559 [m/s]
object density	2000 [$\frac{\text{kg}}{\text{m}^3}$]
object radius	5 – 80 [μm]
Distance of object from pressure node	$\lambda/8$ (Force is maximum here for small object)
Speed of sound in the fluid	1480 [m/s]
Fluid density	1000 [$\frac{\text{kg}}{\text{m}^3}$]
Fluid domain dimensions	140 \times 70 [μm^2]
Frequency of sound	1 [MHz]
Wavelength of sound in fluid (λ)	1.48 [mm]

The 3D model is shown in Fig. 2.3. In both 2D and 3D simulation, the exerted acoustic radiation force is produced by a standing wave in a frequency of 1 MHz and a pressure amplitude of 200 kPa and the model is implemented using the Acoustic-Structure Interaction interface. Also, in both 2D and 3D finite element simulations, the static or time-averaged acoustic radiation force, acting on an object oscillating at ω_0 under the influence of external excitation is calculated. The oscillation of the object is indirectly captured by modulating the incident acoustic pressure field in the simulation. Specifically, the transition is made from a simple sinusoidal representation of the pressure (Eq. 2.6) to a modulated form (Eq. 2.9). This approach effectively represents the interaction between the oscillating object and the external excitation without directly implementing a moving boundary condition on the object. Instead, the modulation incorporates the dynamics introduced by the external excitation, allowing us to study its influence on the time-averaged F_{rad} . This methodology is particularly relevant in the 2D and 3D models, where the modulation improves accuracy by capturing the complex interactions between the acoustic field and the object's oscillatory behaviour. In 3D model, the surrounding fluid domain is shown as a cylindrical domain with the radius of 70 μm and the height of 140 μm .

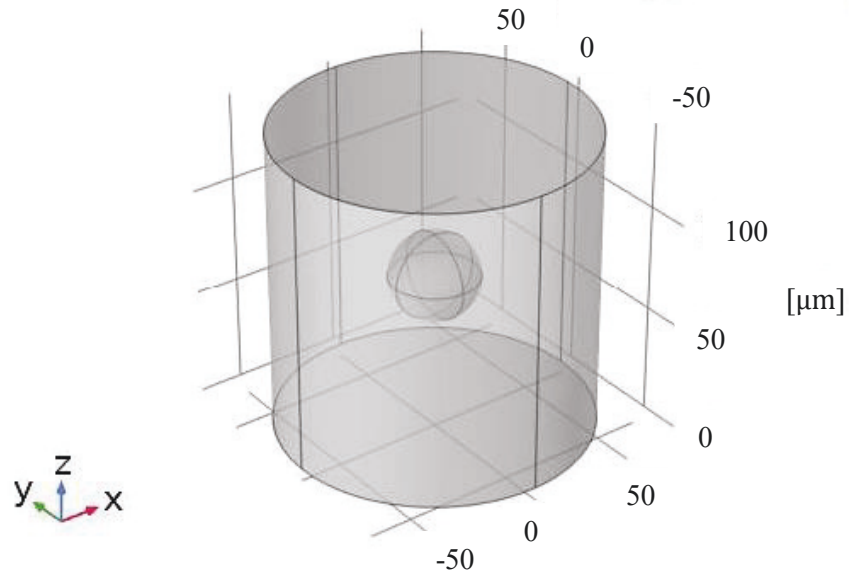


Fig. 2.3. The 3D model of a spherical object immersed in an acoustic fluid domain.

In simulations, accurately identifying the point where the acoustic radiation force reaches its peak magnitude is important. Understanding this maximized force location aids in optimizing the design of acoustic manipulation devices and predicting the behaviour of levitated objects within an acoustic field. If the first-order pressure follows a simple cosine function, the corresponding velocity field will exhibit a sine function pattern according to Eq. (1.18). Also, according to Eq. (1.21), the acoustic radiation force, being proportional to the second order of the pressure, would also manifest as a sine function, with a wave number twice that of the velocity field. This simple example leads to two important conclusions: First, the maximum velocity occurs at the pressure nodes, and vice versa. Second, the maximum force is located at one-eighth of the wavelength, while the pressure nodes are at one-fourth [61]. Therefore, the distance of one-eighth of the wavelength corresponds to the distance between the pressure node, defined as the datum, and the centre of the object where the maximum radiation force occurs. In the 2D and 3D simulations, this distance is chosen to be one-eighth of the wavelength to ensure the object experiences the maximum radiation force. In the COMSOL simulation, an automatic meshing approach with fluid dynamics calibration was utilized. Predefined mesh settings were adjusted to achieve a finer mesh size. The total number of elements in the 3D model is 267912, while the 2D-axisymmetric model comprises 65992 elements. This indicates that the 3D model requires more time to run compared to the 2D-axisymmetric model.

Fig. 2.4 illustrates the velocity and scattered pressure around the object with a radius of $20\text{ }\mu\text{m}$.

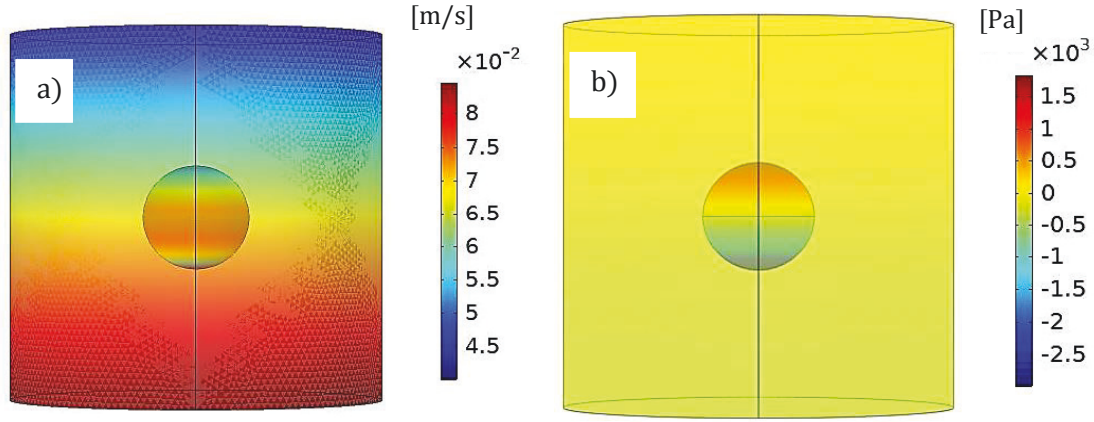


Fig. 2.4. a) Velocity field, and b) scattered pressure around the object in the fluid domain ($r = 20\text{ }\mu\text{m}$).

The 3D model accommodates both symmetrical and asymmetrical objects. Fig. 2.5 shows the simulation steps in COMSOL Multiphysics for an object with a radius of $10\text{ }\mu\text{m}$.

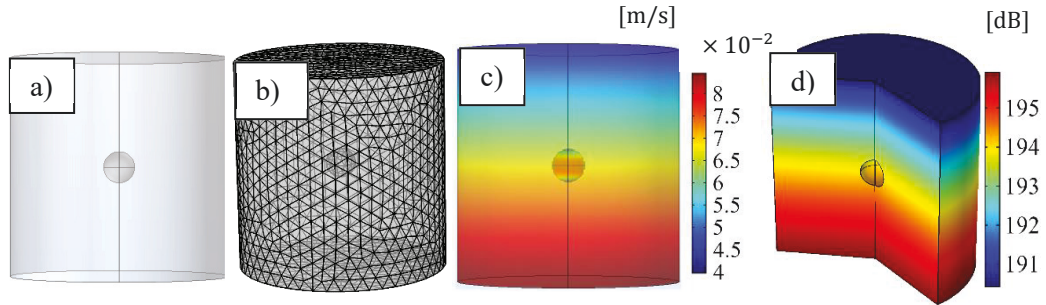


Fig. 2.5. Simulation steps in COMSOL to calculate \bar{F}_{rad} for a spherical object with a radius of $10\text{ }\mu\text{m}$, a) Modelling, b) meshing, c) velocity field (m/s), and d) sound pressure level (dB).

2.4.2. Numerical simulation based on time averaged method

To validate the numerical method described in Eq. (2.25), the fact that the time-averaged radiation force depends on the object's position [60-64] is utilized. Considering a time step of Δt , and for $t = 0$ the mean distance of the spherical object from the pressure node is $z_0 = \lambda/8$. Further, the so-called static radiation force, reads

$$\bar{F}_{\text{rad}} = \frac{1}{T} \sum_{n=0}^N F_{\text{rad}}(z_n) \Delta t, \quad (2.26)$$

with $F_{\text{rad}}(z_n)$ being the analytical formulation of the time-averaged radiation force [60], with $z_n = z_0 - A_0 \sin(\omega_0 t_n)$ and $t_n = n\Delta t$, $n \in [0, 1, \dots, N]$, where T represents the period time of the external sinusoidal excitation, ω_0 . By substituting the Gorkov equation [21] into Eq. (2.22), the expression for the static radiation force changes to

$$\bar{F}_{\text{rad}} = \frac{1}{T} \sum_{n=0}^N (4k\pi r^3 E_{\text{ac}} \phi(\tilde{\kappa}, \tilde{\rho}) \sin(2kz_n)) \Delta t, \quad (2.27)$$

which is the discretised formulation of the time-averaged acoustic radiation force. The time step, Δt , should be small enough to capture force variations across the oscillation period. For this study, time step, $\Delta t = 10^{-6}$ s was selected using the approach discussed in section 3.2.1, where time step optimization is addressed through a statistical method.

2.5. Numerical and theoretical model validation

To validate the 3D COMSOL model, the external excitation amplitude in Eq. (2.9) is set to zero, and the object and fluid properties are according to Table 2.1. In this scenario, the results from the presented 3D COMSOL model closely match those from the 2D-axisymmetric model-based approach presented in [61] and analytical results, with a difference of less than 1 percent.

Table 2.2. Comparison of FEM perturbation result based on the 3D model with 2D-axisymmetric model and analytical results.

Object's radii [μm]	\bar{F}_{rad} (Our 3D model) [pN]	\bar{F}_{rad} (2D model based on [61]) [pN]	\bar{F}_{rad} (King's formula [62]) [pN]	\bar{F}_{rad} (Hasegawa's formula [133]) [pN]	Percent of difference (Hasegawa/our 3D model)
5	15.84	15.96	16.23	15.97	0.81
10	127.62	127.64	129.8	127.68	0.04
20	1017.5	1018.7	1039.2	1017.9	0.04
40	8032.3	8033.0	8313.5	8031.6	0.009
80	60732	60682	66450	60824	0.15

It can be observed that there is a good agreement between the King [62] and Hasegawa [133] formulation and the presented simulation (2D and 3D). Fig. 2.6 shows a comparison

for acoustic radiation forces obtained by our 3D FEM results with Gorkov [64] and King formulations [62].

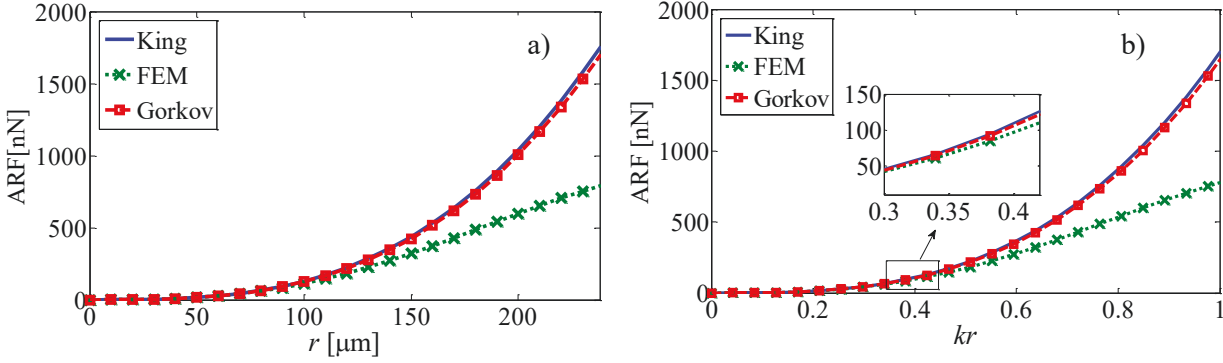


Fig. 2.6. A comparison of obtained acoustic radiation force (ARF) between a) King formulation [62], FEM (our 3D COMSOL simulation presented in section 2.4.1), and Gorkov formulation [64] versus the sphere radius, b) the same comparison plotted against the dimensionless parameter kr .

As expected, they compare reasonably well for small spherical object radius where the analytical solution considered is valid, and the acoustic radiation force starts to deviate considerably from the analytical solutions as the sphere become larger. Fig. 2.6 shows that the theoretical approach is only valid for $kr < 1$ and from about $kr \sim 0.3$ the deviation between numerical simulation and theoretical approach starts [41,42]. Fig. 2.7 illustrates the acoustic radiation force variations within the range of 0 to half wavelength for two different object radii using King formulation and 3D FEM.

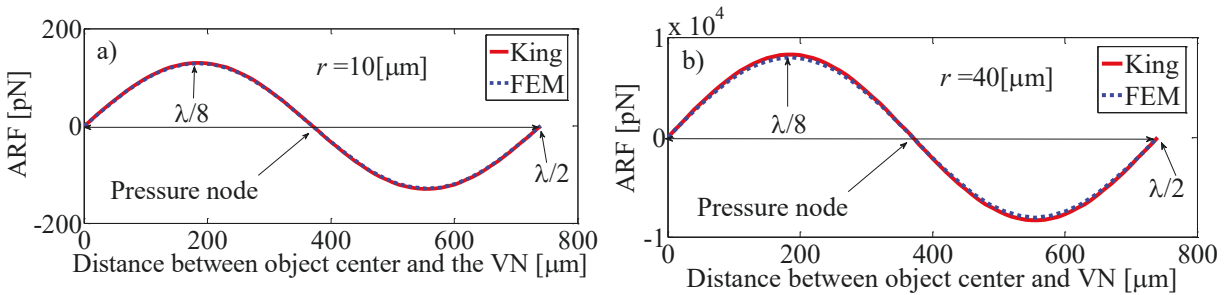


Fig. 2.7. Acoustic radiation force (ARF) vs the distance between object centre and the velocity node (VN) for a) an object with $r = 10 \mu\text{m}$, and b) $r = 40 \mu\text{m}$.

It is observed that the maximum force occurs at $1/8$ wavelength, and the force magnitude at the pressure node is zero. To validate the theoretical approach presented by Eqs. (2.22, 2.23), the time-averaged method shown in Eq. (2.27) is applied to the experimental results outlined in [118], which study a spherical object with radius of $r = 0.71 \text{ mm}$, and density

of $\rho_1 = 34 \frac{\text{kg}}{\text{m}^3}$ and drag coefficient of $C_d = 1.06$, fluid density of $\rho_0 = 1.19 \frac{\text{kg}}{\text{m}^3}$. In this study, the object is levitated in air within a standing acoustic wave with wavelength of $\lambda = 8.6 \text{ mm}$, and the following values for $\gamma_1 = -3.06 \times 10^{-6} \text{ N}$ and $\gamma_2 = 1315 \text{ m}^{-1}$ in Eq. (2.17) is considered [118]. In Fig. 2.8 and by using Eq. (2.17) F_{rad} is plotted by solid blue line, and its mean value by dashed red line, when $A_0 = 0.15 \text{ mm}$ and $\omega_0 = 30 \text{ Hz}$ and $\omega_1 = 40 \text{ kHz}$ has been selected according to [118]. Here, the dimensionless value for the steady-state acoustic radiation force, known as the “static acoustic radiation force function” [41,42], is used, which is expressed as follows for a spherical object

$$Y_{\text{st}} = \frac{\bar{F}_{\text{rad}}}{\pi r^2 E_{\text{ac}}}. \quad (2.28)$$

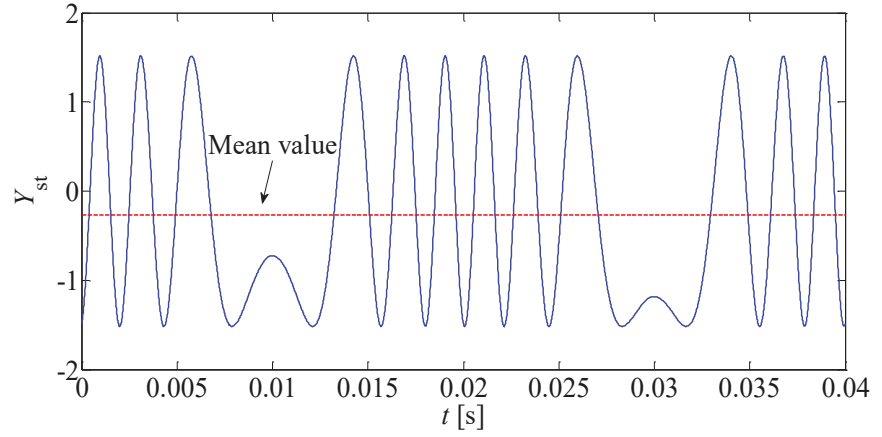


Fig. 2.8. The acoustic contrast factor for an oscillatory object trapped in an acoustic radiation force field using data provided in [118]. The non-zero mean value is for the time-averaged component of the radiation force which matches the results of Eqs. (2.22) and (2.23). The object’s location corresponds to different spatial positions within the acoustic field during its oscillation, as the force is time-averaged and evaluated under steady-state conditions.

The mean value of the time-averaged force is negative, implying a pull effect on the object towards the closest pressure node. By applying the Fourier series expansion using Eqs. (9,11), one can write

$$\gamma_1 \sin(\gamma_2 \xi(t)) = a_0 + \sum_{n=1}^{\infty} \{a_n \cos(2n\pi t/T) + b_n \sin(2n\pi t/T)\} \quad (2.29)$$

with a_0 representing the time-averaged static component,

$$\bar{F}_{\text{rad}} = a_0 = \frac{1}{T} \int_{-T/2}^{T/2} (\gamma_1 \sin(\gamma_2 \xi(t))) dt = -0.5370 [\mu\text{N}]. \quad (2.30)$$

In the case of using the proposed theoretical approach with Eqs. (2.22) and (2.23), the values for the contrast factor and the acoustic radiation force become $\phi = -0.1227$, and $\bar{F}_{\text{rad}} = -0.5438 [\mu\text{N}]$, respectively. By comparing the theoretical results obtained using Eqs. (2.22) and (2.23) with result derived from Eq. (2.30), as extracted through the Fourier series expansion in the model outlined by [118], we observe a relative error of less than 1.3%. This finding serves to further validate the theoretical formulation.

2.6. Effects of external excitation on acoustic radiation force sign

Following the validation of the presented model, the analysis is extended to include the effects of external excitation, as described by Eq. (2.23). Here, for the object and fluid properties, Table 2.1 is used, and the external excitation frequency is $f_0 = 10 \text{ kHz}$ when object radius is $r = 10 \text{ }\mu\text{m}$. Fig. 2.9 shows the acoustic contrast factor based on the time average of $C_m(t)^2$, for different kA_o .

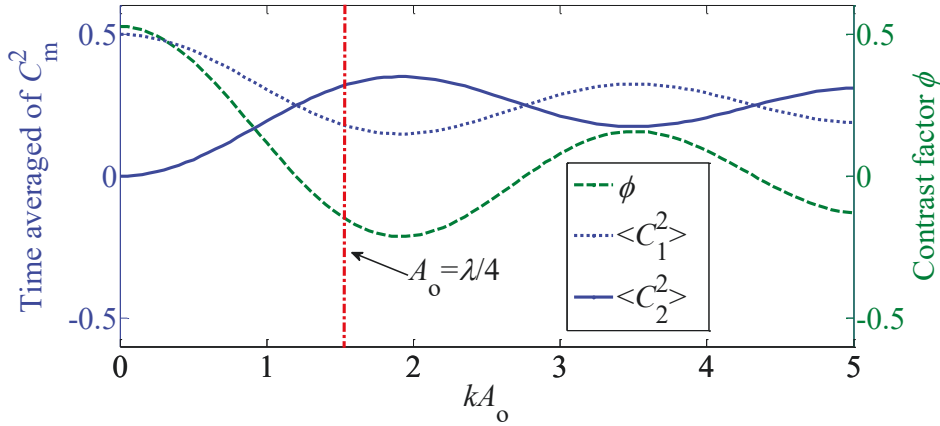


Fig. 2.9. The acoustic contrast factor and $\langle C_m(t)^2 \rangle$ with respect to the oscillation amplitude oscillation, kA_o , showing the variation of \bar{F}_{rad} from positive to negative value. The vertical “dot-dash line” represents the theoretical limit for the maximum value of the external excitation amplitude.

The distance between a stable PN and an unstable VN is only $1/4$ wavelength. $kA_o = \pi/2$ corresponds to $1/4$ of a wavelength, for an object trapped near the pressure node it can be observed that at $A_o > \lambda/4$ the spherical object is nearly transitioning from one stable PN to another unstable VN. The vertical “dot-dash line” in Fig. 2.9 indicates the

theoretical limit; but the figure is extended to $kA_0 = 5$ to observe the theoretical change in the contrast factor by changing kA_0 .

In the absence of an external excitation, we have $C_1(t) = \cos(\omega t)$, $\langle C_1(t)^2 \rangle = 0.5$, and $C_2(t) = 0$. If external excitation introduces $C_2(t)$, we observe from Fig. 2.10 those areas with larger $C_2(t)$ relative to $C_1(t)$ yield a negative acoustic radiation force, and vice versa. This suggests that external excitation amplitude at a certain frequency can influence the force sign and change it from positive to negative. Certain points exhibit a cancellation effect in which a zero acoustic radiation force is achievable. The first point of force cancellation occurs at $kA_0 = 1.202$. If we run the finite element simulation and plot the pressure and velocity field around the object with radius of $r = 20 \mu\text{m}$ we receive to Fig. 2.10.

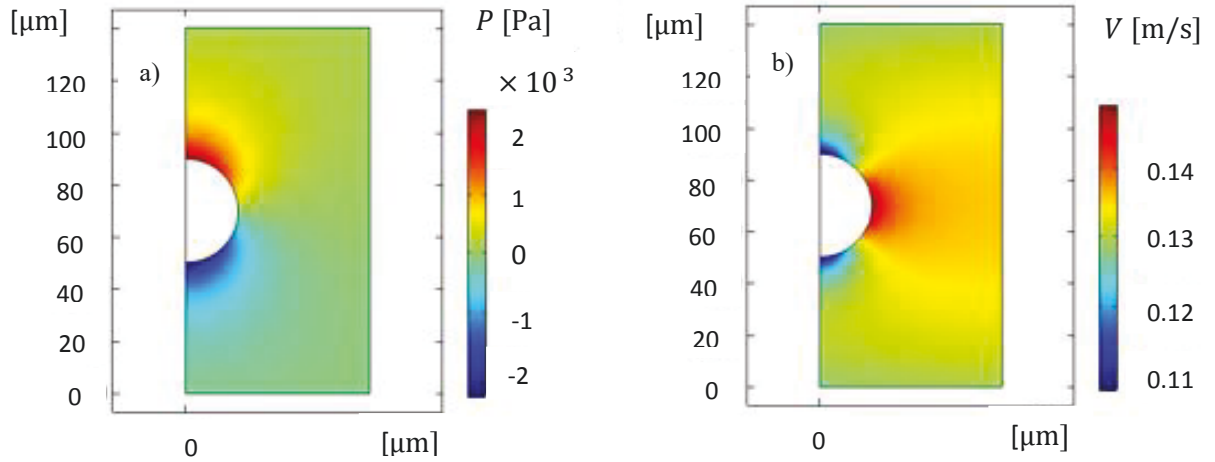


Fig. 2.10. The symmetry in the field variables a) acoustic pressure, and b) velocity field, in case of acoustic radiation force cancellation when $r = 20 \mu\text{m}$ and $kA_0 = 1.202$.

In Fig. 2.10, it is evident that the field variables (acoustic pressure and fluid velocity around the object) exhibit symmetry. This symmetry in the field variables suggests an evenly distributed acoustic energy around the object, akin to the condition where the spherical object is positioned at a pressure node or anti-node in a standing wave field without external excitation. In such a scenario, the net force along the z-direction is zero. The finite element simulation in this instance supports the theoretical prediction regarding the cancellation of radiation forces.

Another advantage of the presented 3D FEM model is its versatility, as it can accommodate not only symmetrical objects but also those with asymmetrical geometries. Table 2.3 presents some 3D geometries, featuring non-spherical but simple objects characterized by parameters such as radius (r), side length (L), and height (z).

Table 2.3. Dimensions for calculating the acoustic radiation force using the presented 3D FEM for some simple nonspherical objects.


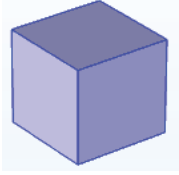
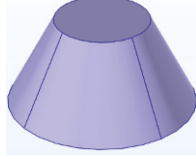
Shape			
Geometrical properties	Ellipsoid: $r = 10 \text{ } [\mu m]$ $z = 15 \text{ } [\mu m]$	Cube: $L = 10 \text{ } [\mu m]$	Truncated Cone: $r_{up} = 5 \text{ } [\mu m]$ $r_{base} = 10 \text{ } [\mu m]$ $z = 10 \text{ } [\mu m]$

Fig. 2.11 shows the contrast factor for some simple nonspherical objects with respect to the oscillation amplitude kA_0 , which shows similar behaviour to the spherical object in Fig. 2.9.

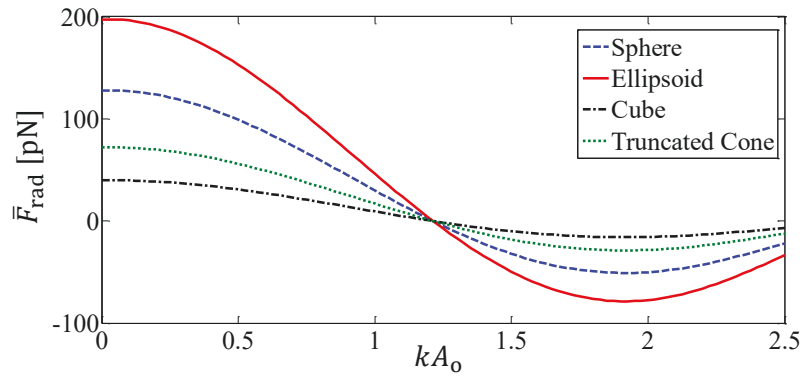


Fig. 2.11. A comparison of \bar{F}_{rad} for some non-spherical objects using the current FEM study which shows similar behaviour to the spherical object in Fig. 2.9.

To compare the theoretical and numerical approaches presented in Eqs. (2.22), (2.25), and (2.27) Fig. 2.12 shows Y_{st} for $kA_0 = 2$ and $kA_0 = 3.5$.

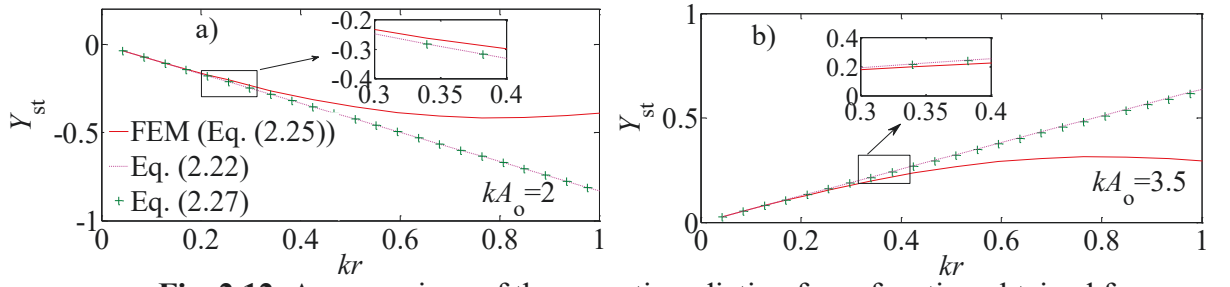


Fig. 2.12. A comparison of the acoustic radiation force function obtained from the current study, Eq. (2.22), FEM (Eq. (2.25)), and the time-averaged radiation force, Eq. (2.27), with respect to kr for an oscillating object, showing both (a) negative and (b) positive contrast factors as function of the oscillation amplitude kA_o , and deviation occurs at $kr \sim 0.3$.

Past studies [60-76] show that for an object with a certain position and geometry in an acoustic standing wave field, the magnitude of \bar{F}_{rad} is a certain value and its direction cannot be changed. However, Figs. 2.9-2.12 reveal that introducing an external excitation allows for the alteration of \bar{F}_{rad} value based on the amplitude of the external excitation, enabling the assignment of positive, negative, and zero values to it. Fig. 2.13a shows the acoustic radiation force function, Y_{st} , plotted against non-dimensional value of object oscillation, A_o/r with r being fixed and indicates that increasing the object's oscillation amplitude decreases the acoustic radiation force. Also, the acoustic radiation force decreases as the object size decreases. Fig. 2.13b presents the acoustic radiation force function, Y_{st} , plotted against non-dimensional value of object position, z/r . Fig. 2.13b illustrates that as the object's initial position relative to the pressure node increases, the acoustic radiation force also increases, effectively restoring the object to its equilibrium position.

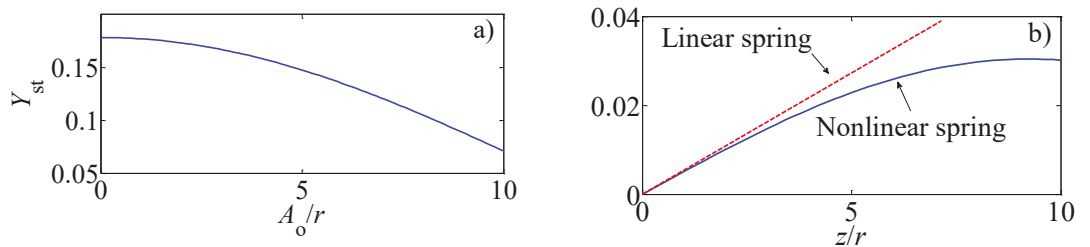


Fig. 2.13. a) The acoustic radiation force function, Y_{st} , plotted against non-dimensional value of object oscillation, A_o/r and b) The acoustic radiation force function, Y_{st} , plotted against non-dimensional value of object position, z/r [37].

Behaviour observed in Fig. 2.13b is very similar to the action of a spring force. In the scenario of a linear spring, when an object connected to it deviates from the equilibrium position, the spring force exhibits a linear proportionality with the object displacement. However, Fig. 2.13b demonstrates that the acoustic force can be effectively modelled using a nonlinear spring model with softening stiffness, as previously shown in [117,118].

2.7. Nonlinear dynamical model of the acoustic radiation forces

According to Eq. (2.17), for a lossless fluid, the acoustic radiation force for a spherical object trapped in a standing wave field and undergoing a rigid-body oscillation $Z_o = A_o \sin(\omega_o t)$, due to the secondary excitation, can be described as a sinusoidally varying force [117,118] by $F_{\text{rad}} = \gamma_1 \sin(\gamma_2 \xi(t))$, in which, γ_1 and γ_2 are constants, and $\xi(t) = z - Z_o(t)$. These constants can be written using the formulation by King [62] and Yoshioka [63], respectively as follows

$$\gamma_1 = V_p E_{\text{ac}} k \hat{\rho}, \quad \gamma_2 = 2k, \quad (2.31)$$

by applying Newton's second law to an object oscillation in one degree freedom of motion in an acoustic radiation force field, the equation of motion becomes

$$M_o \ddot{z} = F_{\text{rad}} + F_{\text{drag}} + F_{\text{gravity}}, \quad (2.32)$$

where M_o is the mass of the object. From the Stokes flow theory, the drag force on a sphere can be written as [118]

$$F_{\text{drag}} = -\frac{1}{2} C_d (\pi r^2) \rho_o \dot{z} |\dot{z}|, \quad (2.33)$$

where C_d denotes the drag coefficient that depends on the geometric shape of the object and the physical properties of the fluid such as Reynolds number, Froude number, Mach number, and usually determined experimentally. [134]. Here, it is assumed that the acoustic field is applied normal to the direction of gravity acceleration; hence, the weight force, F_{gravity} , is excluded from the derivations without loss of generality, and it is assumed that the whole the system is excited using a vibration platform (e.g, an electrodynamic shaker). Substituting Eqs. (2.17) and (2.33) into Eq. (2.32) provides

$$M_o \ddot{z} = -\gamma_1 \sin(\gamma_2 z) \cos(\gamma_2 A_o \sin(\omega_o t)) + \gamma_1 \cos(\gamma_2 z) \sin(\gamma_2 A_o \sin(\omega_o t)) - \frac{1}{2} C_d (\pi r^2) \rho_o \dot{z} |\dot{z}|. \quad (2.34)$$

Eq. (2.34) is a nonlinear equation of one degree freedom system that is an acoustically trapped object in a plane standing wave subjected to a secondary excitation. By introducing $\theta = (\gamma_2 z)$, and $\gamma_2 A_0 < 1$, $\cos(\gamma_2 A_0 \sin(\omega_0 t)) \sim 1$ and $\sin(\gamma_2 A_0 \sin(\omega_0 t)) \sim \gamma_2 A_0 \sin(\omega_0 t)$, then Eq. (2.34) can be re-written as

$$\ddot{\theta} + C_1 \dot{\theta} |\dot{\theta}| + C_2 \sin(\theta) - C_3 \cos(\theta) \sin(\omega_0 t) = 0, \quad (2.35)$$

where the constant coefficients are

$$C_1 = \frac{1}{2M_0} C_d \frac{\pi}{4} (2r)^2 \frac{\rho_0}{\gamma_2} [-], C_2 = \frac{\gamma_2}{M_0} \gamma_1 [s^{-2}], C_3 = \frac{\gamma_2^2}{M_0} \gamma_1 A_0 [s^{-2}], \quad (2.36)$$

using the Taylor series expansion for $\sin(\theta)$, Eq. (2.35) can be rewritten as

$$\ddot{\theta} + C_1 \dot{\theta} |\dot{\theta}| + C_2 \theta - \frac{C_2}{3!} \theta^3 + \frac{C_2}{5!} \theta^5 - \dots = C_3 \cos(\theta) \sin(\omega_0 t), \quad (2.37)$$

Eq. (2.37) shows a Duffing-like oscillator with the cubic and quintic terms.

2.8. Asymptotic methods

Nonlinear dynamical analysis often employs asymptotic methods to study complex systems. These methods are particularly useful for investigating the behaviour of systems near equilibrium points or in the presence of small perturbations [135]. By utilizing asymptotic techniques, we can derive approximate solutions to nonlinear differential equations, providing valuable insights into dynamical systems' long-term behaviour. Asymptotic methods involve expanding solutions in power series or other types of expansions, such as Fourier series or Bessel functions. These expansions allow for the approximation of solutions in terms of simpler functions, making it easier to analyse the behaviour of the system. Common asymptotic techniques include perturbation methods, multiple scales analysis, and averaging methods [135-138]. Using asymptotic methods to calculate natural frequencies is fundamental in studying system vibration behaviour. In linear systems with one degree of freedom, the vibrating system has a single natural frequency for varying vibration amplitudes. However, in nonlinear systems, natural frequencies can vary, yielding different values depending on the vibration amplitude [135].

2.8.1. Nonlinear free undamped vibration analysis

For the first time, two effective and convenient methods, the global residue harmonic balance method (GRHBM) [139-141] and homotopy perturbation with multiparameter expansion (HPMPE) [142-154], are employed to obtain the analytical solution of nonlinear free undamped vibration of a small acoustically spherical object trapped in an acoustic radiation force field within a carrier standing wave to obtain natural frequencies. Moreover, the influence of the initial condition, compressibility, and density, on the nonlinear natural frequency is discussed widely.

2.8.1.1. Global residue harmonic balance method (GRHBM)

In this section, an approximate method, namely the global residue harmonic balance method, is used to determine the natural frequencies of the nonlinear free vibration of an object trapped in an acoustic radiation force field. This method was first introduced and validated in [139] and is based on the harmonic balance method [155]. This method is widely used in analytically solving nonlinear problems. In this method, all the residual errors are considered in the process of every-order approximation to obtain higher-order analytical approximations. Unlike other harmonic balance methods, all the former residual errors are introduced in the present approximation to improve the accuracy. The basic idea of the method's work can be found in [139-141]. The damping term and external force excitation are ignored to find the natural frequencies in Eq. (2.37). Then, Eq. (2.37) till order five can be rewritten in the following form

$$\ddot{\theta}(t) + C_2\theta(t) - \frac{C_2}{3!}\theta(t)^3 + \frac{C_2}{5!}\theta(t)^5 - \dots = 0, \quad (2.38)$$

It is assumed that the initial condition are

$$\theta(0) = \theta, \quad \dot{\theta}(0) = 0, \quad (2.39)$$

in which $\theta = \beta A_0$ is the dimensionless amplitude of the object oscillation when A_0 is the amplitude of the free oscillation.

a) First-order approximation using GRHBM

By introducing Eq. (2.38) in non-dimensional time domain, $\tau = \omega_1 t$, one can write [139]

$$\omega_1^2 \ddot{\theta}(\tau) + C_2\theta(\tau) - \frac{C_2}{3!}\theta(\tau)^3 + \frac{C_2}{5!}\theta(\tau)^5 = 0, \quad (2.40)$$

in which ω_1 is the first-order of the natural frequency of the object oscillation, the simplest form of equation which can satisfy the initial conditions is [139]

$$\theta_1(\tau) = \Theta \cos(\tau), \quad (2.41)$$

it should be noted that the symbolic mathematical software, Maple 18, was employed to solve equations. Substituting Eq. (2.41) into Eq. (2.40), becomes

$$\begin{aligned} \left(-\Theta\omega_1^2 + C_2\Theta - \frac{C_2}{8}\Theta^3 + \frac{C_2}{192}\Theta^5\right)\cos(\tau) + \left(-\frac{C_2}{24}\Theta^3 + \frac{C_2}{120}\Theta^5\right)\cos(3\tau) + \\ \frac{C_2}{120}\Theta^5\cos(5\tau) = 0. \end{aligned} \quad (2.42)$$

To avoid the secular terms in the next step, we must set the coefficient of $\cos(\tau) = 0$ equal to zero, resulting in

$$\omega_1 = \omega_L \left(\sqrt{1 - \frac{1}{8}\Theta^2 + \frac{1}{192}\Theta^4} \right), \quad (2.43)$$

in which $\omega_L = \sqrt{C_2}$ is the linear frequency of oscillation. In Eq. (2.43), nonlinearity shows itself in the amplitude of oscillation through the introduction of a new function. This function, referred to as the nonlinear amplitude function, can be defined by

$$\Theta F = \frac{\omega_N}{\omega_L}, \quad (2.44)$$

in which ω_N represents the nonlinear approximate natural frequency. Consequently, the first-order expression for the nonlinear amplitude function can be expressed as

$$\Theta F_1(\Theta) = \sqrt{1 - \frac{1}{8}\Theta^2 + \frac{1}{192}\Theta^4}, \quad (2.45)$$

by using King model [13] for non-compressible solid objects, the first-order nonlinear natural frequency can be written as

$$\omega_1 = \omega_L \Theta F_1 = \frac{\sqrt{2}}{2} \frac{kP_a}{(\rho_0 c_0)} \sqrt{\frac{\bar{\rho}}{\bar{\rho}}} \Theta F_1. \quad (2.46)$$

$Z = \rho c$ defines the resistance of an acoustic medium to the propagation of acoustic waves. Utilizing the definition of acoustic impedance and the King model [62], one can derive

$$\omega_1 = (\omega_1)^K \Theta F_1, \quad (2.47)$$

$$(\omega_1)^K = \frac{\sqrt{2}}{2} \frac{kP_a}{(Z_0)} \sqrt{\frac{\bar{\rho}}{\bar{\rho}}}, \quad (2.48)$$

where Z_0 represents the acoustic impedance of the medium. Using the Yoshika model [63], the first-order analytical approximate solution can be expressed as

$$\omega_1 = (\omega_1)^Y \Theta F_1, \quad (2.49)$$

$$(\omega_1)^Y = \frac{\sqrt{2}}{2} \left(\frac{kP_a}{Z_0} \right) \sqrt{\left(\frac{\bar{\rho}}{\bar{\rho}} - \frac{\bar{\kappa}}{\bar{\rho}} \right)}, \quad (2.50)$$

substituting ω_1 from Eq. (2.43) into Eq. (2.42), becomes the residual error for the first-order approximation can be obtained as

$$R_1(\tau) = \left(-\frac{c_2}{24} \theta^3 + \frac{c_2}{120} \theta^5 \right) \cos(3\tau) + \frac{c_2}{120} \theta^5 \cos(5\tau). \quad (2.51)$$

b) Second-order approximation GRHBM

To obtain the first-order approximation, it is considered [139-141]

$$\theta(\tau) = \theta_1(\tau) + p\theta_2(\tau), \quad (2.52)$$

$$\omega^2 = \omega_1^2 + p\omega_2, \quad (2.53)$$

where, p is a bookkeeping parameter, and the second-order approximation can be assumed as

$$\theta_2(\tau) = a_{13}(\cos(\tau) - \cos(3\tau)). \quad (2.54)$$

in which ω_2 and a_{13} are two unknown constants which should be determined. Substituting Eq. (2.54) into Eq. (2.40) and then sorting with respect to the coefficients of the p , one can obtain

$$\begin{aligned} F_2(\tau, \omega_2, a_{13}) = & \left(-\frac{5}{16} \theta^4 a_{13} \frac{c_2}{120} \right) \cos(7\tau) + \left(\frac{3}{4} \theta^2 a_{13} \frac{c_2}{6} - \right. \\ & \left. \frac{15}{16} \theta^4 a_{13} \frac{c_2}{120} \right) \cos(5\tau) + \left(\frac{85}{16} \theta^4 a_{13} \frac{c_2}{120} - 6\theta^2 a_{13} \frac{c_2}{6} + 8a_{13} c_2 \right) \cos(3\tau) + \\ & \left(\frac{15}{16} \theta^4 a_{13} \frac{c_2}{120} - \frac{3}{4} \theta^2 a_{13} \frac{c_2}{6} - \theta \omega_2 \right) \cos(\tau). \end{aligned} \quad (2.55)$$

Eq. (2.55) is called the equation of the coefficients of cosine functions. By using Eq. (2.51) and Eq. (2.55) the residual error for the second-order approximation can be obtained as [139]

$$F_2(\tau, \omega_2, a_{13}) + R_1(\tau) = 0, \quad (2.56)$$

by equating the coefficients of $\cos(\tau)$ and $\cos(3\tau)$ to zero in Eq. (2.55), the unknown constants a_{13} and ω_2 can be obtained. Hence, by some mathematical manipulation, the unknown coefficient of ω_2 can be written as

$$\omega_2 = -\frac{3}{16} \frac{\theta^4 \left(\frac{1}{120} \theta^2 - \frac{2}{3} \right)^2}{\frac{17}{24} \theta^4 - 16 \theta^2 + 128} C_2, \quad (2.57)$$

and according to Eq. (2.53) and equating $p = 1$, the second-order analytical approximation solution of nonlinear frequency can be written as

$$\omega_{(2)} = \sqrt{\omega_1^2 + \omega_2} = \omega_L \left(\sqrt{\left(\left(1 - \frac{1}{8} \theta^2 + \frac{1}{192} \theta^4 \right) - \frac{3}{16} \frac{\theta^4 \left(\frac{1}{120} \theta^2 - \frac{2}{3} \right)^2}{\frac{17}{24} \theta^4 - 16 \theta^2 + 128} \right)} \right). \quad (2.58)$$

Therefore, ΘF_2 which is the second-order of nonlinear amplitude function can be written as

$$\Theta F_2 = \sqrt{\left(1 - \frac{1}{8} \theta^2 + \frac{1}{192} \theta^4 \right) - \frac{3}{16} \frac{\theta^4 \left(\frac{1}{120} \theta^2 - \frac{2}{3} \right)^2}{\frac{17}{24} \theta^4 - 16 \theta^2 + 128}}, \quad (2.59)$$

similar to Eq. (2.48) and Eq. (2.50) and by using King [62] or Yosioka model [63], two expressions for ω_L according to solid or comprisable object can be obtained. By using the same procedure and constructing function $R_2(\tau)$ and $F_3(\tau, \omega_3, a_{23})$ the third order analytical approximate solution is achievable.

c) The effect of higher order terms in the Taylor series expansion on the approximate natural frequency

Here, the effect of higher-order terms in the Taylor series expansion of $\sin(\theta)$ in approximate natural frequency solution is examined. By neglecting the damping term and the external excitation term—appropriate when deriving the natural frequency since these terms influence amplitude decay and forced response rather than the system's intrinsic oscillatory behaviour—Eq. (2.35) can be rewritten as

$$\ddot{\theta} + C_2 \left(\sum_{n=0}^{\infty} \frac{(-1)^n}{(2n+1)!} \theta^{(2n+1)} \right) = 0, \quad (2.60)$$

For simplicity, the first-order approximation solution of GRHBM is concentrated on. If the steps outlined in section 2.9.2 are followed, the nonlinear natural frequency can be determined as

$$\omega_1 = \omega_L \sqrt{\sum_{n=0}^{\infty} \frac{\sqrt{2\Theta\pi^{3/2}\Gamma\left(\frac{n}{2}+\frac{3}{2}\right)\Theta^n\Gamma\left(\frac{n}{2}+1\right)}}{\Theta\pi\Gamma\left(\frac{n}{2}+\frac{3}{2}\right)}}, \quad (2.61)$$

in which Γ is the gamma function and can be defined by

$$\Gamma(n) = \int_0^{\infty} t^{(n-1)} e^{-t} dt, \quad (2.62)$$

with respect to choosing King [62] or Yoshoka model [63], the linear analytical approximate solution, ω_L , can be written according to Eq. (2.48) or (2.50), when the first-order of nonlinear amplitude function can be written as

$$\Theta F_1 = \sqrt{\sum_{n=0}^{\infty} \frac{\sqrt{2\Theta\pi^{3/2}\Gamma\left(\frac{n}{2}+\frac{3}{2}\right)\Theta^n\Gamma\left(\frac{n}{2}+1\right)}}{\Theta\pi\Gamma\left(\frac{n}{2}+\frac{3}{2}\right)}}. \quad (2.63)$$

Using Eq. (2.61) and by expanding the $\sin \theta$ till order-7 and 9 the nonlinear natural frequency can be written as

$$(\Theta F_1)_7 = \sqrt{\left(1 - \frac{1}{8}\Theta^2 + \frac{1}{192}\Theta^4 - \frac{1}{9216}\Theta^6\right)}, \quad (2.64)$$

$$(\Theta F_1)_9 = \sqrt{\left(1 - \frac{1}{8}\Theta^2 + \frac{1}{192}\Theta^4 - \frac{1}{9216}\Theta^6 + \frac{1}{737280}\Theta^8\right)}, \quad (2.65)$$

which shows that as the number of sentences in the Taylor series expansion of $\sin \theta$ increases, the coefficients of Θ^n , ($n = [2,4,6,\dots]$), decrease significantly. To validate this, the results obtained using the GRHBM will be compared with those obtained using another analytical technique known as the Homotopy Perturbation Method with Multiple Expanding Parameters (HPMEP) in the next section.

2.8.1.2. Homotopy perturbation method with multiple expanding parameters (HPMEP)

Homotopy perturbation method with multiple expanding parameters (HPMEP) first proposed and validated in [153]. The method is especially effective for a nonlinear equation with several nonlinear terms, which might have different effects on the solution.

In general, and for an equation with a linear operator (L) and non-linear operator (N_i) with multiple nonlinear terms $i = (1, \dots, k)$ we can write

$$L\{\theta(t)\} + \sum_i N_i \{\theta(t)\} = 0, \quad (2.66)$$

the homotopy equation [135-143] can be constructed by multiple parameters expanding as

$$L\{\theta(t)\} + \sum_i p_i N_i \{\theta(t)\} = 0, \quad (2.67)$$

where p_i are homotopy parameters, and the solution can be expressed as a power series of p in the form [153]

$$\theta(t) = \theta_0(t) + \sum_i p_i \theta_i(t) + \sum_{i,j} p_i p_j \theta_{ij}(t) + \sum_{i,j,k} p_i p_j p_k \theta_{ijk}(t) + \dots, \quad (2.68)$$

In this section, the homotopy perturbation method with two expanding parameters is employed to derive an analytical approximate solution for Eq. (2.38). This method is particularly effective for nonlinear equations featuring two nonlinear terms, each potentially influencing the solution differently. An essential step in applying the standard homotopy perturbation method is constructing a suitable homotopy equation that accurately approximates solution properties. With Eq. (2.38) containing two nonlinear terms of order three and five, the construction of a homotopy equation with two expanding parameters can be achieved using two homotopy parameters as follows

$$\ddot{\theta}(t) + C_2 \theta(t) - p_1 \frac{C_2}{3!} \theta(t)^3 + p_2 \frac{C_2}{5!} \theta(t)^5 = 0, \quad (2.69)$$

where p_1 and p_2 are homotopy parameters, when $p_1 \in [0, 1]$ and $p_2 \in [0, 1]$. Therefore, and according to HPMPE, solution, $\theta(t)$, and $\omega_L^2 = C_2$ which is the linear frequency of oscillation can be expanded in the forms

$$\theta(t) = \theta_0(t) + p_1 \theta_1(t) + p_2 \theta_2(t) + p_1^2 \theta_3(t) + p_1 p_2 \theta_4(t) + p_2^2 \theta_5(t), \quad (2.70)$$

and

$$C_2 = \omega^2 + p_1 \omega_1 + p_2 \omega_2 + p_1^2 \omega_3 + p_1 p_2 \omega_4 + p_2^2 \omega_5, \quad (2.71)$$

where ω is the nonlinear natural frequency of oscillation and ω_i , $i = (0, 1, 2, \dots)$ are arbitrary parameters that should be determined. This procedure is like modified Lindstedt – Poincare method with double series expansion [153-155]. Substituting Eq. (2.71) and

(2.70) into Eq. (2.69), collecting and rearranging the same power of $[p^n p^m]$, and setting coefficients zero, the following equations can be obtained

$$\ddot{\theta}_0(t) + \omega^2 \theta_0(t) = 0, \quad (2.72)$$

$$\ddot{\theta}_1(t) + \omega^2 \theta_1(t) - \frac{C_2}{3!} (\theta_0(t))^3 + \omega_1 \theta_0(t) = 0, \quad (2.73)$$

$$\ddot{\theta}_2(t) + \omega^2 \theta_2(t) + \frac{C_2}{5!} (\theta_0(t))^5 + \omega_2 \theta_0(t) = 0, \quad (2.74)$$

$$\ddot{\theta}_3(t) - \frac{3C_2}{3!} (\theta_0(t))^2 \theta_1(t) + \omega^2 \theta_3(t) + \omega_1 \theta_1(t) + \omega_3 \theta_0(t) = 0, \quad (2.75)$$

$$\begin{aligned} \ddot{\theta}_4(t) + \frac{5C_2}{5!} (\theta_0(t))^4 \theta_1(t) - \frac{3C_2}{3!} (\theta_0(t))^2 \theta_2(t) + \omega^2 \theta_4(t) + \omega_2 \theta_1(t) + \\ \omega_1 \theta_2(t) + \omega_4 \theta_0(t) = 0, \end{aligned} \quad (2.76)$$

$$\ddot{\theta}_5(t) + \frac{5C_2}{5!} (\theta_0(t))^4 \theta_2(t) + \omega^2 \theta_5(t) + \omega_5 \theta_0(t) = 0. \quad (2.77)$$

The initial conditions for solving Eq. (2.72) are like those in (2.39), while for Eqs. (2.73) to (2.77), they are set to zero. Solving Eq. (2.72) yields the following result

$$\theta_0(t) = \theta \cos(\omega t), \quad (2.78)$$

substituting Eq. (2.78) into Eq. (2.73) results in

$$\ddot{\theta}_1(t) + \omega^2 \theta_1(t) + \left(-\frac{1}{8} C_2 \theta^3 + \theta \omega_1 \right) \cos(\omega t) - \frac{1}{24} C_2 \theta^3 \cos(3\omega t) = 0, \quad (2.79)$$

to avoid the secular terms in solving Eq. (2.79), the coefficient of $\cos(\omega t)$ should be vanished, which leads to

$$\omega_1 = \frac{1}{8} C_2 \theta^2, \quad (2.80)$$

by repeating the same procedure, ω_i , $i = (2,3,4,5)$ can be obtained as follows

$$\omega_2 = -\frac{1}{192} C_2 \theta^4, \quad (2.81)$$

$$\omega_3 = -\frac{1}{1536} C_2^2 \frac{\theta^4}{\omega^2}, \quad (2.82)$$

$$\omega_4 = \frac{1}{3072} C_2^2 \frac{\theta^6}{\omega^2}, \quad (2.83)$$

$$\omega_5 = -\frac{11}{491520} C_2^2 \frac{\theta^8}{\omega^2}, \quad (2.84)$$

substituting Eqs. (2.80) till (2.84) into Eq. (2.71) and equating $p_1 = p_2 = 1$, the nonlinear natural frequency can be obtained as

$$\omega_{(H)} = \omega_L \sqrt{\left(\frac{1}{2} + \frac{1}{384} \theta^4 - \frac{1}{16} \theta^2 + \sqrt{\frac{1}{36864} \theta^8 - \frac{1}{1536} \theta^6 + \frac{1}{192} \theta^4 - \frac{1}{16} \theta^2 + \frac{1}{4}} \right)}, \quad (2.85)$$

in which the linear analytical approximate solution, ω_L , can be written according to Eq. (2.48) or (2.50). The nonlinear amplitude function can be written as

$$\Theta F_{(H)} = \sqrt{\left(\frac{1}{2} + \frac{1}{384} \theta^4 - \frac{1}{16} \theta^2 + \sqrt{\frac{1}{36864} \theta^8 - \frac{1}{1536} \theta^6 + \frac{1}{192} \theta^4 - \frac{1}{16} \theta^2 + \frac{1}{4}} \right)}, \quad (2.86)$$

Eq. (2.86) shows the relation between nonlinear frequency and the linear analytical approximate solution, $\omega_L = C_2^2$, representing the restoring force coefficient defined by Eq. (2.36) and the variable θ , representing the object dimensionless displacement. To show the pure effect of the nonlinearity, “the nonlinear frequency deviation”, $\Delta\omega$, is defined as follows

$$\Delta\omega = \frac{|\omega_N - \omega_L|}{\omega_L} * 100[\%] = |\Theta F - 1| * 100[\%]. \quad (2.87)$$

2.8.2. The effect of the viscosity on the nonlinear response

The purpose of this section is to investigate the effect of the viscosity on the nonlinear behaviour of an object trapped in an acoustic radiation force field in a carrier standing wave as presented in Eq. (2.37). In general, vibrational system with damping and without external force is defined as follows [156-158]

$$f(\ddot{\theta}, \dot{\theta}, \theta) = 0, \quad (2.88)$$

in general, the solution to Eq. (2.88) is selected as [147]

$$\theta(t) = \sum_{i=1}^n e^{-at} [b_i \cos(\omega_i t + \phi_i)], \quad (2.89)$$

when $\{a, b_i, \omega_i, \phi_i\}$ are the constant coefficients and can be obtained by applying the initial conditions. The initial conditions are as below

$$\theta(0) = \theta, \quad \dot{\theta}(0) = V, \quad (2.90)$$

the initial conditions (IC)s can be applied on the answer function Eq. (2.89) and on the Eq. (2.88) shown by $f(\theta(\text{IC}))$ and on its derivatives as expressed as [156-158]

$$f(\theta(\text{IC})) = 0, \dot{f}(\theta(\text{IC})) = 0, \ddot{f}(\theta(\text{IC})) = 0, \dots, \quad (2.91)$$

in this method which called Akbari-Ganji Method (AGM) [156], after applying the initial conditions on answer function presented in Eq. (2.89), and also the function differential equation and on its derivatives from Eq. (2.91), a set of algebraic equations are created which is consisted of n equations with n unknowns. Therefore, the constants at Eq. (2.89) are achieved. In Eq. (2.91), we can use the derivatives of $f(\theta(\text{IC}))$ with higher orders until the number of obtained equations is equal to the number of the mentioned constant coefficients of the assumed answer [158]. Eq. (2.37) with damping term and ignoring the external force excitation can be rewritten in the following form

$$\ddot{\theta} \pm C_1 \dot{\theta}^2 + C_2 \theta - \frac{C_2}{3!} \theta^3 + \frac{C_2}{5!} \theta^5 = 0. \quad (2.92)$$

Here and for simplicity the expansion of $(\sin \theta)$ is restricted to order five, with higher-order terms ignored. Further, the absolute value operator is replaced with ' \pm ' which depends on the sign of $\dot{\theta}$ in the equation of motion. This allows the damping effect on the system's behaviour to be examined, specifically how it influences the natural frequency. To solve the Eq. (2.92) by AGM, it is assumed that the answer can be written as [157]

$$\theta(t) = e^{-at} [b \cos(\omega_d t + \varphi)], \quad (2.93)$$

in this equation, a represents the power of the logarithmic decrement, b stands for the amplitude of the free damped vibration, ω_d denotes the nonlinear frequency of the damping oscillation, and φ signifies the phase difference. When the initial conditions stated in Eq. (2.90) are applied to the solution function, the result obtained is

$$b \cos(\varphi) = \theta, \quad (2.94)$$

and

$$a \cos(\varphi) + \sin \varphi = -\frac{V}{b}, \quad (2.95)$$

applying the initial conditions on the governing equation of motion, Eq. (2.92) results in

$$\begin{aligned} a^2 b \cos(\varphi) + 2ab\omega \sin \varphi - b\omega^2 \cos(\varphi) \pm C_1(-ab \cos(\varphi) - b\omega \sin \varphi)^2 + \\ C_2 b \cos(\varphi) - \frac{1}{6} C_2 b^3 \cos(\varphi)^3 + \frac{1}{120} C_2 b^5 \cos(\varphi)^5 = 0, \end{aligned} \quad (2.96)$$

and also applying the initial conditions on the first derivative of the differential equation, $\dot{f}(\theta(\text{IC}))$, results in

$$\begin{aligned} -a^3 b \cos(\varphi) - 3a^2 b \omega \sin(\varphi) + 3ab\omega^2 \cos(\varphi) + b\omega^3 \sin(\varphi) \pm \\ 2C_1(-ab \cos(\varphi) - b\omega \sin(\varphi))(a^2 b \cos(\varphi) + 2ab\omega \sin(\varphi) - b\omega^2 \cos(\varphi)) - \\ C_2 ab \cos(\varphi) - C_2 b \omega \sin(\varphi) + \frac{1}{2} C_2 b^3 a \cos(\varphi)^3 + \frac{1}{2} C_2 b^3 \omega \cos(\varphi)^2 \sin(\varphi) - \\ \frac{1}{24} C_2 b^5 a \cos(\varphi)^5 - \frac{1}{24} C_2 b^5 \omega \cos(\varphi)^4 \sin(\varphi) = 0. \end{aligned} \quad (2.97)$$

By solving the set of nonlinear algebraic equations considering of four equations with four unknowns from Eq. (2.94) to Eq. (2.97), the constant coefficients of the answer function can be obtained

$$a = \frac{(\psi_1)}{(\psi_2)}, \quad (2.98)$$

when

$$\begin{aligned} \psi_1 = V(\theta^6(\pm C_1)C_2 - 2\theta^5 C_2 - 20\theta^4(\pm C_1)C_2 + 120\theta(V C_1)^2 + 20\theta^3 C_2 + \\ 120\theta^2(\pm C_1)C_2 + 60V^2(\pm C_1)), \end{aligned} \quad (2.99)$$

and

$$\begin{aligned} \psi_2 = (\theta^6 C_2 - 20\theta^4 C_2 - 20\theta^4(\pm C_1)C_2 + 120\theta(\pm C_1)V^2 + 120\theta^2 C_2 + \\ 120V^2), \end{aligned} \quad (2.100)$$

and the nonlinear frequency of the damping oscillation can be written as

$$\omega_d = \frac{\sqrt{\theta}}{\theta} \sqrt{\frac{1}{120} C_2 \theta^5 - \frac{1}{6} C_2 \theta^3 - a \theta^2(\pm C_1)V^2 + \theta C_2 - 2Va}, \quad (2.101)$$

in which a should be replaced from Eq. (2.98), and the phase difference, φ , can be obtained as

$$\varphi = -\tan^{-1}\left(\frac{\theta a + V}{\theta \omega_d}\right), \quad (2.102)$$

and the amplitude of the free damped vibration, b , can be obtained as

$$b = \frac{\theta}{\cos \varphi}, \quad (2.103)$$

after obtaining all coefficients in Eq. (2.93), the analytical approximate solution for the nonlinear differential equation (2.92) is successfully derived.

2.8.3. Parametric study of analytical solutions

In this section, the advantages and the accuracy of the analytical proposed methods are assessed by making a comparison analytical methods with each other and with numerical results obtained by Runge–Kutta method of order four. The parameters of the object and medium properties have taken as: $r = 0.71$ mm, $f_o = \frac{\omega_o}{2\pi} = 30$ Hz, $f = 40$ kHz, $\rho_0 = 1.19 \frac{\text{kg}}{\text{m}^3}$, $\rho_1 = 34 \frac{\text{kg}}{\text{m}^3}$, $c_0 = 334 \frac{\text{m}}{\text{s}}$, $c_1 = 540 \frac{\text{m}}{\text{s}}$, $C_d = 1.06$.

The nonlinear frequency deviation obtained by Eq. (2.87) for first order and second order of GRHBM and HPMPE is presented in Fig. 2.14. It can be observed that the difference between the first order and second order of GRHBM and HPMPE starts to deviate considerably at $A_o \sim \lambda/5$, which shows that at this point the significance of higher order terms in the trail solution is not negligible. Also, for $A_o < \lambda/5$ the difference between analytical solutions is less than 5 %.

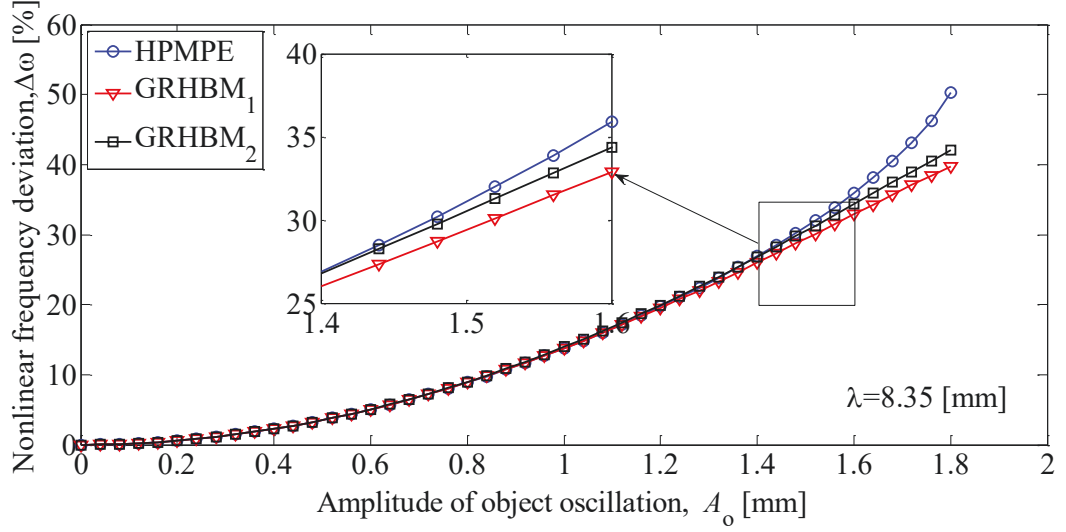


Fig. 2.14. The nonlinear frequency deviation obtained by Eq. (2.87) for first order and second order of GRHBM and HPMPE.

Fig. 2.15 shows the effect of the higher order terms in Taylor series in expanding $\sin(\theta)$ in calculating natural frequency using Eq. (2.61) which shows that expanding till θ^3 the deviation starts at $A_0 \sim \lambda/8$ and for θ^5 the deviation starts at $A_0 \sim \lambda/5$, which means that Duffing equation with order 3 is only valid for $A_0 < \lambda/8$, and with order 5 is only valid for $A_0 < \lambda/5$, and for bigger amplitude, higher order terms is required.

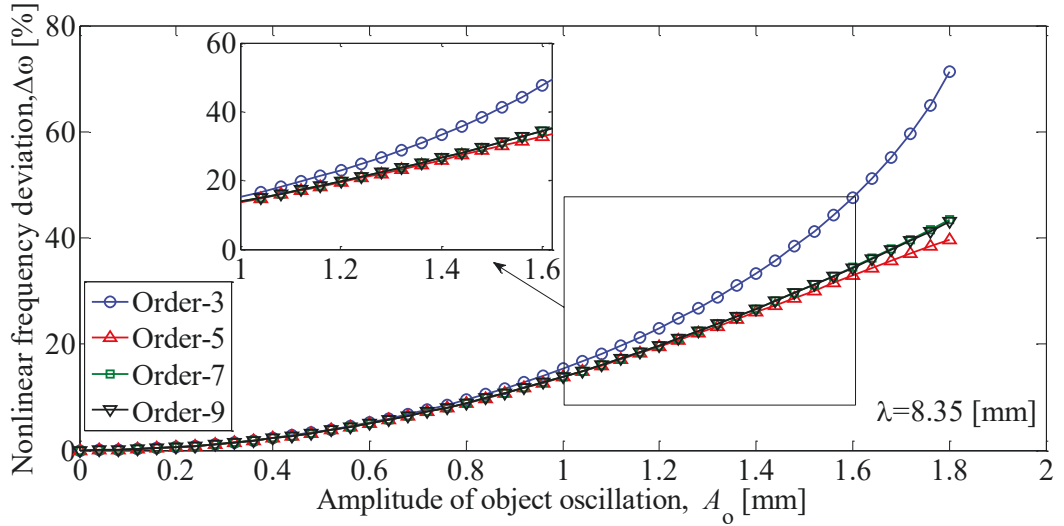


Fig. 2.15. The effect of the higher order terms in Taylor series in expanding $\sin(\theta)$ in calculating natural frequency using Eq. (2.61).

Fig. 2.16 shows the effect of the density on the linear natural frequency according to the King model. This figure shows that increasing the relative density, $\tilde{\rho} = \rho_1/\rho_0$, decreases the natural frequency.

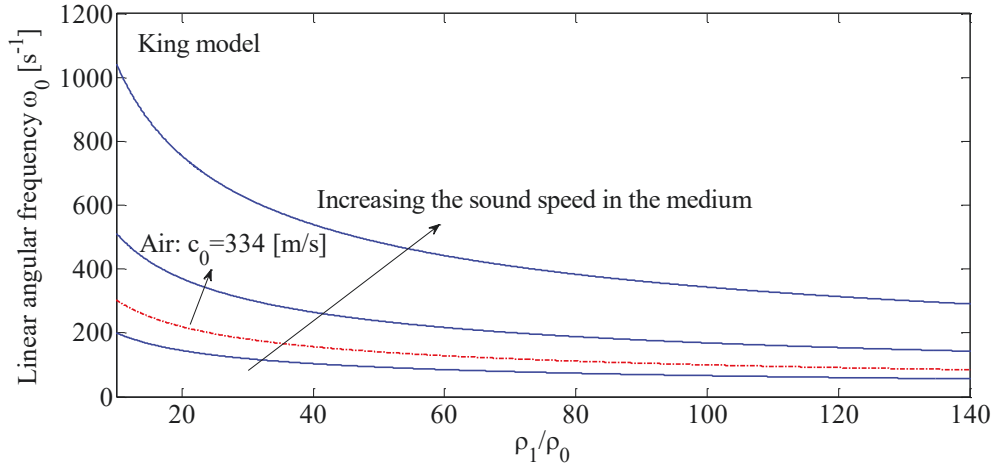


Fig. 2.16. The effect of the density on the linear natural frequency according to model of King.

Fig. 2.17 shows the effect of the compressibility on the linear natural frequency. This figure shows more than 10% difference to less than 1% difference between the compressible assumption (Yoshioka model [63]) and the solid assumption (King model [62]) when the sound speed in the object is varying from 100 to 600 m/s. In this parameter study, the variation in sound speed (from 100 to 600 m/s) is modelled to explore its effects on the frequency. Materials with low sound speeds (e.g., near 100 m/s) are rare and typically correspond to specialized cases, such as high-compliance or low-density media. Examples include elastomeric polymers, gels, or foams, which exhibit these properties due to their low stiffness and density [159]. It is obvious that by increasing the sound speed in the object the Yoshioka model tends to the King model.

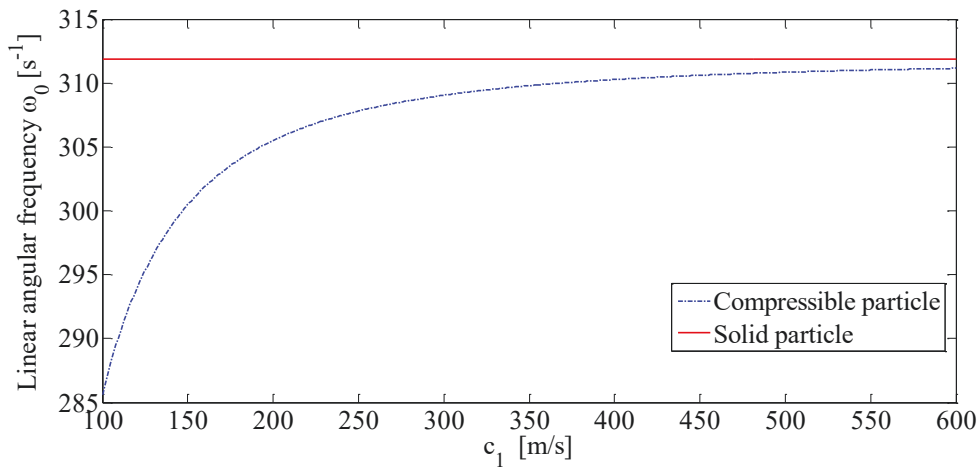


Fig. 2.17. The effect of the compressibility on the linear natural frequency.

The solution for nonlinear response, considering the viscosity, are depicted and compared by numerical solution in Fig. 2.18, and a good agreement can be seen between analytical

solution, Eq. (2.93) and numerical solution obtained by Runge–Kutta method of order four. This figure has been plotted with two different initial condition and shows that after about 60 [s], the object attract to its trap with small oscillation around its equilibrium point.

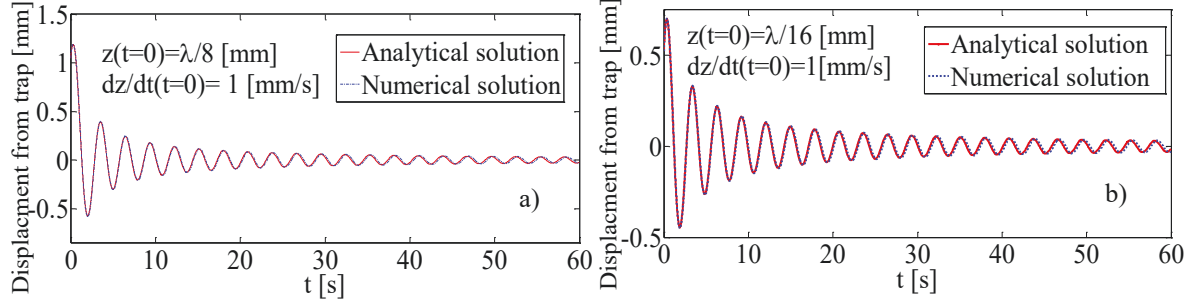


Fig. 2.18. A comparison study between analytical solution obtained by AGM and numerical simulation for two different initial condition: a) $z(t = 0) = \lambda/8$, and b) $z(t = 0) = \lambda/16$.

The effect of the viscosity on the nonlinear frequency deviation and phase of oscillation for various amplitude $[A_o = \frac{\lambda}{5}, \frac{\lambda}{8}, \frac{\lambda}{12}, \frac{\lambda}{16}]$ and constant initial velocity $V = 1$ [mm/s] vs the drag coefficient has been depicted in Fig. 2.19. It can observe that increasing the drag coefficient increase the $|\varphi|$ and $\Delta\omega$. The same trend, also, can be observed for $\Delta\omega$ by increasing the initial amplitude, A_o .

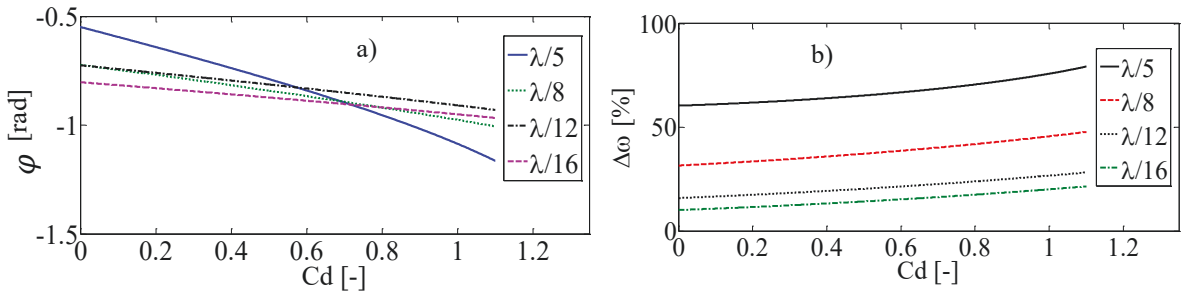


Fig. 2.19. The effect of the viscosity on the a) phase and the b) nonlinear frequency deviation of oscillation for various initial condition.

In this chapter, it has been demonstrated that acoustic pressure modulation introduces dynamic components, resulting in nonlinear dynamical behaviour. An equation of motion similar, but not identical, to the Duffing equation for the vibrational motion of the object has been derived. In the following, nonlinear free and damped vibrational analysis is conducted to determine the natural and damped frequencies of vibration. Nonlinear dynamic analysis, including techniques like bifurcation analysis and frequency response,

plays a crucial role in understanding and predicting the behaviour of complex systems [160-162] and will be discussed in the next Chapter.

2.9. Conclusion

Using the Gorkov formulation, the acoustic contrast factor of an acoustically small spherical object levitated in a plane standing wave under the influence of an external sinusoidal excitation was calculated. The results show that the time-averaged component of the acoustic radiation force can be positive, negative, or zero, with its direction influenced by the external sinusoidal excitation. Traditionally, the acoustic contrast factor describes the scattering properties of a particle and is determined by intrinsic material properties such as density and compressibility, along with the acoustic characteristics of the surrounding medium. However, this study reveals that vibration-induced dynamics, introduced by external excitation, significantly alter the overall radiation force, highlighting the role of oscillatory behaviour as a distinct and influential factor. This finding emphasises the importance of considering both intrinsic object properties and external dynamic effects when analysing and predicting the behaviour of acoustically levitated systems. This indirect way of controlling a levitated object through the external excitation properties of an object held within an acoustic radiation force field has never been attempted. To facilitate a comprehensive comparison with theoretical approaches, this Chapter introduced both 2D and 3D numerical models of acoustic radiation force. Using COMSOL Multiphysics, the 3D model was developed to extend the analysis beyond the limitations of traditional approaches. This model incorporates the ability to simulate objects with larger dimensions and non-rotational symmetry, analyse interactions between multiple objects, and evaluate the effects of external vibrations, particularly in near-wall scenarios. These capabilities are critical for capturing the complex behaviours of acoustic radiation forces in realistic settings, making the 3D model an invaluable tool for advancing both theoretical understanding and practical applications in acoustic levitation and manipulation. The idea that the contrast factor varies with the magnitude of external excitation assumes of a harmonic response. This assumption and its implications are explored further in the subsequent Chapters, where nonlinear dynamics are addressed in detail. The acoustic contrast factor is a time-averaged static quantity that determines the steady-state acoustic radiation force acting on levitated objects. However, it does not directly govern the system's dynamic response. By applying Newton's second law, a nonlinear governing equation of motion is derived, unveiling a

Duffing-like oscillator behaviour in the time-varying radiation force, which shows a restoring harmonic force as a nonlinear softening spring. The nonlinear dynamical model introduced in this Chapter (Eq. 2.35) provides the foundation for these analyses, offering key insights validated through bifurcation studies and time-series methods. Chapters 3 and 4 thoroughly examine the dynamic effects, analysing the system's response to external excitation.

Based on the King and Yoshioka model, the governing equation for an object trapped in an acoustic radiation force field within a carrier standing wave was derived. This is an ordinary differential equation. Then, the Global Residue Harmonic Balance Method (GRHBM) and the Homotopy Perturbation Method with Multi-Parameter Expanding (HPMPE) were utilized to obtain analytical approximate frequencies under free vibration conditions. In the GRHBM approach, the aim was to enhance accuracy by determining the residual error at each order of approximation, which was subsequently utilized in subsequent orders. With the obtained analytical expressions, the influence of nonlinear terms on the nonlinear frequency was examined. The HPMPE method, known for its straightforwardness and effectiveness, proved suitable for systems involving multiple nonlinear terms. Comparing these analytical methods for $A_0 \leq \lambda/5$ revealed discrepancies of less than 5%, validating the use of analytical solutions within this interval. Moreover, it was found that considering only the cubic term in the nonlinear governing equation was valid for $A_0 \leq \lambda/8$, while incorporating both cubic and quintic terms extended validity to $A_0 \leq \lambda/5$. For higher amplitudes, inclusion of higher-order nonlinear terms became necessary. Furthermore, the influence of compressibility and density on the natural frequency was investigated. Subsequently, the Akbari-Ganji (AG) method was employed to solve nonlinear damped vibration, exploring its impact on the natural frequency and phase of oscillation. The findings were corroborated by numerical solutions obtained via the fourth-order Runge-Kutta method. The results underscored the role of damping effects in the absence of external excitation and demonstrated that object vibration decays towards its static position at its equilibrium point. It should be noted that although there is a novelty in deriving the solution using analytical approaches, as stated in this Chapter, these methods are inherently limited to simple acoustic pressure fields. Unlike numerical continuation methods, which allow for parameter studies in more complex acoustic environments, the analytical approach assumes small deviations, restricting its applicability to highly nonlinear or spatially varying fields.

CHAPTER 3: EXPERIMENTS AND STATISTICAL ANALYSIS

3.1. Introduction

In a dynamical system with specified input and output, the modelled inputs are in real-life applications influenced by uncertainties in measurement, requiring to be considered in the output of the model. Therefore, the conduct of a sensitivity analysis to identify sensitive parameters prone to become uncertain is one of the essential goals of research in this Chapter. [163-165]. Here, the Sobol method for sensitivity analysis is introduced and then it is applied to the equation of motion obtained in Chapter 2. With the help of the Sobol method the effect of changing the coefficients of the equation on the dynamic behaviour of the system is discussed and investigated [165-170]. In Chapter 2, the governing equation of motion of a small spherical object levitated in an acoustic radiation force field was driven by the assumption that in response to external harmonic excitation, the levitated object also shows a simple harmonic behaviour. Here, an experiment is conducted to validate this assumption and extract time series data related to the movement of a levitated object. The object in the first case follows the small spherical object (Gorkov) theory, while in the second case, a large spherical object is used for which Gorkov theory is no longer valid. The presented experimental analysis of the small object shows a clear correlation between the amplitude and frequency of the external harmonic excitation and the object's response. As theoretically shown in Chapter 2, the dependence of the levitated object's movement on the application of external excitation and the force reversal are new features that can potentially be used for non-contact control of small objects (subwavelength) with the help of acoustic radiation forces [116-121].

Also, by using the theoretical formulation presented in Chapter 2 and with the help of the time series data extracted from the experiment presented here, the system's analytical and experimental bifurcation diagrams are extracted [171-177]. By carefully comparing bifurcation diagrams, the aim is to understand the similarities and differences between bifurcation plots, especially for objects below and above the wavelength limit. This comparative study is a key step in the research, not only improving the understanding of the system's behaviour but also laying the groundwork for practical applications in the acoustic manipulation of objects.

3.2. Statistical model and Sobol sensitivity analysis

Recently, global sensitivity analysis methods are widely used for the analysis of nonlinear models [178-180]. Unlike local sensitivity analysis methods that analyse one system's variable at a time, global sensitivity analysis methods change all variables simultaneously over their entire range and thus provide a more comprehensive approach in comparison with the local sensitivity analysis [180]. Among these methods, variance-based methods such as Sobol's method, are considered very valuable tools due to their special characteristics [181]. Unlike traditional methods [182–184], global sensitivity analysis does not rely on model linearity or uniformity. This feature makes it applicable to many types of nonlinear problems, which is invaluable for gaining deeper insights into the influence of input parameters on the overall system behaviour [165-170]. In the following, Sobol's method is applied to the nonlinear dynamical model of a spherical object levitated in an acoustic radiation force field (Eq. (2.35)). However, before employing Sobol's method, it is essential to determine an optimal time step for the numerical solution of the equation of motion.

3.2.1. Optimizing time step selection in numerical solutions: A statistical approach

The use of statistical visual representation data has a long history [185-188]. Mary Eleanor Spear introduced the range-bar method, also known as the range bar chart, in her book "Charting Statistics" [185]. This method was later more described in detail in her 1969 book "Practical Charting Techniques" [186]. The method proposed by Mary Eleanor Spear used vertical bars to indicate the range between the minimum and maximum values in the data to provide a visual representation of the dispersion of the data. Inspired by this method, John Tukey introduced the "Box and Whisker plot" in his book entitled 'Exploratory Data Analysis', which became very popular and is now widely used in the analysis of statistical problems [187, 188]. The box plot, as it's commonly known, provides a more detailed view of data distribution. The "Box and Whisker plot," usually called a box plot [189-191] is one of the most famous charts showing many indicators of data-related descriptive statistics. This chart can give information about the existence of outlier data, symmetry in the data, and skewness of the data. A box plot is a straightforward and clear visual representation of the distribution and variability of a dataset. It consists of a box that represents the interquartile range (IQR), which is the

middle 50% of the data. The line within the box denotes the median, or the middle value of the dataset. The “whiskers” extend from the box to the minimum and maximum values, excluding outliers which are represented as individual points beyond the whiskers. Box plots are easy to understand and use, making them a valuable tool for comparing distributions between different groups or datasets and identifying outliers or extreme values within the data [188]. In this study and by using the 4th order Runge-Kutta method, Eq. (2.35), with a different time step Δt varying from $\Delta t = 10^{-4}$ s to a reference time step at $\Delta t = 10^{-7}$ s, is solved numerically. To investigate the dynamic response of the system, the following values of parameters are extracted from [118] which studies an object with radius of $r = 0.71$ mm, and density of $\rho_1 = 34 \frac{\text{kg}}{\text{m}^3}$ and drag coefficient of $C_d = 1.06$, fluid density of $\rho_0 = 1.19 \frac{\text{kg}}{\text{m}^3}$. The object is levitated in air within a single-axis levitator which produce standing acoustic wave with wavelength of $\lambda = 8.6$ mm. During each step of the numerical simulation, the relative error can be calculated as

$$E_R = |\theta - \theta_R|. \quad (3.1)$$

Here θ_R represents the relative reference response solution for $\Delta t_R = 10^{-8}$ s. The relative errors for these time steps are normalised by dividing to θ_R , and are plotted in the Fig. 3.1 which shows 95% Confidence Interval (CI) for the median (notched boxplot diagram [192]). By using this chart, $\Delta t = 10^{-6}$ s can be chosen as an appropriate time step with $\text{CI} = [9.60, 9.81] \times 10^{-4}$.

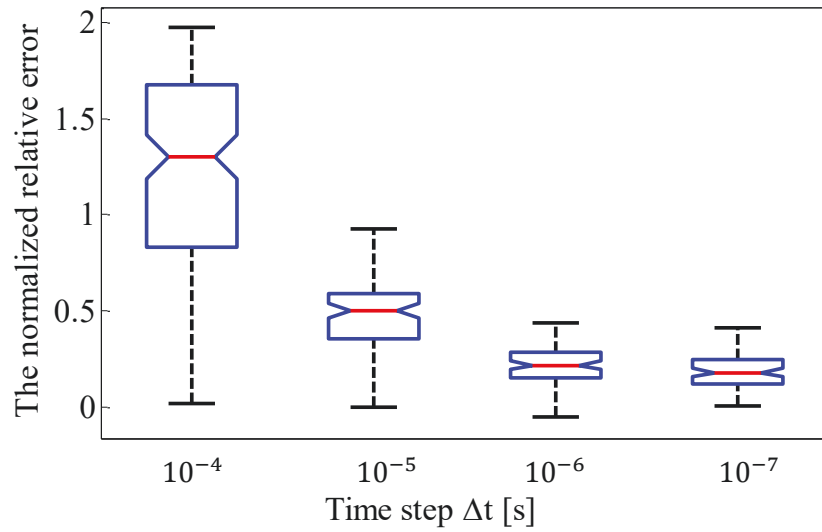


Fig. 3.1. Time step convergence study using a box plot. The whiskers show the minimal and maximal values, the edges of the box indicate the 25 – and 75 – percentile the red line represents the median and the notches show the 95% confidence interval of the median. Non-overlapping notches show non-significant difference in median estimates of the relative error.

3.2.2. Sobol's method of sensitivity analysis

Global sensitivity analysis methods, especially variance-based approaches, use variance to measure the influence of input parameters on output of a system. Variance-based methods rely on sampling and the statistical distribution of input data. The sensitivity index in these methods shows how much the change in the input parameter in the model affects the output of the model. The higher the value of the sensitivity index for each input parameter is measured, the greater the impact of the on the model's output behaviour. Sobol's method was introduced by Ilya Sobol in the late 1990s as an extension of variance-based sensitivity analysis [165-171]. It allows for the decomposition of the total variance of the model output into components attributable to individual input variables and their combinations. This method provides a systematic way to rank the importance of input variables, identify influential factors, and assess the interactions among them. In the Sobol sensitivity analysis method, for a model defined by $Y = f(\vec{X})$ where Y is the output of the system and $\vec{X} = [x_1, x_2, \dots, x_3]$ is the vector of input parameters, $V(Y)$, the variance of the system can be defined through [170]

$$V(Y) = \sum_{i=1}^n V_i + \sum_{i \leq j \leq n}^n V_{ij} + \dots + V_{1,\dots,n} \quad (3.2)$$

in which, V_i is the variance because of the first order effects for each parameter and V_{ij} to $V_{1,\dots,n}$ are second and higher order effects for each parameter which shows the variance because of the interaction between parameters. The first-order sensitivity coefficient for the i^{th} parameter can be defined by

$$S_i = \frac{V_i}{V(Y)} \quad (3.3)$$

and the total sensitivity coefficient for the i^{th} parameter can be defined by

$$S_{Ti} = S_i + \sum_{i \neq j}^n S_{ij} + \dots \quad (3.4)$$

where, $S_{ij} + \dots$ are the second and higher order sensitivity coefficient for each parameter. In summary, this analysis can be divided into five steps, which step by step will ultimately lead to understanding the system's behaviour [178-180]:

1. **Parameter Selection and Distribution Assignment:** Initially, parameters of interest are selected, and probabilities or distributions are assigned to each parameter.
2. **Random Input Vector Generation:** A set of random input vectors is generated for each parameter according to the probability distribution assigned to it.
3. **Model Evaluation:** The model is evaluated for each generated input vector set. This step involves running the model to obtain corresponding outputs.
4. **Output Distribution Uncertainty Determination:** The uncertainty of the output distribution is analysed and understood, accounting for variations in input parameters.
5. **Sensitivity Ranking:** Finally, sensitivity analysis ranks the input parameters based on their influence on the output. This ranking helps identify which parameters significantly impact the model's behaviour and output variability.

For the sensitivity analysis and according to the Eq. (2.35) the model inputs $\vec{X} = [C_1, C_2, C_3, \omega_0]$ are set to be uniformly distributed. The constant coefficients C_1 , C_2 , and C_3 represent the damping, restoring force, and external excitation, respectively. These coefficients can be determined using can be obtained using Eq. (2.36) by using the object

and medium properties. The parameter ω_o refers to the object frequency in the acoustic radiation force field. Assuming the following ranges for the test variables: $C_1 = [6, 8] \times 10^4 [-]$, $C_2 = [1.2, 1.8] \times 10^{-2} [s^{-2}]$, $C_3 = [8, 10] \times 10^4 [s^{-2}]$, $\omega_o = [10, 25] [Hz]$, the first order effects and the total effects of the parameters are shown in Fig. 3.2.

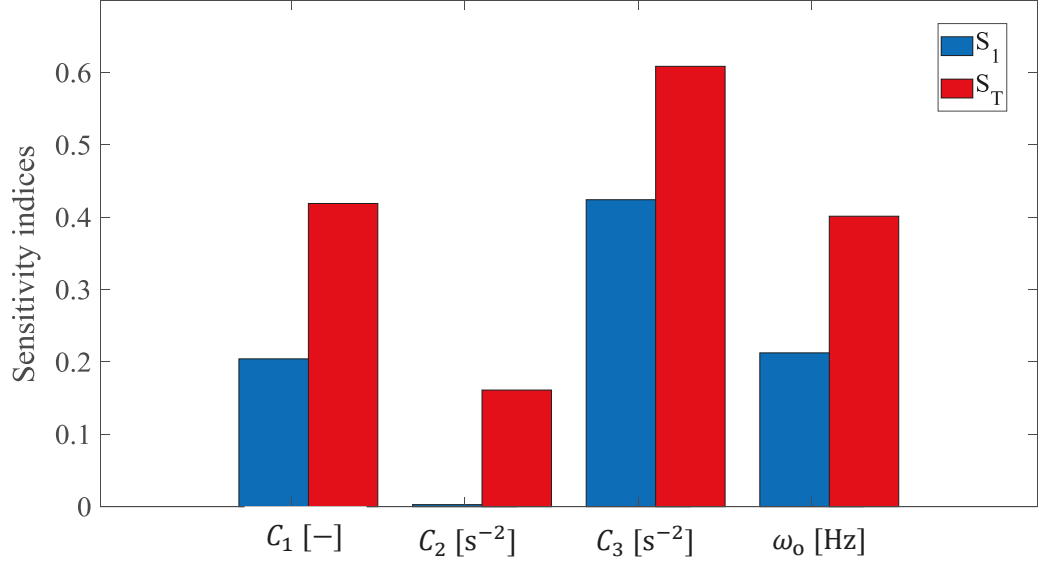


Fig. 3.2. Results of the variance-based sensitivity analysis when S_1 and S_T are the first-order and total sensitivity coefficient, respectively. Importance ranking of the coefficients in Eq. (2.35) by sensitivity analysis using uniformly distribution. The external excitation has the strongest influence on the C_3 coefficient in the equation of motion (Eq. (2.35)), C_2 is having a rather small influence on the dynamics.

Using result obtained by the sensitivity analysis the amplitude of the external excitation which influences C_3 in the Eq. (2.35), can be selected as bifurcation parameters. The results reveal that the coefficients C_3 and ω_o are the most sensitive parameter, respectively. It is also observed that the total effects of C_2 are smaller than other parameters, i.e., there is not much interaction between C_2 and other parameters. These results reveal that the amplitude and frequency of the external excitation in Eq. (2.35) plays an important role in the dynamical behaviour of the system.

3.3. Numerical frequency response and bifurcation diagram

One of the characteristics of dynamical systems is their frequency response curve, which is a measurement of the amplitude or phase of the output as a function of input frequency of the system [160-162]. Here, the frequency response of the system in low external amplitude of excitation is plotted using Eq. (2.35), then a comparison with experimental

results reported in [118] is conducted. Fig. 3.3 compares the peak response amplitude of the object, A_{out} , trapped in a standing wave levitator obtained by dynamical equation of motion presented in Eq. (2.35) and the experimental results presented in Ref. [118] in the stable region. The amplitude of the external excitation, denoted as A_{in} , is adjusted to 0.15 mm. A good agreement can be observed between analytical formulation presented in this study and the previous experimental work [118].

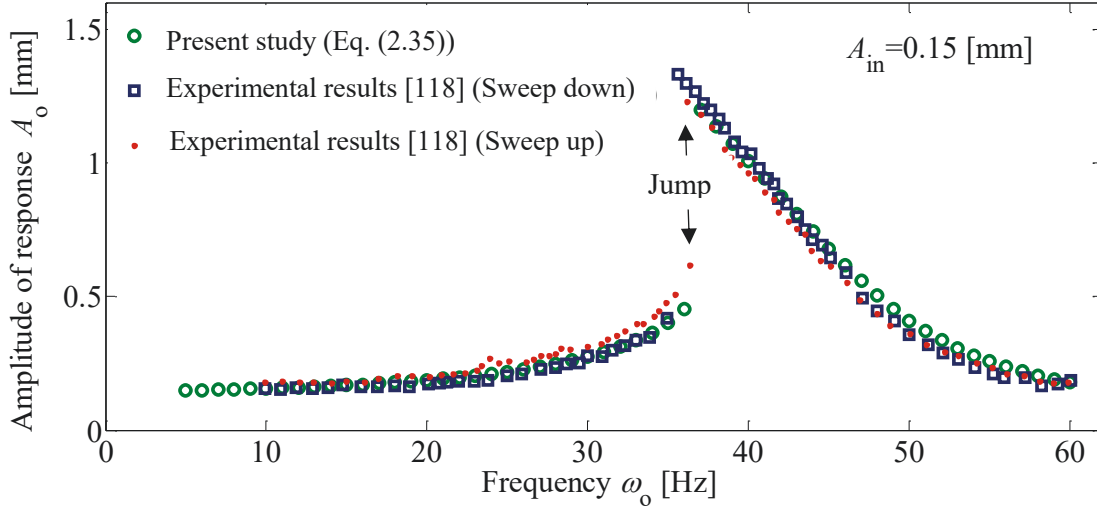


Fig. 3.3. A comparison between the predicted frequency responses from Eq. (2.35) with the experimental results [118] for an object trapped in a standing wave levitator. The observed jump between different states indicates a softening behaviour. The theoretical predicted curve was generated by increasing the frequency, corresponding to the “sweep up” scenario in the experimental work.

Fig. 3.3 shows the jump phenomenon. In the theory of dynamical systems, the jump phenomenon refers to a sudden and discontinuous change in the behaviour or state of the system [171-177]. Jump phenomenon is usually visible at the bifurcation points of the system. Plotting and analysing the bifurcation diagram is also used in many physical applications, especially the dynamical analysis of nonlinear systems [177]. The bifurcation diagram shows the fact that a slight change in a parameter value of a dynamic system, which called the bifurcation parameter, leads to a sudden change in the dynamics of the system. In other words, in bifurcation point, a change in the number or stability of the equilibrium points of the system can be observed. In this study, the bifurcation diagram is investigated, and it is used to identify the behaviour of a levitated object trapped in an acoustic radiation force field. Here, the bifurcation parameter of the system is selected using sensitivity analysis and the time series obtained with the help of the

theoretical formula and experimental results in steady state are used to plot the bifurcation diagram [175]. According to the sensitivity analysis presented in section 3.2, the external excitation amplitude ranging from $A_{in} \in [0 \ 1]$ [mm] has been chosen as bifurcation parameter for which four distinct regions (Fig. 3.4) have been observed.

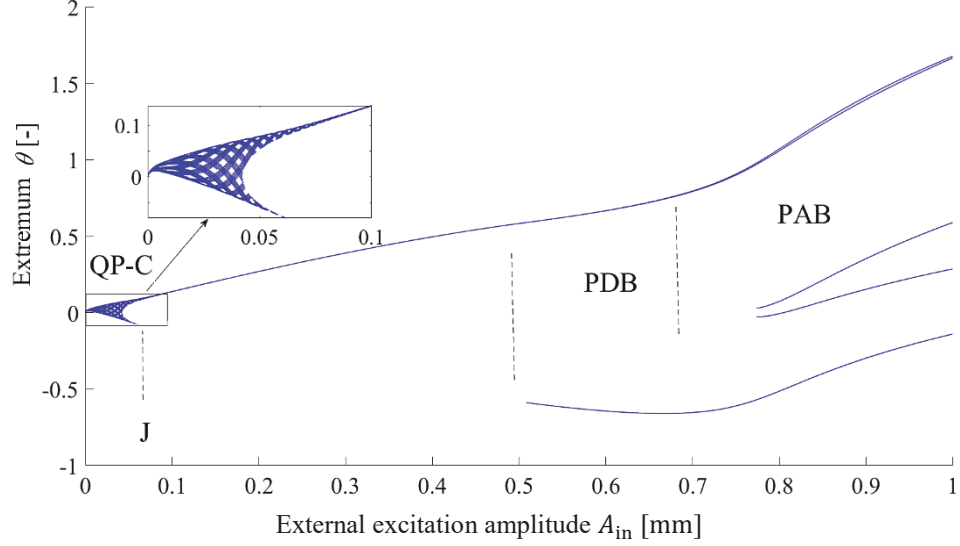


Fig. 3.4. The bifurcation diagram for a spherical object trapped in an oscillating radiation force field using Eq. (2.35), $\omega_o = 10$ Hz. The chaotic (C) or quasi-periodic (QP) area from $A_{in} \sim 0$ to $A_{in} \sim 0.05$ indicates the intricate high-order periodic behaviour in low amplitude, the jump (J) phenomenon occurs at $A_{in} \sim 0.06$, period-doubling bifurcation (PDB) can be observed at $A_{in} \sim 0.5$ and increasing in periodic solutions or period adding bifurcations (PAB) occurs at $A_{in} > 0.7$.

In the low amplitude, $A_{in} < 0.05$ [mm], the system shows chaotic (C) or quasi-periodic (QP) behaviour. At low amplitudes, the system's response is highly sensitive to small variations in external inputs and internal parameters. This sensitivity amplifies minor nonlinear effects, leading to intricate periodic or chaotic dynamics. The behaviour is driven by the inherent nonlinearity of the system and the interaction between acoustic radiation forces and external excitation. These nonlinear interactions magnify small perturbations, resulting in unpredictable and complex motion. The bifurcation diagram (Fig. 3.4) illustrates this behaviour, highlighting the system's sensitivity and the onset of chaos even at small amplitudes. By increasing the value of the bifurcation parameter jump (J) phenomenon can be observed. The discontinuity in the bifurcation diagram shows jumps and period-doubling bifurcation (PDB) and period adding bifurcations (PAB) are next different area in the bifurcation diagram. Fig. 3.4 shows that by increasing the value of the bifurcation parameter the period doubling bifurcation diagram is not valid anymore

as predicted in [118], and period-2 changes to period-5. This study shows that the classical Duffing equation with a cubic nonlinearity term [193] is insufficient to describe the full spectrum of nonlinear dynamical system behaviour. However, Eq. (2.35) can be categorized as a Duffing-like equation, and the findings suggest the possibility of more intricate dynamics, indicating the necessity for further investigation and experimentation.

3.4. Experimental analysis

In recent years, acoustic levitation has significantly advanced and used for manipulating objects by sound waves [110-118]. Ultrasonic transducers are the central part of an acoustic levitator device (Fig. 3.5a). Using ultrasonic transducers, we can create a specific sound pattern enveloping the object in acoustical energy [124]. When multiple transducers are connected and powered by strong electrical signals, they generate a powerful enough sound for levitation. This technology enables the levitation of small objects such as insects, individual cells, etc. In 2017, Marzo et al. introduced Tiny-Lev, a uniaxial acoustic levitator that is freely available to the public [14]. Tiny-Lev works like a simplified PAL [92,93]. The special Tiny-Lev geometry reduces the need for complex electronics and allows work with commercially available microcontroller boards. This affordability, cheapness and ease of assembly make Tiny-Lev a relatively simple and accessible device. Timing is crucial in controlling the sound from each transducer. When timed correctly, the sound waves converge to form a correct pattern of loud and quiet regions required for acoustic levitation. A crucial component of this functioning is a region called the “trap,” where the object remains suspended as if in a cage of sound. Stable traps show the pressure node in the acoustic radiation force field. Any attempt by the object to move is counter-acted by the sound, pushing it back into the trap. The strength of trap is not uniform in the radiation force field because of the Tiny-Lev setting, which is prohibitive in generating a plane acoustic wave so that the strongest trap can be found in the centre between the two transducer shells [114-127]. Fig. 3.5b illustrates the pattern of sound waves [125], indicating that the trap with maximum force occurs in the middle. This phenomenon, depicted in Fig. 3.5c, facilitates the levitation process within a single-axis levitator device or Tiny-Lev, as shown in Fig. 3.5d.

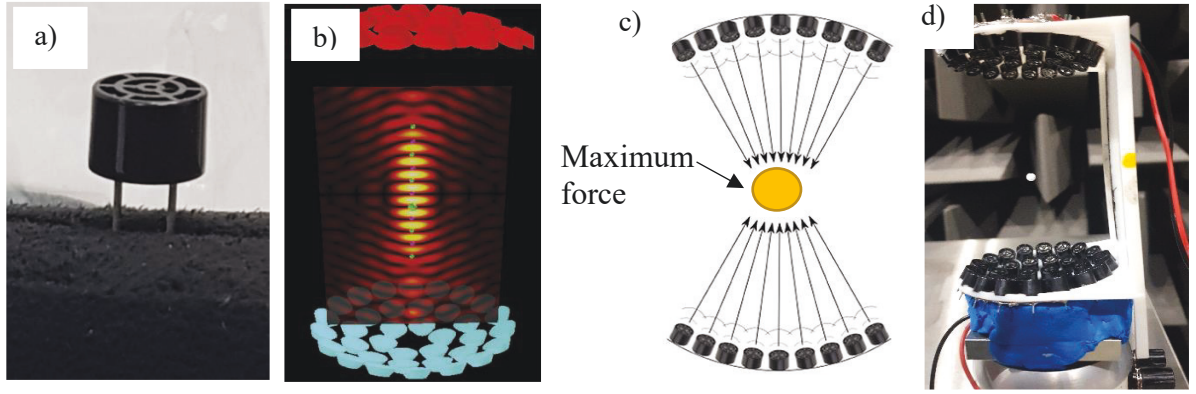


Fig. 3.5. a) A single ultrasonic transducer, b) Simulation illustrating acoustic traps [125]. c) Visualization of traps exhibiting maximum strength in the middle. d) Image showcasing the Tiny-Lev apparatus with a spherical object levitated in mid-air.

3.4.1. Tiny-Lev and levitated object properties

In the experiment, an off-the-shelf single-axis acoustic levitator (Tiny-Lev), with 72 circularly arranged transducers at the top and bottom support plates is used to levitate small objects near acoustic pressure nodes [125]. All transducers are operating at frequency, $f = 40$ kHz. This frequency corresponds to an acoustic wave with a wavelength of $\lambda \sim 8.5$ mm at a temperature of 25°C . It is common to choose ultrasonic transducers with a working frequency of 40 kHz. In addition to producing sound waves with a frequency beyond the threshold of human hearing, these transducers are widely available in the market and have many applications. For example, in the automotive industry, these converters are used to make parking sensors.

For the Tiny-Lev, the distance between the two upper and lower plates is 105 mm, and the ultrasonic transducers on these plates have been arranged according to the configuration shown in Fig. 3.6a. A simple tool, as shown in Fig. 3.6b, is also used to insert objects into the equilibrium point within the acoustic radiation force field. Before each experiment and to ensure the position of the levitated object is within the Tiny-Lev, a visual inspection with the help of a ruler is conducted (Fig. 3.6c). The purpose of this inspection is to ensure that the levitated object is correctly positioned at the most stable node located in the middle between the two planes of the Tiny-Lev.

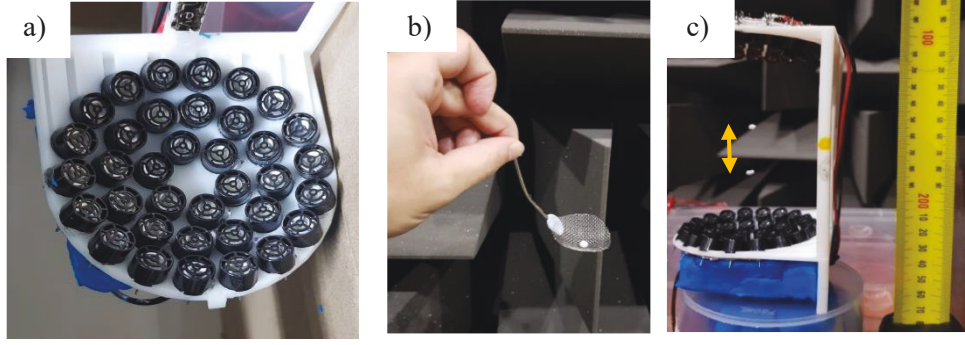


Fig. 3.6. a) Ultrasonic transducers arranged on one plate of the Tiny-Lev, b) the tool used for inserting objects into the standing wave's node, c) visual inspection process employing a ruler.

Fig. 3.6c depicts two small objects trapped in the acoustic force field within the Tiny-Lev, positioned approximately $25.5 \text{ mm} = 3 \times 8.5 \text{ mm}$ apart, vertically. This spacing aligns closely with the distance between pressure nodes or traps, which is half of the wavelength. This consistent measurement validates the effectiveness of the Tiny-Lev in generating the desired acoustic wave. This repeatable measurement highlights the Tiny-Lev setup's reliable functionality in accurately trapping objects within the acoustic force field along an approximate single axis, thereby confirming its suitability for further experimentation and comparison later with the analytical model of Chapter 2.

The spherical objects utilized in the levitation experiments conducted in the Tiny-Lev, consist of Expanded Polystyrene (EPS). These EPS beads were procured in bulk, each possessing unique radius, r_p , and mass characteristics, m_p . The radius of these objects fell within the range of 0.75 mm to 2.4 mm. The mass of objects was precisely measured using a Kern ABJ 120-4NM analytical balance, Fig. 3.7a, provided in the Lab with a resolution of 0.0001g. The measurements of mass and radius were used to calculate the density of the object, ρ_p :

$$\rho_p = \frac{m_p}{V_p} \quad (3.5)$$

In which $V_p = 4/3\pi r_p^3$ is the object volume. The object density was determined by measuring 10 distinct objects, each with varying mass and radius. A statistical box plot (Fig. 3.7b) was generated to visualize the statistical properties of the object density. This result shows that with a 95% confidence level, falls within the range of 23 to 29 $\text{kg} \cdot \text{m}^{-3}$.

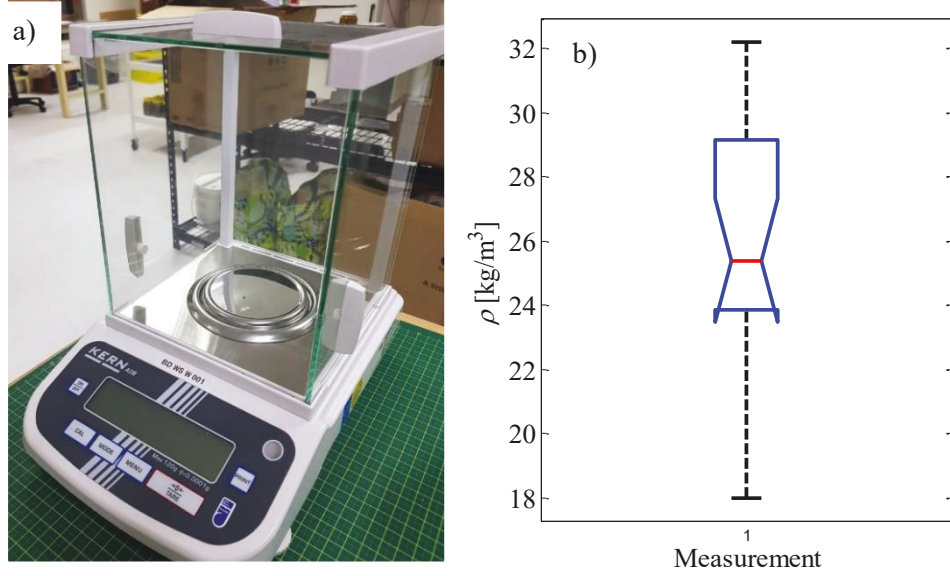


Fig. 3.7. a) The analytical balance device used for object mass measurement, b) statistical box plot illustrating object density.

3.4.2. Experimental set up

In the experiment the Tiny-Lev transducers are driven by a square-wave signal with a peak-to-peak voltage of 9 V from a function generator (Model: MFG-2260MFA), while the excitation signal is also sent to an oscilloscope for monitoring. The Tiny-Lev is mounted vertically on an electrodynamic shaker (Bruel & Kjaer: LDS V201), which is connected to an amplifier (Bruel & Kjaer: LDS LPA100), and driven by a sinusoidal signal of variable amplitude. The vibration of the levitated object was measured using a portable digital Laser Doppler Vibrometer (LDV) (Polytec: PDV-100, 500/4 mm/s/volt sensitivity factor). The output of the LDV and the shaker input signal are monitored with an oscilloscope (Keysight: InfiniiVision DSOX2004a) and recorded at 4 kHz sampling frequency. The LDV was aligned with the acoustic levitator in the vertical direction and the laser beam reached the levitated objects through the 4 mm hole at the centre of the levitator head plate. To minimise off-axis motion, a reusable adhesive putty was used to firmly attach the Tiny-Lev to the shaker (Fig.3.8a), ensuring that the Tiny-Lev remained stationary relative to the shaker during operation. Also, the shaker's stroke length was small at the selected frequencies, preventing significant horizontal motion from influencing the levitation behaviour. Furthermore, the LDV was precisely aligned perpendicular to the Tiny-Lev to provide accurate measurements and minimise any contributions from off-axis motion, also, to reduce the background noise, the experiment was conducted in a hemi-anechoic chamber (Fig. 3.8b).

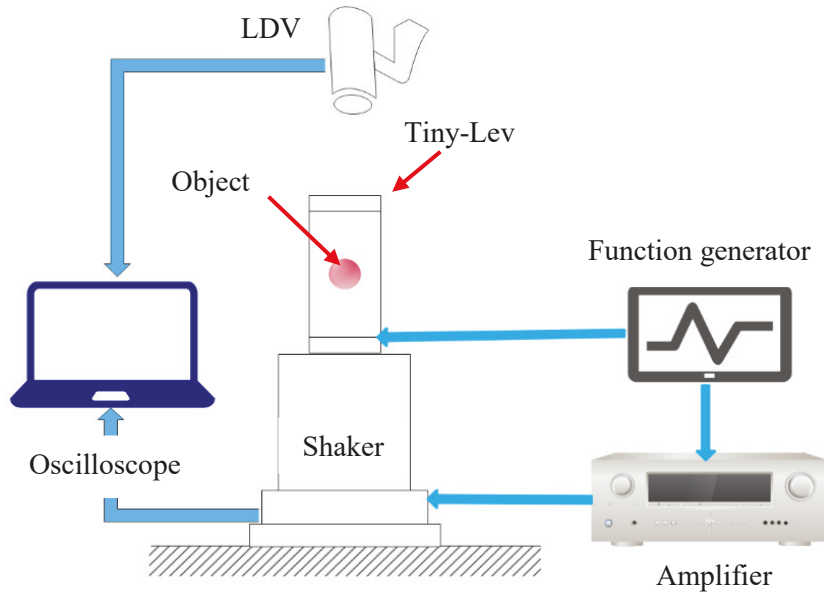
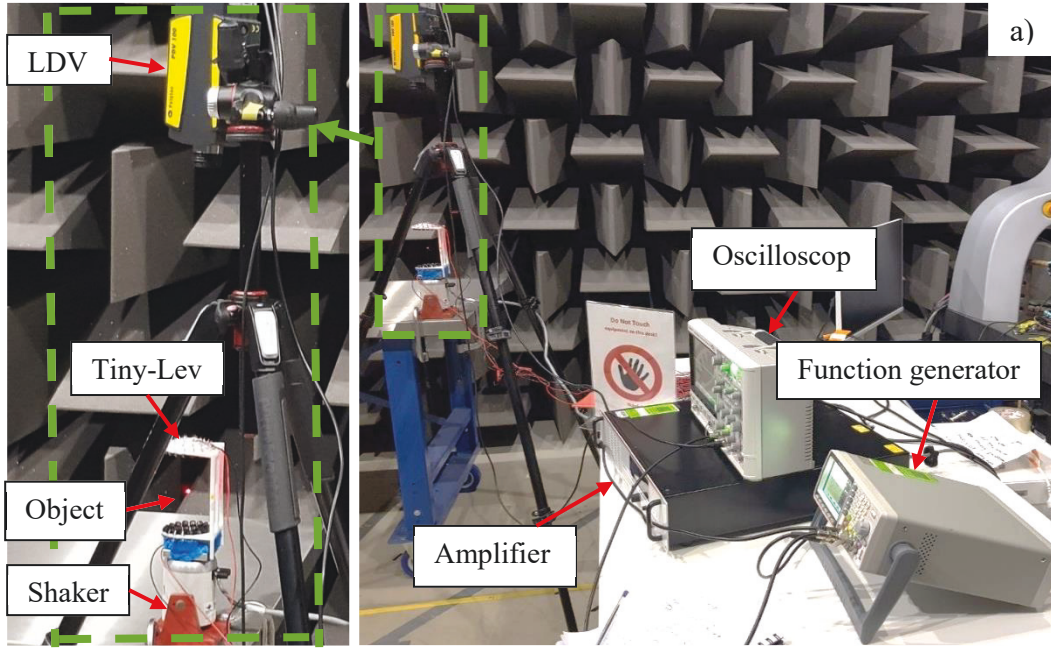


Fig. 3.8. a) Entire Experimental setup located within the hemi-anechoic chamber. b) Schematic representation of the complete experimental setup.

The LDV measures target velocity in the direction of the incident laser beam, and its output is a voltage proportional to this velocity. In the setup, the LDV voltage is converted to the object velocity as the time series data. The object's amplitude of velocity (V_o) can be determined using the voltage (v_o) measured by the LDV as follows

$$V_o = \frac{V_{elo}}{4} \times v_o, \quad (3.6)$$

and by assuming a sinusoidal motion, the object's amplitude of displacement (A_o) can be determined as

$$A_o = V_o/\omega_o. \quad (3.7)$$

Finally, using this experimental setup, the time series data can be extracted to investigate the object's dynamic response and its relationship with the frequency and amplitude of the external excitation applied by the shaker.

3.4.3. Filtering method in experimental time series data

Experimental time series data refers to observations or successive measurements of experimental values collected over time. If the underlying dynamics exhibit nonlinear behaviour, these collected data sets are called nonlinear time series data [194-196]. Unlike linear time series data, which follow a predictable and stable pattern, nonlinear time series data can exhibit complex and irregular patterns with relationships between variables that are nonlinear in nature [194]. Sometimes, the collected time series data is contaminated with noise. The use of filters in this case can be very beneficial. Filters are effective in noise reduction and effectively reduce the influence of unwanted noise in experimental data. Filters increase the quality of measured data by increasing the signal-to-noise ratio and can reduce irregularities and disturbances caused by external factors on the system. However, using filters to reduce noise in data also has some disadvantages. For example, one of these disadvantages is the possibility of losing system information due to selecting a wrong filter, where the filter removes essential system information along with noise. Also, over-filtering can lead to over-smoothing of data, blurring important features and obscuring tiny changes. This understanding helps us to choose the appropriate filter and adjust filter parameters to suit for the data analysis [197-200].

Various techniques have been introduced for noise filtering. Among these techniques we can mention the moving average filter [197], the Wiener filter [198], the Savitzky-Golay filter [189], and the local projection (LP) method [200]. For example, the moving average method is a technique more suitable for linear time series data. This method smooths the noise in the data by averaging the points in neighbouring data sets in a specified window. This technique uses simple averaging method to reduce noise and calculates the average of consecutive data points. It then replaces the original value with this mean, resulting in a smoother data set [197]. In contrast, the LP method is a non-linear approach that is primarily used to denoise non-linear and chaotic signals. It identifies and projects noisy

state vectors onto a local manifold within the reconstructed state space, where clean data reside. By approximating this manifold linearly and performing a Singular Value Decomposition (SVD) of a covariance matrix, noisy data are projected onto the local manifold, preserving essential signal features while minimizing noise [200].

Grassberger et al. proposed a noise reduction method named GHKSS filter which is The GHKSS method is a version of LP method and can be generalized for nonlinear chaotic time series noisy data. Unlike traditional methods such as the extended Kalman filter (EKF), which operates under linear assumptions and linearizes nonlinear systems using Taylor series expansion, GHKSS provides a more robust approach to noise reduction. Instead of relying on a predefined model, GHKSS directly maps the system's patterns to distinguish noise from the actual signal, which makes it particularly effective for handling highly nonlinear systems, short time series, and complex noise types [201]. The GHKSS algorithm nonlinearly filters the data by dynamically representing it on a low-dimensional manifold. It aims to separate the low-dimensional dynamics from the noise and reveal the inherent nonlinear dynamics of the system, whose effectiveness and accuracy in noise reduction have been shown in past research [202]. It identifies a local manifold within the reconstructed state space and utilizes SVD to project noisy state vectors onto it, effectively isolating the underlying signal from noise. In the thesis, GHKSS filter is used to denoise the experimental nonlinear time series data. Implementing the GHKSS filter is facilitated using the Tisean Package provided in the Octave software [203]. Octave is an open-source software package widely used for numerical computing and data analysis, making it accessible to researchers and practitioners in various fields. The experimental setup detailed in section 3.4 allowed us to extract time series data by measuring the velocity of the levitated object by changing the amplitude and frequency of the external excitation. For instance, Fig. 3.9a presents a segment of the time series data derived from LDV measurements for the object's velocity. During this measurement, the object had a radius of $r = 1.87$ [mm], the shaker operated at a frequency of $f_o = \frac{\omega_o}{2\pi} = 32$ Hz, and the acoustic wave frequency was $f = 40$ kHz. Fig. 3.9b shows the time series data after applying the GHKSS filter.

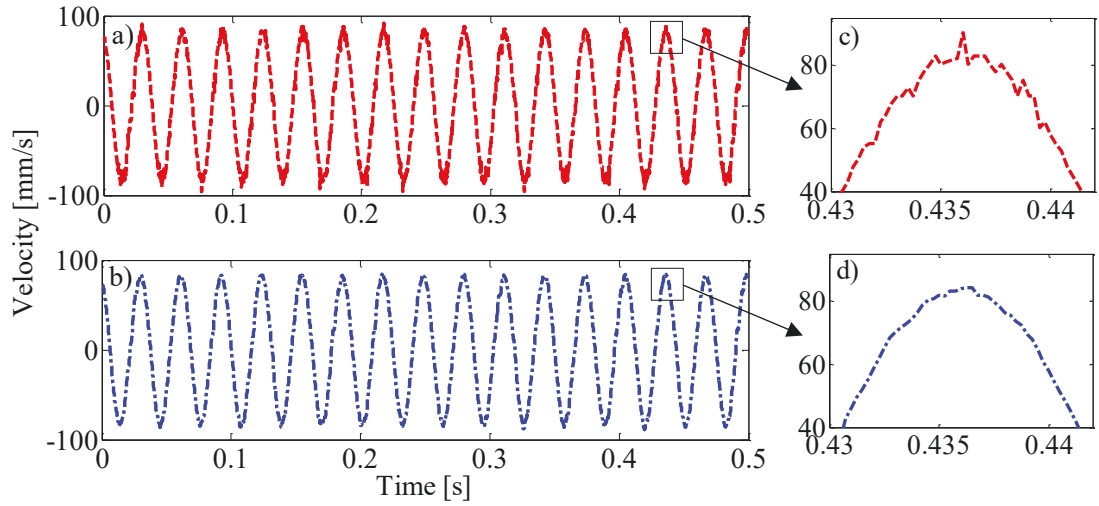


Fig. 3.9. a) A segment of the measured time series data in the experimental work, b) the same time series data after applying the GHKSS filter, and c) zoomed-in area of a peak in the measured time series data, and d) the same peak after applying the GHKSS filter.

Comparing the visual representations provided by Fig. 3.9c and d, it becomes apparent that the application of the GHKSS filter has notably enhanced the signal quality by effectively smoothing out fluctuations and reducing noise interference.

3.4.4. Experimental verification

In Chapter 2, to derive the theoretical formulation for nonlinear equation of motion, it was assumed that the object responds with harmonic oscillation in response to external sinusoidal stimulation around its equilibrium point. In this response, the small acoustically levitated object aligns its amplitude and frequency according to the external excitation. In this Chapter, an experimental study is conducted to verify this theoretical assumption. Throughout this study, the external excitation frequency is systematically varied from 10 Hz to 100 Hz. This experimental investigation aims to confirm whether the levitated object exhibits the expected response to varying frequencies of external excitation, thereby verifying the assumptions made in the theoretical model. To implement this verification, A small acoustically levitated object was used with radius of $r = 0.71$ mm and mass density of $\rho_p = 25$ kg/m³ (according to Fig. 3.7b) and the amplitude of the external excitation was set to 200 mV (peak-to-peak) and incrementally increase it until it reaches its maximum. The maximum point is determined either by reaching the amplifier's cut-off threshold or by the levitated object dropping due to excessively transmitted vibration. At each frequency, the object response was monitored

using the oscilloscope, and the object's response frequency (dominant frequencies) was measured by applying Fast Fourier Transform (FFT) to the LDV's output voltage. The harmonic response shown in Fig. 3.10a illustrates the relationship between the input frequency and the output frequencies. Fig. 3.10b, 3.10c, and 3.10d show the power spectral density (PSD) of the object's response at the points indicated by arrows in Fig. 3.10a, highlighting the magnitude of various frequency components. The red line indicates the threshold for identifying the dominant frequencies.

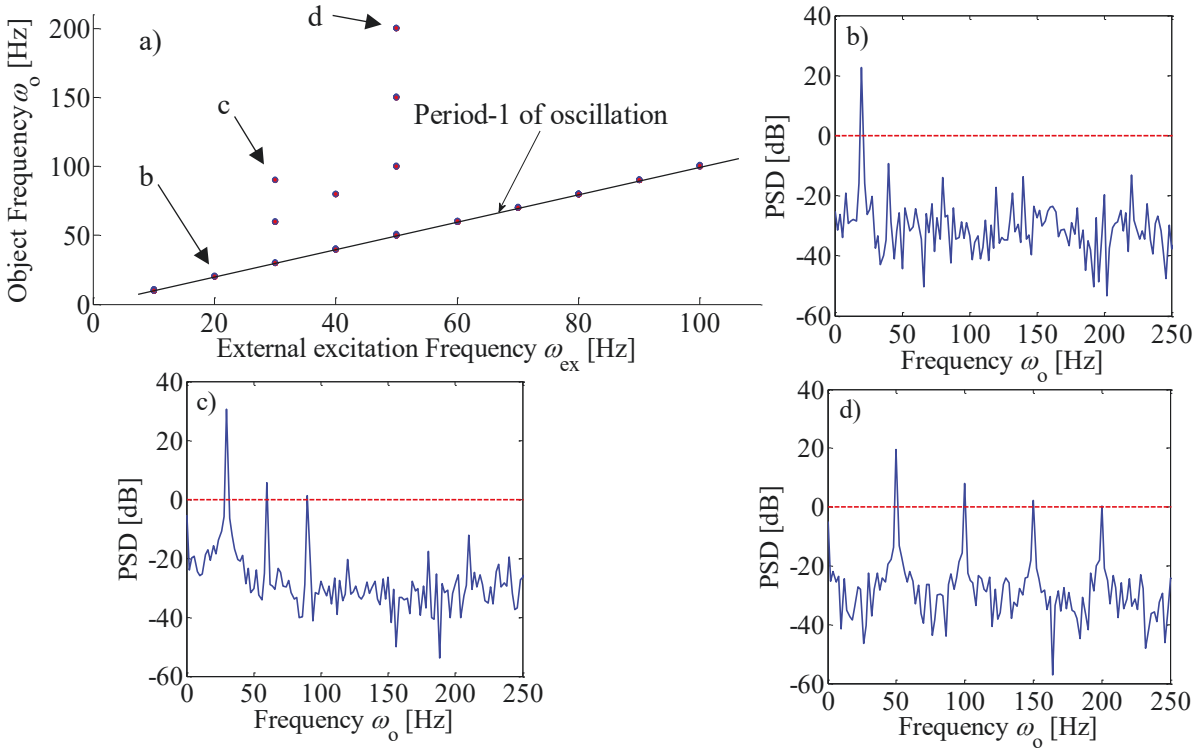


Fig. 3.10. Linear relationship in period-1 of oscillation and more frequencies, which could relate to bifurcation phenomena in some frequencies. b-d) PSD of the object's response at points marked by arrows in, with the red line indicating the threshold for identifying dominant frequencies.

Fig. 3.10 was obtained through experimental measurements of the object's response to external excitation frequencies using the setup described in section 3.4.3. For period-1 oscillations, the object response frequency behaves linearly to the external excitation frequency. As the external excitation amplitude was increased, bifurcation-like behaviours occurred at certain frequencies, as indicated by the presence of more than one dot at specific frequency points in Fig. 3.10. Chapter 4 elaborates on how the frequency domain data supports the system's nonlinear dynamics and validates the experimental

observations discussed here. For examples of the frequency components and their magnitudes, including PSD studies, readers are referred to Chapter 4. The difference in frequency of ω and phase of φ between the external excitation and the object response can be defined by

$$\text{Difference (\%)} = \left| \frac{(\varphi \text{ or } \omega)_{\text{ex}} - (\varphi \text{ or } \omega)_o}{(\varphi \text{ or } \omega)_{\text{ex}}} \right| \times 100. \quad (3.8)$$

This difference in frequency and phase of oscillations between the external excitation and the object's response and the system linear behaviour are plotted in Fig. 3.11 a, b using 20 measurements at each frequency ranging between 10 till 100 Hz each.

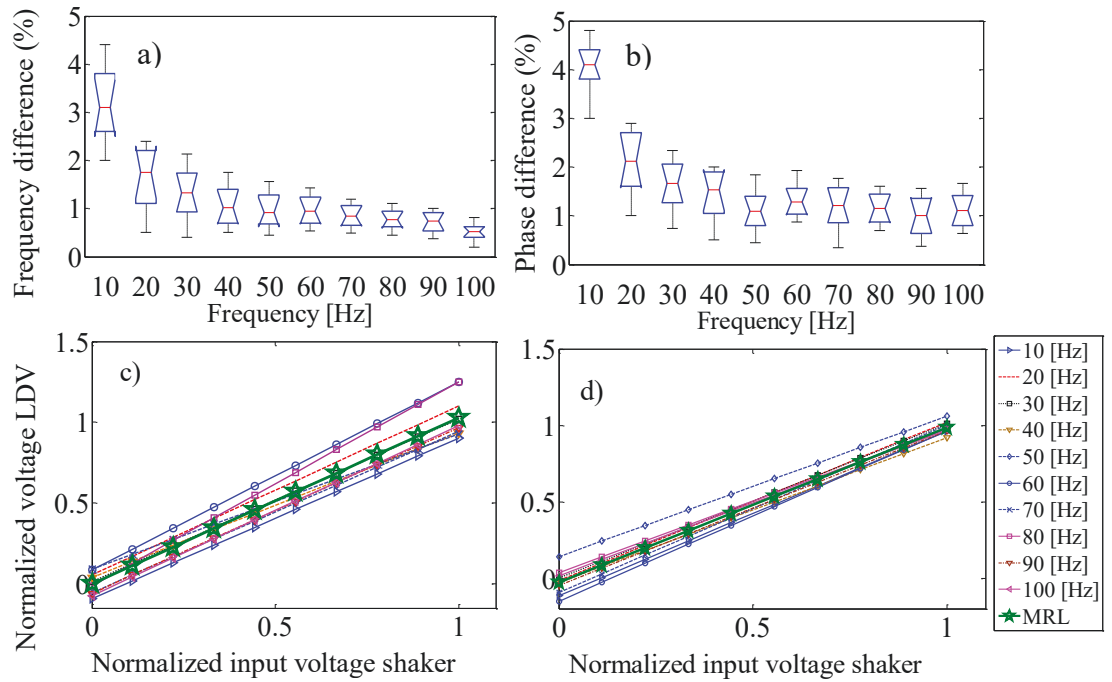


Fig. 3.11. Statistical analysis of a) frequency and b) phase difference, between external excitation and object response at various external excitation frequencies ($n = 20$ measurements). The notches indicate that phase and frequency differences are not significantly different anymore for frequencies greater than 20 Hz, and c) linear relationship between shaker input voltage and measured LDV signal on Tiny-Lev vibrations, and d) on object response employing excitation frequencies ranging from 10 Hz to 100 Hz.

The frequency and phase differences (Eq. 3.8) are both less than 5% (Fig. 3.11 a, b). This observation supports the theoretical model assumption, indicating that when the levitated object is subjected to a sinusoidal external excitation, $Z_{\text{ex}}(t) = A_{\text{ex}} \sin(\omega_{\text{ex}} t)$, the object aligns its amplitude and frequency with the external excitation by oscillating about its

equilibrium point in an harmonic motion $Z_o(t) = A_o \sin(\omega_o t)$. Then, the relation between the input voltage to the shaker amplifier and the resulting amplitude of the shaker's vibrations was explored. To achieve this, the amplifier gain was varied while maintaining a consistent output voltage from the function generator at a certain frequency. Simultaneously, the input voltage supplied to the shaker was measured, and the shaker vibration amplitude was recorded using the LDV. When plotting the input voltage to the shaker against the LDV-recorded voltage for Tiny-Lev vibration, a consistent linear relationship across frequencies was observed from 10 Hz to 100 Hz. Fig. 3.11c, d visually illustrates a linear response of Tiny-Lev vibrations against the shaker vibrations using max-normalized voltage levels (while the non-normalized figures can be found in Figs. 3.12, 13). MRL represents the Mean Regression Line which uses the average slope and intercept parameters, and which illustrates a typical relationship between independent and dependent variables observed across various datasets or observations. For Fig. 3.11c, the confidence intervals for the slopes of the regression lines fall within the interval of $[0.942, 1.114]$, indicating a 95% confidence level in the true slope lying within this interval. Correspondingly, the confidence interval for the intercepts falls within the interval of $[-0.048, 0.048]$, with a 95% confidence level in the true intercept being within this range indicating strong correlation between external excitation and vibration response. Next, the spherical ESP object was levitated within the Tiny-Lev. The object's oscillation corresponding to the shaker's input voltage was measured via LDV. Similarly, for Fig. 3.11d, the confidence intervals for the slopes of the regression lines fall within the interval of $[0.961, 1.061]$, and the confidence interval for the intercepts fall within the interval of $[-0.086, 0.033]$. Fig. 3.12 shows the non-normalized correlation between input voltage into the shaker and LDV voltage.

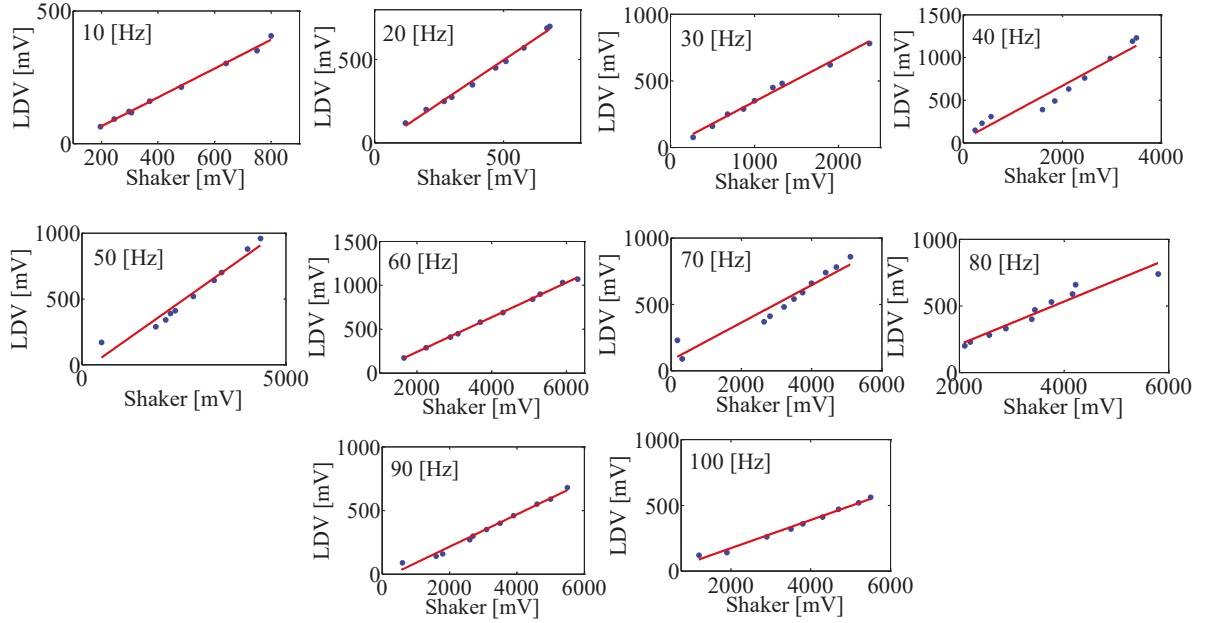


Fig. 3.12. Linear relationship between shaker input and LDV voltage for Tiny-Lev vibrations (10–100 Hz) with irregular x-axis intervals from manual adjustments.

Fig. 3.13 illustrates the non-normalized correlation between the object's oscillations corresponding to the shaker's input voltage via LDV.

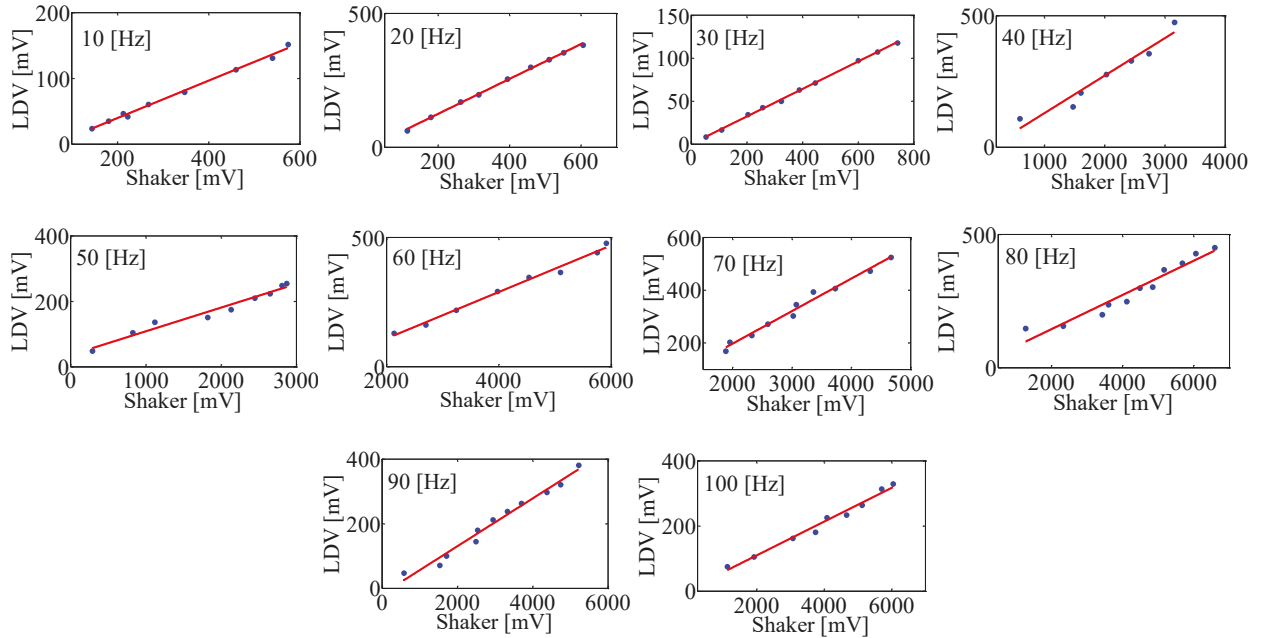


Fig. 3.13. Linear relationship between shaker input and LDV voltage for object vibrations (10–100 Hz) with irregular x-axis intervals due to manual adjustments.

Comparing Figs. 3.13 and 3.14 and considering the linear relation between shaker input voltage and LDV-measured voltage, it can be concluded that, at a specific frequency and

when the output voltage is measured on the Tiny-Lev, the oscillation's amplitude is higher than that measured on the object. In simple words, the external excitation amplitude has a linear relation with the object amplitude and consistently surpasses the object's amplitude. Given that the object radius in the experiment is 0.71 mm and it is positioned near a pressure node, oscillating around its equilibrium with an amplitude much smaller than $\lambda/4 = 2.13$ mm, the ratio of the object position to its radius is equal to or smaller than 3. Referring to Fig. 2.13 Chapter 2, which predicts linear behaviour for small non-dimensional values of object position (z/r), the observed linearity is expected. Thus, this anticipated linearity reflects the behaviour of a nonlinear spring at low displacements, resembling that of a linear spring. Also, the observed quasi-linear behaviour is reasonable for the behaviour of a nonlinear spring at low displacements.

In this section, after introducing the experimental setup and characterizing the Tiny-Lev device, we are ready to extract the experimental time series data which is required for further analysis. The next step consists of plotting and comparing the bifurcation diagrams with the help of theoretical formulation and experimental time series data. The purpose of this work is to investigate the deviation between theoretical predictions and real-world observations which help us to improve our understanding about system's behaviour.

3.4.5. Experimental bifurcation diagram

Experimental bifurcation diagrams are valuable tools for understanding and classifying the behaviour of real-world systems. With their help, the response to changes in system parameters can be observed and used as a basis for validating theoretical models and hypotheses [160-162]. This validation process is crucial, as it helps researchers to refine their understanding of complex nonlinear phenomena.

Unlike theoretical bifurcation diagrams, which are often derived from mathematical models (here, Eq. (2.35)), experimental bifurcation diagrams are constructed from experimental data obtained through experiments and observations (here, section 3.4). The unique value of experimental bifurcation diagrams lies in their ability to provide insights into the underlying dynamics of complex systems, particularly those exhibiting nonlinear behaviour. By systematically varying a control parameter (here the amplitude of the external excitation) and observing the resulting behaviour of the system (here the levitated object's response), experimental bifurcation diagrams can reveal important information such as the presence of bifurcation points, the stability of different dynamical regimes,

and the emergence of complex phenomena such as chaos. In this section with the help of the theoretical formulation and experimental time series data, the bifurcation diagram is plotted, and then the deviation between the theory and the real-world is investigated. In the experiment, The LDV measures the levitated object response (velocity of a suspended polystyrene bead, Fig. 3.14a) through a hole drilled in the centre of the upper transducer array (Fig. 3.14b), which enables the measurement beam to reach the suspended polystyrene bead (Fig. 3.14c).

By changing the amplitude of the external excitation generated by the shaker as the input parameter, the measured velocity of the levitated object within the field can be saved as time series data and used to plot corresponding bifurcation diagram experimentally. Here, the focus was solely on the increasing amplitude scenario. As the amplitude of the external excitation rises, the system either hits the amplifier's cut-off threshold or the levitated object drops due to excessive vibration. Once the object drops, stability cannot be maintained, and the system resets to its initial state, making a controlled sweep down from higher amplitudes impossible to realise.

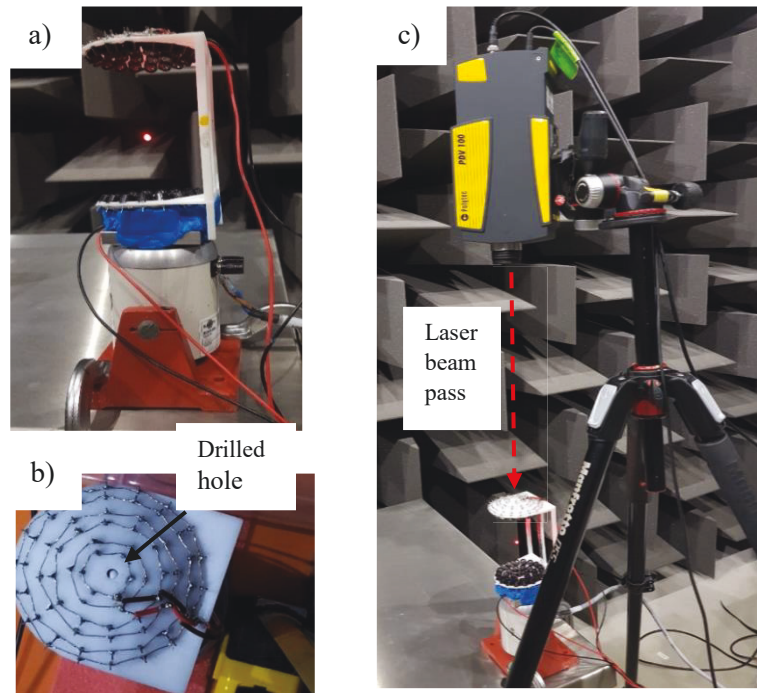


Fig. 3.14. a) Levitated object in the Tiny-Lev on a vibrating shaker, with a red hue from LDV laser illumination; b) drilled hole in the Tiny-Lev's top plate showing the object; c) laser beam path through the hole.

To plot the theoretical bifurcation diagram, specific parameters related to the object and medium properties were selected as: $f_0 = \frac{\omega_0}{2\pi} = 32$ Hz, $f = 40$ kHz, $\rho_0 = 1.19 \frac{\text{kg}}{\text{m}^3}$, $\rho_1 = 25 \frac{\text{kg}}{\text{m}^3}$, $c_0 = 334 \frac{\text{m}}{\text{s}}$, $c_1 = 540 \frac{\text{m}}{\text{s}}$, $C_d = 1.06$ [61,115]. The velocity of the levitated spherical object, measured by LDV and displayed on the oscilloscope as an output voltage, is used as the time series data. The measured signals are denoised using the GHKSS filter. Then, the object displacement is calculated to generate the bifurcation diagram, which is plotted against the amplitude of external excitation provided by the shaker. Additionally, the bifurcation diagram is plotted by solving the theoretical nonlinear equation of motion for comparison purposes, considering two different spherical object radii.

- a) Acoustically small spherical objects ($r = 0.71$ mm):** Fig. 3.15 displays the bifurcation diagram for an acoustically small object ($kr < 1$) at $kr = 0.55$, derived analytically from Eq. 2.35 (solid line), alongside experimental data (dots) extracted using discussed experimental setup in section 3.2. This figure uses the original equation without utilizing the Taylor series approximation.

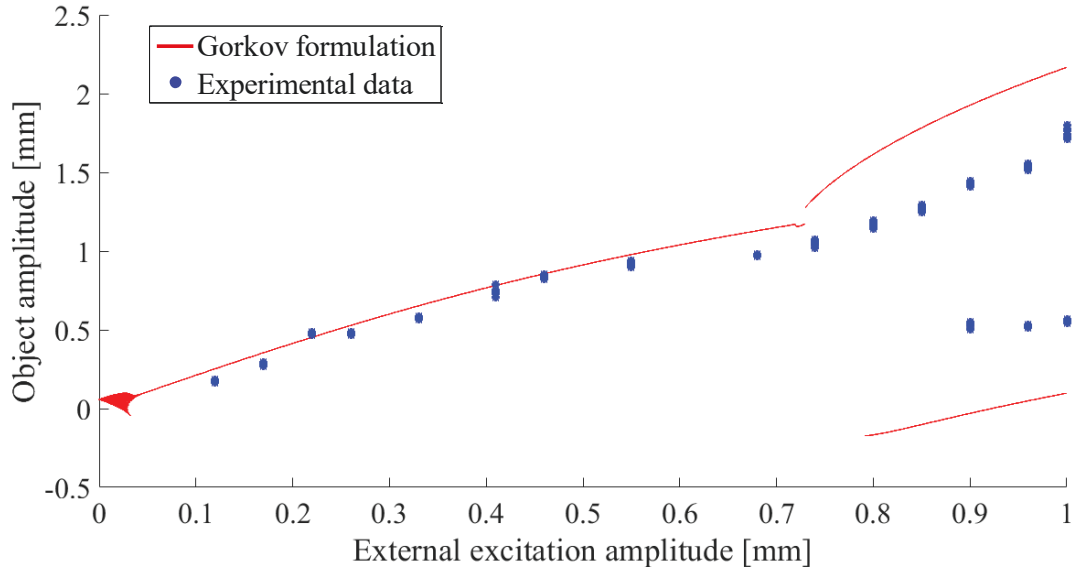


Fig. 3.15. The bifurcation diagram for an acoustically small object ($kr < 1$) derived analytically from Eq. (2.35) (solid line), and experimental data (dots).

Both Fig. 3.10 and Fig. 3.15 depict bifurcation phenomena, but they approach it from distinct perspectives. Fig. 3.10 demonstrates how bifurcation begins to emerge in the frequency domain as the external excitation frequency increases. It focuses on the linear relationship between the excitation and response frequencies

during period-1 oscillations. The appearance of multiple frequencies in the object's response at certain excitation points suggests the onset of bifurcation-like behaviour. On the other hand, Fig. 3.15 presents a bifurcation diagram explicitly mapping the object's amplitude response as a function of the external excitation amplitude. It provides a detailed comparison of analytical predictions and experimental results for an acoustically small object. This figure highlights the amplitude-based bifurcation behaviour, showing how the object's response transitions from stable, periodic motion to more complex regimes as the excitation amplitude increases. Therefore, while both figures illustrate bifurcation, Fig. 3.10 focuses on frequency-based bifurcation, whereas Fig. 3.15 captures amplitude-based bifurcation. Together, they provide a comprehensive view of the system's nonlinear behaviour. Fig. 3.15 shows that the theoretical model closely aligns with the experimental data, demonstrating good agreement. However, as the external excitation amplitude increases, deviations between theory and experiment become apparent. This discrepancy is expected, given the assumption in Chapter 2, Section 2.7, where it was stated that $\gamma_2 A_{\text{in}}$ should be less than 1, with γ_2 representing a coefficient equal to double the wave number. Moreover, examining the frequency response in Section 3.3, it can be found that for $A_{\text{in}} = 0.15$ mm, there is a strong correspondence between the theoretical model and experimental data presented in [118]. This alignment further validates the theory, particularly for small external excitation amplitudes. However, the bifurcation diagram reveals that deviations begin to occur at around 0.6 mm for the/an object with $r = 0.71$ mm, equivalent to $\lambda/14$. These deviations indicate the limitations of the theoretical framework beyond specific excitation amplitudes and should be the subject of further investigation in the future.

- b) Acoustically large spherical objects ($r = 1.87$ mm):** Fig. 3.16 presents the bifurcation diagram for an acoustically large object ($kr > 1$) at $kr = 1.38$, derived from equation 2.35, alongside experimental data extracted using discussed experimental setup in section 3.2. In Fig. 3.16 depicts the original equation without utilizing the Taylor series approximation.

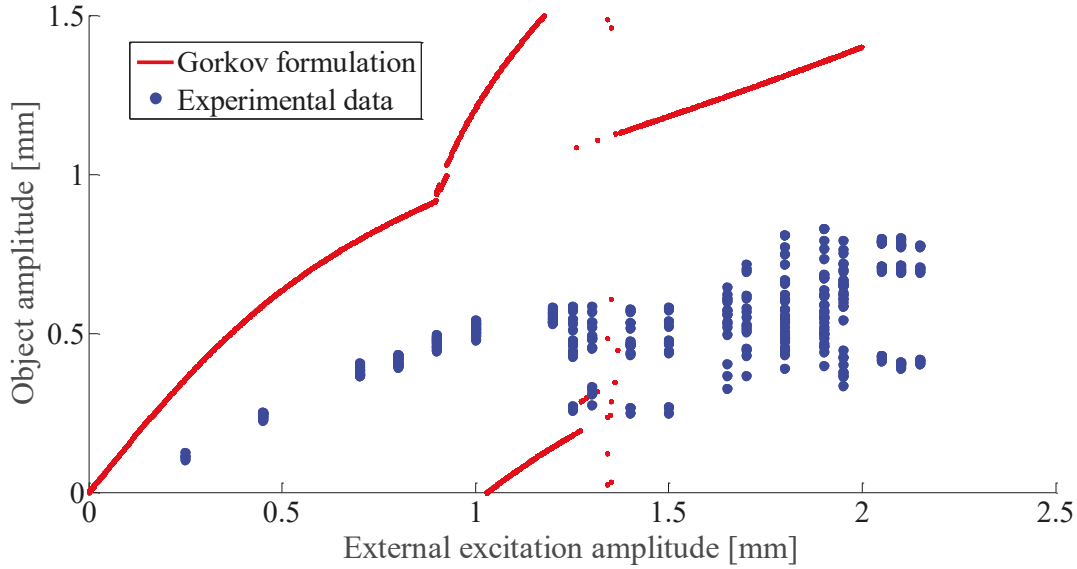


Fig. 3.16. The bifurcation diagram for an acoustically large object ($kr > 1$) derived analytically from Eq. (2.35) (solid line), and experimental data (dots). It should be noted that the Gorkov model, which is derived for acoustically small particles, doesn't match the experimental results for large particles. The discrepancy arises because the Gorkov formulation assumes small particle sizes relative to the wavelength, while larger particles exhibit more complex behaviour that this model cannot accurately capture.

The bifurcation diagram in Fig. 3.16 illustrates the global dynamic behaviour of the system across varying external excitation amplitudes, derived from a theoretical model presented in Chapter 2 for acoustically large objects and real-world observations obtained through experimental work. In contrast, methods such as the Sparse Identification of Nonlinear Dynamics (SINDy), discussed in the next Chapter, focus on identifying governing equations tailored to specific conditions, and excel in capturing system dynamics and explores data-driven techniques for analysing the system behaviour.

3.5. Conclusion

Changing the external excitation is an indirect way of controlling a levitated object through external excitation of the object held within an acoustic radiation force field has never been attempted before. By changing the viewpoint from the acoustic radiation force field to the dynamical behaviour of a levitated object, the changes in the object's behaviour with respect to the amplitude of external excitation and varying object size

were examined and questioned. To investigate the dynamics of the system, it is necessary to solve its equation of motion. The governing equation of motion, as presented in Eq. (2.35), was solved using the fourth order of Rang-Kutta method. This theoretical formulation is based on the Gorkov formulation, which is applicable to acoustically small objects (and theoretically for spherical objects). For implementing numerical solution method, we should choose an appropriate time step. A statistical method based on the box plot diagram was used to select the appropriate time step. The sensitivity analysis of the system was investigated by calculating the Sobol indices for different parameters of the coefficient in nonlinear governing equation of motion (Eq. 2.35). The sensitivity analysis showed the significant effect of frequency and amplitude of external stimulation on the dynamic behaviour of the system. The frequency response curve obtained using the theoretical model based on the Gorkov formulation at low external amplitudes of excitation shows good agreement with experimental results reported in [118]. This confirms the validity of the theory for acoustically small objects, especially under low external excitation. In bifurcation diagrams obtained from theoretical formulation for small object, both periodic and non-periodic behaviours were observed, shedding light on the intricate nature of the system's response.

Our theoretical study in Chapter 2 assumes that the object exhibits a harmonic response under the influence of external sinusoidal excitation. In Chapter 3, this assumption was experimentally verified by applying external excitation to the ultrasonic standing wave generator. The experiments demonstrated that the disturbance vibration frequency and amplitude are effectively transmitted to the object. Furthermore, the experimental results confirm a linear relationship between the object's response and the amplitude and frequency of the external excitation, validating the theoretical predictions presented earlier. In this experimental study, the GHKSS filter was employed to enhance the quality of the extracted time series data by reducing noise, thereby improving the accuracy and reliability of the analysis and results. While the theoretical and experimental bifurcation diagrams align closely for a small acoustically levitated spherical object and low external vibration amplitudes, a significant discrepancy emerges when considering large acoustically levitated spherical objects. This disparity suggests a fundamentally distinct dynamic regime for a large spherical object, diverging markedly from theoretical predictions in Eq. (2.35). This means that theory predicting a Duffing-like equation needs to be revised to describe the behaviour of acoustically large objects accurately. While the

Duffing-like model may be suitable for small objects, its limitations become apparent when applied to larger objects, necessitating alternative approaches for accurate prediction and analysis. In the subsequent Chapter, nonlinear time series analysis techniques, such as the SINDy algorithm, recurrence plots, and network analysis, will be employed to analyse further and comprehensively characterize the nonlinear behaviour, paving the way for more accurate and efficient manipulation of objects in the future.

CHAPTER 4: DATA-DRIVEN MODELLING FOR LARGE OBJECT MOTION

4.1. Introduction

One of the challenges in analysing complex systems is dealing with a large amount of data and information. Today, with the advancement of technology and the emergence of computers and high-speed processors that are available to everyone, the analysis of such systems has become much easier than in the past. Moreover, the need to analyse complex systems with large amounts of data from real-world experiments has led to the popularity of methods based on nonlinear time series analysis (NTSA) in recent years [204-208] and have found various applications to fields from physics and engineering, biology and finance [204-211]. NTSA is a powerful approach to studying complex dynamical systems where traditional linear methods are not usable [212-216]. Unlike linear time series analysis, which assumes a linear relationship between variables, NTSA acknowledges and explores the inherent nonlinearities present in the data. NTSA techniques, such as phase space reconstruction, recurrence plots (RPs), and recurrence networks (RNs) are powerful tools to uncover hidden patterns, identify underlying dynamics, and predict future states of nonlinear systems in physics, engineering, biology, finance, and climate science [217-222].

Also, with advancements in machine learning techniques and data-driven modelling, we can predict a system's behaviour by analysing a segment of its time series data [223-225]. Data-driven models, a class of computational models, are practical tools that rely on historical data collected throughout a system's or process' lifetime to establish relationships between input, internal, and output variables [226]. These models, which have evolved from earlier statistical models, have overcome limitations posed by strict assumptions about probability distributions. Machine learning, a subfield of artificial intelligence, is closely related to data-driven modelling [227]. It also uses historical data to create models that can make predictions and identify patterns. Sparse Identification of Nonlinear Dynamical Systems (SINDy) is a data-driven method that uses machine learning algorithms to uncover the underlying dynamics of a system directly from observational nonlinear time series data. By systematically analysing the data, SINDy extracts sparse representations of the system's dynamics, enabling the discovery of

governing equations or models without relying on explicit mathematical formulations [228-233].

In this Chapter, the dynamic equation of motion for a spherical object oscillating around its equilibrium point in an acoustic radiation force field is derived. After briefly introducing the method of SINDy, it is used to derive a set of ordinary differential equations from both theoretical and experimental data, including clean and noisy sources. By employing the SINDy method, sets of ordinary differential equations are extracted from both clean and noise-contaminated theoretical data (bottom-up, explicit model) and experiments using the Tiny-Lev device. The robustness of the SINDy algorithm against noisy data is first evaluated, confirming its theoretical robustness under low-noise conditions. For high-noise data, it is recommended to filter experimental data, employing the GHKSS filter detailed in Chapter 3, which significantly reduces noise, enhancing the quality and reliability of the analysis.

Moreover, NTSA, particularly the RP, is utilized in the first step to classify the presented model across periodic and chaotic states at various bifurcation points. The presented model, based on experimental time series data collected through the experimental setup outlined in Chapter 3. In this case, the system's phase space must be reconstructed using its time series data to obtain RPs. The first minimum of the mutual information (MI) and false nearest neighbours (FNN) method is used to reconstruct the phase space using experimental nonlinear time series data [234, 235]. Using the generated adjacency matrix, RNs are formed to search for motifs that classify the dynamics of the system and enable further analysis.

4.2. SINDy algorithm

Several mathematical approaches have been developed in recent years to extract differential equations of motion describing the dynamical behaviour of nonlinear systems from experimental time series data [228-233]. Brunton et al. introduced the SINDy method to extract nonlinear governing equations of motion using time series data, and they showed the SINDy capability by extracting the equations of motion associated with some simple conventional systems such as linear and nonlinear oscillators, Lorentz chaotic system, and the fluid vortex shedding behind an obstacle [228]. They also showed that this method can be extended to systems with an external control signal or stimulation [229]. Moreover, this method has proven effective in recovering chaotic systems even

from noisy data and shows robustness [230]. The basic assumption of SINDy is that identifying a set of sparse terms in the nonlinear model best explains the observed dynamics of the system. This goal is typically done by considering a library function consisting of polynomial terms, trigonometric functions, or other basis functions and using regression techniques to identify the non-zero significant terms.

SINDy assumes that identifying a sparse set of terms in the nonlinear model is enough to best explain observed system dynamics. In the context of SINDy, regression is employed to identify the significant terms in a mathematical model that best explain the observed dynamics of a system, and a technique known as sequential thresholded least squares is utilized to enforce sparsity in the model. An iterative process involves fitting the data to different combinations of functions from the library. Terms with coefficients significantly far from zero are kept, while others are discarded. By systematically removing less significant terms, SINDy efficiently reduces the complexity of the model while still capturing the essential dynamics of the system, resulting in a sparse representation of its behaviour. The SINDy algorithm is based on artificial intelligence. In other words, the goal is to build an algorithm that receives a set of data and outputs of an anonymous system and uses them to predict a model that not only optimally approximates this data set but also predicts the system's future. To introduce the theoretical basis behind the SINDy algorithm [218], consider a general nonlinear dynamical system in the form of

$$\ddot{x} + F(x, \dot{x}) = u(t), \quad (4.1)$$

and it can be represented by a set of first order nonlinear differential equations, using state space vectors:

$$\frac{d}{dt} \vec{x}_n(t_m) = f_n(\vec{x}_n, t_m, u). \quad (4.2)$$

where $\vec{x}_n(t_m)$ is a time history of the state vector, $\frac{d}{dt} \vec{x}_n(t_m)$ is its derivative with respect to the time, and n is the number of the state vector. The key observation is that for most of dynamical systems the functions of f_n consists of only a few terms, making it sparse in the space of linear and nonlinear possible functions.

A time history of state space variables should be collected as a sample collection to learn the system and determine the functions of $f_n(\vec{x}_n)$, the sample data at several times $[t_1, t_2, \dots, t_m]$ are arranged into two matrices as:

$$X(t) = \begin{bmatrix} X_1(t_1) \\ \dots \\ X_n(t_1) \end{bmatrix} = \begin{bmatrix} x_1(t_1) & \dots & x_1(t_m) \\ \vdots & \ddots & \vdots \\ x_n(t_1) & \dots & x_n(t_m) \end{bmatrix}, \frac{d}{dt}X(t) = \begin{bmatrix} \frac{d}{dt}x_1(t_1) & \dots & \frac{d}{dt}x_1(t_m) \\ \vdots & \ddots & \vdots \\ \frac{d}{dt}x_n(t_1) & \dots & \frac{d}{dt}x_n(t_m) \end{bmatrix}. \quad (4.3)$$

Next, a library matrix of potential candidate nonlinear functions, $\Theta(X)$, consisting of estimates of state vectors $X(t)$, and external excitation, $u(X, t)$, should be constructed. Using Symbolic regression which involves the determination of a function that relates input–output data, and it may be viewed as a form of machine learning, the relation between state space vectors can be obtained as:

$$\frac{d}{dt}X(t) = \Theta(X) \times \Xi + \eta \times u(t), \quad (4.4)$$

where Ξ and η are a sparse vector of coefficients and should be determined using sparse regression method, and u represents external excitation or noise in the dynamical system (Fig. 4.1) [228-230]. It should be noted that the SINDy method highly depends on the correct choice of measurement variables, data quality, and the appropriate selection of library functions to approximate the nonlinear governing equation of motion [230,231].

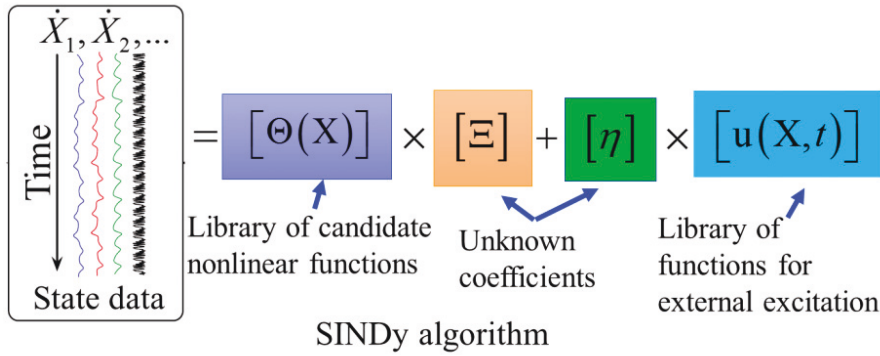


Fig. 4.1. Schematic of SINDy algorithm to identify governing equation from nonlinear time series data including a time history of the states X and derivatives \dot{X} . $[\Xi]$ and $[\eta]$ are unknown coefficients.

In the following sections, SINDy is used to extract nonlinear differential equation of motion presented in Eq. (2.35) in different dynamical regime, using theoretical and experimental data.

4.3. Nonlinear time series analysis techniques – system identification

In this section, from an applied perspective, NTSA is introduced as a tool for studying the dynamic regimes of a large, levitated object.

4.3.1. Phase space reconstruction

Each state of a system can be represented by assigning it to a point in the phase space, and the system's time evolution creates a path [234,235]. Reconstruction of phase space approaches rooted in nonlinear dynamics and has found widespread applications in various fields ranging from physics to biology and finance [236]. To reconstruct the phase space, we need to determine the values of the time delay of τ and the embedding dimension of m . MI, rooted in information theory, and estimates the time delay to reconstruct the phase space of a dynamic system using the time series associated with that system. This technique is based on finding the mutual information function between the time series data and its time-delayed versions related to the system under investigation. Choosing the minimum possible embedding dimension is another step to reconstructing the phase space using the time series data. One of the most widely used and standard methods to reveal the dynamics and dimensions of a system from the observed time series is false nearest neighbours (FNN) method. FNN aims to identify “false neighbours” in the reconstructed state space. False neighbours are points that appear close in the reconstructed phase space but are part of different paths in the original phase space. This helps avoid mistaking points from different trajectories as part of the same trajectory, which can lead to incorrect conclusions about the system's behaviour. The reconstruction of phase space using MI and FNN methods is based on a prominent theorem posed by Takens, which says the time series of one signal of a system contains information about other signals in the system [234,235]. Mathematically, MI measures a statistical dependence between two random variables X and Y , Eq. (4.5), which can be defined by the sum (or integral in the continuous case) over all possible joint and marginal probability distribution function of the variables X and Y

$$MI(X, Y) = \sum_{X, Y} P(X, Y) \log \frac{P(X, Y)}{P(X)P(Y)} \quad (4.5)$$

when $P(X, Y)$ is the joint probability distribution function of the variables X and Y , $P(X)$ and $P(Y)$ are the marginal probability distribution functions of X and Y respectively. To

calculate the time delay parameter τ using the mutual information method, the mutual information function of the signal $S(t)$ with its time delay version $S(t - \tau)$ should be calculated and plotted for different values of τ ; then, the idea is to find an appropriate time delay such that the mutual information between the original signal and its time-delayed version is optimal. This optimal value can be determined by exploring a local first minimum value, an absolute mean for all investigated time delays, or an average of the mutual information function for all explored time delays [224,225]. The FNN method is used to determine the appropriate value of the embedded dimension using the determined time delay, τ , and the time series data related to the system to reconstruct the system's phase space in a way that more accurately describes the system's dynamics. This method measures the neighbourhood distance of points in a time series data $X = \{x_1, x_2, \dots, x_N\}$ with its version in an m -dimensional space $X = \{x_i, x_{i+\tau}, x_{i+2\tau}, \dots, x_{i+(m-1)\tau}\}$ when $i = 1, 2, \dots, N$, in that may appear as neighbours in the reconstructed phase space. Then, this method looks for whether this neighbourhood remains close by increasing the system dimension, m . If the answer is “no”, then the points become “false neighbors”, and it indicates that the embedding dimension should be increased; if the distance did not change significantly, then they are true neighbours and m is the true embedded dimension.

4.3.2. Recurrence plot

Ekman et al. introduced the RP [211]. This method is based on tracking the system's state in the phase space and the system comeback to a neighbourhood within a specific range of its phase space. This neighbourhood is recognized by determining the small value of ε . In most dynamical systems, the phase space has dimensions higher than two or three dimensions and hence cannot be drawn or imagined. However, creating an RP enables us to visualize certain aspects of the phase space path. RP can be mathematically expressed by defining an adjacency matrix as

$$R_{i,j} = H(\varepsilon - \|\vec{x}_i - \vec{x}_j\|), \quad i, j = 1, 2, \dots, N, \quad (4.6)$$

where N is the number of the states in the time series data, \vec{x} is the state space vector, ε is a selected threshold distance, $\|-\|$ is the norm function and H is the Heaviside function. It should be noted that systems usually do not return exactly to their previous state but repeat approximately, so the ε value must always be sufficiently greater than zero, and in this case, selecting an appropriate neighbourhood value is a challenge.

Examining RPs and their patterns is very important. In these patterns, we can see dense points, vertical or diagonal lines, and scattered points. Each of which pattern expresses a specific behaviour in the system being investigated. For example, diagonal lines indicate periodic behaviour, while dense clusters indicate the existence of an attractor. Also, the density of points and their distribution patterns help us to understand the complexity and stability of the system [211-216].

4.3.3. Recurrence networks and motifs

Another method of analysing complex systems is plotting RNs using the system adjacency matrix. In the context of RNs, the adjacency matrix serves as a binary representation indicating the presence (1) or absence (0) of connections between state space pairs. For RNs, nodes depict system states, and edges signify relationships. This network shows the connections between different states in the phase space and plays an essential role in understanding the system. Motifs, recurring subpatterns within networks, are crucial in understanding system organization and functional characteristics. Observing these repeating patterns allows us to gain insight into dynamic processes and underlying structures and behaviours [217-222].

4.4. Results from the application of the SINDy algorithm

In this section, the results of applying the SINDy algorithm and NTSA techniques to investigate the complex dynamics of acoustically levitated objects are presented. First, theoretical time series data is generated using the Gorkov formulation, which is valid for acoustically small objects, and then the study is extended to acoustically large objects.

4.4.1. Application of the SINDy algorithm to time series data based on the noise free theoretical model

To benchmark the SINDy algorithm for the theoretical study described in Eq. (2.35) and by using the Taylor series expansion for $\sin(\theta)$ till order 3, two different case studies are explored. Training data is collected over a time interval of $t = [0 \ 2]$ seconds, with a time step of $dt = 10^{-6}$ seconds. This enables us to construct the state space vector as follows

$$\frac{d}{dt}x_1 = x_2 = \dot{\theta}, \quad (4.7a)$$

$$\frac{d}{dt}x_2 = \ddot{\theta} = -C_1|x_2|x_2 - C_2x_1 + \frac{C_2}{6}x_1^3 + C_3\cos(x_1)A_0\sin(\omega_0 t). \quad (4.7b)$$

The library functions consist of polynomials and trigonometric functions, as

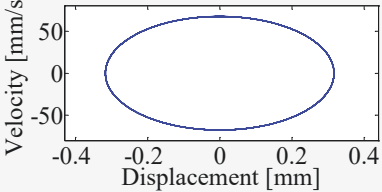
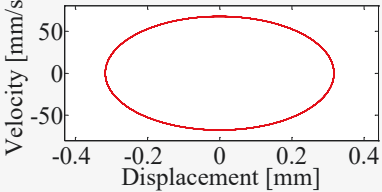
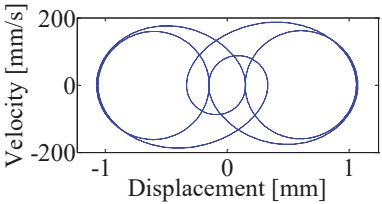
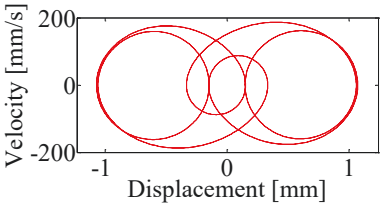
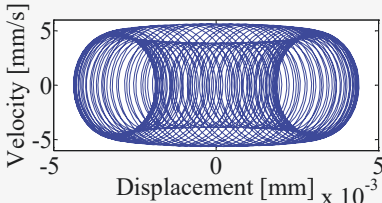
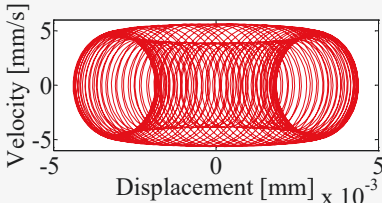
$$\Xi \times \Theta(X) + \eta \times u(t) \quad (4.8)$$

$$= \begin{pmatrix} a_{11} & \dots & a_{1n} \\ \vdots & \ddots & \vdots \\ a_{m1} & \dots & a_{mn} \end{pmatrix} \begin{bmatrix} x_1 \\ x_2 \\ x_1 x_2 \\ \dots \\ x_1^2 \\ x_2^2 \\ \dots \\ x_1^3 \\ \dots \\ x_2^4 \end{bmatrix} + \begin{pmatrix} b_{11} & \dots & b_{1n} \\ \vdots & \ddots & \vdots \\ b_{m1} & \dots & b_{mn} \end{pmatrix} \begin{bmatrix} x_1 \\ x_2 \\ \sin x_1 \\ \sin x_2 \\ \cos x_1 \\ \cos x_2 \end{bmatrix} \sin(\omega_o t)$$

Here the main goal is that finding a_{mn} and b_{mn} coefficients. In the below theoretical case studies, the following parameters were utilized for both the object and medium properties: object radius, $r = 0.71$ mm, sound wave frequency, $f = 40$ kHz, medium density, $\rho_0 = 1.19 \frac{\text{kg}}{\text{m}^3}$, object density, $\rho_1 = 34 \frac{\text{kg}}{\text{m}^3}$, speed of sound in the medium, $c_0 = 340 \frac{\text{m}}{\text{s}}$, speed of sound in the object $c_1 = 570 \frac{\text{m}}{\text{s}}$, and drag coefficient, $C_d = 1.06$.

The study is continued by assuming three theoretical case studies, as presented in Table 4.3: Case 1 with $A_{\text{in}} = 0.15$ mm and $\omega_o = 34$ Hz, Case 2 with $A_{\text{in}} = 0.25$ mm and $\omega_o = 600$ Hz, and case 3 with $A_{\text{in}} = 0.25$ mm and $\omega_o = 600$ Hz. In all three cases, the nonlinear differential equation described in Eq. (4.7) is solved using the fourth-order Runge-Kutta method. The resulting two-dimensional phase space is plotted using displacement versus velocity (Table 4.1).

Table 4.1. Application of the SINDy algorithm to a time series model based on theoretical model taken from Chapter 2: Case studies, their coefficients extracted and phase portraits.

Case	Coff.	Theory	SINDy	Phase space (Theory)	Phase space (SINDy)
1	C_1	0.0149	0.0149		
	C_2	78941	78943		
	C_3	15571	15578		
2	C_1	0.0149	0.0149		
	C_2	78941	78947		
	C_3	98617	98622		
3	C_1	0.0149	0.0149		
	C_2	78941	78947		
	C_3	25952	25958		

The resulting phase portrait, depicted in case1, and 2 illustrates a harmonic oscillation pattern around a stable point. In case 3, the phase space shows a torus structure. In this structure, we see paths in the phase space that show themselves as a torus in the phase space without converging to a fixed point or a simple limit cycle. After comparing the coefficients of the nonlinear equation of motion obtained theoretically with those derived from SINDy, presented in Table 4.1, we observed a maximum difference of 0.04% for Case 1, 0.04%. for case 2, and 0.05%. for case 3.

This study indicates that SINDy is capable of accurately capturing and predicting the dynamics of the system based on the noise free theoretical model. However, before applying SINDy to the time series data extracted from experimental studies, its robustness against theoretical data contaminated with noise is evaluated.

4.4.2. Application of the SINDy algorithm to a time series model based on the noisy theoretical model

To apply SINDy and assess its robustness against noise, Eq. (4.7) is deliberately contaminated with Gaussian noise. All parameters for the object and fluid are similar to

the previous section, and to create Gaussian noise, the “*randn*” function in MATLAB software is used, with a mean value of zero and a standard deviation of σ between 0.05 and 0.5. This Gaussian noise is added to the $\dot{\theta}$ values, which can be obtained by applying the Range-Kuta numerical method to Eq. (4.7), using θ and noisy $\dot{\theta}$ values and then SINDy algorithm is used to reconstruct Eq. (4.7). If we define the phase vector obtained by SINDy algorithm applied to the noisy data by \hat{X} for and the phase vector of Eq. (4.5) by $X = (x_1, x_2)$, the error estimation function for each σ value can be defined by

$$\text{Error}(\sigma) = \|X - \hat{X}\| \quad (4.9)$$

In which $\|-\|$ is the norm function. As the noise increases, the error value is calculated, and Fig. 4.2 is drawn to illustrate the effect.

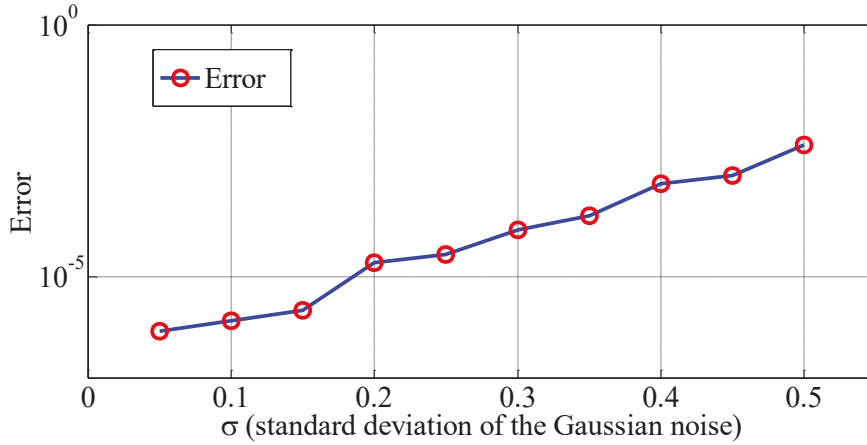


Fig. 4.2. Error estimation values according to Eq. (4.7) evaluating the resilience of the SINDy algorithm to theoretical noisy time series data. Here, σ represents the standard deviation of the Gaussian noise deliberately added to the system.

Fig. 4.2 shows the Error value against the σ value and demonstrates SINDy’s resilience in low noise conditions while by adding the noise value the estimated error will increase exponentially and applying a noise filter is recommended. Another advantage of using a filter is that the noise-free data are always easier to analyse and model. As it discussed in Chapter 3, it is important to note that the selection of the filtering method depends on the noise characteristics and the system under investigation. Here, The GHKSS filter is used to process the noisy experimental data [190-192].

4.4.3. SINDy for acoustically small object: Experimental time series data

In this section, SINDy is used to obtain the nonlinear equation of motion of an object below the wavelength limit levitated in an acoustic radiation force field. For the experimental work, the properties of the object and the medium are similar to those in the previous section, except for the object's radius, $r = 0.75$ mm, and object density, $\rho_1 = 25 \frac{\text{kg}}{\text{m}^3}$.

The measurements were conducted with the experimental setup described in Chapter 3 within the hemi-anechoic room (with a signal-to-noise ratio (SNR) of 50.1 dB at 55 Hz), ensuring that the noise level was low. The initial condition was assumed to be zero, and the frequency ω_{in} produced by the shaker was adjusted to 30 Hz. By adjusting the system to its period-1 oscillation, SINDy was applied to the experimental time series data measured by LDV to reconstruct the nonlinear equation of motion. To implement SINDy [202], the library functions are chosen according to Eq. (4.10). This library consists of polynomial functions with order four plus trigonometric functions as indicated in the following

$$\frac{d}{dt}X(t) = [\Xi] \begin{bmatrix} 1 \\ x_1 \\ x_2 \\ x_1 x_2 \\ \dots \\ x_1 x_2^2 \\ x_2^3 \\ \dots \\ x_2^4 \end{bmatrix} + [\eta] \begin{bmatrix} 1 \\ x_1 \\ x_2 \\ \dots \\ \sin \omega_o t \\ \dots \\ \cos x_2 \end{bmatrix}. \quad (4.10)$$

According to Eq. (4.10), the constructed library has two parts consisting of candidate nonlinear functions related to the coefficients contained in $[\Xi]$ which represent the nonlinear governing equation of motion without external excitation part, and candidate nonlinear functions related to coefficients contained in $[\eta]$ which represent the external excitation. The output time series data is measured by an LDV and correlated to the object's velocity in z -direction (Fig. 3.8, and Eq. (3.6)). To determine the coefficient matrices $[\Xi]$ and $[\eta]$ from the experimental data, A time history of the vector state, $X = [x_1(t), x_2(t)]$, is collected. The data is sampled at several times $[t_1, t_2, \dots, t_m]$ and inserted into SINDy. In this case and after applying the SINDy algorithm, $[\Xi]$ and $[\eta]$ can be obtained as

$$\frac{dX_1(t)}{dt} = \begin{bmatrix} 0 \\ 0 \\ 1 \\ 0 \\ 0 \\ \dots \\ 0 \\ 0 \\ \dots \\ 0 \end{bmatrix}^T \begin{bmatrix} 1 \\ x_1 \\ x_2 \\ x_1 x_2 \\ \dots \\ x_1 x_2^2 \\ x_2^3 \\ \dots \\ x_2^4 \end{bmatrix} \text{ and } \frac{dX_2(t)}{dt} = \begin{bmatrix} 0 \\ -36422 \\ 0 \\ \dots \\ 0 \\ -0.02171 \\ 0 \\ \dots \\ 0 \\ 5070 \\ 0 \\ \dots \\ 16211 \\ 0 \end{bmatrix}^T \begin{bmatrix} 1 \\ x_1 \\ x_2 \\ \dots \\ x_2 x_2 \\ \dots \\ x_1^3 \\ x_1 x_2^2 \\ \dots \\ x_1 \sin(\omega_0 t) \\ \dots \\ \cos(x_1) \sin(\omega_0 t) \\ \cos(x_2) \sin(\omega_0 t) \end{bmatrix}, \quad (4.11)$$

which can be further simplified to a governing equation of motion

$$\frac{d}{dt} X_1(t) = x_2, \quad (4.12a)$$

$$\frac{d}{dt} X_2(t) = -36422x_1 - 0.02171x_2x_2 + 5070x_1^3 + 16211 \cos(x_1) \sin(\omega_0 t). \quad (4.12b)$$

The coefficients in Eq. (4.12) are taken as the average of twelve experimental data sets. For comparison with theory, the average values of the coefficients from the SINDy results are used. A comparison between time series obtained from theory, experimental data, and SINDy can be observed in Fig. 4.3.

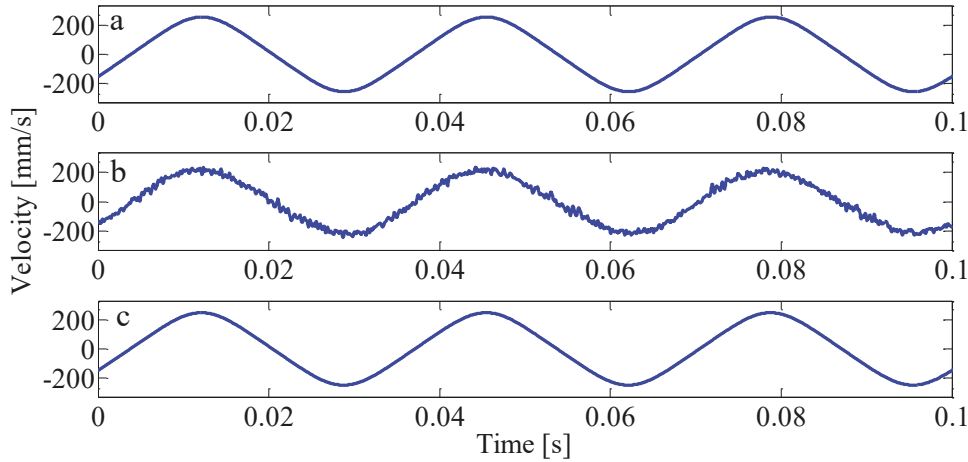


Fig. 4.3. Nonlinear time series data a) the theoretical dynamical equation of motion and the b) measured by the LDV and collected by oscilloscope. This data set and a library of nonlinear functions of the state variables are used to determine the matrix coefficients of $[\Xi]$ and $[\eta]$ and c) sparse identified model.

Results of period-1 dynamics, generated through the equation of motion based on Eq. (4.7), experimental data (see bifurcation diagram, Fig. 3.15), and the sparse identified model (based on Eq. (4.12)) and are displayed in Fig. 4.4 and graphically confirm with phase portraits that SINDy correctly identified the system dynamics.

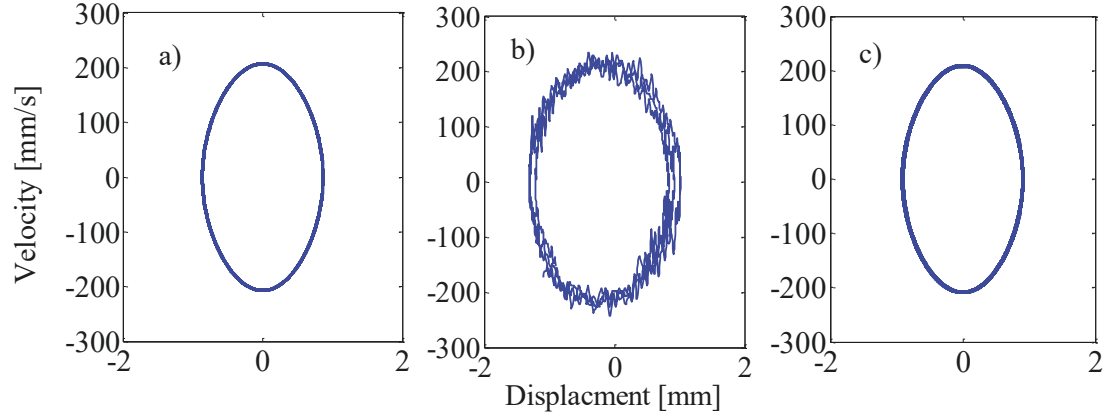


Fig. 4.4. A comparison between a) the theoretical dynamical equation of motion and the b) experimental data which shows the s well-captured by sparse identified system and c) sparse identified model.

It should be noted that, due to the high sensitivity of the experimental setup, several factors, including unavoidable external influences - which can include slight signal offsets, signal distortion, minor electrical current fluctuations, environmental noise, initial conditions, trapping position, airflows, and deformation of the polystyrene bead (e.g., slight squashing by forceps during handling) - can affect the results and may lead to variations in the observed dynamics due to error. It is crucial to carefully minimise these effects to ensure the accuracy and reliability of the experimental outcomes.

4.4.4. SINDy for acoustically large object: Experimental time series data

In this section, the question is that whether the SINDy algorithm can adequately capture the dynamics of large objects using the extracted time series data. In this part, time series data for three different bifurcation points, as indicated in the bifurcation diagram (Fig. 3.16), are used to approximate the nonlinear governing equation of motion. The library in the SINDy algorithm consists of polynomial functions up to the fifth order and trigonometric functions. In the following, three experimental case studies, labelled as Example 1, Example 2, and Example 3, will be discussed. when x is the object displacement from its equilibrium point.

Example 1: $A_{\text{in}} = 0.35$ mm, $\omega_o = 32$ Hz. By applying the SINDy algorithm as discussed in section 4.3., the equation of motion can be obtained as

$$\begin{aligned} \ddot{x} + 60985.4x - 351.109\dot{x} - 667030x^3 + 10283x^2\dot{x} - 8.64x\dot{x}^2 \\ + 0.2903\dot{x}^3 - 1884x^3\dot{x} - 0.4985x^2\dot{x}^2 + 398500x^5 \\ + 60.452x^3\dot{x}^2 - 4.6975x^2\dot{x}^3 - 9255x\sin(\omega t) \\ + 9254\sin(x)\sin(\omega t) = 0 \end{aligned} \quad (4.13)$$

For this Example, four measurements were conducted over time, and SINDy was applied to each set of data. Table 4.4 presents the SINDy-obtained coefficients for reconstructing the equation of motion according to four performed measurements. To derive Eq. (4.13), the average of the coefficients listed in Table 4.2 was used. In this context, x represents the object's displacement from its equilibrium point in mm, and \dot{x} is the object's velocity in mm/s.

Table 4.2. Coefficient predicted by SINDy for example 1 according to four measurements.

Coefficient	Measurements					
	M1	M2	M3	M4	Mean (μ)	Standard deviation (σ)
x	62104	57936	63795	59996	60985	2544.1
\dot{x}	350.84	352.37	350.35	352.86	351.10	1.064
x^2	0	0	-8.6628×10^{-6}	0	0	0
$x\dot{x}$	0	1.1634×10^{-6}	-1.0520×10^{-6}	0	0	0
\dot{x}^2	0	-1.6682×10^{-6}	9.4217×10^{-7}	0	0	0
x^3	-650352	-683701	-663699	-670363	-667030	13884.0
$x^2\dot{x}$	10129.1	10437.2	10235.4	10334.1	10283.2	132.081
$x\dot{x}^2$	-8.57	-8.63	-8.59	-8.76	-8.64	0.0854
\dot{x}^3	0.2904	0.2879	0.2953	0.2875	0.2903	0.0036
x^4	0	0	0	0	0	0
$x^3\dot{x}$	-1885	-1883	-1889	-1875	-1884	5.888
$x^2\dot{x}^2$	-0.5252	-0.4922	-0.4886	-0.4881	-0.4985	0.0179
$x\dot{x}^3$	-0.031	0.0201	-0.0252	0.0332	0	0.0323
\dot{x}^4	-0.0002	0	0.0001	0.0003	0	0
x^5	398500	398450	398530	398520	398500	35.59
$x^4\dot{x}$	0	0	0	0	0	0
$x^3\dot{x}^2$	59.542	61.360	60.153	60.752	60.452	0.781
$x^2\dot{x}^3$	-4.698	-4.750	-4.893	-3.986	-4.697	0.0451
$x\dot{x}^4$	0.0007	-0.0005	0	0	0	0
\dot{x}^5	0	0	-3.5388×10^{-6}	0	0	0
$x\sin(\omega t)$	-9266	-9394	-9264	-9281	-9255	62.30
$\sin(x)\sin(\omega t)$	9251	9336	9447	9240	9254	122.38

Fig. 4.5 compares the measured experimental time series data, the filtered time series data, and the SINDy results obtained using averaged values from Table 4.2.

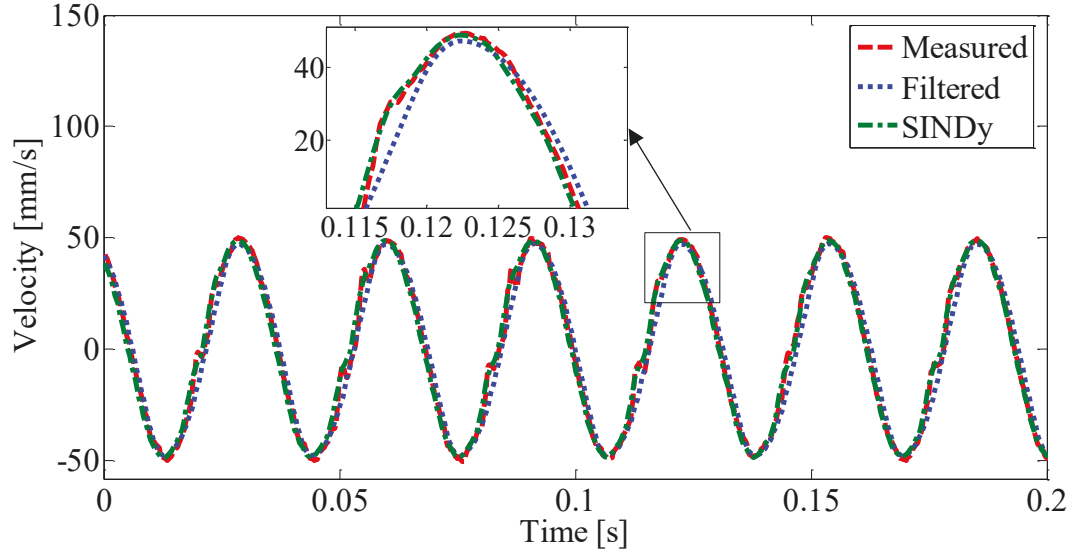


Fig. 4.5. Comparison of experimentally measured data and SINDy predictions using averaged coefficients from Table 4.2 with filtered data for example 1. The plot highlights the accuracy of the SINDy algorithm in predicting the system dynamics.

To generate a formulation using SINDy that not only displays the average of the measured data but also includes uncertainty bounds, the mean value $\pm 2\sigma$ for each coefficient should be used, which covers 95% of the data for a normal distribution. This approach provides a more conservative and comprehensive representation of uncertainty [186-190]. Below, Eq. (4.14) is presented according to this definition

$$\begin{aligned}
 \ddot{x} + (60985.4 \pm 2 \times 2544.1)x - (351.109 \pm 2 \times 1.0641)\dot{x} & \quad (4.14) \\
 - (667030 \pm 2 \times 13884)x^3 + (10283 \pm 2 \times 132.08)x^2\dot{x} \\
 - (8.64 \pm 2 \times 0.0854)x\dot{x}^2 + (0.2903 \pm 2 \times 0.0036)\dot{x}^3 \\
 - (1884 \pm 2 \times 5.888)x^3\dot{x} - (0.4985 \pm 2 \times 0.0179)x^2\dot{x}^2 \\
 + (398500 \pm 2 \times 35.59)x^5 + (60.452 \pm 2 \times 0.781)x^3\dot{x}^2 \\
 - (4.697 \pm 2 \times 0.0451)x^2\dot{x}^3 - (9255 \pm 2 \times 62.30)x\sin(\omega t) \\
 + (9254 \pm 2 \times 122.38)\sin(x)\sin(\omega t) = 0
 \end{aligned}$$

Fig.4.6 shows the power spectral density (PSD) of measured signal by LDV before applying filter, after applying filter and according to the SINDy results in Eq. (4.13).

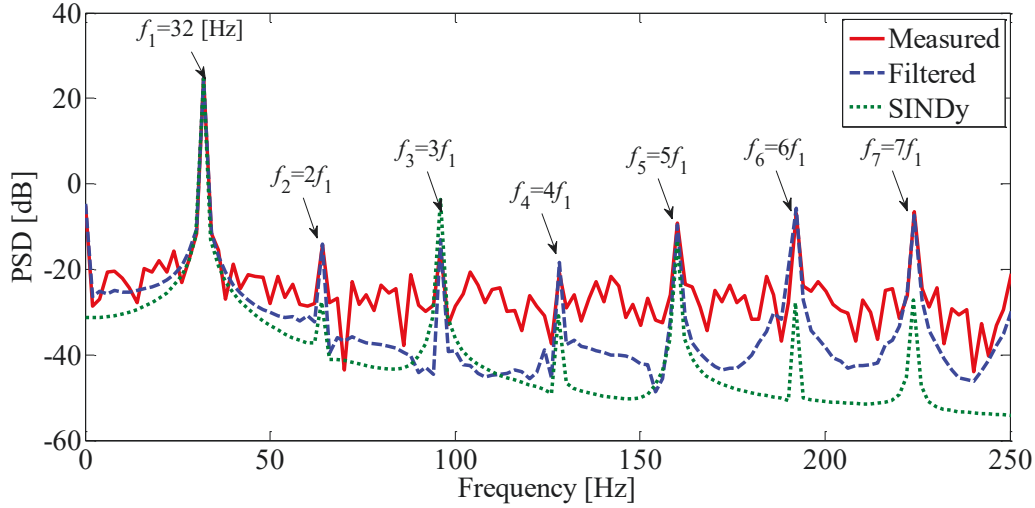


Fig. 4.6. PSD of original signal measured by LDV before applying filter, after applying filter and according to Eq. (4.13) for example 1.

In signal processing and acoustics, harmonics are frequencies that are integer multiples of a fundamental frequency, the fundamental frequency is the lowest frequency of a periodic waveform (here 32 [Hz]). For a system with a fundamental frequency f , the harmonics would be $2f, 3f, 4f$, and so on. When PSD shows multiple peaks at frequencies that are harmonics or subharmonics of the fundamental frequency, it indicates the presence of nonlinearities in the system. In a perfectly linear system, the output signal in response to a sinusoidal input, will have the same frequency as the input, and there should be no harmonics. In the system where harmonic peaks are much weaker than the fundamental peak, this indicates a period-1 which exhibits one primary cycle corresponding to the fundamental frequency. Harmonics do not change the fundamental period of the system but will affect the shape of the trajectory and can cause the phase space plot to appear more complex with potentially distorted loop, but it will still be fundamentally a period-1 system [171-176].

Example 2: $A_{in} = 0.6$ mm, $\omega_o = 32$ Hz. By applying the SINDy algorithm, the equation of motion can be obtained as

$$\begin{aligned} \ddot{x} + 85680x + 1212.1\dot{x} - 358700x^3 + 10548.5x^2\dot{x} - 19.023x\dot{x}^2 \\ + 0.24701\dot{x}^3 - 888.76x^3\dot{x} - 5.2717x^2\dot{x}^2 + 188530x^5 \\ + 170.34x^3\dot{x}^2 - 1.68914x^2\dot{x}^3 - 14646.6x\sin(\omega t) \\ + 14635.6\sin(x)\sin(\omega t) = 0 \end{aligned} \quad (4.15)$$

Similarly, Table 4.3 presents the SINDy-obtained coefficients for reconstructing the equation of motion according to four performed measurements for case 2.

Table 4.3. Coefficient predicted by SINDy for example 2 according to four measurements.

Coefficient	Measurement				Mean (μ)	Standard deviation (σ)
	M1	M2	M3	M 4		
x	84395	86965	86110	85250	85680	1106.4
\dot{x}	1193.8	1206.2	1218.01	1230.02	1212.1	15.55
x^2	0	0	0	0	0	0
$x\dot{x}$	0	0	0	0	0	0
\dot{x}^2	0	0	0	0	0	0
x^3	-353653	-364434	-368022	-350064	-358700	8551
$x^2\dot{x}$	10812.2	10707.7	10285.3	10390.8	10548.5	251.014
$x\dot{x}^2$	-19.1181	-18.7377	-18.9279	-19.3083	-19.023	0.2455
\dot{x}^3	0.2359	0.2581	0.2384	0.2557	0.24701	0.0115
x^4	0	0	0	0	0	0
$x^3\dot{x}$	-848.76	-928.75	-857.65	-919.87	-888.76	41.3717
$x^2\dot{x}^2$	-5.4562	-5.0872	-5.6144	-4.9290	-5.2717	0.3178
$x\dot{x}^3$	-0.000600	0	-0.000511	0.000583	0	0
\dot{x}^4	-8.5502 $\times 10^{-5}$	0	2.0235 $\times 10^{-6}$	0	0	0
x^5	178165	198900	183820	193245	188530	9298.5
$x^4\dot{x}$	0	-8.6628 $\times 10^{-7}$	1.2343 $\times 10^{-6}$	0	0	0
$x^3\dot{x}^2$	174.59	160.97	166.08	179.70	170.34	8.40
$x^2\dot{x}^3$	-1.5793	-1.7989	-1.6300	-1.7483	-1.68914	0.1018
$x\dot{x}^4$	0.0007591	0	1.0278 $\times 10^{-5}$	0.000851	0	0
\dot{x}^5	0	0	0	0	0	0
$x\sin(\omega t)$	-13760.3	-14991.3	-14455.4	-14396.1	-14646.6	1005.0
$\sin(x)\sin(\omega t)$	13977.5	15294.4	14123.6	15148.7	14635.6	590.304

Likewise, Fig. 4.7 presents the experimental measured data without applying the GHKSS filter compared to the SINDy results obtained using averaged values from Table 4.3 and the filtered data obtained from the experimental setup.

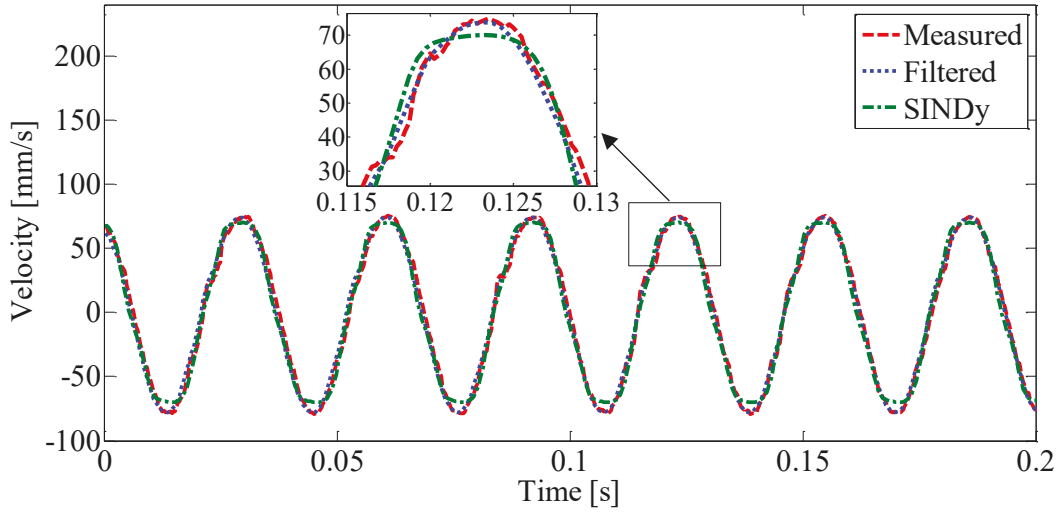


Fig. 4.7. Comparison of experimentally measured data and SINDy predictions using averaged coefficients from Table 4.3 with filtered data for example 2.

Also, Fig. 4.8 shows the PSD of measured signal by LDV before applying filter, after applying filter and according to Eq. (4.15).

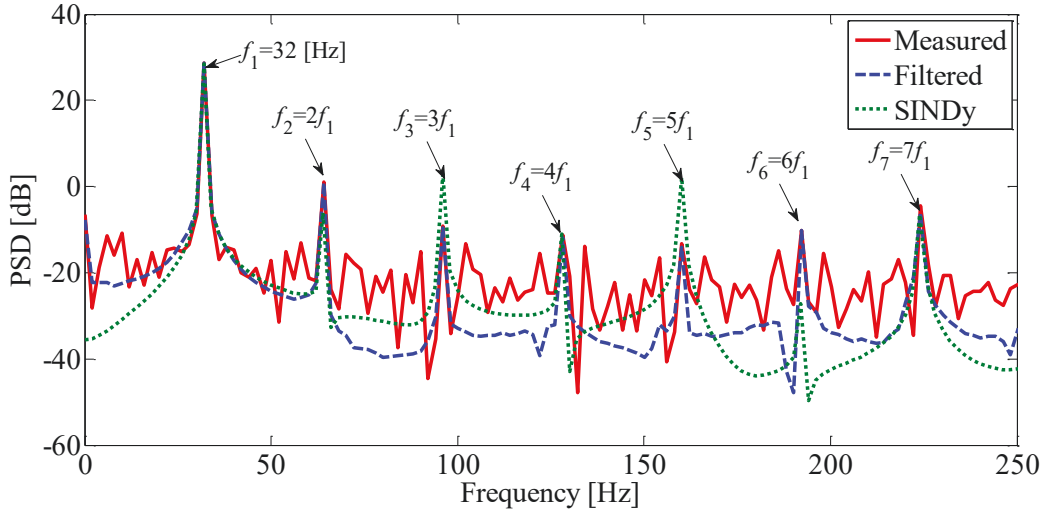


Fig. 4.8. PSD of original signal measured by LDV before applying filter, after applying filter and according to Eq. (4.15) for example 2.

Similarly, to generate a formulation using SINDy that not only displays the average of the measured data but also includes uncertainty bounds, we can use the mean $\pm 2\sigma$. This approach covers 95% of the data for a normal distribution which provide a more comprehensive representation of the uncertainty. The results, including these uncertainty bounds, are presented in Table 4.3.

Example 3: $A_{\text{in}} = 0.7$ mm, $\omega_o = 32$ Hz. By applying the SINDy algorithm, the equation of motion can be obtained as

$$\begin{aligned} \ddot{x} + 98467.2x + 396.204\dot{x} - 565600x^3 + 2566.4x^2\dot{x} - 7.1664x\dot{x}^2 \\ + 0.068832\dot{x}^3 - 438.48x^3\dot{x} - 1.8012x^2\dot{x}^2 + 1452000x^5 \\ + 34.928x^3\dot{x}^2 - 0.40176x^2\dot{x}^3 - 17641x\sin(\omega t) \\ + 17648\sin(x)\sin(\omega t) = 0 \end{aligned} \quad (4.16)$$

Similarly, Table 4.4 presents the SINDy-obtained coefficients.

Table 4.4. Coefficient predicted by SINDy for example 3 according to four measurements.

Coefficient	Measurement				Mean (μ)	Standard deviation (σ)
	M1	M2	M3	M4		
x	96006.7	96991.2	99944.9	98523.7	98467.2	1729.8
\dot{x}	389.206	401.203	390.526	388.056	396.204	6.504
x^2	0	-5.5403×10^{-6}	0	8.3909×10^{-6}	0	0
$x\dot{x}$	0	-1.2438×10^{-6}	2.1488×10^{-6}	-1.0203×10^{-6}	0	0
\dot{x}^2	0	0	0	0	0	0
x^3	-551460	-579740	-557116	-574084	-565600	1346.4
$x^2\dot{x}$	2502.2	2630.6	2630.5	2527.9	2566.4	67.504
$x\dot{x}^2$	-6.9872	-7.3456	-7.2739	-7.0589	-7.1664	0.1706
\dot{x}^3	0.067839	0.066628	0.068853	0.062385	0.068832	0.0028
x^4	0	-1.8831×10^{-7}	0	0	0	0
$x^3\dot{x}$	-445.08	-431.98	-449.41	-427.51	-438.48	10.418
$x^2\dot{x}^2$	-1.80055	-1.86025	-1.77023	-1.81231	-1.8012	0.0378
$x\dot{x}^3$	-0.011449	-0.012851	0.02184	-0.01591	-0.01144	0.0177
\dot{x}^4	-3.3006×10^{-5}	0	0	-8.2019×10^{-6}		0
x^5	1451500	1465200	1431500	1472250	1452000	1794.5
$x^4\dot{x}$	0	0	1.2863×10^{-7}	-1.5388×10^{-7}	0	0
$x^3\dot{x}^2$	34.054	35.805	34.408	35.458	34.928	0.8335
$x^2\dot{x}^3$	-0.40176	-0.40177	-0.40258	-0.40401	-0.40176	0.0011
$x\dot{x}^4$	-7.608×10^{-5}	-6.002×10^{-5}	0	0	0	0
\dot{x}^5	0	0	0	0	0	0
$x\sin(\omega t)$	-17200	-18081	-17376	-17906	-17641	419.73
$\sin(x)\sin(\omega t)$	17320	17576	17669	18217	17648	307.82

In like manner, Fig. 4.9 presents the experimentally measured data in comparison with the SINDy results, and the filtered data obtained from the experimental setup.

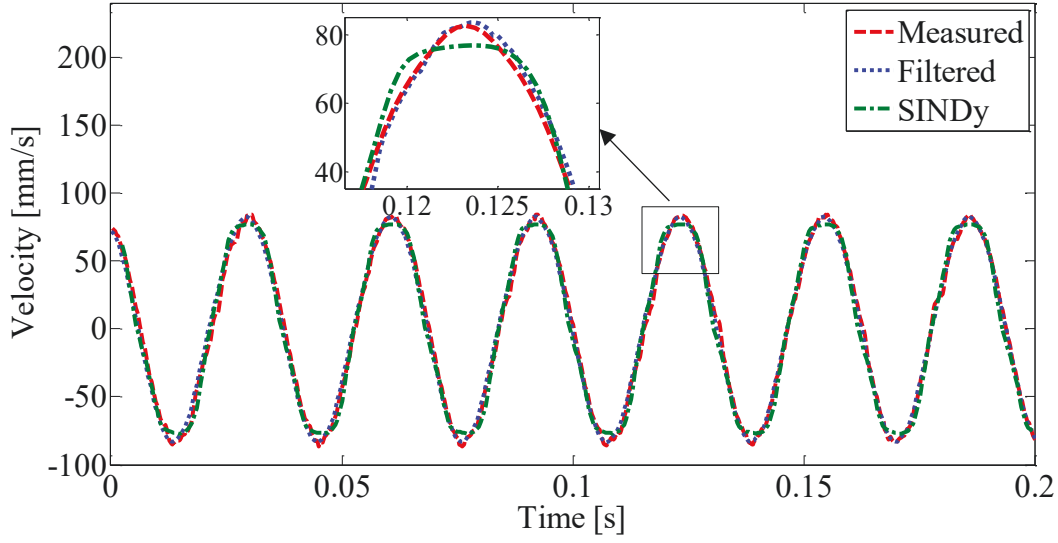


Fig. 4.9. Comparison of experimentally measured data and SINDy predictions using averaged coefficients from Table 4.4 with filtered data for example 3.

Also, Fig.4.10 shows the PSD of original signal measured by LDV before applying filter, after applying filter and according to Eq. (4.16). Similarly, to generate a SINDy-based formulation that includes uncertainty bounds, we can use the mean $\pm 2\sigma$, covering 95% of the data for a normal distribution.

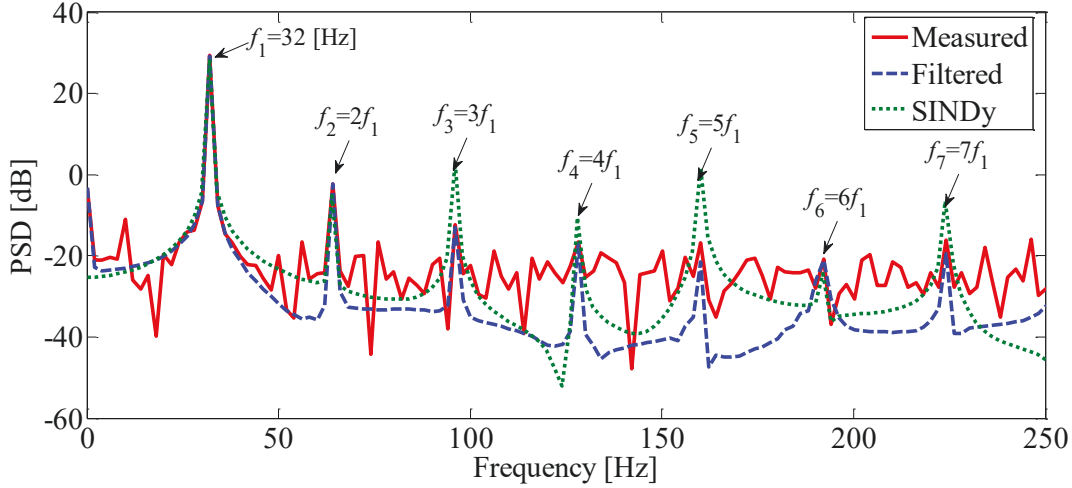


Fig. 4.10. PSD of original signal measured by LDV before applying filter, after applying filter and according to Eq. (4.16) for example 3.

In Figs. 4.6, 4.8, and 4.10 the alignment of the PSD peaks from the measured signal, filtered signal and SINDy-reconstructed data strongly suggests that the SINDy algorithm has successfully captured the essential dynamics of the system. This validates the nonlinear equation of motion and indicates that the model can be reliably used for further analysis, prediction, and control of the system. The distinct amplitude variations across

the harmonics observed in the SINDy results in Figs. 4.6, 4.8, and 4.10 may stem from the algorithm's sensitivity to nonlinearities in the system. The SINDy model identifies sparse nonlinear terms, which can accentuate certain harmonics, particularly under idealized conditions where noise and damping effects are minimized. In contrast, the experimental data reflect a broader range of physical factors, including system damping, measurement noise, and other uncertainties that are present in real-world systems. These factors tend to smooth out the amplitude variations observed in the harmonics, leading to a less pronounced harmonic structure in the experimental data when compared to the SINDy predictions. This discrepancy highlights the idealized nature of the SINDy model and the influence of external factors in the experimental setup.

SINDy is a powerful tool for identifying governing equations from data. However, it provides an approximation rather than an exact representation of the governing equations. This approximation arises because SINDy relies on a predefined library of candidate functions whose suitability affects the model's accuracy. If the library we had chosen had been inappropriate for the problem at hand (i.e., if the dynamics could not be well-approximated as a sparse linear combination of library functions), SINDy would have failed to produce a reasonable model. For example, if our problem's nature is governed by exponential or logarithmic functions, and we try to solve the same problem but using sines and cosines as our basic functions, SINDy is unable to find a sparse model for the dynamics [220,221].

In Chapter 2, by using Gorkov formulation and expanding the Tylor series till order five and for a small object levitated in the air and influenced by an external excitation, the governing equation of motion obtained as

$$\ddot{\theta} + C_1\dot{\theta} + C_2\theta^3 + C_3\theta^5 + C_d\dot{\theta}|\dot{\theta}| = F \cos(\theta) \sin(\omega t), \quad (4.17)$$

where $\theta, \dot{\theta}$ were non-dimensional displacement and velocity of the object, respectively, and C_i coefficient was related to the object and fluid properties, C_d was a coefficient related to viscosity and drag coefficient and F was a coefficient related to the amplitude of the external excitation. By using SINDy and using a library till order 5 for 3 case studies in period-1 of oscillation for a large spherical object we can see the governing equation of motion in general can be described by

$$\ddot{\theta} + c_1\dot{\theta} + c_2\theta^3 + c_3\theta^5 + \mathcal{F}(\theta, \dot{\theta}) = (f_1\dot{\theta} + f_2\sin(\theta))\sin(\omega t), \quad (4.18)$$

when $\mathcal{F}(\theta, \dot{\theta})$ is a nonlinear function and can be written as

$$\mathcal{F}(\theta, \dot{\theta}) = d_1 \dot{\theta} + d_2 \theta^2 \dot{\theta} + d_3 \theta \dot{\theta}^2 + d_4 \dot{\theta}^3 + d_5 \theta^3 \dot{\theta} + d_6 \theta^2 \dot{\theta}^2 + d_7 \theta^3 \dot{\theta}^2 + d_8 \theta^2 \dot{\theta}^3, \quad (4.19)$$

in which all c_i coefficient in Eq. (4.18) and d_i coefficient in Eq. (4.19) are related to the external excitation amplitude and $\mathcal{F}(\theta, \dot{\theta})$ is a nonlinear function of $\theta, \dot{\theta}$ that can be replaced instead of $C_d \dot{\theta} |\dot{\theta}|$ in Eq. (4.17). Also, the right hand of the Eq. (4.17), $F \cos(\theta) \sin(\omega t)$, has be replaced by $(f_1 \theta + f_2 \sin(\theta)) \sin(\omega t)$. All coefficient in Eq. (4.18) and (4.19) can be obtained using SINDy algorithm. Looking at Examples 1, 2, and 3, it can be seen that f_1 and f_2 are very close to each other. Because of this, they can be treated as a single coefficient, f . The interesting part is that the ratio of f to A_{in} in all three equations is about 25,000. This suggests a consistent relationship between f and A_{in} , which might be an important characteristic of the system.

Also, in comparison with Eq. (4.17), Eq. (4.18) indicate more complex behaviour of the viscosity and complicated interaction between object, fluid, and dynamical properties of the system. For comparison with the SINDy result, if Fig. 3.16 from Chapter 3 is presented again as Fig. 4.11a, it can be seen that the bifurcation diagram for acoustically large objects highlights the discrepancies and mismatches between the global dynamic behaviour of the system, as predicted by the theoretical model using the Gorkov formulation, and the real-world observations obtained from experimental data across varying external excitation amplitudes. This divergence arises because the Gorkov formulation is only valid for acoustically small spherical objects. As demonstrated in the experimental measurements (Examples 1, 2, and 3), the obtained coefficients in the governing equation of motion correspond to a specific external excitation amplitude and describe only localized system dynamics. When the governing equation of motion changes only in its coefficients due to variations in the bifurcation parameter, this can be described as a parametric variation within the same dynamical model. This means that the functional form of the equation remains unchanged, but the system exhibits different behaviours (e.g., transitions between periodic, quasi-periodic, or chaotic states) as the bifurcation parameter is varied. Additionally, it is observed that all the unknown coefficients vary with changes in the amplitude of the external excitation, indicating a dependency of the system's governing parameters on the excitation level. To include the complex behaviour of the viscosity, the bifurcation diagram should be plotted by varying the bifurcation parameter using the equation of motion obtained through SINDy, as outlined in Eq. (4.18). Since all the coefficients in examples 1-3 represent local dynamics

rather than global behaviour, to choose unknown d_i coefficients, we use the coefficients from Example 1. To account for the effect of the amplitude of the external excitation on the system, the ratio discussed earlier is used, where $f = 25000 \times A_{\text{in}}$, then the bifurcation diagram is plotted. Fig. 11b shows the bifurcation diagram comparing the analytical results derived from the SINDy results (red line) with experimental data (blue dots). The SINDy model captures the primary dynamics well at lower excitation amplitudes, aligning closely with experimental trends.

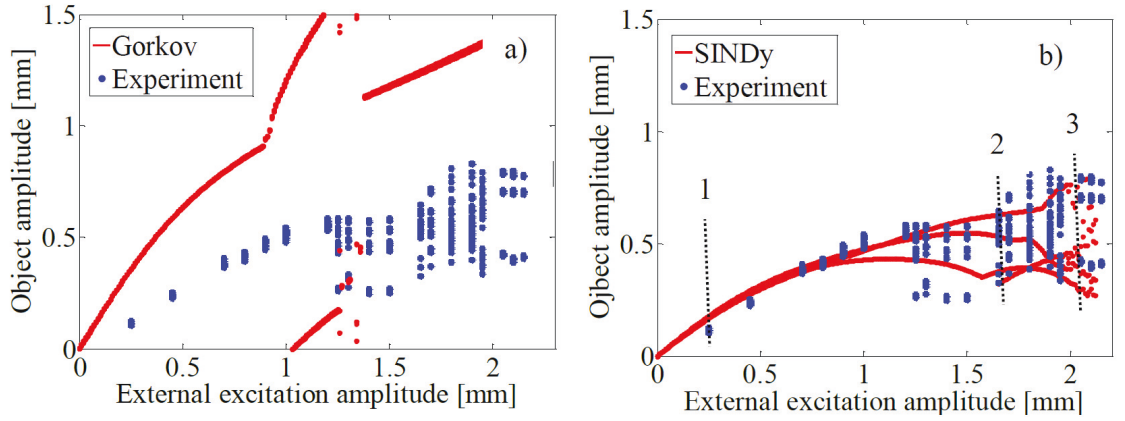


Fig. 11. a) Bifurcation diagram for an acoustically large object: analytical (solid line) vs. experimental data (dots), showing discrepancies due to Gorkov’s small-object assumption. b) Comparison of the SINDy results (red), and experimental data (blue), highlighting deviations at higher excitation amplitudes due to the polynomial-based library limitations. Some distinct regions with different dynamics are selected for further analysis.

In comparison with Fig. 11a, Fig. 11b highlights an improvement in the estimation of the system’s behaviour. By leveraging SINDy, the model in Fig. 11b captures the intricate nonlinear dynamics and the complex role of viscosity more effectively. Despite choosing the coefficients by using Example 1 and using a simple library consisting of polynomial functions up to the fifth order, SINDy can accurately reconstruct the underlying dynamical model for an acoustically large, levitated object. However, at higher amplitudes, significant deviations arise, especially in bifurcation regions where experimental data exhibit multiple branches. Although the chosen library may not fully capture all aspects of the bifurcation behaviour, the primary challenge lies not in selecting the appropriate function library, but in determining the correct coefficient values for the obtained model. The observed deviations at higher excitation amplitudes arise primarily from fluctuations in the extracted coefficients rather than limitations in the functional

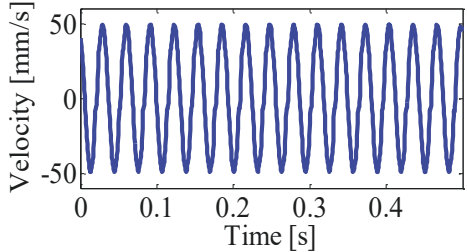
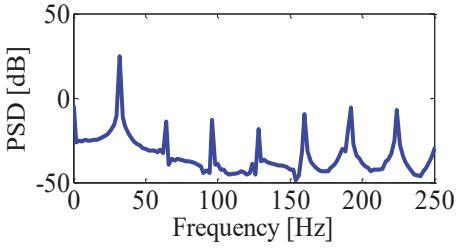
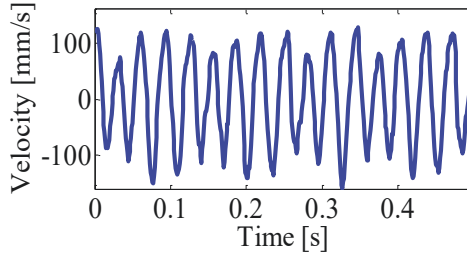
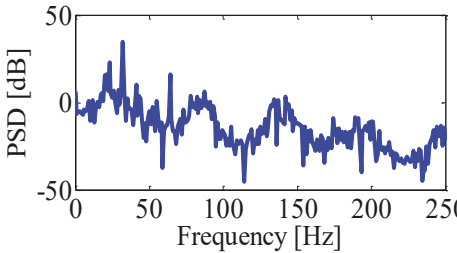
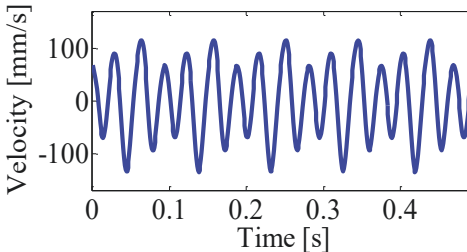
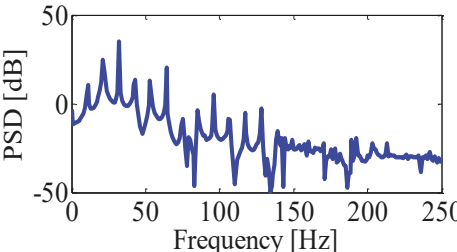
basis itself. This suggests that refining coefficient estimation through repeated measurements and statistical averaging is key to improving accuracy rather than expanding the function library. The results from Examples 1, 2, and 3 demonstrate that even with a minimalistic SINDy library, the essential system dynamics are well captured, highlighting the effectiveness of SINDy as a data-driven modelling tool. SINDy can yield more consistent and reliable governing equations by systematically analysing coefficient variability across multiple trials, further strengthening its applicability to complex nonlinear systems. For further analysis, by selecting three different regions denoted as Case 1, 2, and 3 in the bifurcation diagram, three different dynamic regimes are studied in the bifurcation diagram in Fig. 11b. Table 4.5 in the next section presents segments of these three distinct time series along with their corresponding PSD. These data were obtained by measuring voltage using LDV in the experimental setup, applying the GHKSS filter, and then processing the results.

4.5. Results for nonlinear time series analysis - System identification

As discussed in Chapters 2 and 3, Gorkov formulation cannot be used to predict the behaviour of acoustically large spherical objects. In this section, nonlinear time series analysis (NTSA) techniques are applied to study the behaviour of objects whose size exceeds the wavelength limit, with $kr > 1$. By selecting specific case studies, the behaviour of an acoustically large object levitated in an acoustic radiation force field is examined, using experimental time series data as discussed in Chapter 3.

Table 4.5 presents segments of three distinct time series and their corresponding power spectral densities (PSD), obtained by measuring voltage using LDV in the experimental setup and after application of GHSS filter for an object with a radius of $r = 1.87$ mm and subsequently processed using the GHKSS filter. These datasets show how different dynamical regimes can be observed as the amplitude of the external excitation varies from 0.25 mm to 2.5 mm (see bifurcation diagram, Fig. 11b), when the frequency of the external excitation is $\omega_{in} = 32$ Hz.

Table 4.5. Three different filtered time series data and their PSD, obtained by measuring voltage by using LDV in the experimental setup, when A_{in} varies from 0.25 mm to 2.5 mm for an object with a radius of 1.87 mm, with the external excitation frequency of $\omega_{in} = 32$ Hz.

	Time series data	PSD
Case 1 A_{in} $= 0.25$ mm		
Case 2 A_{in} $= 1.7$ mm		
Case 3 A_{in} $= 2.1$ mm		

Time series data from three bifurcation points were used to reconstruct the phase space, as shown in Table 4.5. Fig. 4.12 presents the MI and FNN function results for these time series, respectively.

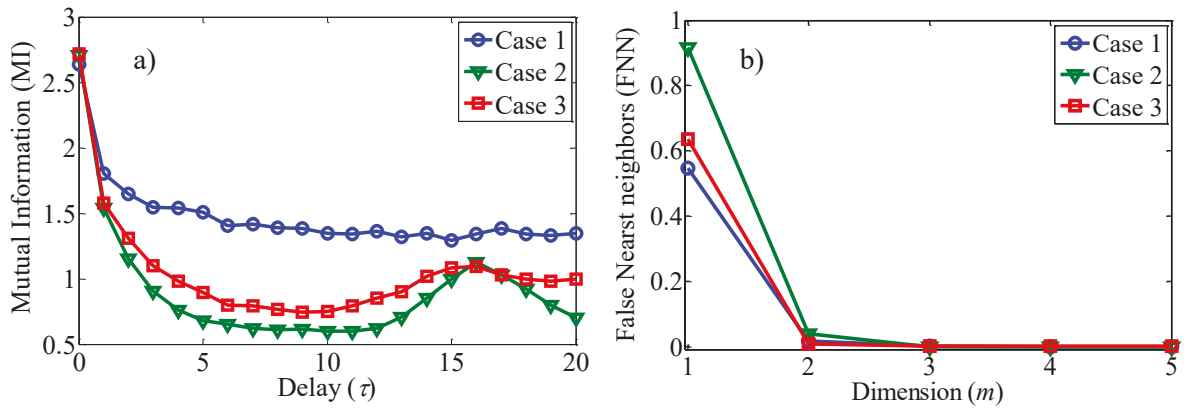
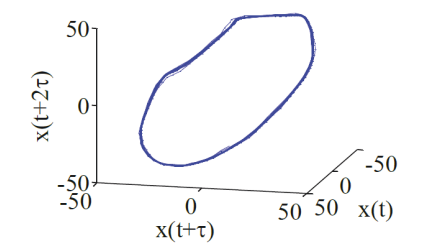
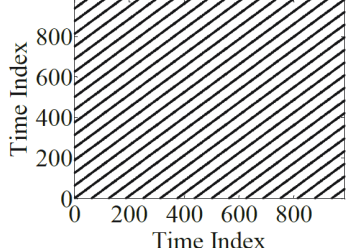
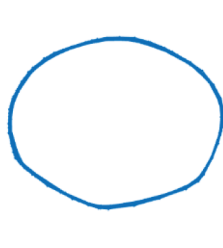
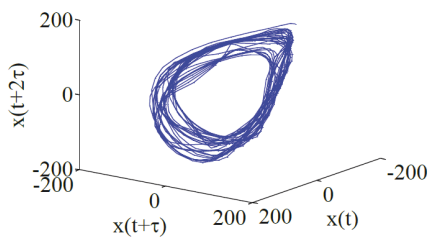
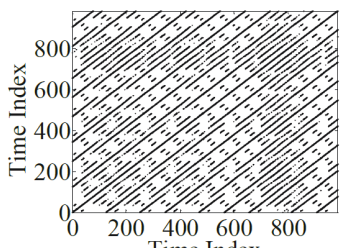
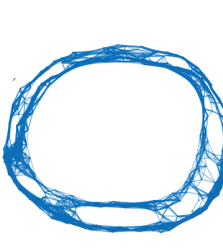
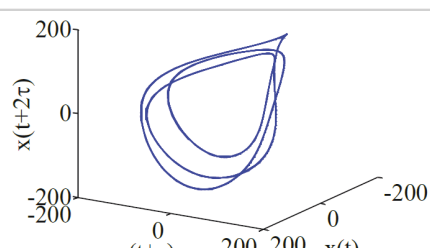
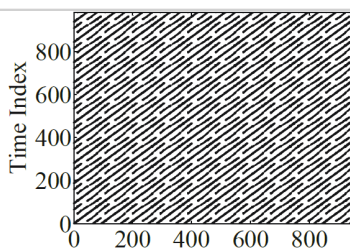



Fig. 4.12. a) MI test for selecting time delay of τ and b) FNN functions for selecting embedding dimension of m , according to case studies presented in Table 4.5.

Table 4.6 displays reconstructed phase space, RP, and RN for different cases in Table 4.5.

Table 4.6. Reconstructed phase space, RP, and RN for three cases presented in Table 4.5.

	Phase space	Recurrence Plot	Recurrence Network
1			
2			
3			

Reconstructed phase space for case 1 shows a regular motion corresponding to period-1 of oscillation which indicate an attractor which shows itself as a limit cycle in the phase space. A torus in the phase space in case 2 can be observed. A torus is a geometric shape that looks like a doughnut and occurs when a system's dynamics can be described by oscillations with two or more incommensurate frequencies. Here according to the PSD represented for the corresponding time series data in Table 4.5 two main frequencies are 32 Hz and 23 Hz, which shows the presence of incommensurate frequencies. These frequencies do not share a common multiple, leading to a trajectory that never exactly repeats but fills out a toroidal surface in phase space. Also, the PSD for case 2 is not smooth and appears noisy, indicating an irregular trajectory in the phase space. This irregularity suggests the presence of a chaotic torus in the phase space. A chaotic torus is a concept in dynamical systems where the trajectory on a torus becomes chaotic. This occurs when the motion, which would otherwise be quasi-periodic (regular and non-

repeating), is disrupted and becomes chaotic [237,238]. This means the system still follows a path around the torus but irregularly and unpredictably.

In the concept of RP, the parallel diagonal lines in case 1 indicate a harmonic regular motion. In contrast, the dashed diagonal lines, and high transitions in case 2 suggest intricate dynamics and unpredictable patterns which means a transition to chaotic behaviour. The system in its period-3 in case 3 shows more complex patterns than period-1 presented in case 1 with regular intervals of three-time steps. The sensitivity of the recurrence plot to changes in the bifurcation parameter shows that the dynamics of the system are strongly dependent on the external excitation amplitude, and understanding the specific details of these changes requires a deeper analysis of the system equations, examination of the bifurcation diagrams, and consideration of other measures such as the Lyapunov exponent, fractal dimension, etc. Here, the recurrence network is proposed to be plotted for a deeper analysis of the system's behaviour. The importance of plotting RP is that by defining a threshold of ε , the adjacency matrices can be derived. For these three case studies, the adjacency matrices have a size of 983×983 , which is essential for plotting RN. The size 983 by 983 was chosen based on the length of the time series data after preprocessing after reconstructing the phase space and the threshold parameter, ε .

In the network related to the regular recurrence plot for case 1, a closed loop can be observed in the recurrence network, which is a strong indicator of periodic behaviour. It indicates that the system returns to its initial state after a certain period and completes a motion cycle. Since the specific structure of the closed loop, including the size, shape, and density of connections, can provide more information about the nature of the periodic motion, the presence of a regular and symmetric loop indicates a simple periodic behaviour. However, the system's dynamic changes with the variation of the bifurcation parameter, and irregularity occurs in the system's behaviour. In the network related to recurrence plot in case 2, two oval-like closed loops with different densities of connections and irregular patterns can be seen. Closed loops in the network indicate quasi-periodic movement in the investigated system. The two oval-like shapes in this pattern indicate that the system has two distinct modes, each with different amplitude or frequency regimes. It should be noted that the system has two main incommensurate frequencies. The variation in connection density within these loops reflects the chaotic nature of the system, where two incommensurate frequencies interact. The network says that the object is sometimes on the outer loop and sometimes on the inner oval loop, but

the transition between these two loops is irregular. Irregular patterns and junctions between oval loops indicate transitions or jumps between these two states, and observed irregularity between these two states predict chaotic or transitional behaviour. In the network corresponding to the regular recurrence plot in case 3, the presence of three interconnected loops indicates that the system cycles through three distinct states. This structure is characteristic of a period-3 of oscillation. A connected graph that has many occurrences in a network is called a motif of the network. In other words, network motifs are sub-graphs that repeat themselves in a specific network or even among various networks. Motif discovery problem comprises two main steps: first, calculating the number of occurrences of a sub-graph and then, evaluating the sub-graph significance. Various solutions have been proposed for the challenging problem of network motif discovery [222]. These algorithms can be classified under various paradigms such as exact counting methods, sampling methods, pattern growth methods and so on [222]. Network and motif analysis further enhances our understanding of the system's dynamics, revealing intricate relationships and patterns within the data. Before bifurcation, the system typically exhibits harmonic motion, characterized by simple, regular oscillations. In the regular network in case 1, smaller motifs of sizes 3 and 4 (Fig. 4.13a), indicate stable and predictable interactions. However, in Fig. 4.13b, case 2, where dynamics are governed by a chaotic torus, system shows more complex and intricate patterns. This complexity is captured by larger motifs of sizes 4 to 8 in the network (Fig. 4.2b), highlighting the increased interactions and two different loops.

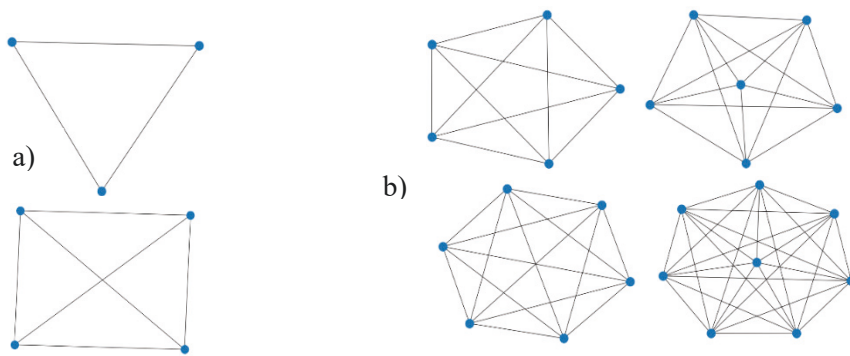


Fig. 4.13. Motifs for a) regular harmonic motion related to network in Table 4.2: case 1, and b) irregular quasi-periodic motion related to network in Table 4.2: case 2.

4.6. Conclusion

In this Chapter, and for the first time, the Sparse identification of nonlinear dynamics (SINDy) algorithm has been applied to reconstruct the nonlinear differential equation of

motion of a levitated object trapped in an acoustic radiation force field, using experimental time series input data. The results indicate a good correlation with the theory for objects smaller than the wavelength limit. However, when dealing with more complex dynamics using objects larger than the wavelength limit, the theoretical predictions become inadequate. In these cases, SINDy accurately predicts the object's dynamic behaviour. The theoretical robustness of SINDy against noise is observed under low noise conditions, while filtering is recommended for highly noisy data. The application of the GHKSS filter effectively reduces noise in experimental data. For acoustically small objects, changes in the amplitude of external excitation primarily affect the external excitation part in the nonlinear equation of motion, while for larger objects, SINDy reveals complex and nonlinear relationships between the amplitude of external excitation and all coefficients. This evaluation showed that SINDy performs well in theoretical scenarios, successfully extracting equations of motion for small objects exhibiting complex dynamic regimes, as demonstrated in Table 4.1. For acoustically large objects, the results obtained using a library with polynomial functions up to the fifth order and simple trigonometric functions demonstrate SINDy's ability to capture the primary dynamics of the system that underscores the potential of developing data-driven models for complex nonlinear systems. Although the chosen library may not fully capture all aspects of the bifurcation behaviour, it provides valuable insights into the dominant dynamics of the system.

To further analyze the experimental bifurcation diagram, nonlinear time series analysis (NTSA) techniques such as phase space reconstruction, recurrence plots (RPs), and recurrence networks (RNs) were employed to examine the complex dynamics of acoustically levitated objects, particularly in the case of acoustically large objects where the traditional Gorkov formulation fails (i.e., when kr is greater than 1). In the presented case studies, parallel diagonal lines in the RPs indicate regular motion. However, as the bifurcation parameter changes, by changing the bifurcation parameter, the presence of dashed diagonal lines and high transitions in the system's behaviour suggests intricate dynamics, indicating quasi-periodic behaviour, which can signify chaos.

Network and motif analysis further enhances our understanding of the system's dynamics, revealing intricate relationships and patterns within the data. Different motif sizes before and after bifurcation highlight the transition from simple harmonic motion to more complex regime in a dynamical system.

CHAPTER 5: CONCLUSION

Below are summarised the main contributions of this research:

- 1- In this study, with the help of Gorkov's potential function theory, a new formula for the acoustic contrast factor was obtained by considering a harmonic external excitation. This harmonic disturbance causes the spherical object immersed in an ideal fluid to undergo rigid body oscillations.
- 2- To validate the theoretical model to obtain acoustic contrast factor, a 3D finite element analysis (FEA) was conducted using perturbation theory in COMSOL Multiphysics 5.5. The numerical model presented here not only includes spherical objects with dimensions larger than the wavelength limit, but it can also be applied on non-spherical objects that lack analytical formulation.
- 3- Using Newton's second law and assuming a small amplitude of the object's oscillation compared to the wavelength, and for a spherical object with dimensions smaller than the wavelength limit, the nonlinear governing equation of motion was obtained, which has a Duffing-like oscillatory behaviour. To investigate the effect of cubic, fifth, and higher-order terms, as well as object and fluid properties and damping on the nonlinear frequency of the system, the global residual harmonic balance method (GRHBM), the homotopy perturbation method with multi-parameter expansion (HPMPE), and the Akbari-Ganji (AG) method were introduced. Based on this, analytical formulas for the nonlinear frequency of the system were obtained.
- 4- The sensitivity of the dynamic behaviour of the system was investigated by calculating the Sobol indices using various system parameters, including coefficients related to the properties of the object and fluid, as well as the frequency and amplitude of external vibrations. The results reveal that the amplitude and frequency of external excitation significantly influence the system's response. Utilizing these sensitivity results, a bifurcation diagram was plotted using amplitude of external excitation as the bifurcation parameter. This diagram illustrates that the rich dynamical regime is possible and highlight that an experimental investigation is required.

- 5- An experiment was introduced and designed to extract time series data for an object levitated in an acoustic radiation force field. This experimental set up designed to extract time series data which are required to analyse the dynamical behaviour of the system under varying conditions.
- 6- The system's phase space was reconstructed using time series data to obtain Recurrence Plots (RPs). Phase space reconstruction employed the first minimum of mutual information (MI) and the false nearest neighbours (FNN) method. By forming recurrence networks and searching for motifs, the system's dynamics were classified. RPs revealed transitions from regular to intricate, chaotic patterns, with network and motif analysis providing deeper insights into system behaviour.
- 7- For the first time, the SINDy algorithm was used to reconstruct the nonlinear differential equation of motion of a levitated object trapped in the acoustic radiation force field using experimental time series input data. In the first step, the robustness of the SINDy algorithm against noisy data was evaluated. This study confirms the theoretical robustness of SINDy against noise in low-noise conditions, while filtering is recommended for high-noise data. The results show that the SINDy algorithm is a promising method for accurately identifying data-driven models. For acoustically small objects, as predicted by the theoretical formula, changes in the external excitation amplitude only affect the external excitation part of the governing equation of motion. In contrast, SINDy shows complex and nonlinear relationships between the external excitation field and all coefficients for larger objects.

5.1. Summary

When an object is acoustically excited with an acoustic wave some of this momentum is transferred to the object and acoustic radiation exerts a force on the object. Static acoustic radiation force is known to be steady when the incident field is continuous with constant amplitude, and dynamic (oscillatory) acoustic radiation force for a continuous wave-field whose intensity varies slowly with time.

By changing the viewpoint from the acoustic field to the dynamics of a levitated object, this question arises of how external excitation changes the dynamics of the object. In this scenario, and for acoustically small objects, the Gorkov potential function theory and its acoustic contrast factor are revisited, considering a harmonic disturbance that causes a spherical object to undergo rigid body oscillations within an ideal fluid in a standing plane

ultrasonic wave field. This is interesting as it raises the question of whether it is possible, in principle, to make use of the potential field to control the acoustic radiation force on an object through external disturbance without changing the other field parameters. The findings show that the contrast factor not only depends on the object and fluid properties, but also on the external vibration amplitude. Positive, negative and zero acoustic radiation forces are achievable, causing the object to constantly being pushed towards the nearest pressure or velocity node. The dependence on disturbance amplitude and force reversal are the novel features that can be employed in acoustic manipulation for non-contact dynamic characterization of smallest objects.

To validate the theoretical model, a finite element analysis (FEA) was conducted using perturbation theory in COMSOL Multiphysics 5.5. The presented 3D numerical model of acoustic radiation force in COMSOL has then been applied to objects (a) with larger dimensions than wavelength limit and (b) using non-spherical shapes that lack analytical formulation and shows the same qualitative behaviour in terms of the acoustic contrast factor over a range of wavelengths.

By applying Newton's second law and assuming a small amplitude of external object oscillation compared to the wavelength, as well as a spherical object with dimensions smaller than the wavelength limit, a nonlinear governing equation of motion was derived, unveiling a Duffing-like oscillator behaviour in the time-varying radiation force, which exhibited a restoring harmonic force as a nonlinear softening spring. Using the obtained analytical relations, the effect of cubic, quintic and higher order terms, and the object and fluid properties on the nonlinear frequency of the system were discussed, subsequently. In this case, Global residue harmonic balance method (GRHBM) and homotopy perturbation method with multi parameter expanding (HPMPE) employed in obtaining the analytical approximate frequencies of free vibration condition. The difference between these analytical methods for amplitude of object oscillation less than $\lambda/5$, when λ is the wavelength of the acoustic wave, is less than 5% which shows the validation of using the analytical solution for this interval. Also, the result shows that considering only cubic term in nonlinear governing equation of motion can only be valid for amplitude of object oscillation less than $\lambda/8$ considering only cubic term and considering cubic and quintic term can be valid, for amplitude of object oscillation less than $\lambda/5$, and for higher amplitude considering the higher order nonlinear terms is required. Then, the effect of the compressibility and density on the angular frequency was investigated. Then, AG method

was employed for solving nonlinear damped vibration to investigate the effect of the nonlinearity on the angular frequency and phase of oscillation and the results validated by using a numerical solution obtained by Runge-Kutta order fourth. The results show that because of the damping effects, the vibration of the object decays to its static position on the pressure node.

To solve the governing equation of motion numerically using the fourth-order Runge–Kutta method, an appropriate time step was selected based on statistical observation and the box plot method. The frequency response of the system in low amplitude verified by comparison of results with the experimental findings from [118]. The sensitivity of the dynamic behaviour of the system was investigated by calculating the Sobol indices in relation to various system parameters, including coefficients related to object and fluid properties, external vibration frequency and amplitude, and the results show that the external vibration amplitude and frequency have a significant effect on the system response. Using sensitivity results, the bifurcation diagram was plotted using the external amplitude oscillation as the bifurcation parameter. The result shows that a rich dynamical regime exists, including bifurcation points and quasi-periodic behaviour. While these theoretical results are potentially important for practical object manipulation, only experiments in highly nonlinear regimes can verify our findings and their physical relevance; this will be the subject of future Chapters.

The presented study assumes that the object exhibits a simple harmonic response under the influence of external sinusoidal excitation. To validate these assumptions and extract nonlinear time series data for further analysis, an experimental setup was introduced and conducted. The validated experimental results confirm this assumption with a near linear relationship between the object's response and the amplitude or frequency of external excitation. As verified also experimentally the object is oscillating and changes its amplitude and frequency with regards to the external excitation. The resulting vibration amplitudes are consistent across frequencies from 10 to 100 Hz which suggests a well-characterized reproducible and controlled experimental setup. It is experimentally verified – through external excitation of the ultrasonic standing wave generator – that the disturbance vibration frequency and amplitude are transmitted to the levitated object. Experimental findings presented here exemplify for the first time that full non-contact vibration testing campaigns and modal analysis using a levitated object which is indirectly

excited via a shaker and measured using a laser Doppler vibrometer is possible in principle.

Recently, the sparse identification of nonlinear dynamic (SINDy) approach has been proposed with the aim of identifying nonlinear dynamical systems from time series data, if the equations of motion have only a few important terms. Here, the SINDy algorithm was applied to reconstruct the nonlinear differential equation of motion of a levitated object larger than the wavelength limit trapped in an acoustic radiation force field using experimental time series data. In the first step, the aim was to evaluate the robustness of the SINDy algorithm against noisy data. The study confirmed the theoretical robustness of SINDy against noise in low-noise conditions, while experimental data filtering was recommended for high-noise data. Here, and due to the nonlinear nature of the problem, the GHKSS filter was used, which effectively reduced the noise in the experimental data. In the work, SINDy was applied by defining a library of possible functions and solving a sparse regression problem by eliminating terms whose coefficients were smaller than a threshold. The results show that the SINDy algorithm is a promising methodology to accurately identify interpretable data-driven models. It can be observed that for acoustically small objects, changes in the amplitude of external excitation primarily affect the external excitation part in the equation of motion. In contrast, SINDy reveals complex and nonlinear relationships between the external excitation part and all coefficients for larger objects.

Recurrence was a fundamental property of dynamical systems, and recurrence plots (RP), a powerful tool for visualizing and analysing a nonlinear system's behaviour, were used to study the system for large acoustically levitated objects in its phase space. In this case, the system's phase space was reconstructed using its time series data to obtain RPs. The first minimum of the mutual information (MI) and false nearest neighbours (FNN) method were used to reconstruct the phase space using experimental nonlinear time series data. Using the generated adjacency matrix, recurrence networks were formed, and motifs were searched for to classify the dynamics of the system. By plotting RPs for different dynamical regimes using experimentally extracted time series data, a progression was observed from parallel diagonal lines to intricate patterns with irregularities and transitions. Presence of parallel diagonal lines in the RP shows a regular motion. At the same time, by changing the bifurcation parameter, high transitions in the system's RP

suggest intricate dynamics, possibly indicating a chaos regime. Network and motif analysis further enhances our understanding of the system's dynamics.

It is hoped that this connection between nonlinear time series analysis, SINDy, and the acoustic radiation force community will spur new techniques for trapping, handling, and levitating small objects using acoustical energy.

5.2. Recommendations for future work

The investigation into the nonlinear dynamics of objects levitated in an acoustic radiation force field has opened new avenues of research for trapping, handling, and levitating objects using acoustical energy. A few examples of such avenues are mentioned below.

5.2.1. Multi-object dynamics

When multiple objects are placed in an acoustic radiation force field, secondary acoustic radiation forces arise due to object-object interactions and acoustic scattering effects [29]. This phenomenon complicates the manipulation process and necessitates the development of advanced dynamic models capable of accurately capturing the motion of multiple objects.

Developing these sophisticated models is crucial for several reasons. Firstly, they will significantly enhance our understanding of the dynamics involved in multi-object systems within acoustic fields. By accurately modelling the interactions between multiple objects, we can gain deeper insights into the complex behaviours and responses in such environments. This understanding is fundamental for advancing the field of acoustic manipulation.

Secondly, these advanced models will improve control and manipulation techniques in various applications. For instance, precise manipulation of multiple particles or cells is often required in biomedical engineering. Advanced dynamic models can enable more accurate and reliable control, improving outcomes in applications such as targeted drug delivery, tissue engineering, and diagnostic procedures. Moreover, developing these models will open new research and technological innovation avenues. For example, they can inspire novel methodologies in object manipulation, such as designing new acoustic devices and systems that leverage the intricate dynamics of multiple objects. These methodologies could lead to breakthroughs in materials science to robotics, where precise control over multiple objects is often crucial. Future work should concentrate on the formulation and validation of these advanced dynamic models. This involves integrating

factors such as nonlinearities, object shapes, and material properties to create comprehensive and robust models. Furthermore, experimental studies should be conducted to validate the theoretical models and ensure their applicability in real-world scenarios.

5.2.2. More analysis for SINDy coefficients and its library functions

To investigate the deviation between the coefficients in Gorkov's formula and the results from SINDy's algorithm, it is necessary to extend the experiment presented in Chapter 3 to include a broader range of spherical object radii, varying from those smaller than the wavelength limit to larger values. This will provide insight into how changes in object size influence the deviation between theoretical predictions and real-world experimental data. Although the current experiment did not encompass such a range, the study and results outlined in Chapter 3 serve as a foundation for future investigations in this area. Future work should also focus on expanding the library of candidate functions in SINDy to better capture the finer details of system dynamics, particularly in complex dynamical regimes, as indicated by the bifurcation diagram. This will enable comparisons of coefficients for specific experiments under varying parameters across different dynamical regimes. Furthermore, it is recommended to continue refining the SINDy algorithm to improve its ability to capture complex dynamics in real-world data. Addressing the challenges posed by experimental noise and system complexity will be critical to extending SINDy's application to more intricate dynamic behaviours. Integrating complementary methods could also enhance its robustness, providing more accurate and reliable predictions in complex real-world scenarios.

5.2.3. Nonlinear dynamics and synchronization

The dynamical behaviour of two spherical objects in an acoustic field, including the coupling between them, offers an attractive area for future research. An important question arises: can we model this coupled system analytically and experimentally, and how similar is this behaviour to that of coupled Duffing-like oscillators [229] for acoustically small and large objects?

Understanding whether the system exhibits chaotic dynamics or synchronized motion is crucial for determining the stability and achieving synchronization between objects. This stability analysis is important and novel because finding a chaotic attractor that absorbs all initial conditions is particularly interesting. Future studies can explore a deeper

understanding of these complex systems by focusing on the chaotic behaviour and synchronization of coupled objects.

By addressing these challenges, future research can contribute significantly to advancing science and technology in areas where precise object manipulation is essential. This exploration into the chaotic behaviour and synchronization of coupled objects promises to open new research and technological innovation avenues.

REFERENCES

- [1] J. H. Cantrell, Acoustic-radiation stress in solids. I. Theory, Phys. Rev. B Condens. Matter. 30(6) (1984) 3214-3220.
- [2] G. R. Torr, The acoustic radiation force, Am. J. Phys. 52(5) (1984) 402-408.
- [3] L. Rayleigh, On the pressure of vibrations, Phil. Mag. 3 (1902) 338–346.
- [4] N. Pamme, Magnetism and microfluidics, Lab Chip. 6(1) (2006) 24-38.
- [5] H. Bruus, Acoustofluidics 7: The acoustic radiation force on small particles, Lab Chip. 12(6) (2012) 1014-1021.
- [6] L. A. Crum, Acoustic force on a liquid droplet in an acoustic stationary wave, J. Acoust. Soc. Am. 50 (1971) 157-163.
- [7] G. T. Silva, H. Bruus, Acoustic Interaction Forces between Small Particles in an Ideal Fluid, Phys. Rev. E Stat. Nonlin. Soft Matter Phys. 90 (2014) 063007.
- [8] P. Zhang, H. Bachman, A. Ozcelik, T. J. Huang, Acoustic Microfluidics, Annu. Rev. Anal. Chem., 13 (1) (2020) 17-43.
- [9] K. Saeedabadi, G. Tosello, M. Calaon, Optimization of injection molded polymer lab-on-a-chip for acoustic blood plasma separation using virtual design of experiment, Procedia CIRP. 107 (2022) 40-45.
- [10] Z. Chen, L. Shen, X. Zhao, H. Chen, Y. Xiao, Y. Zhang, X. Yang, J. Zhang, J. Wei, N. Hao, Acoustofluidic micromixers: From rational design to lab-on-a-chip applications, Appl. Mater. Today. 26 (2022) 101356.
- [11] S. Chen, M. Fatemi, and J. F. Greenleaf, Quantifying elasticity and viscosity from measurement of shear wave speed dispersion, J. Acoust. Soc. Am. 884(112) (2002) 2781.
- [12] N. Nitta, Y. Ishiguro, H. Sasanuma, N. Takayama, K. Rifu, N. Taniguchi, I. Akiyama, *In Vivo* Temperature Rise Measurements of Rabbit Liver and Femur Bone Surface Exposed to an Acoustic Radiation Force Impulse, Ultrasound Med. Biol. 48 (7) (2022) 1240-1255.
- [13] K. Rifu, J. Watanabe, H. Sasanuma, N. Taniguchi, Evaluation of the Elasticity of the Pancreas Using Acoustic Radiation Force Impulse Elastography in Patients with Acute Pancreatitis: A Systematic Review and Meta-Analysis, Ultrasound Med. Biol. 48 (3) (2022) 406-413.
- [14] A. Marzo, A. Barnes, B. W. Drinkwater, Tiny-Lev: A multi-emitter single-axis acoustic levitator, Rev. Sci. Instrum. 88 (2017) 085105.

- [15] N. Brunetiere M. Wodtke, Considerations about the applicability of the Reynolds equation for analyzing high-speed near field levitation phenomena, *J. Sound Vib.* 783(29) (2020) 115496.
- [16] Y. Han, Sh. Kala, S. Yan, J. Palacios, Partial melting time model verification of a levitated ice particle, *Cold. Reg. Sci. Technol.* 173 (2020) 103013.
- [17] K. Aono, M. Aoyagi, J. Palacios, Rapid rise of planar object by near-field acoustic levitation on recessed acoustic radiation surface, *Ultrasonic.* 119 (2022) 106596.
- [18] E. C. Jaque, J. M. Diaz, Y. V. Hernández, L. G. Garretón, On the dynamics of a big drop in acoustic levitation, *Ultrason. Sonochem.* 101 (2023) 106705.
- [19] V. Contreras, K. V. Sepúlveda, Enhanced standing-wave acoustic levitation using high-order transverse modes in phased array ultrasonic cavities, *Ultrasonic.* 138 (2024) 107230.
- [20] A. P. Sarvazyan, O. V. Rudenko, S. D. Swanson, J. B. Fowlkes, S. Y. Emelianov, Shear wave elasticity imaging: a new ultrasonic technology of medical diagnostics, *Ultrasound Med. Biol.* 24 (9) (1998) 1419-35.
- [21] M. Fatemi, J. F. Greenleaf, Ultrasound-stimulated vibro-acoustic spectrography, *Science*, 280 (5360) (1998) 82-5.
- [22] K. Nightingale, M. S. Soo, R. Nightingale, G. Trahey, Acoustic radiation force impulse imaging: in vivo demonstration of clinical feasibility, *Ultrasound Med. Biol.* 227 (28) (2002) 35.
- [23] A. Sarvazyan, Diversity of biomedical applications of acoustic radiation force, *Ultrasonics.* 10(2) (2010) 230-234.
- [24] P. Li, Z. Mao, Z. Peng, L. Zhou, Y. Chen, P. H. Huang, C. I. Truica, J. J. Drabick, W. S. El-Deiry, M. Dao, T. J. Huang, Acoustic separation of circulating tumor cells, *Proc. Natl. Acad. Sci. U.S.A.*, 112 (2015) 4970–4975.
- [25] F. Guo, Z. Mao, Y. Chen, Z. Xie, J. P. Lata, P. Li, L. Ren, J. Liu, J. Yang, M. Dao, S. Suresh, T. J. Huang, Three-dimensional manipulation of single cells using surface acoustic waves, *Proc. Natl. Acad. Sci. U.S.A.* 113 (6) (2016) 1522-1527.
- [26] M. G. Kim, J. Park, H. G. Lim, S. Yoon, C. Lee, J. H. Chang, K. K. Shung, Label-free analysis of the characteristics of a single cell trapped by acoustic tweezers, *Sci. Rep.* 7 (2017) 14092.
- [29] R. M. Abhishek, S. Sepehrirahnama, K. M. Lim, Experimental measurement of interparticle acoustic radiation force in the rayleigh limit, *Phys. Rev. E*, 97 (2018) 053105.

- [30] M. A. Ghanem, A. D. Maxwell, O. A. Sapozhnikov, V. A. Khokhlova, M. R. Bailey, Quantification of Acoustic radiation forces on solid objects in fluid, *Phys. Rev. Appl.* 12 (2019) 044076.
- [31] M. Kandemir, M. Beelen, R. Wagterveld, D. Yntema, K. Keesman, Dynamic acoustic fields for size selective particle separation on centimeter scale, *J. Sound Vib.* 490 (6), (2021) 115723.
- [32] M. Akbarzadeh, S. Oberst, S. Sepehrihnama, Y. K. Chiang, B. J. Halkon, A. Melnikov, D. A. Powell, A Numerical Study of Acoustic Radiation Forces for the Contactless Excitation of a Microcantilever, in *NODYCON Conference Proceedings Series*, Springer International Publishing (2021) 335 – 345 NODYCON 2021.
- [33] Y. Liu, Q. Yin, Y. Luo, Z. Huang, Q. Cheng, W. Zhang, B. Zhou, Y. Zhou, Z. Ma, Manipulation with sound and vibration: A review on the micromanipulation system based on sub-MHz acoustic waves, *Ultrason. Sonochem.* 96 (2023) 106441.
- [34] T. M. Huber, Noncontact modal analysis of a pipe organ reed using airborne ultrasound stimulated, vibrometry. *J. Acoust. Soc. Am.*, 4 (2006) 2476-2482.
- [35] T. M. Huber, D. Calhoun, M. Fatemi, R. R. Kinnick, J. F. Greenleaf, Noncontact modal testing of hard-drive suspensions using ultrasound radiation force, *Proceedings of International Modal Analysis Conference 2* (2006) IMAC XXIV.
- [36] T. M. Huber, D. C. Abell, C. B. Mellema, M. Spletzer, A. Raman, Mode-selective noncontact excitation of microcantilevers and microcantilever arrays in air using the ultrasound radiation force. *Appl. Phys. Lett.*, 97 (2010) 21410.
- [37] T. M. Huber, J. R. Beaver, N. M. Helps, Noncontact modal excitation of a classical guitar using ultrasound radiation force, *Exp. Tech.*, 37 (2013) 38-46.
- [38] G. T. Silva, S. Chen, J. F. Greenleaf, M. Fatemi, Dynamic ultrasound radiation force in fluids, *Phys. Rev. E.* 71 (2005) 056617.
- [39] S. M. Z. Uddin, Y. X. Qin, Dynamic acoustic radiation force retains bone structural and mechanical integrity in a functional disuse osteopenia model, *Bone.* 75 (2015) 8-17.
- [40] C. P. Lee, T. G. Wang, Acoustic radiation Pressure, *J. Acoust. Soc. Am.* 94 (2), 1099-1109 (1993).
- [41] H. Bruus, Acoustofluidics 2: Perturbation theory and ultrasound resonance modes, *Lab Chip.* 12(1), 20–28, (2012).
- [42] K. M. Lim, S. Sepehrihnama, Calculation of acoustic radiation force and moment in microfluidic devices, *Int. J. Mod. Phys. Conf. Ser.* 34 (2014) 1460380.

- [43] B. T. Chu, R. E. Apfel, Acoustic radiation pressure produced by a beam of sound, *J. Acoust. Soc. Am.* 72(6) (1982) 1673-1687.
- [44] G. T. Mase, G. E. Mase, *Continuum Mechanics for Engineers*, Second Edition, CRC Press LLC, 1999.
- [45] Z. J. Wang, High-order methods for the Euler and Navier–Stokes equations on unstructured grids, *Prog. Aerosp. Sci.* 43(1-3) (2007) 1-41.
- [46] C.Y. Wang, Review of similarity stretching exact solutions of the Navier–Stokes equations, *Eur. J. Mech. B Fluids.* 30(5) (2011) 475-479.
- [47] K. K. Jaber, R. S. Ahmad, Analytical solution of the time fractional Navier-Stokes equation, *Ain Shams Eng. J.* 9(4) (2018) 1917-1927.
- [48] B. E. Rapp, Conservation of mass: the continuity equation, in *Microfluidics (Second edition): Modeling, Mechanics and Mathematics, Micro and Nano Technologies*, (2023) 283-289.
- [49] Y. Zhang, N. Li, N. Gao, H. Zhang, CFD studies of the nonlinearity of NewWave group propagation and wave-structure interaction, *Ocean Eng.* 270 (2023) 113410.
- [50] Y. Cong, D. Wei, H. Kang, X. Su, Y. Jiang, Theoretical and CFD investigation on nonlinear dynamics of a cable under vortex-induced vibration with different aerodynamic shapes, *J. Fluids Struct.* 125 (2024) 104061.
- [51] D. Xie, N. Huang, A. Wang, A perturbation bound on a class of dynamical model updating problem and a method of keeping its sparse structure, *Mech. Syst. Signal Process.* 70-71 (2016) 300-307.
- [52] H. Meshki, A. Rezaei, A. Sadeghi, Homotopy Perturbation–Based Dynamic Analysis of Structural Systems, *J. Eng. Mech.* 146(12) (2020) 04020136.
- [53] C. S. Liu, C. W. Chang, A novel perturbation method to approximate the solution of nonlinear ordinary differential equation after being linearized to the Mathieu equation, *Mech. Syst. Signal Process.* 178 (2022) 109261.
- [54] E. B. Lima, J. P. Leão-Neto, A. S. Marques, G. C. Silva, J. H. Lopes, G. T. Silva, Nonlinear Interaction of Acoustic Waves with a Spheroidal Particle: Radiation Force and Torque Effects, *Phys. Rev. Appl.* 13 (2020) 064048.
- [55] S. Sepehrirhnama, K. M. Lim, Generalized Potential Theory for Close-Range Acoustic Interactions in the Rayleigh Limit, *Phys. Rev. E.* 102 (2020) 043307.

- [56] J. H. Lopes, M. Azarpeyvand, G. T. Silva, Acoustic Interaction Forces and Torques Acting on Suspended Spheres in an Ideal Fluid, *IEEE Trans. Ultrason. Ferroelect. Freq. Contr.* 63 (2016) 186–197.
- [57] S. Sepehrirahnama, K. M. Lim, Acoustophoretic Agglomeration Patterns of Particulate Phase in a Host Fluid, *Microfluid Nanofluid.* (2020) 24, 1–14
- [58] P. B. Muller, R. Barnkob, M. J. H. Jensen, and H. Bruus, A numerical study of microparticle acoustophoresis driven by acoustic radiation forces and streaming-induced drag forces, *Lab Chip* 12 (22) (2012) 4617–4627.
- [59] M. A. B. Andrade, N. Pérez, J. C. Adamowski, Review of progress in acoustic levitation, *Braz. J. Phys.* 48 (2018) 190-213.
- [60] A. A. Doinikov, Acoustic radiation forces Classical theory and recent advances, *Transworld Research Network*, Chapter 3, (2003) 39-67.
- [61] P. G. Jones, P. P. Mishra, R. J. Boltryk, M. Hill, Efficient finite element modeling of radiation forces on elastic particles of arbitrary size and geometry, *J. Acoust. Soc. Am.* 133(4) (2013) 1885-1893.
- [62] L. V. King, On the acoustic radiation pressure on spheres, *Proc. Royal Soc. of London A.* 147 (861) (1934) 212-240.
- [63] K. Yosioka, Y. Kawasima, Acoustic radiation pressure on a compressible sphere, *Acustica.* 5(3) (1955) 167-173.
- [64] L. P. Gorkov, On the Forces Acting on a Small Particle in an Acoustical Field in an Ideal Fluid, *Sov. Phys. Dokl.* 6 (1962) 773.
- [65] J. J. Faran, Sound Scattering by Solid Cylinders and Spheres, *J. Acoust. Soc. Am.* 23 (4) (1951) 405-418.
- [66] T. Hasegawa, K. Saka, N. Inoue, K. Matsuzawa, Acoustic radiation force experienced by a solid cylinder in a plane progressive sound field, *J. Acoust. Soc. Am.* 83 (5) (1988) 1770-1775.
- [67] J. Wu, G. Du, S. S. Work, D. M. Warshaw, Acoustic radiation pressure on a rigid cylinder: an analytical theory and experiments, *J. Acoust. Soc. Am.* 87 (2) (1990) 581-586.
- [68] F. G. Mitri, Theoretical calculation of the acoustic radiation force acting on elastic and viscoelastic cylinders placed in a plane standing or quasistanding wave field, *Eur. Phys. J. B.* 44 (2005) 71-78.

- [69] F. G. Mitri, Acoustic radiation force acting on elastic and viscoelastic spherical shells placed in a plane standing wave field, *Ultrasonics*. 43 (6) (2005) 681-691.
- [70] F. G. Mitri, Acoustic radiation force due to incident plane-progressive waves on coated cylindrical shells immersed in ideal compressible fluids, *Wave Motion*. 43 (6) (2006) 445-457.
- [71] F. G. Mitri, Z. E. A. Fellah, Theoretical calculation of the acoustic radiation force on layered cylinders in a plane standing wave - Comparison of near- and far-field solutions, *J. Phys. A*. 39 (20) (2006) 6085.
- [72] F. G. Mitri, Acoustic radiation force on a cylindrical particle near a planar rigid boundary II. – Viscous fluid cylinder example and inherent radiation torque, *Phys. Open*. 4 (2020) 100029.
- [73] F. G. Mitri, Radiation force of compressional plane waves on a sphere embedded in an elastic medium, *Forces Mech*. 12 (2023) 100221.
- [74] F. G. Mitri, Negative axial radiation force on a fluid and elastic spheres illuminated by a high-order Bessel beam of progressive waves. *Journal of Physics. A, Mathematical and Theoretical*, (2009) 42 (24), 245202.
- [75] C. Andersson, Acoustic levitation of multi-wavelength spherical bodies using transducer arrays of non-specialized geometries, *J. Acoust. Soc. Am*. 151 (2022) 2999–3006.
- [76] A. A. Doinikov, Theory of acoustic radiation pressure for actual fluids, *Physical Review E*, 54(6) (1996) 6297-6303.
- [77] G. T. Silva, S. Chen, L. P. Viana, Parametric Amplification of the Dynamic Radiation Force of Acoustic Waves in Fluids, *Physical Review Letters*, 96 (2006) 234301.
- [78] G. T. Silva, M. W. Urban, M. Fatemi, Multifrequency radiation force of acoustic waves in fluids, *Physica D*, 232 (2007) 48–53.
- [79] F. G. Mitri, M. Fatemi, Dynamic acoustic radiation force acting on cylindrical shells: theory and simulations, *Ultrasonics*, 43 (2005) 435–445.
- [80] S. Oberst, J.C.S. Lai, S. Marburg, Guidelines for numerical vibration and acoustic analysis of disc brake squeal using simple models of brake systems, *J. Sound Vib*. 332(9) (2013) 2284-2299.
- [81] M. Colakoglu, Factors effecting internal damping in aluminum, *J. Theor. App. Mech*. 44(1) (2004) 95-105.

- [82] Q. Cao, X. Han, L. Li, Configurations and control of magnetic fields for manipulating magnetic particles in microfluidic applications: magnet systems and manipulation mechanisms, *Lab Chip*. 14 (2014) 2762-2777.
- [83] M. Hassan, C. Williamson, J. Baptiste, S. Braun, A. J. Stace, E. Besley, B. Stamm, Manipulating Interactions between Dielectric Particles with Electric Fields: A General Electrostatic Many-Body Framework, *J. Chem. Theory Comput.* 18 (10) (2022) 6281–6296.
- [84] T. Karasu, E. Ozgur, L. Uzan, MIP-on-a-chip: Artificial receptors on microfluidic platforms for biomedical applications, *J. Pharm. Biomed. Anal.* 226 (2023) 115257.
- [85] X. Li, Y. Zhou (Eds.), *Microfluidic Devices for Biomedical Applications*, Woodhead Publishing Series in Biomaterials, Woodhead Publishing, 2013. ISBN: 978-0-85709-697-5.
- [86] J. Friend, L. Y. Yeo, Microscale acoustofluidics: Microfluidics driven via acoustics and ultrasonics, *Rev. Mod. Phys.* 83 (2011) 647–704.
- [87] R. Hirayama, D. M. Plasencia, N. Masuda, S. Subramanian, Acoustic levitation for multimodal volumetric display, *Conference: Optical Trapping and Optical Micromanipulation XVII* (2020) 11463.
- [88] W. S. Gan, J. Yang, T. Kamakura, A review of parametric acoustic array in air, *Appl. Acoust.* 73 (2012) 1211–1219.
- [89] H. Chen, S. Bansal, D. M. Plasencia, L. Di-Silvio, J. Huang, S. Subramanian, R. Hirayama, Omnidirectional and multi-material in situ 3D printing using acoustic levitation, *Adv. Mater. Technol.* 9 (2024) 2401792.
- [90] M. A. B. Andrade, A. Marzo, Numerical and experimental investigation of the stability of a drop in a single-axis acoustic levitator, *Phys. Fluids* 31 (2019) 117101.
- [91] Y. Gao, M. Wu, Y. Lin, J. Xu, Acoustic Microfluidic Separation Techniques and Bioapplications: A Review, *Micromachines* 11 (2020) 921.
- [92] A. Marzo, T. Corkett, B. W. Drinkwater, Ultraino: An Open Phased-Array System for Narrowband Airborne Ultrasound Transmission, *IEEE Trans. Ultrason. Ferroelectr. Freq. Control* 65 (2018) 102–111.
- [93] Y. Ochiai, T. Hoshi, J. Rekimoto, Three-Dimensional Mid-Air Acoustic Manipulation by Ultrasonic Phased Arrays, *PLoS ONE* 9 (2014) e97590.

- [94] S. A. Seah, B. W. Drinkwater, T. Carter, R. Malkin, S. Subramanian, Dexterous ultrasonic levitation of millimeter-sized objects in air, *IEEE Trans. Ultrason. Ferroelectr. Freq. Control* 61 (2014) 1233–1236.
- [95] A. Marzo, S. A. Seah, B. W. Drinkwater, D. R. Sahoo, B. Long, S. Subramanian, Holographic acoustic elements for manipulation of levitated objects, *Nat. Comm.* 6 (2015) 8661.
- [96] M. Azarpeyvand, M. Azarpeyvand, Acoustic radiation force on a rigid cylinder in a focused Gaussian beam, *J. Sound Vib.* 332(9) (2013) 2338–2349.
- [97] Y. Qiao, H. Wang, X. Liu, X. Zhang, Acoustic radiation force on an elastic cylinder in a Gaussian beam near an impedance boundary, *Wave Motion*. 93 (2020) 102478.
- [98] M. Rajabi, A. Mojahed, Acoustic manipulation of active spherical carriers: Generation of negative radiation force, *Ann. Phys. (N. Y.)* 372 (2016) 182–200.
- [99] P. L. Marston, Axial Radiation Force of a Bessel Beam on a Sphere, Direction Reversal of the Force, and Solid Sphere Examples, *J. Acoust. Soc. Am.* 121 (2007) 3109.
- [100] P. L. Marston, Scattering of a Bessel Beam by a Sphere, *J. Acoust. Soc. Am.* 121 (2007) 753–8.
- [101] F. G. Mitri, Acoustic Radiation Force of High-Order Bessel Beam Standing Wave Tweezers on a Rigid Sphere, *Ultrasonics*. 49 (2009) 794–8.
- [102] M. Rajabi, A. Mojahed, Acoustic manipulation of oscillatory spherical bodies: emergence of axial negative acoustic radiation force, *J. Sound Vib.* 383 (2016) 265–276.
- [103] M. Rajabi, A. Mojahed, Acoustic manipulation: Bessel beams and active carriers, *Phys. Rev. E*. 96 (4) (2017) 043001.
- [104] M. Rajabi, A. Mojahed, Acoustic radiation force control: Pulsating spherical carriers, *Ultrasonics*. 83 (2018) 146–156,
- [105] A. Mojahed, M. Rajabi, Self-motile swimmers: Ultrasound-driven spherical model, *Ultrasonics*. 86 (2018) 1–5.
- [106] M. Rajabi, A. Mojahed, Acoustic active two-body clusters, *J. Sound Vib.* 429 (2018). 34–44.
- [107] M. Rajabi, H. Khodavirdi, A. Mojahed, Acoustic steering of active spherical carriers, *Ultrasonics*. 105 (2020) 106112.
- [108] H. Khodavirdi, M. Rajabi, Sustainable pulling motion of an active scatterer, *Wave Motion*. 119 (2023) 103134.

- [109] A. Dolev, S. Davis, and I. Bucher, Noncontact dynamic oscillations of acoustically levitated particles by parametric excitation, *Phys. Rev. Appl.* 12 (2019) 034031 (2019).
- [110] V. Paneva, A. Fleig, D. MartíNez Plasencia, T. Faulwasser, J. Müller, OptiTrap: Optimal Trap Trajectories for Acoustic Levitation Displays, *ACM Trans. Graph.* 41 (2022) 173.
- [111] N. Sugita, T. Oshino, T. Shinshi, "Nonlinear coupling between radial and axial vibrations during single-axis acoustic levitation in mid-air," *Int. J. Mech. Sci.* 246 (2023) 108159.
- [112] K. Hasegawa, Y. Abe, A. Fujiwara, Y. Yamamoto, K. Aoki, Internal flow of an acoustically levitated droplet, *Microgravity Sci. Technol.* 20(3–4) (2008) 277–280.
- [113] D. Ilssar, I. Bucher, The effect of acoustically levitated objects on the dynamics of ultrasonic actuators, *J. Appl. Phys.* 121(11) (2017) 114504.
- [114] J. Rudnick, M. Barmatz, Oscillational instabilities in single-mode acoustic levitators, *J. Acoust. Soc. Am.* 87(1) (1990) 81–92.
- [115] D. Foresti, M. Nabavi, D. Poulikakos, On the acoustic levitation stability behaviour of spherical and ellipsoidal particles, *J. Fluid Mech.* 709 (2012) 581–592.
- [116] N. Pérez, M. A. B. Andrade, R. Canetti, J. C. Adamowski, Experimental determination of the dynamics of an acoustically levitated sphere, *J. Appl. Phys.* 116 (2014) 18.
- [117] M. A. B., Andrade, T. S. Ramos, F. T. A. Okina, C. A. Julio, Nonlinear characterization of a single-axis acoustic levitator, *Rev. Sci. Instrum.* 85 (2014) 045125.
- [118] T. Fushimi, T. L. Hill, A. Marzo, B. W. Drinkwater, Nonlinear trapping stiffness of mid-air single-axis acoustic levitators, *Appl. Phys. Lett.* 113(3) (2018) 34102.
- [119] T. Kozuka, K. Yasui, T. Tuziuti, A. Towata, Y. Iida, Noncontact acoustic manipulation in Air, *Jpn. J. Appl. Phys.* 46(7B) (2007) 4948–50.
- [120] S. Tsujino, Y. Sato, Y. Takeda, T. Tomizaki, Oscillation resonances and anisotropic damping of the motion of acoustically levitated droplets in single-axis acoustic levitators, *Appl. Phys. Lett.* 115 (5) (2019) 053702.
- [121] K. Hasegaw, M. Murata, Oscillation dynamics of multiple water droplets levitated in an acoustic field, *Micromachines.* 13 (2022) 1373
- [122] X. Lu, J. Twiefel, Z. Ma, T. Yu, J. Wallaschek, P. Fischer, Dynamic acoustic levitator based on subwavelength aperture control, *Adv. Sci.* 8 (2021) 2100888.

- [123] M. Naka, K. Hasegawa, Breakup characteristics of levitated droplets in a resonant acoustic field, *Phys. Fluids*. 32 (2020) 124109.
- [124] T. Vasileiou, D. Foresti, A. Bayram, D. Poulikakos, A. Ferrari, A. Toward contactless biology: Acoustophoretic DNA transfection, *Sci. Rep.* 6 (2016) 20023.
- [125] M. A. B. Andrade, A. Marzo, J. C. Adamowski, Acoustic levitation in mid-air: Recent advances, challenges, and future perspectives, *Appl. Phys. Lett.* 116 (25) (2020) 250501.
- [126] P. L. Marston, D. B. Thiessen, Manipulation of fluid objects with acoustic radiation pressure, *Ann. N. Y. Acad. Sci.* 1027 (1) (2004) 414–34.
- [127] J. Nakahara, J. R. Smith, Acoustic balance: Weighing in ultrasonic non-contact manipulators, *IEEE Robot. Autom. Lett.* 7 (4) (2022) 9145–50.
- [128] D. Foresti, M. Nabavi, D. Poulikakos, Time-averaged acoustic forces acting on a rigid sphere within a wide range of radii in an axisymmetric levitator, *AIP Conf. Proc.* 1433 (2012) 795–798.
- [129] P. L. Marston, T. D. Daniel, A. R. Fortuner, I. P. Kirsteins, A. T. Abawi, Specular-reflection contributions to static and dynamic radiation forces on circular cylinders, *J. Acoust. Soc. Am.* 149(5) (2021) 3042–3051.
- [130] P. L. Marston, T. D. Daniel, A. R. Fortuner, Specular reflection contributions to dynamic radiation forces on highly reflecting spheres (L), *J. Acoust. Soc. Am.* 150 (1) (2021) 25–28.
- [131] P. L. Marston, Finite-size radiation force correction for inviscid spheres in standing waves, *J. Acoust. Soc. Am.* 142 (2017) 1167-1170.
- [132] P. L. Marston, Phase-shift expansions for approximate radiation forces on solid spheres in inviscid-acoustic standing waves, *J. Acoust. Soc. Am.* 142 (2017) 3358-3361.
- [133] T. Hasegawa, K. Yosioka, Acoustic-Radiation Force on a Solid Elastic Sphere, *J. Acoust. Soc. Am.* 46 (1969) 1139–1143.
- [134] W. R. A. Goossens, Review of the empirical correlations for the drag coefficient of rigid spheres, *Powder Technol.* 352 (2019) 350-359.
- [135] A. H. Nayfeh, D.T. Mook, *Nonlinear Oscillations*, Wiley, New York, (1979).
- [136] D. Xie, N. Huang, A. Wang, A perturbation bound on a class of dynamical model updating problem and a method of keeping its sparse structure, *Mech. Syst. Signal Process.* 70-71 (2016) 300-307.

- [137] J. G. Carbajal, J. Domínguez, Non-linear vibrating systems excited by a nonideal energy source with a large slope characteristic, *Mech. Syst. Signal Process.* 96 (2017) 366-384.
- [138] G. M. Ismail, Md. A. Hosen, M. Mohammadian, M. M. El-Moshneb, Mahmoud Bayat, Nonlinear Vibration of Electrostatically Actuated Microbeam, *Mathematics.* 10 (24) (2022) 4762.
- [139] P. Ju, X. Xue, Global residue harmonic balance method for large-amplitude oscillations of a nonlinear system, *Appl. Math. Model.* 39 (2015) 449–454.
- [140] M. Akbarzade, A. Farshidianfar, Nonlinear transversely vibrating beams by the improved energy balance method and the global residue harmonic balance method, *Appl. Math. Model.* 45 (2017) 393–404.
- [141] J. Lu, Global residue harmonic balance method for strongly nonlinear oscillator with cubic and harmonic restoring force, *J. Low Freq. Noise Vib. Act. Control.* 41 (4) (2022) 1402-1410.
- [142] F. Massa, I. Turpin, T. Tison, From homotopy perturbation technique to reduced order model for multiparametric modal analysis of large finite element models, *Mech. Syst. Signal Process.* 96 (2017) 291-302.
- [143] J. H. He, The simpler, the better: Analytical methods for nonlinear oscillators and fractional oscillators, *J. Low Freq. Noise Vib. Act. Control.* 38 (3-4) (2019) 1252-1260.
- [144] L. Cveticanin, M. Zukovic, I. Ninkov, G. Mester, Nonlinear lightweight metastructure with effective negative stiffness, *Acta Mechanica.* 233 (2022) 4311–4325.
- [145] M. Bayat, M. Head, L. Cveticanin, P. Ziehl, Nonlinear analysis of two-degree of freedom system with nonlinear springs, *Mech. Syst. Signal Process.* 171 (2022) 108891.
- [146] Y. O. El-Dib, N. S. Elgazery, Y. M. Khattab, H. A. Alyousef, An innovative technique to solve a fractal damping Duffing-jerk oscillator, *Commun. Theor. Phys.* 75 (2023) 055001.
- [147] C. S. Liu, C. W. Chang, A novel perturbation method to approximate the solution of nonlinear ordinary differential equation after being linearized to the Mathieu equation, *Mech. Syst. Signal Process.* 178 (2022) 109261.
- [148] J. H. He, F. Y. Ji, H. M. Sedighi, Difference equation vs differential equation on different scales, *Int. J. Numer. Methods Heat Fluid Flow.* 31 (1) (2021) 391-401.
- [149] S. S. Ghadikolaei, Kh. Hosseinzadeh, D.D. Ganji, Numerical study on magnetohydrodynamic CNTs-water nanofluids as a micropolar dusty fluid influenced by

non-linear thermal radiation and joule heating effect, *Powder Technol.* 340(2018) 389-399.

[150] J. H. He, M. L. Jiao, K. A. Gepreel, Y. Khan, Homotopy perturbation method for strongly nonlinear oscillators, *Math. Comput. Simul.* 204(2023) 243-258.

[151] M. Akbarzade, A. Farshidianfar, Nonlinear dynamic analysis of an elastically restrained cantilever tapered beam, *J. Appl. Mech. Tech. Phys.* 58 (3) (2017) 1-11.

[152] Z. Iskakov, K. Bissembayev, N. Jamalov, Resonance vibrations of a gyroscopic rotor with linear and nonlinear damping and nonlinear stiffness of the elastic support in interaction with a non-ideal energy source, *Mech. Syst. Signal Process.* 170 (2022) 108773.

[153] J. H. He, Homotopy perturbation method with two expanding parameters, *Ind. J. Phys.* 88(2) (2014) 193–196.

[154] J. H. He, M. L. Jiao, C. H. He, Homotopy perturbation method for fractal Duffing oscillator with arbitrary conditions, *Fractals.* 30(9) (2022) 2250165.

[155] Md. A. Hosen, M. S. H. Chowdhury, G. M. Ismail, A. Yildirim, A modified harmonic balance method to obtain higher-order approximations to strongly nonlinear oscillators, *J. Interdiscip. Math.* 23(2) (2020) 1-21.

[156] S. Hosseinzadeh, Kh. Hosseinzadeh, M. Rahai, D. D. Ganji, Analytical solution of nonlinear differential equations two oscillators mechanism using Akbari–Ganji method, *Mod. Phys. Lett B.* 35(31) (2021) 2150462.

[157] K. Al-Sankoor, H. Al-Gayyim, S. Al-Musaedi, Z. Asadi, D.D. Ganji, Analytically investigating of heat transfer parameters with presence of graphene oxide nanoparticles in Williamson-magnetic fluid by AGM and HPM methods, *Case Stud. Therm. Eng.* 27 (2021) 101236.

[158] M. A. Attar, M. Roshani, Kh. Hosseinzadeh, D.D. Ganji, Analytical solution of fractional differential equations by Akbari–Ganji’s Method, *Partial Differ. Equ. Appl. Math.* 6 (2022) 100450.

[159] L. Forest, V. Gibiat, A. Hooley, Impedance matching and acoustic absorption in granular layers of silica aerogels, *J. Non-Cryst. Solids* 285 (2001) 230–235.

[160] S. Oberst, J. C. S. Lai, Nonlinear transient and chaotic interactions in disc brake squeal, *J. Sound Vib.* 342 (2015) 272–289.

- [161] S. Lu, S. Oberst, G. Zhang, Z. Luo, Bifurcation analysis of dynamic pricing processes with nonlinear external reference effects, *Commun. Nonlinear Sci. Numer. Simul.* 79 (2019) 104929.
- [162] R. Bavi, H. M. Sedighi, A. Hajnayeb, M. Shishesaz, Parametric resonance and bifurcation analysis of thin-walled asymmetric gyroscopic composite shafts: An asymptotic study, *Thin-Walled Struct.* 184 (2023) 110508.
- [163] J. Więckowski, W. Sałabun, Sensitivity analysis approaches in multi-criteria decision analysis: A systematic review, *Appl. Soft Comput.* 148 (2023) 110915.
- [164] A. Saltelli, S. Tarantola, K. Chan, A role for sensitivity analysis in presenting the results from MCDA studies to decision makers, *J. Multi-Crit. Decis. Anal.* 8 (3) (1999) 139-145.
- [165] Z. Pang, Z. O'Neill, Y. Li, F. Niu, The role of sensitivity analysis in the building performance analysis: A critical review, *Energy Build.* 209 (2020) 109659.
- [166] A. Saltelli, P. Annoni, I. Azzini, F. Campolongo, M. Ratto, S. Tarantola, Variance based sensitivity analysis of model output. Design and estimator for the total sensitivity index, *Comput. Phys. Commun.* 181 (2010) 259–270.
- [167] F. Kabakcioglu, E. Bayraktarkatal, SOBOL sensitivity analysis and acoustic solid coupling approach to underwater explosion, *Ocean Eng.* 281 (2023) 114752.
- [168] W. Zouhri, L. Homri, J. Y. Dantan, Handling the impact of feature uncertainties on SVM: A robust approach based on Sobol sensitivity analysis, *Expert Syst. Appl.* 189 (2022) 115691.
- [169] I. M. Sobol, B. V. Shukhman, Document details - Quasi-Monte Carlo method for solving Fredholm equations, *Monte Carlo Methods Appl.* 25(3) (2019) 253-257.
- [170] G. Glen, K. Isaacs, Estimating Sobol sensitivity indices using correlations, *Environ. Model. Softw.* 37 (2012) 157-166.
- [171] E. B. M. Ngouonkadi, H. B. Fotsin, P. L. Fotso, V. K. Tamba, H. A. Cerdeira, Bifurcations and multistability in the extended Hindmarsh–Rose neuronal oscillator, *Chaos Solit. Fractals.* 85 (2016) 151-163.
- [172] C. Grebogi, E. Ott, J. A. Yorke, Crises, sudden changes in chaotic attractors, and transient chaos, *Physica D.* 7(1-3) (1983) 181-200.
- [173] O.E. Rössler, An equation for continuous chaos, *Phys. Lett. A.* 57(5) (1976) 397-398.

- [174] I. Lengyel, D. H. West, Numerical bifurcation analysis of large-scale detailed kinetics mechanisms, *Curr. Opin. Chem. Eng.* 21 (2018) 41-47.
- [175] E. Wang, K. Ramesh, S. Killen, I. M. Viola, On the nonlinear dynamics of self-sustained limit-cycle oscillations in a flapping-foil energy harvester, *J. Fluids Struct.* 83 (2018) 339-357.
- [176] H. Ying, M. Chao, H. Yuda, Nonlinear stochastic flutter analysis of a three-degree-of-freedom wing in a two-dimensional flow field under stochastic perturbations, *Aerosp. Sci. Technol.* 138 (2023) 108323.
- [177] H. G. Schuster, W. Just, (2006), *Deterministic Chaos: An Introduction*, John Wiley & Sons.
- [178] G. Sin, Global sensitivity analysis using Monte Carlo estimation under fat-tailed distributions, *Chem. Eng. Sci.* 294 (2024) 120124.
- [179] I. M. Sobol, Global sensitivity indices for nonlinear mathematical models and their Monte Carlo estimates, *Math. Comput. Simul.* 55(1-3) (2001) 271-280.
- [180] D. Peng, L. Liu, Importance of global spherical geometry for studying slab dynamics and evolution in models with data assimilation, *Earth Sci. Rev.* 241 (2023) 104414.
- [181] A. Subramanian, S. Mahadevan, Variance-based sensitivity analysis of dynamic systems with both input and model uncertainty, *Mech. Syst. Signal Process.* 166 (2022) 108423.
- [182] E. Borgonovo, E. Plischke, Sensitivity analysis: A review of recent advances, *Eur. J. Oper. Res.* 248(3) (2016) 869-887.
- [183] O. Tsvetkova, T. B. M. J. Ouarda, A review of sensitivity analysis practices in wind resource assessment, *Energy Convers. Manag.* 238 (2021) 114112.
- [184] X. Y. Sun, L. T. H. Newham, B. F.W. Croke, J. P. Norton, Three complementary methods for sensitivity analysis of a water quality model, *Environ. Model. Softw.* 37 (2012) 19-29.
- [185] Mary Eleanor Spear, (1952), *Charting statistics*, McGraw-Hill.
- [186] Mary Eleanor Spear, (1969), *Practical Charting Techniques*, McGraw-Hill.
- [187] John Tukey, (1977), *Exploratory Data Analysis*, Addison–Wesley.
- [188] P. J. Rousseeuw, I. Ruts, J. W. Tukey, The Bagplot: A Bivariate Boxplot, *Am. Stat.* 53(4) (1999) 382-387.

- [189] D. F. Williamson, R. A. Parker, J. S. Kendrick, The box plot: A simple visual method to interpret data, *Ann. Intern. Med.* 10(11) (1989)916-21.
- [190] F. M. Ramos, T. S. Tian, The shifting boxplot. A boxplot based on essential summary statistics around the mean, *Int. J. Psychol.* 3(1) (2010) 37-45.
- [191] J. A. Ndako, J. A. Olisa, I. C. Ifeanyichukwu, S. K. S. Ojo, C. E. Okolie, Evaluation of diagnostic assay of patients with enteric fever by the box-plot distribution method, *New Microb. New Infec.* 38 (2020) 100795.
- [192] O. Yilmaz, I. R. Chen, G. Kulczycki, William B Frakes, Performance Analysis of Spillover-Partitioning Call Admission Control in Mobile Wireless Networks, *Wirel. Pers. Commun.* 53(1) (2010) 111-131.
- [193] A. H. Nayfeh, N. E. Sanchez, Bifurcations in a forced softening duffing oscillator, *Int. J. Nonlin. Mech.* 24(6) (1989) 483-497.
- [194] Holger Kantz, Thomas Schreiber, (2004), *Nonlinear Time Series Analysis*, Cambridge University Press.
- [195] F. S. L. G. Duarte, R. A. Rios, E. R. Hruschka, R. F. de Mello, Decomposing time series into deterministic and stochastic influences: A survey, *Digit. Signal Process.* 95 (2019) 102582.
- [196] Ruey S. Tay, Rong Chen, (2018), *Nonlinear Time Series Analysis*, John Wiley & Sons.
- [197] O. F. Yalcin, M. Dicleli, Effect of the high frequency components of near-fault ground motions on the response of linear and nonlinear SDOF systems: A moving average filtering approach, *Soil Dyn. Earthq. Eng.* 129 (2020) 105922.
- [198] V. Göreke, A novel method based on Wiener filter for denoising Poisson noise from medical X-Ray images, *Biomed. Signal Process. Control.* 79 (2023) 104031.
- [199] G. Fábíán, Generalized Savitzky–Golay filter for smoothing triangular meshes, *Comput. Aided Geom. Des.* 100 (2023) 102167.
- [200] J. M. Moore, M. Small, A. Karrech, Improvements to local projective noise reduction through higher order and multiscale refinements, *Chaos* 25(6) (2015) 063114.
- [201] P. Grassberger, R. Hegger, H. Kantz, C. Schaffrath, and T. Schreiber, On noise reduction methods for chaotic data, *Chaos* 3 (1993) 127.
- [202] K. Urbanowicz, H. Kantz, Improvement of speech recognition by nonlinear noise reduction, *Chaos* 17(2) (2007) 023121 063114.
- [203] https://wiki.octave.org/TISEAN_package
- [204] M.C. Casdagli, Recurrence plots revisited, *Physica D* 108(1-2) (1997) 12-44.

- [205] Y. Zou, R. V. Donner, N. Marwan, J. F. Donges, J. G. Kurths, Complex network approaches to nonlinear time series analysis, *Phys. Rep.* 787 (2019) 1-97.
- [206] G. Camps-Valls, A. Gerhardus, U. Ninad, G. Varando, G. Martius, B. Ballester, R. Vinuesa, E. Diaz, L. Zanna, J. Runge, Discovering causal relations and equations from data, *Phys. Rep.* 1044 (2023) 1-68.
- [207] M. H. Trauth, N. Marwan, Introduction-Time series analysis for Earth, climate and life interactions, *Quat. Sci. Rev.* 284 (2022) 107475.
- [208] F. S. L. G. Duarte, R. A. Rios, E. R. Hruschka, R. F. de Mello, Decomposing time series into deterministic and stochastic influences: A survey, *Digit. Signal Process.* 95, (2019) 102582.
- [209] T. Subba Rao, The bispectral analysis of nonlinear stationary time series with reference to bilinear time-series models, *Handbook of Statistics* 3 (1983) 293-319.
- [210] S. Ganguly, K. Roy, Performance assessment of time-domain damage indicators based on output-only measurement and Poincaré map: A comparative review on nonlinear structures, *Measurement* 216 (2023) 112847.
- [211] N. Marwan, A historical review of recurrence plots, *Eur. Phys. J. Spec. Top.* 164 (2008) 3-12.
- [212] N. Marwan, M. C. Romano, M. Thiel, J. Kurths, Recurrence plots for the analysis of complex systems, *Phys. Rep.* 438 (5-6), (2007) 237-329.
- [213] C. L. Webber Jr., N. Marwan, A. Facchini, A. Giuliani, Simpler methods do it better: Success of Recurrence Quantification Analysis as a general-purpose data analysis tool, *Phys. Lett. A.* 373 (41) (2009) 3753-3756.
- [214] S. Schinkel, N. Marwan, J. Kurths, Brain signal analysis based on recurrences, *J. Physiol. Paris.* 103 (6) (2009) 315-323.
- [215] N. Marwan, J. Kurths, S. Foerster, Analysing spatially extended high-dimensional dynamics by recurrence plots, *Phys. Lett. A.* 379 (10-11) (2015) 894-900.
- [216] S. Wallot, Recurrence Quantification Analysis of Processes and Products of Discourse: A Tutorial in R, *Discourse Process.* 54 (5-6) (2017) 382-405.
- [217] R. V. Donner, Y. Zou, J. F. Donges, N. Marwan, J. Kurths, Recurrence networks—a novel paradigm for nonlinear time series analysis, *New J. Phys.* 12 (2010) 033025.
- [218] J. F. Donges, J. Heitzig, R. V. Donner, J. Kurths, Analytical framework for recurrence network analysis of time series, *Phys. Rev. E.* 85 (2012) 046105.

- [219] Y. Chen, A. Lin, Order pattern recurrence for the analysis of complex systems, *Phys. A: Stat. Mech. Appl.* 607 (2022) 128204.
- [220] S. Oberst, S. Marburg, N. Hoffmann, Determining periodic orbits via nonlinear filtering and recurrence spectra in the presence of noise, *Procedia Eng.* 199 (2017) 772-777.
- [221] N. Marwan, J. F. Donges, R. V. Donner, D. Eroglu, Nonlinear time series analysis of palaeoclimate proxy records, *Quat. Sci. Rev.* 274 (2021) 107245.
- [222] S. Y., Y. Feng, D. Zhang, H. D. Bedru, B. Xu, F. Xia, Motif discovery in networks: A survey, *Comput. Sci. Rev.* 37 (2020) 100267.
- [223] F. Abdullah, P. D. Christofides, Data-based modeling and control of nonlinear process systems using sparse identification: An overview of recent results, *Comput. Chem. Eng.* 174 (2023) 108247.
- [224] M. Raissi, Deep hidden physics models: Deep learning of nonlinear partial differential equations, *Vibration J. Mach. Learn. Res.* 19 (2018) 1-24.
- [225] G. Tran, R. Ward, Exact recovery of chaotic systems from highly corrupted data, *Multiscale Model. Simul.* 15(3) (2017) 1108-1129.
- [226] S. K. Bishnu, S. Y. Alnouri, D. M. Al-Mohannadi, Computational applications using data driven modeling in process Systems: A review, *Digit. Chem. Eng.* 8 (2023) 100111.
- [227] I. H. Sarker, Machine Learning: Algorithms, Real-World Applications and Research Directions, *SN Comput. Sci.* 2(160) (2021) 1007.
- [228] S. L. Brunton, J. L. Proctor, J. N. Kutz, Discovering governing equations from data by sparse identification of nonlinear dynamical systems, *Proc. Natl. Acad. Sci.* 113 (15) (2016) 3932-3937.
- [229] S. L. Brunton, J. L. Proctor, J. N. Kutz, Sparse Identification of Nonlinear Dynamics with Control (SINDYc), *IFAC-PapersOnLine.* 49(18) (2016) 710-715.
- [230] A. R. Ugolini, V. Breschi, A. Manzoni, M. Tanelli, SINDy vs Hard Nonlinearities and Hidden Dynamics: a Benchmarking Study, *arXiv:2403.00578v1 [eess.SY]* (2024).
- [231]
https://pysindy.readthedocs.io/en/latest/examples/2_introduction_to_sindy/example.html
 1.

- [232] M. Stender, S. Oberst, N. P. Hoffmann, Recovery of Differential Equations from Impulse Response Time Series Data for Model Identification and Feature Extraction, *Vibration* 2(1) (2019) 25-46.
- [233] J. Wentz, A. Doostan, N. P. Hoffmann, Derivative-based SINDy (DSINDy): Addressing the challenge of discovering governing equations from noisy data, *Comput. Methods Appl. Mech. Eng.* 413 (2023) 116096.
- [234] A. Krakovská, K. Mezeiová, H. Budálová, Use of False Nearest Neighbours for Selecting Variables and Embedding Parameters for State Space Reconstruction, *J. Complex Syst.* 2015 (2015) 932750.
- [235] S. Wallot, D. Mønster, Calculation of Average Mutual Information (AMI) and False-Nearest Neighbors (FNN) for the Estimation of Embedding Parameters of Multidimensional Time Series in Matlab, *Front. Psychol.* 9 (2018) 1679.
- [236] S. H. Lang, H. Zhu, G. D. Sun, Y. Jiang, C. L. Wei, A Study on Methods for Determining Phase Space Reconstruction Parameters, *J. Comput. Nonlinear Dynam.* 17(1) (2022) 011006.
- [237] J. F. Yamagishi, K. Kaneko, Chaos with a high-dimensional torus, *Phys. Rev. Res.* 2 (2020) 023044.
- [238] T. Kapitaniak, *Chaos for Engineers: Theory, Applications, and Control*, Springer; 2nd rev. ed. 2000 edition.
- [239] C. Geier, M. Stender, N. Hoffmann, Building functional networks for complex response analysis in systems of coupled nonlinear oscillators, *J. Sound Vib.* 590 (2024) 118544.

APPENDIX

MATLAB Code: SENSITIVITY ANALYSIS

```
clc
clear all
n_base=35;
X=[(10.*rand(n_base,1)) (0.15.*rand(n_base,1)) (10.*rand(n_base,1))];
X1=X(:,1);
X2=X(:,2);
X3=X(:,3);

for i=1:n_base

    a=X(i,1);
    b=X(i,2);
    f=X(i,3);

    Output(i)=SOBOL_fun(a,b,f);

end

VARY=var(Output);

for i=1:n_base
    a=X(i,1);
    for j=1:n_base

        b=X(j,2);
        f=X(j,3);
        Output(j)=SOBOL_fun(a,b,f);

    end
    Ei(i,1)=mean(Output);
end

S1=var(Ei)/VARY;

for i=1:n_base
    b=X(i,2);
    for j=1:n_base

        a=X(j,1);
        f=X(j,3);
        Output(j)=SOBOL_fun(a,b,f);

    end
    Ei(i,1)=mean(Output);
end
S2=var(Ei)/VARY;

for i=1:n_base
    f=X(i,3);
```

```

    for j=1:n_base

        a=X(j,1);
        b=X(j,2);

        Output(j)=SOBOL_fun(a,b,f);

    end
    Ei(i,1)=mean(Output);
end
S3=var(Ei)/VARY;

S=[S1 S2 S3]

for i=1:n_base
    b=X(i,2);
    f=X(i,3);

    for j=1:n_base

        a=X(j,1);
        Output(j)=SOBOL_fun(a,b,f);

    end
    Ei(i,1)=mean(Output);
end

ST1=1-var(Ei)/VARY;

for i=1:n_base
    a=X(i,1);
    f=X(i,3);

    for j=1:n_base

        b=X(j,2);
        Output(j)=SOBOL_fun(a,b,f);

    end
    Ei(i,1)=mean(Output);
end

ST2=1-var(Ei)/VARY;

for i=1:n_base
    a=X(i,1);
    b=X(i,2);

    for j=1:n_base

        f=X(j,3);
        Output(j)=SOBOL_fun(a,b,f);

    end
end

```

```

    Ei(i,1)=mean(Output);
end

ST3=1-var(Ei)/VARY;

ST=[ST1 ST2 ST3]

function out=SOBOL_fun(A,B,F)
% a function that works with thfe trial Sobol Method program

x0=0.00001;
y0=0;
Omega=10;
omega=Omega*2*pi;

alpha=A;
beta=B;
gama=F;
T=10;
i=0;
h=.001;
t1=0;
x1=x0;
y1=y0;

while t1<=T
    i=i+1;
    f1=(-alpha*abs(y1)*y1^1-
beta*sin(x1)+1*gama*sin(omega*t1)*cos(x1));
    t2=t1+h/2;
    x2=x1+y1*h/2;
    y2=y1+f1*h/2;
    f2=(-alpha*abs(y2)*y2^1-
beta*sin(x2)+1*gama*sin(omega*t2)*cos(x2));
    t3=t1+h/2;
    x3=x1+y2*h/2;
    y3=y1+f2*h/2;
    f3=(-alpha*abs(y3)*y3^1-
beta*sin(x3)+1*gama*sin(omega*t3)*cos(x3));
    t4=t1+h;
    x4=x1+y3*h;
    y4=y1+f3*h;
    f4=(-alpha*abs(y4)*y4^1-
beta*sin(x4)+1*gama*sin(omega*t4)*cos(x4));
    x=x1+(h/6)*(y1+2*y2+2*y3+y4);
    y=y1+(h/6)*(f1+2*f2+2*f3+f4);
    TT(i)=t1;
    X(i)=x;
    Y(i)=y;
    t1=t4;
    x1=x;
    y1=y;

end

out=var(Y);

```

```
end
```

MATLAB Code: PSD AND TIME SERIES DATA

```
clc
clear all
close all
fmax = 500;

% Initialize variables.
load('G:/OCTAVECSV1/data1195de.mat');

%Volt = noisy_s;
Volt = denoised_s;

signal = Volt;
time = t;

% Define the sampling frequency and time step
Fs = 1 / (time(2) - time(1)); % Sampling frequency (Hz)
dt = 1 / Fs;                  % Time step

% Perform the FFT
N = length(signal);           % Length of the signal
freq = Fs * (0:(N/2)) / N;    % Frequency vector
fft_signal = fft(signal);
fft_amplitude = abs(fft_signal / N); % FFT amplitude in volts (V)

% Compute the Power Spectral Density (PSD)
psd = (1 / (Fs * N)) * abs(fft_signal).^2; % PSD in volts squared per
hertz (V2/Hz)

% Plot the time series data

figure
plot(time, signal, 'LineWidth', 2)
xlabel('Time [s]', 'FontName', 'Times New Roman', 'FontSize', 24)
ylabel('Amplitude [V]', 'FontName', 'Times New Roman', 'FontSize', 24)

set(gca, 'FontName', 'Times New Roman', 'FontSize', 24)

% plot 2: Power Spectral Density (PSD) with logarithmic y-axis
figure
semilogy(freq, psd(1:N/2+1), 'LineWidth', 2)
xlim([0 fmax])
xlabel('Frequency [Hz]', 'FontName', 'Times New Roman', 'FontSize',
24)
ylabel('PSD [V2/Hz]', 'FontName', 'Times New Roman', 'FontSize', 24)

set(gca, 'FontName', 'Times New Roman', 'FontSize', 24)

% Display the maximum PSD value and its corresponding frequency
[max_psd, max_psd_idx] = max(psd);
disp(['Maximum PSD: ' num2str(max_psd) ' V2/Hz at frequency: '
num2str(freq(max_psd_idx)) ' Hz'])
```

```

%%%%%%%%%%%%%%%%%%%%%%%%%%%%%%%%%%%%%%%%%%%%%%%%%%%%%%%%%%%%%%%%%%%%%%%%
psd_dB = 10 * log10(psd);
psd=psd_dB;
%%%%%%%%%%%%%%%%%%%%%%%%%%%%%%%%%%%%%%%%%%%%%%%%%%%%%%%%%%%%%%%%%%%%%%%%
figure
plot(freq, psd(1:N/2+1), 'LineWidth', 2)
xlim([0 250])
figure;
subplot(3,1,1);
plot(time, velocity, 'k');
xlabel('Time');
ylabel('Velocity');
title('Velocity vs Time');

subplot(3,1,2);
plot(time(1:end-1), acceleration_smoothed);
xlabel('Time');
ylabel('Acceleration');
title('Acceleration vs Time');

subplot(3,1,3);
plot(time, displacement_stationary);
xlabel('Time');
ylabel('Displacement');
title('Displacement vs Time');

%Plot the Phase Space
figure
plot(displacement_stationary, velocity);
xlabel('Displacement');
ylabel('Velocity');
title('Phase space-Moving Average');
hold on

load('G:/OCTAVECSV/data21142DENOIS.mat');
denoised_s=500/4*denoised_s;
displacement2 = cumtrapz(t, denoised_s);
% Estimate and remove the trend
trend = polyval(polyfit(t, displacement2, 1), t); % Estimate the
linear trend
displacement_stationary2 = displacement2 - trend; % Subtract the
trend from the original data

%Plot the Phase Space
figure
plot(displacement_stationary2, denoised_s);
xlabel('Displacement');
ylabel('Velocity');
title('Phase space-GHKSS');
hold on

% Set default font properties
set(0, 'DefaultAxesFontName', 'Times New Roman');
set(0, 'DefaultAxesFontSize', 20);

```

MATLAB Code: RECURRENCE PLOT AND NETWORK

```

clc

clear all

```



```

close all
load('G:/OCTAVECSV/data1142de.mat');

% Allocate imported array to column variable names

Volt = denoised_s;

signal = Volt;
time = t;
ecg=500/4*Volt;
%%%%%%%%%%
ecg = ecg + 0*randn(size(ecg));
window_size = 4;
velocity_smoothed = zeros(size(ecg));  vector

for i = 1:numel(ecg)
    start_idx = max(1, i - floor(window_size/2));
    end_idx = min(numel(ecg), i + floor(window_size/2));
    velocity_smoothed(i) = mean(ecg(start_idx:end_idx));
end

%add noise

velocity_smoothed = velocity_smoothed +
0*randn(size(velocity_smoothed));

% Add the noise to the original vector
ecg=velocity_smoothed;
%%%%%%%%%%%%%%%%%%%%%%%%%%%%%%%%%%%%%%%%%%%%%%%%%%%%%%%%%%%%%%%%%%%%%%%%
% mutual information test to determine the time delay
mutual(ecg);

% fnn test to determine the embedding dimension
out=false_nearest(ecg,1,10,8);
fnn = out(:,1:2);
figure('Position',[100 400 460 360]);
plt=plot(fnn(:,1),fnn(:,2),'o-','MarkerSize',4.5);
title('False nearest neighbor
test','FontSize',10,'FontWeight','bold');
xlabel('dimension','FontSize',10,'FontWeight','bold');
ylabel('FNN','FontSize',10,'FontWeight','bold');
get(gcf,'CurrentAxes');
set(gca,'LineWidth',2,'FontSize',10,'FontWeight','bold');
grid on;

% phase space plot
y = phasespace(ecg,3,8);
figure('Position',[100 400 460 360]);
plot3(y(:,1),y(:,2),y(:,3),'-','LineWidth',1);

set(gca,'CameraPosition',[25.919 27.36 13.854]);
xlabel('x(t)','FontSize',24,'FontWeight','normal');
ylabel('x(t+\tau)','FontSize',30,'FontWeight','normal');
zlabel('x(t+2\tau)','FontSize',30,'FontWeight','normal');
set(gca,'LineWidth',2,'FontSize',30,'FontWeight','normal');

%%%%%%%%%%%%%%%%%%%%%%%%%%%%%%%%%%%%%%%%%%%%%%%%%%%%%%%%%%%%%%%%%%%%%%%%

% Calculate the distance matrix based on Euclidean distance

```

```

dist_matrix = squareform(pdist(y));

%%%%%%%%%%%%%%%%%%%%%%%%%%%%%%%%%%%%%%%%%%%%%%%%%%%%%%%%%%%%%%%%%%%%%%%% Set a distance threshold to determine the
adjacency %
distance_threshold = 34; % Adjust this threshold as needed

% Create the binary adjacency matrix
adjacency_matrix = dist_matrix <= distance_threshold;

% Specify the file path and name for the CSV file
folderPath = 'C:\Users\Mehdi\Desktop\New folder (8)\adjmatrix\';
filename = 'adj_Matrix.csv';
filePath = fullfile(folderPath, filename);

% Save the adjacency matrix as a CSV file
%writematrix(adjacency_matrix, filePath);

% Display a summary of the adjacency matrix
disp('Summary of Adjacency Matrix:');
disp(['Matrix Size: ', num2str(size(adjacency_matrix, 1)), ' x ',
num2str(size(adjacency_matrix, 2))]);
disp(['Number of Edges: ', num2str(nnz(adjacency_matrix))]);

%%%%%%%%%%%%%%%%%%%%%%%%%%%%%%%%%%%%%%%%%%%%%%%%%%%%%%%%%%%%%%%%%%%%%%%%

% Create the graph object from the adjacency matrix
G = graph(adjacency_matrix);

figure;
% Remove self-connections
G = rmedge(G, find(G.Edges.EndNodes(:,1) == G.Edges.EndNodes(:,2)));

% Plot the graph without node labels and self-connections
plot(G, 'NodeLabel', '', 'LineWidth', 1.5);

%%%%%%%%%%%%%%%%%%%%%%%%%%%%%%%%%%%%%%%%%%%%%%%%%%%%%%%%%%%%%%%%%%%%%%%%
% color recurrence plot
cerecurr_y(y);
recurdata = cerecurr_y(y);

% black-white recurrence plot
tdrecurr_y(recurdata,distance_threshold);
recurrpt = tdrecurr_y(recurdata,distance_threshold);

%Recurrence quantification analysis
% rqa_stat - RQA statistics - [recreate DET LMAX ENT TND LAM TT]
rqa_stat = recurrqa_y(recurrpt);

function buffer = cerecurr_y(signal)

len = length(signal);
N = len;
Y = signal;

```

```

buffer=zeros(N);

%h = waitbar(0,'Please wait...');
for i=1:N
    %waitbar(i/N);
    x0=i;
    for j=i:N
        y0=j;
        % Calculate the euclidean distance
        distance = norm(Y(i,:)-Y(j,:));
        % Store the minimum distance between the two points
        buffer(x0,y0) = distance;
        buffer(y0,x0) = distance;
    end
end
%close(h);

rmin=min(min(buffer));
rmax=max(max(buffer));

%%%%%%%%%%%%%%%%%%%%%%%%%%%%%%%%%%%%%%%%%%%%%%%%%%%%%%%%%%%%%%%%%%%%%%%%
if nargin == 0
    figure('Position',[100 100 550 400]);
    imagesc(buffer);
    colormap Jet;
    colorbar;
    axis image;
    xlabel('Time Index','FontSize',10,'FontWeight','bold');
    ylabel('Time Index','FontSize',10,'FontWeight','bold');
    title('Recurrence Plot','FontSize',10,'FontWeight','bold');
    get(gcf,'CurrentAxes');
    set(gca,'YDir','normal')
    set(gca,'LineWidth',2,'FontSize',10,'FontWeight','bold');
end

function rqa_stat = recurrqa_y(recurrpt,linepara)

if nargin<2 || isempty(linepara)
    linepara = 2;
end

W=max(recurrpt(:,1));
matrixsize=size(recurrpt);
if matrixsize(2)~=2
    fprintf('Please provide the right recurrence point matrix! Thank you!');
end

ptdiff = diff(recurrpt,1,2);
indices = find(ptdiff);
duprecurr = recurrpt(indices,:);
recurrpt = duprecurr;
clear duprecurr;

if isempty(recurrpt)
    rqa_stat = zeros(1,6);
else

```

```

recreate=100*length(recurrpt)/(W*(W-1)/2)
recurrpt = sortrows(recurrpt,1);
recurrpt = horzcat(recurrpt,recurrpt(:,2)-recurrpt(:,1));
recurrpt = sortrows(recurrpt,3);

%%%%%%%%%%%%%%%%%%%%%%%%%%%%%%%%%%%%%%%%%%%%%%%%%%%%%%%%%%%%%%%%%%%%%%%%
% Horizorntal Line Structure Search
%%%%%%%%%%%%%%%%%%%%%%%%%%%%%%%%%%%%%%%%%%%%%%%%%%%%%%%%%%%%%%%%%%%%%%%%
k=1;
j=1;
[row,col]=size(recurrpt);
for i=1:row-1
    if recurrpt(i,3)==recurrpt(i+1,3)
        s{k}(j)=recurrpt(i,1);
        displace(k)=recurrpt(i,3);
        j=j+1;
        if i==length(recurrpt)-1
            s{k}(j)=recurrpt(i+1,1);
        end
    else
        s{k}(j)=recurrpt(i,1);
        j=1;
        k=k+1;
    end
end

k=1;
diag = [];
len=1;
for i=1:length(s)
    for j=1:length(s{i})-1
        if s{i}(j)+1==s{i}(j+1)
            len=len+1;
        else
            diag(k)=len;
            disp(k)=displace(i);
            k=k+1;
            len=1;
        end
        if j==length(s{i})-1
            diag(k)=len;
            disp(k)=displace(i);
            k=k+1;
            len=1;
        end
    end
end

%TND=(disp')\ (diag');
if isempty(diag);diag = 0; end

%Entropy Calculation
diag=diag(find(diag>linepara));
vect = diag(:);
region = max(vect) - min(vect) + 1;
freq = hist (vect, region);
prob = freq / sum (freq);
nonz = prob (find (prob));
ENT = sum (nonz .* (-log2 (nonz)));

```

```

DET = 100*sum(diag)/length(recurrpt);
LMAX = max(diag);

%%%%%%%%%%%%%%%%%%%%%%%%%%%%%%%%%%%%%%%%%%%%%%%%%%%%%%%%%%%%%%%%%%%%%%%%
% Vertical Line Structure Search
%%%%%%%%%%%%%%%%%%%%%%%%%%%%%%%%%%%%%%%%%%%%%%%%%%%%%%%%%%%%%%%%%%%%%%%%
clear s;
recurrpt = sortrows(recurrpt,1);
k=1;
j=1;
for i=1:row-1
    if recurrpt(i,1)==recurrpt(i+1,1)
        s{k}(j)=recurrpt(i,2);
        j=j+1;
        if i==length(recurrpt)-1
            s{k}(j)=recurrpt(i+1,2);
        end
    else
        s{k}(j)=recurrpt(i,2);
        j=1;
        k=k+1;
    end
end

k=1;
len=1;
vert = [];
for i=1:length(s)
    for j=1:length(s{i})-1
        if s{i}(j)+1==s{i}(j+1)
            len=len+1;
        else
            vert(k)=len;
            k=k+1;
            len=1;
        end
        if j==length(s{i})-1
            vert(k)=len;
            k=k+1;
            len=1;
        end
    end
end
if isempty(vert); vert = 0; end

vert=vert(find(vert>linepara));
LAM = 100*sum(vert)/length(recurrpt);
TT = mean(vert);

if isempty(DET)||isnan(DET);DET = 0; end
if isempty(LMAX)||isnan(LMAX);LMAX = 0; end
if isempty(ENT)||isnan(ENT);ENT = 0; end
if isempty(LAM)||isnan(LAM);LAM = 0; end
if isempty(TT)||isnan(TT);TT = 0; end

rqa_stat=[recreate DET LMAX ENT LAM TT];
%rqa_stat=[recreate DET LMAX ENT TND LAM TT];
end

```

```

function [ Y ] = phasespace(signal,dim,tau)

N = length(signal);
% Total points on phase space
T=N-(dim-1)*tau;
% Initialize the phase space
Y=zeros(T,dim);

for i=1:T
    Y(i,:)= signal(i+(dim-1)*tau-sort((0:dim-1),'descend')*tau)';
end

sizeY=size(Y,2);

if nargin == 0
    if sizeY == 2
        plot(Y(:,1),Y(:,2));
        xlabel('y1','FontSize',10,'FontWeight','bold');
        ylabel('y2','FontSize',10,'FontWeight','bold');
        get(gcf,'CurrentAxes');
        set(gca,'FontSize',10,'FontWeight','bold');
        grid on;
    else
        plot3(Y(:,1),Y(:,2),Y(:,3));
        xlabel('y1','FontSize',10,'FontWeight','bold');
        ylabel('y2','FontSize',10,'FontWeight','bold');
        zlabel('y3','FontSize',10,'FontWeight','bold');
        get(gcf,'CurrentAxes');
        set(gca,'FontSize',10,'FontWeight','bold');
        grid on;
    end
end

function mi = mutual(signal,partitions,tau)

av = mean(signal);
variance = var(signal);
minimum = min(signal);
maximum = max(signal);
interval = maximum-minimum;
len = length(signal);

if nargin<2 | isempty(partitions)
    partitions = 16;
end
if nargin<3 | isempty(tau)
    tau = 20;
end

for i = 1:1:len
    signal(i) =(signal(i)- minimum)/interval;
end

for i = 1:1:len
    if signal(i) > 0
        array(i) = ceil(signal(i)*partitions);
    else

```

```

        array(i) = 1;
    end
end

shannon = make_cond_entropy(0,array,len,partitions);

if (tau >= len)
    tau=len-1;
end

for i = 0:1:tau
    mi(i+1) = make_cond_entropy(i,array,len,partitions);
end

if nargout == 0
    figure('Position',[100 400 460 360]);
    plot(0:1:tau,mi,'o-','MarkerSize',5);
    title('Mutual Information Test (first local
minimum)','FontSize',10,'FontWeight','bold');
    xlabel('Delay (sampling time)','FontSize',10,'FontWeight','bold');
    ylabel('Mutual Information','FontSize',10,'FontWeight','bold');
    get(gcf,'CurrentAxes');
    set(gca,'FontSize',10,'FontWeight','bold');
    grid on;
end

function mi = make_cond_entropy(t,array,len,partitions)

hi=0;
hii=0;
count=0;
hpi=0;
hpj=0;
pij=0;
cond_ent=0.0;

h2 = zeros(partitions,partitions);

for i = 1:1:partitions
    h1(i)=0;
    h11(i)=0;
end

for i=1:1:len
    if i > t
        hii = array(i);
        hi = array(i-t);
        h1(hi) = h1(hi)+1;
        h11(hii) = h11(hii)+1;
        h2(hi,hii) = h2(hi,hii)+1;
        count = count+1;
    end
end

norm=1.0/double(count);

```

```

cond_ent=0.0;

for i=1:1:partitions
    hpi = double(h1(i))*norm;
    if hpi > 0.0
        for j = 1:1:partitions
            hpj = double(h11(j))*norm;
            if hpj > 0.0
                pij = double(h2(i,j))*norm;
                if (pij > 0.0)
                    cond_ent = cond_ent + pij*log(pij/hpj/hpi);
                end
            end
        end
    end
end

mi = cond_ent;

function out = false_nearest(signal,mindim,maxdim,tau,rt,eps0)

if nargin<2 | isempty(mindim)
    mindim = 1;
end
if nargin<3 | isempty(maxdim)
    maxdim = 5;
end
if nargin<4 | isempty(tau)
    tau = 1;
end
if nargin<5 | isempty(rt)
    rt = 10;
end
if nargin<6 | isempty(eps0)
    eps0=1/1000;
end

minimum = min(signal);
maximum = max(signal);
interval = maximum-minimum;
len = length(signal);
BOX = 1024;
ibox = BOX-1;
theiler = 0;
global aveps vareps variance box list toolarge

for i = 1:1:len
    signal(i) =(signal(i)- minimum)/interval;
end
av = mean(signal);
variance = std(signal);

out = zeros(maxdim,4);

for dim = mindim:maxdim
    epsilon=eps0;
    toolarge=0;

```



```

alldone=0;
donesofar=0;
aveps=0.0;
vareps=0.0;

for i=1:len
    nearest(i)=0;
end

fprintf('Start for dimension=%d\n',dim);

while (~alldone && (epsilon < 2*variance/rt))
    alldone=1;
    make_box(signal,len-1,dim,tau,epsilon);
    for i=(dim-1)*tau+1:(len-1)
        if (~nearest(i))

nearest(i)=find_nearest(i,dim,tau,epsilon,signal,rt,theiler);
            alldone = bitand(alldone,nearest(i));
            donesofar = donesofar+nearest(i);
        end
    end

    fprintf('Found %d up to
epsilon=%d\n',donesofar,epsilon*interval);

    epsilon=epsilon*sqrt(2.0);
    if (~donesofar)
        eps0=epsilon;
    end
end
if (donesofar == 0)
    fprintf('Not enough points found!\n');
    fnn = 0;
else
    aveps = aveps*(1/donesofar);
    vareps = vareps*(1/donesofar);
    fnn = toolarge/donesofar;
end

out(dim,:) = [dim fnn aveps vareps];

end

function y = find_nearest(n,dim,tau,eps,signal,rt,theiler)
global aveps vareps variance box list toolarge

element=0;
which= -1;
dx=0;
maxdx=0;
mindx=1.1;
factor=0;
ibox=1023;

x=bitand(ceil(signal(n-(dim-1)*tau)/eps),ibox);
if x==0
    x=1;

```

```

end
y=bitand(ceil(signal(n)/eps),ibox);
if y==0
    y=1;
end

for x1=x-1:x+1
    if x1==0
        continue
    end
    x2= bitand(x1,ibox);
    for y1=y-1:y+1
        if y1==0
            continue
        end
        element = box(x2,bitand(y1,ibox));
        while (element ~= -1)
            if (abs(element-n) > theiler)
                maxdx=abs(signal(n)-signal(element));
                for i=1:dim
                    i1=(i-1)*tau;
                    dx = abs(signal(n-i1)-signal(element-i1));
                    if (dx > maxdx)
                        maxdx=dx;
                    end
                end
                if ((maxdx < mindx) && (maxdx > 0.0))
                    which = element;
                    mindx = maxdx;
                end
            end
            element = list(element);
        end
    end
end

if ((which ~= -1) && (mindx <= eps) && (mindx <= variance/rt))
    aveps = aveps+mindx;
    vareps = vareps+mindx*mindx;
    factor=abs(signal(n+1)-signal(which+1))/mindx;
    if (factor > rt)
        toolarge=toolarge+1;
    end
    y = 1;
else
    y = 0;
end
end

function make_box(ser,l,dim,del,eps)
global box list
bs=1024;
ib=bs-1;

box = -ones(bs,bs);

for i=(dim-1)*del+1:l

```

```

x = bitand(ceil (ser (i-(dim-1)*del)/eps),ib);
if x==0
    x=1;
end
y = bitand(ceil (ser (i)/eps),ib);
if y==0
    y=1;
end
list(i)=box(x,y);
box(x,y)=i;
end

```

MATLAB Code: SINDy

```

clear all, close all, clc
figpath = '../figures/';
addpath('../utils');

%% generate Data
polyorder = 4; % search space up to fifth order polynomials
usesine = 1; % no trig functions
n = 2; % 3D system

Ain=1*0.001;
Omega=39;

Cd=1.06;
r=0.71*0.001;
rhoa=1.19;
Alpha=3.06*10^-6;
Beta=1315;
rhop=34;
Mp=4/3*pi*r^3*rhop;
a=1/Mp*1/Beta*pi/8*Cd*(2*r)^2*rhoa
b=Beta*Alpha/Mp
b/6
f=Beta^2/Mp*Alpha*Ain

A = [0 1; -b 0];
B= [0 0; 0 -a];
C= [0 0; b/6 0];
F= [0 0; f 0];

tspan=0:.00001:2; % time span
x0 = [0.001; 0]; % initial conditions
options = odeset('RelTol',1e-4,'AbsTol',1e-4*ones(1,n));

[t,x]=ode45(@funxyp,tspan,x0,options); % integrate

%% compute Derivative

```

```

eps = 0;          % noise strength
for i=1:length(x)
    dx(i,:) = A*(x(i,:).^1)' + B*(x(i,:).^2)' + C*(x(i,:).^3)' +
    F*(cos(x(i,:)).*[sin(Omega*t(i)) sin(Omega*t(i))])';
end
dx = dx + eps*randn(size(dx));    % add noise

%% pool Data (i.e., build library of nonlinear time series)
Theta = poolData(x,n,polyorder,usesine);
%%%%%%%%%%%%%%%%%%%%%%%%%%%%%%%%%%%%%%%%%%%%%%%%%%%%%%%%%%%%%%%%%%%%%%%%

%%%%%%%%%%%%%%%%%%%%%%%%%%%%%%%%%%%%%%%%%%%%%%%%%%%%%%%%%%%%%%%%%%%%%%%%
m = size(Theta,2);

%% compute Sparse regression: sequential least squares
lambda = .000001;          % lambda is our sparsification knob.
Xi = sparsifyDynamics(Theta,dx,lambda,n);

digits(4);
Yi=vpa(Xi)

%%%%%%%%%%%%%%%%%%%%%%%%%%%%%%%%%%%%%%%%%%%%%%%%%%%%%%%%%%%%%%%%%%%%%%%%
syms y1 y2 y1y1 y1y2 y2y2 y1y1y1 y1y1y2 y1y2y2 y2y2y2 y1y1y1y1
y1y1y1y2 y1y1y2y2 y1y2y2y2 y2y2y2y2 y1Sin(Omegat) y2Sin(Omegat)
Siny1Sin(Omegat) ...
    Siny2Sin(Omegat) Cosy1Sin(Omegat) Cosy2Sin(Omegat)

VS=[1 y1 y2 y1y1 y1y2 y2y2 y1y1y1 y1y1y2 y1y2y2 y2y2y2 y1y1y1y1
y1y1y1y2 y1y1y2y2 y1y2y2y2 y2y2y2y2 y1Sin(Omegat) y2Sin(Omegat)
Siny1Sin(Omegat) ...
    Siny2Sin(Omegat) Cosy1Sin(Omegat) Cosy2Sin(Omegat)];

ydot1=VS.'.*Xi(:,1)

ydot2=vpa(VS.'.*Xi(:,2))

clc
clear all

%% Initialize variables.
filename = 'C:\Users\Mehdi\Desktop\New folder
(2)\scop5\scope_905.csv';
delimiter = ',';
startRow = 3;

formatSpec = '%f%f%[\n\r]';

%% Open the text file.
fileID = fopen(filename,'r');

dataArray = textscan(fileID, formatSpec, 'Delimiter', delimiter,
'EmptyValue', NaN, 'HeaderLines', startRow-1, 'ReturnOnError', false);

%% Close the text file.
fclose(fileID);
second = dataArray(:, 1);
Volt = dataArray(:, 2);

```

```

%% Clear temporary variables
clearvars filename delimiter startRow formatSpec fileID dataArray ans;

%% Laser Doppler Vibrometer Volt--->Velocity;
% Sensitivity of LDV
Velo=500; % Check it from LDV
Sen=Velo/4;
second=second-second(1,1);

second(1,:)=[];
Volt(1,:)=[];
Velocity=Sen*Volt; % Unit : [mm/s]
displacment=cumtrapz(second,Velocity); % Unit : [mm]
figure
plot(second,Velocity,'b')
%% Figures: Displacment, Accelaration
figure
plot(second,displacment,'r')
figure
plot(displacment,Velocity)
acc = diff(Velocity)./diff(second); % Unit : [mm/s^2]
k1=size(second);
kn=k1(1,1);
second(kn,:)=[];
figure
plot(second,acc,'g')
%%%%%%%%%%%%%%%%%%%%%%%%%%%%%%%%%%%%%%%%%%%%%%%%%%%%%%%%%%%%%%%%%%%%%%%%%%%%%%
%%
%V = diff(displacment)./diff(second);
%L1=size(second);
%Ln=L1(1,1);
%second(Ln,:)=[];
%acc=diff(V)./diff(second);
%second(Ln-1,:)=[];
%plot(second,acc,'g')

%% generate Data %SINDy
polyorder = 9; % search space up to fifth order polynomials
usesine = 1; % no trig functions
n = 2; % 2D system

x=[displacment,Velocity];
k1=size(x);
kn=k1(1,1);
x(kn,:)=[];
x(kn-1,:)=[];
Velocity(kn,:)=[];
Velocity(kn-1,:)=[];
acc(kn-1,:)=[];
dx=[Velocity,acc];
Theta = poolData(x,n,polyorder,usesine);

m = size(Theta,2);

%% compute Sparse regression: sequential least squares
lambda = .000001; % lambda is our sparsification knob.
Xi = sparsifyDynamics(Theta,dx,lambda,n);

```

```

digits(4);
Yi=vpa(Xi)

syms y1 y2 y1y1 y1y2 y2y2 y1y1y1 y1y1y2 y1y2y2 y2y2y2 y1y1y1y1
y1y1y1y2 y1y1y2y2 y1y2y2y2 y2y2y2y2 y1Sin(Omegat) y2Sin(Omegat)
Siny1Sin(Omegat) ...
    Siny2Sin(Omegat) Cosy1Sin(Omegat) Cosy2Sin(Omegat)

VS=[1 y1 y2 y1y1 y1y2 y2y2 y1y1y1 y1y1y2 y1y2y2 y2y2y2 y1y1y1y1
y1y1y1y2 y1y1y2y2 y1y2y2y2 y2y2y2y2 y1Sin(Omegat) y2Sin(Omegat)
Siny1Sin(Omegat) ...
    Siny2Sin(Omegat) Cosy1Sin(Omegat) Cosy2Sin(Omegat)];

ydot1=VS.'.*Xi(:,1)

ydot2=vpa(VS.'.*Xi(:,2))

function ydot=funxyp(t,Y)

Ain=1*0.001;
Omega=39;

Cd=1.06;
r=0.71*.001;
rhoa=1.19;
Alpha=3.06*10^-6;
Beta=1315;
rhop=34;
Mp=4/3*pi*r^3*rhop;
a=1/Mp*1/Beta*pi/8*Cd*(2*r)^2*rhoa;
b=Beta*Alpha/Mp;
f=Beta^2/Mp*Alpha*Ain;

A = [0 1; -b 0];
B= [0 0; 0 -a];
C= [0 0; b/6 0];
F= [0 0; f 0];

ydot=A*[Y(1);Y(2)].^1+B*[Y(1);Y(2)].^2+C*[Y(1);Y(2)].^3+F*[cos(Y(1))*s
in(Omega*t);cos(Y(2))*sin(Omega*t)];
function yout = poolData(yin,nVars,polyorder,usesine)

Omega=30;
t=0.0001:0.0001:0.1997;
n = size(yin,1);
% yout =
zeros(n,1+nVars+(nVars*(nVars+1)/2)+(nVars*(nVars+1)*(nVars+2)/(2*3))+
11);

ind = 1;
% poly order 0

```

```

yout(:,ind) = ones(n,1);
ind = ind+1;

% poly order 1
for i=1:nVars
    yout(:,ind) = yin(:,i);
    ind = ind+1;
end

if(polyorder>=2)
    % poly order 2
    for i=1:nVars
        for j=i:nVars
            yout(:,ind) = 1*abs(yin(:,i)).*yin(:,j);
            ind = ind+1;
        end
    end
end

if(polyorder>=3)
    % poly order 3
    for i=1:nVars
        for j=i:nVars
            for k=j:nVars
                yout(:,ind) = yin(:,i).*yin(:,j).*yin(:,k);
                ind = ind+1;
            end
        end
    end
end

if(polyorder>=4)
    % poly order 4
    for i=1:nVars
        for j=i:nVars
            for k=j:nVars
                for l=k:nVars
                    yout(:,ind) =
0*yin(:,i).*yin(:,j).*yin(:,k).*yin(:,l);
                    ind = ind+1;
                end
            end
        end
    end
end

if(polyorder>=5)
    % poly order 5
    for i=1:nVars
        for j=i:nVars
            for k=j:nVars
                for l=k:nVars
                    for m=l:nVars
                        yout(:,ind) =
yin(:,i).*yin(:,j).*yin(:,k).*yin(:,l).*yin(:,m);
                        ind = ind+1;
                    end
                end
            end
        end
    end
end

```

```

    end
end

if(polyorder>=6)
    % poly order 6
    for i=1:nVars
        for j=i:nVars
            for k=j:nVars
                for l=k:nVars
                    for m=l:nVars
                        for ml=m:nVars
                            yout(:,ind) =
0*yin(:,i).*yin(:,j).*yin(:,k).*yin(:,l).*yin(:,m).*yin(:,ml);
                            ind = ind+1;
                        end
                    end
                end
            end
        end
    end
end

if(polyorder>=7)
    % poly order 7
    for i=1:nVars
        for j=i:nVars
            for k=j:nVars
                for l=k:nVars
                    for m=l:nVars
                        for ml=m:nVars
                            for m2=m1:nVars
                                yout(:,ind) =
yin(:,i).*yin(:,j).*yin(:,k).*yin(:,l).*yin(:,m).*yin(:,ml).*yin(:,m2)
;
                                ind = ind+1;
                            end
                        end
                    end
                end
            end
        end
    end
end

if(polyorder>=8)
    % poly order 8
    for i=1:nVars
        for j=i:nVars
            for k=j:nVars
                for l=k:nVars
                    for m=l:nVars
                        for ml=m:nVars
                            for m2=m1:nVars
                                for m3=m2:nVars
                                    yout(:,ind) =
0*yin(:,i).*yin(:,j).*yin(:,k).*yin(:,l).*yin(:,m).*yin(:,ml).*yin(:,m
2).*yin(:,m3);
                                    ind = ind+1;
                                end
                            end
                        end
                    end
                end
            end
        end
    end
end

```



```

if(polyorder>=11)
    % poly order 11
    for i=1:nVars
        for j=i:nVars
            for k=j:nVars
                for l=k:nVars
                    for m=l:nVars
                        for m1=m:nVars
                            for m2=m1:nVars
                                for m3=m2:nVars
                                    for m4=m3:nVars
                                        for m5=m4:nVars
                                            for m6=m5:nVars
                                                yout(:,ind) =
yin(:,i).*yin(:,j).*yin(:,k).*yin(:,l).*yin(:,m).*yin(:,m1).*yin(:,m2)
.*yin(:,m3).*yin(:,m4).*yin(:,m5).*yin(:,m6);
                                                ind = ind+1;
                                            end
                                        end
                                    end
                                end
                            end
                        end
                    end
                end
            end
        end
    end

if(usesine)

    yout=[yout (yin).*[sin(Omega*t) ; sin(Omega*t)]'
sin(yin).*[cos(Omega*t) ; cos(Omega*t)]' cos(yin).*[sin(Omega*t) ;
sin(Omega*t)]'];

    %end
end
function Xi = sparsifyDynamics(Theta,dXdt,lambda,n)
Xi = Theta\dXdt; % initial guess: Least-squares

% lambda is our sparsification knob.
for k=1:10
    smallinds = (abs(Xi)<lambda); % find small coefficients
    Xi(smallinds)=0; % and threshold
    for ind = 1:n % n is state dimension
        biginds = ~smallinds(:,ind);
        % Regress dynamics onto remaining terms to find sparse Xi
        Xi(biginds,ind) = Theta(:,biginds)\dXdt(:,ind);
    end
end

function ykplus1 = sparseGalerkinDiscrete(t,y,ahat)

```

```
yPool = poolData1D(y',length(y));  
ykplus1 = (yPool*ahat)';
```